ACOUSTICALLY INDUCED FLUID FLOWS IN A MODEL FISH EAR

A Dissertation
Presented to
The Academic Faculty

by

Charlotte Walker Kotas

In Partial Fulfillment
of the Requirements for the Degree
Doctor of Philosophy in the
School of Mechanical Engineering

Georgia Institute of Technology

December 2008

ACOUSTICALLY INDUCED FLUID FLOWS IN A MODEL FISH EAR

Approved by:

Dr. Peter H Rogers, Co-Adviser
School of Mechanical Engineering
Georgia Institute of Technology

Dr. Minami Yoda, Co-Adviser
School of Mechanical Engineering
Georgia Institute of Technology

Dr. Jeanette Yen
School of Biology
Georgia Institute of Technology

Dr. Don Giddens
College of Engineering
Georgia Institute of Technology

Mr. David Trivett
School of Mechanical Engineering
Georgia Institute of Technology

Dr. Fotis Sotiropoulos
Department of Civil Engineering
University of Minnesota

Date Approved: November 10, 2008

I must admit that I have never liked to work hard. Preparing for college examinations was something I could do, but I hated to do it. Even today, I dislike deadlines. But there is one thing I am always ready to do, and that is to look at beautiful things.

Georg von Békésy

Concerning the Pleasures of Observing, and the Mechanics of the Inner Ear

ACKNOWLEDGEMENTS

I wish to thank my advisers, coworkers, friends and family for their continued support as I have pursued these studies. Without them, this research would not have been possible. The guidance of my advisers was essential in improving this document. Any remaining mistakes are mine alone.

In particular, I wish to thank my husband, whose enduring love and patience has not only brightened my days, it has also kept me sane. In addition, I wish to thank my parents, who taught me to value knowledge and pursue the truth.

I would also like to gratefully acknowledge the financial support received from the National Science Foundation, Achievement Rewards for College Scientists, the General Electric Foundation's Faculty for the Future program, and the Georgia Institute of Technology in the form of graduate student fellowships. This research was also sponsored by the Office of Naval Research under award numbers N00014-04-1-0102 and N00014-07-1-0238.

TABLE OF CONTENTS

LIST OF TABLES

LIST OF FIGURES

NOMENCLATURE

a	Half-dimension of the body along the axis of oscillation, [length]
b	Maximum half-dimension of the body normal to the axis of oscillation, [length]
c	Slot radius, [length]
$c_e^{\,2} = b^2 - a^2$	Focal length of an ellipse, [length]
d	Body length scale (typically the radius or diameter of the object in the oscillating flow), [*length*]
f_0	Fundamental frequency for multiple frequency oscillations, $[\text{time}]^{-1}$
f_i	Oscillation frequency of component i of a multiple frequency oscillation, $[\text{time}]^{-1}$
h	Minimum distance from body to stagnation point in the center of the inner rotating region, [length]
l_{cilia}	Typical length of the hair cell cilia, usually assumed to be 10 μm, [length]
r, z	Cylindrical coordinates
r_{eq}	Equivalent radius, or the radius of a sphere of equal volume, [length]
s	Amplitude of oscillation (particle displacement), [length]
t_s	Start up time, [time]
x, y	Cartesian coordinates
$\vec{v}$	Velocity vector, $[\text{length}][\text{time}]^{-1}$
A	Angular location of stagnation point on grooved body surface
A_p, A_o	Location of the center of the vortical region near a prolate (oblate) body
A, B, C, D, E, F, G, H	Stagnation point locations near axisymmetric body
$AR = a/b$	Spheroid aspect ratio

$L = (a^4/b)^{1/3}$	Body length scale, [length]
$L^* = (ab)^{1/2}$	Alternative body length scale, [length]
$Re_M = \frac{\omega d^2}{\nu}$	Ratio of viscous length scale to body length scale
$Re = \frac{U_0 d}{\nu} = \varepsilon Re_M^{\ 2}$	Reynolds number
$Re_s = \frac{\omega s^2}{\nu} = \varepsilon^2 Re_M^{\ 2}$	Streaming Reynolds number
Re^*	Reynolds number calculated with L^* as the length scale
S.G.	Specific gravity
T	Horizontal distance from edge of spheroid to stagnation point at the edge of the inner rotating region, [length]
$U_0 = s\omega$	Velocity scale (the particle velocity), [length][time]$^{-1}$
U_∞	Maximum velocity of multiple frequency oscillations, [length][time]$^{-1}$
$V_s = \varepsilon s\omega$	Streaming flow velocity scale, [length][time]$^{-1}$
α	Secondary orientation angle for model otolith
$\dot{\gamma}$	Shear rate, [time]$^{-1}$
$\delta_{u,v}$	Standard deviation in the measured (u or v) velocity data, [length][time]$^{-1}$
$\varepsilon = \frac{U_0}{\omega d} = \frac{s}{d}$	Amplitude ratio
$\varepsilon^* \equiv U_\infty / \ (2\pi f_0 L)$	Amplitude ratio for multiple frequency oscillations
ε^*	Amplitude ratio using L^* as the length scale (for angled spheroids)
ϕ	Oscillation phase, [rad/s]
φ	Angular location of stagnation point on ungrooved, angled body
λ, μ	Oblate spheroidal coordinates
μ	Dynamic viscosity, [mass][length]$^{-1}$ [time]$^{-1}$

θ	Orientation angle body, for spheroids it is measured from the axis of symmetry of the body to the axis of oscillation
v	Kinematic viscosity, $[\text{length}]^2[\text{time}]^{-1}$
ρ	Fluid density, $[\text{mass}][\text{length}]^{-3}$
ω	Radial frequency, $[\text{radians}][\text{time}]^{-1}$
$1/\omega$	Time scale, $[\text{time}][\text{radians}]^{-1}$
$\Delta_{u,v}$	Uncertainty in the (u or v) velocity data, $[\text{length}][\text{time}]^{-1}$

SUMMARY

The fish ear contains three dense, bony bodies (otoliths) surrounded by fluid (the endolymph) and tissue. Under acoustic stimulation, the surrounding fluid and tissues oscillate relative to the otoliths, stimulating the endolymph as well as the array of hair cell cilia adjacent to the otolith and embedded in tissue. It is believed that the hair cell cilia move with the surrounding fluid. This doctoral thesis studied the steady streaming (*i.e.*, time-independent) component of the acoustically induced fluid motion inside of the fish ear to determine how the hair cell cilia displacements due to the steady streaming could provide acoustically relevant information to the fish.

This research characterizes the fluid flow around oscillating model otoliths, namely spheroids, grooved spheroids, and a 350% scale model of a cod saccular otolith. This study models the otolithic endorgan as an oscillating body in a Newtonian fluid. The model ignores the surrounding tissues and assumes that the hair cell cilia move like the surrounding fluid. Particle pathline visualizations and particle-image velocimetry (PIV) are used to characterize the flow fields at various oscillation orientations, frequencies and amplitudes. These data are used to determine the location of the stagnation points on the body surface and at the boundaries of the inner rotating region of the flow. Studies are also conducted on bodies sinusoidally oscillated at both a single frequency and two (simultaneous) frequencies along the same direction. Both the steady streaming flow patterns and velocity fields are found to contain acoustically relevant information, but given the very small displacements associated with these flows, it is unclear if the steady streaming flows can be sensed by the fish ear.

CHAPTER 1

INTRODUCTION

Understanding the acoustics of underwater environments allows commercial fishermen to locate schools of fish using sonar, climatologists to measure ocean temperatures, biologists to track marine mammals, and oceanographers to measure the depth of the ocean. Fish also use acoustic sensing to understand their environments, particularly over long distances, where chemical and optical means are less effective. They can sense frequencies from 10 Hz to 1000 Hz (and higher, depending on the species), discriminate sounds separated by an angle of about 10°, and respond to acoustic particle motions as small as 0.1 nm (Popper *et al.* 2003). Given its abilities to sense, discriminate, and directionalize a variety of sounds in a relatively small volume, the fish ear is a unique underwater acoustic sensor. Understanding the fish ear is therefore useful not only in marine biology but also as an inspiration for new biomimetic underwater acoustic sensors.

The transduction mechanism within the fish ear which translates the acoustical stimulus into information about its surroundings is poorly understood. However, it is unlikely that fish use the same inter-aural phase and amplitude differences that terrestrial animals use to directionalize sounds. This is because the fish ear is operating underwater where the sound speed is approximately 1500 m/s, which results in sound wavelengths that are roughly 4.5 times longer than those in air for a given frequency. At the same time, fish are essentially acoustically transparent resulting in ears that are closer together than most terrestrial animals. The sound arriving at each location should have essentially the same phase and amplitude, minimizing any difference between the two ears.

Fish bodies have an acoustic impedance similar to that of water and hence tend to follow the acoustic particle motion. The fish ear, however, is not entirely transparent to

incident sound waves. Inside each ear are three small, dense, bony bodies known as otoliths. In the presence of sound, the otoliths will lag behind the motion of the head of the fish due to their greater inertia. These relative motions deflect the sensory hair cells within the ear and are sensed as sound. Understanding the fluid flows surrounding the otolith is therefore fundamental to understanding how the fish ear transduces acoustic signals.

The fluid flows themselves will be primarily oscillatory, with a small steady streaming component. The steady component, over many oscillation cycles, may tend to bias the flows within the fish ear into patterns. These patterns, shaped by the unusual geometries of the otolith, should contain acoustically relevant information that the fish could extract and use to interpret the sounds. Yoda *et al*. (2001) have suggested in their "Auditory Retina Hypothesis" that these flow patterns could be used to decode the acoustical environment in much the same way as the (visual) retina uses patterns to decode the optical environment.

The goal of this thesis is to explore the auditory retina hypothesis by determining if acoustical information useful to interpreting sound fields is contained within the secondary steady streaming flows. This information is then broadened to the fish ear by exploring the effect of the otolith geometry on the flow fields and by exploring the effect of the hair cell orientation groups in filtering the created flow patterns. The thesis is organized into chapters containing a literature review, experimental setup, steady streaming patterns near spheres and spheroids oscillated at single frequencies, steady streaming patterns near spheres and spheroids oscillated at multiple frequencies, steady streaming patterns near angled spheroids, steady streaming patterns near grooved spheroids, steady streaming patterns near a scale model of a cod otolith, and conclusions.

.

CHAPTER 2

LITERATURE REVIEW

2.1 Underwater Acoustics Primer

Underwater, hearing is the most important sense because sound is the primary means of underwater communication. Light can only penetrate through a few tens of meters of sea water in most cases, limiting the utility of vision. And the relatively slow rates of chemical diffusion in water (*vs.* in air) limit the range of smell and/or taste. Sounds, or acoustic vibrations, especially those at low frequencies, can travel long distances: 1600 km in the case of whale songs (Mercado III and Frazer 1999). This section will introduce some of the relevant concepts of underwater acoustics necessary to understand fish hearing.

Sound waves are longitudinal compressional waves which are formed as density variations propagate through the medium. These waves are also represented by pressure, velocity, displacement, and temperature waves as well. Although acoustic waves include both travelling and standing waves, this thesis is primarily concerned with directionalizing travelling waves.

In order to illustrate the properties associated with underwater sounds, consider a point source in a homogeneous medium radiating sound equally in all directions. The resulting solution for the particle velocity of the spherical wave may be viewed as consisting of two parts. The first, due to the compression of the medium, is inversely proportional to the distance from the source and dominates in the "far-field." The second term, due to the incompressible fluid motion, is inversely proportional to the distance from the source squared and dominates in the "near-field." In the "far field," the curvature of the sound waves will be negligible compared with the wavelength and the

sound will behave locally like a plane wave. Moving closer to the source, into the "near field," the sound radiation pattern is more complicated (Rogers and Cox 1988). This thesis is primarily concerned with the plane sound waves of the "far-field."

The source generates traveling waves which cause pressure, density and temperature fluctuations at each point in space. By monitoring several points, the variations in these scalar quantities can be used to calculate vector quantities associated with the sound, including its propagation speed and direction. As reviewed by Hartmann (1999), this is essentially how terrestrial ears directionalize (*i.e.*, determine the direction of) sound sources. Each human ear independently measures the pressure at two points in space, on either side of the head. We then directionalize sound sources by comparing the signals at each ear. At relatively low audible frequencies (20–1500 Hz), where the wavelengths of incident sounds are longer than the separation distance between the ears, the interaural time difference or the interaural phase difference between the signals at each ear can be used to directionalize the source. [The time delay is better correlated to the lateralization of the sound than the phase delay (Zhang and Hartmann 2006).] At higher frequencies the sound wavelength is shorter than the distance between our ears, which means that the time delay produces ambiguous results because of the (unknown) number of full cycles between the ears. Above about 4000 Hz, humans determine the direction of the sound source by comparing the sound intensity levels at each ear (augmented by the shadowing effect of the head). The body is then acting as a filter which shapes the relative magnitude of each frequency of the sound incident at each ear based on the source direction. This effect is known as the head related transfer function (HRTF). At intermediate frequencies, a combination of the two methods is used, and accurate directionalization in this range requires the presence of multiple frequencies.

Human ears are able to directionalize the azimuthal position of a sound far more quickly than the elevation [less than 3 ms to about 80 ms to get a stable direction from Gaussian noise (Hofman and Van Opstal 1998)]. The auditory techniques used to

determine the elevation of sound relies on the HRTF. However, the HRTF is a monaural sound cue.

Fish, however, cannot use time of arrival or intensity differences between their two ears because the wavelengths of the sounds that are heard by fish are much greater than their inter-ear spacing. Underwater sounds have much longer wavelengths at a given frequency than sounds in air because of the much higher sound speed in water (1500 m/s, *vs*. 340 m/s in air), and fish have a much smaller spacing between their ears [a few cm, *vs.* 17.5 cm for humans (Hartmann 1999)]. The acoustic impedance of the fish body is also roughly the same as that of water [1.5×10^5 g·s^{-1}·cm^{-2} for sea water *vs.* 1.64×10^5 g·s^{-1}·cm^{-2} for fish flesh and 2.57×10^5 g·s^{-1}·cm^{-2} for fish bone (Iida *et al.* 2004)] making it essentially acoustically transparent (van Bergeijk 1967) and eliminating filtering cues similar to the HRTF used by humans.

The directionalization of underwater sound sources is complicated by the presence of the water surface and bottom. The sound waves generated by a point source will travel outward until they encounter either the free surface (the air-water interface) or the sea/river bed, or are turned by refraction (from the vertical variations in the sound speed due to the decreasing temperature and increasing pressure from the surface to the bottom). At the free surface the majority of the acoustic energy will be reflected back into the water. This reflected wave will be out of phase with the incident wave, and may degrade the signal near the water surface. At the bottom, sound waves are usually strongly attenuated by sand and sediment unless the angle of incidence is less than the critical angle [$\theta_c = \arccos\left(c_w / c_s\right)$, where the critical angle θ_c is measured with respect to the horizontal and in the sound speed, c, the subscripts w and s refer to the water and sediment, respectively]. Under the right conditions, sound can even travel extremely long distances without reaching the bottom. The vertical variations in the sound speed profile create acoustic waveguides which refract a majority of the source's energy. Due

to the variety of direct and reflected paths a sound may travel from the source to the receiver, the direction of the incident sound may not be the same as the direction to the source.

The sound propagation is minimally affected by attenuation. Attenuation, such as that from viscous friction forces in the water, chemical relaxation, and absorption and scattering by entrained air bubbles, is only about 0.1 dB/km at 1 kHz, and still less at lower frequencies, and is weak enough to allow significant propagation distances (thousands of miles) to be achieved before becoming an issue (Brekhovskikh and Lysanov 2003). Also, due to the relative slowness of ocean currents compared to the sound speed, underwater sounds are reciprocal. By this we mean that the path a sound wave travels from position A to position B is the same as the path from B to A. A fish trying to avoid being heard by a predator or prey animal must be very quiet, since if the fish can hear them, the other animals can hear him (Rogers and Cox 1988).

Although it is not yet known how fish interpret their acoustical environment, fish would find a biological advantage in hearing many kinds of sounds. Fish must be looking for information not only about potential mates and prey, but also about potential predators. (All fish at some point in their life cycle are prey to larger fish.) These noises may also be masked by the ambient noise in the environment. Figure 2.1 shows a typical map of ocean noise as a function of frequency (Brekhovskikh and Lysanov 2003). From these curves, we can see that man-made noise dominates below 1000 Hz, while environmental noise dominates at higher frequencies. Note that at 100 Hz, a fish ear listening for biological noises (curve 10) must be sensitive enough to detect 80 dB re 20 μ Pa $Hz^{-1/2}$, or a particle displacement of 0.1 nm. Obviously the fish ear must be incredibly sensitive to detect this level of stimulus. These charts also help us to visualize how complex the frequency spectrum of underwater sound sources can be, with fish needing to be aware of, and accurately interpret, multiple sound sources operating in various frequency ranges simultaneously.

The next sections describe the morphology and capabilities of the fish ear, as well as how the fish ear responds to these acoustic signals. Given the importance of acoustics in their environment, fish are presumably able to interpret these signals as well as hear them, despite the complexity of sound propagation. How the experiment models the acoustic stimulation of the fish ear will be discussed after the fish ear and its fluid dynamics are described.

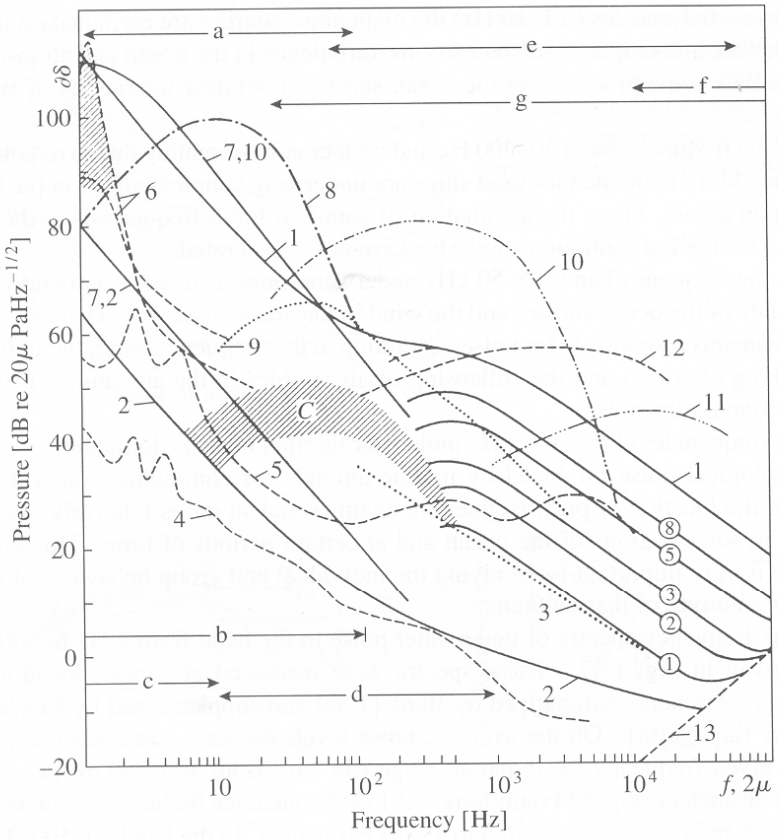

Averaged frequency spectra of ocean ambient noise [1.38] 1, 2—maximum and minimum levels of dynamic noise; 3—noise during a calm, the numbers in circles—wind speed force (Beaufort); 4, 5—under-ice noise; 6—seismic background noise; 7, 2 and 7, 10—pseudo-sound (numbers after comma denote the pulsation speed of turbulent vortex, m/s; 8—noise from earthquakes; 9—traffic noise (region C—noise of shipping lines); 10, 11—noise off fish from the drum and shrimp families; 12—very heavy rain at sea; 13—thermal noise. Horizontal arrows denote frequency ranges of main sources of noise: a—seismic background, explosions, earthquakes, and ice reefing; b—turbulence; c—surface waves; d—industrial activity; e—cavitation and rain; f—thermal noise; g—sea organisms

Figure 2.1 Ocean noise diagram (Figure 1.37 in Brekhovskikh and Lysanov 2003)

2.2 The Fish Ear

2.2.1 Fish Ear Anatomy

The fish ear has been studied by many researchers whose results are reviewed in several articles (e.g. Popper and Coombs 1980; Hawkins 1981; Platt and Popper 1981; Popper *et al.* 1988; Popper and Fay 1993; Schellart and Wubbels 1997; Popper and Lu 2000; Popper *et al.* 2003). In general, each fish has two ears, mirrored at a slight angle to the vertical mid-plane of and on either side of its head. Each ear contains three semicircular canals and three other sac-like features known as otolithic endorgans (Helfman *et al.* 1997). Although the functions of the different components of the ear are inter-related, the semi-circular canals are primarily used for determining rotational accelerations, while the otoliths are responsible for sensing acoustic signals, whole body acceleration, and the vertical orientation of the fish's body (Helfman *et al.* 1997).

The lateral line system, which consists of neuromasts (groups of hair cells enclosed in a gelatinous cupula) running along the fish's body, is related to the fish ear in that it uses hair cells to detect low frequency fluid displacements along the fish's body, such as those generated by nearby fish swimming or flows around obstacles (*e.g.* a rock in a river). These neuromasts can either be on the skin or enclosed in channels along the body which are open to the surrounding fluid at small pores (Helfman *et al.* 1997). There is even some evidence that the lateral line is necessary for some orienting behaviors. Braun and Coombs (2000) report that the mottled sculpin (*Cottus bairdi*) can sense the presence of a 6 mm sphere vibrating at 50 Hz, but cannot orient to it if the lateral line has been deactivated.

The anatomical variations in the nearly 25,000 species of fish (Helfman *et al.* 1997) make it difficult to speak of a "typical" fish. However, for the purposes of illustration, the goldfish will be used as an example of a typical fish. As shown in Figure 2.2, the ears (pink) sit on either side of the brain (green). In some fish, like the goldfish,

small bones known as Weberian ossicles (red) serve to connect the swimbladder (blue) to ears. Fish with adaptations, like Weberian ossicles or extensions of the swimbladder itself, allowing the ears to sense the pressure-induced displacements of the swimbladder are known as "hearing specialists". Fish without these enhancements are known as "hearing generalists" (Popper and Fay 1993). Coupling the fish ear to the pressure sensitive swimbladder lowers the hearing threshold and improves the frequency range of the ear (Popper and Lu 2000). In fact, fish without swimbladders such as flatfish and sharks have little or no sensitivity of acoustic pressure and instead must "hear" the acoustic particle velocity.

The parts of the ear least associated with hearing are the semicircular canals, which consist of ring-shaped tubes of endolymph that define distinct planes. These mechanical devices sense the low frequency accelerations associated with changes in orientation (Helfman *et al.* 1997). Physically, this is accomplished when movement of the fish moves the endolymph, stimulating a gelatinous mass (the cupula) within the swollen regions (the ampulla) at the base of each canal. The motion of the cupula is then sensed by the embedded sensory hair cells (Platt and Popper 1981).

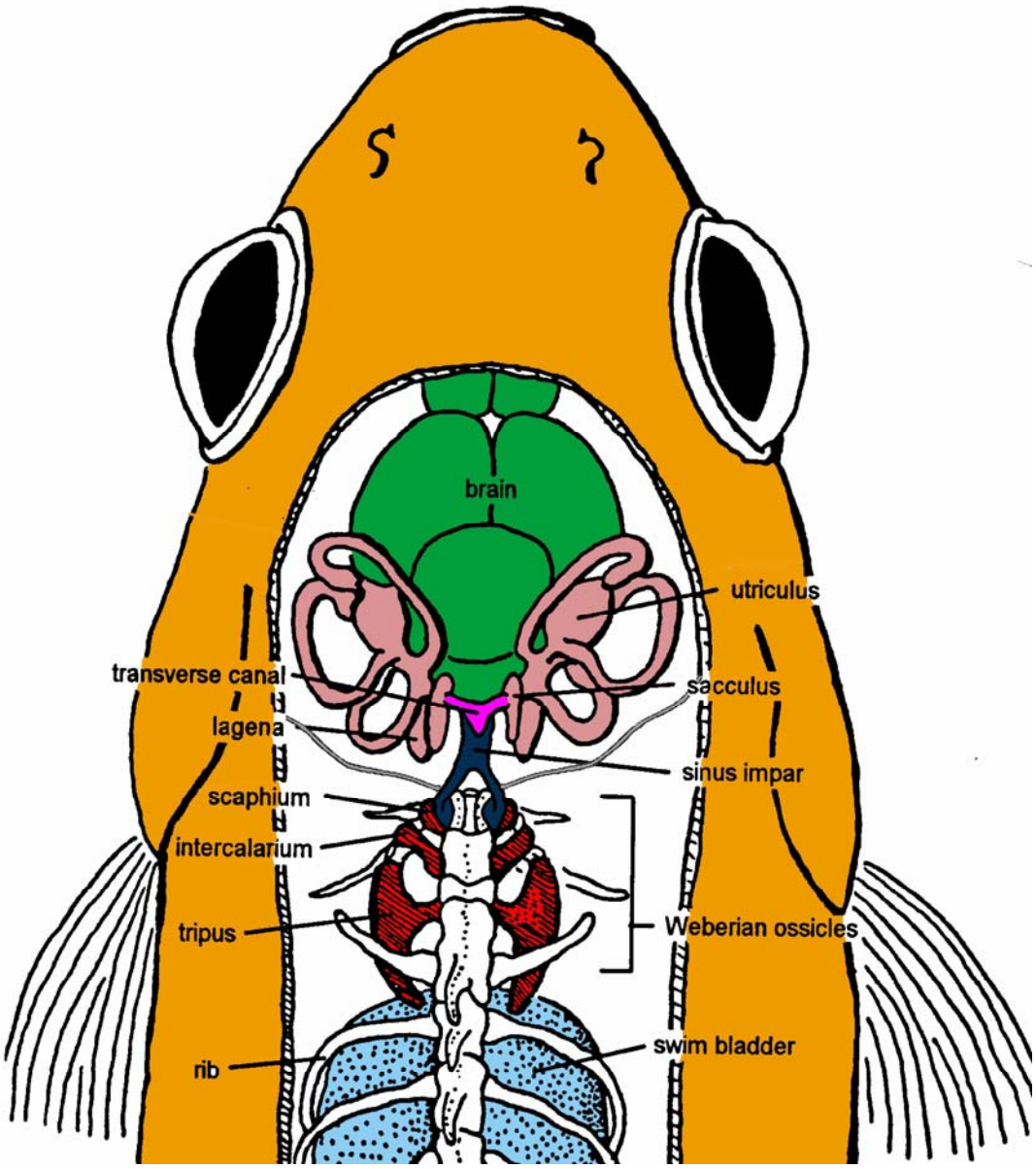

Figure 2.2 Illustration of the goldfish auditory system, with the brain shown in green, inner ear (*i.e.* the utriculus, sacculus, and lagena) in pink, Weberian ossicles in red, and the swimbladder in blue (adapted from Popper and Coombs 1979).

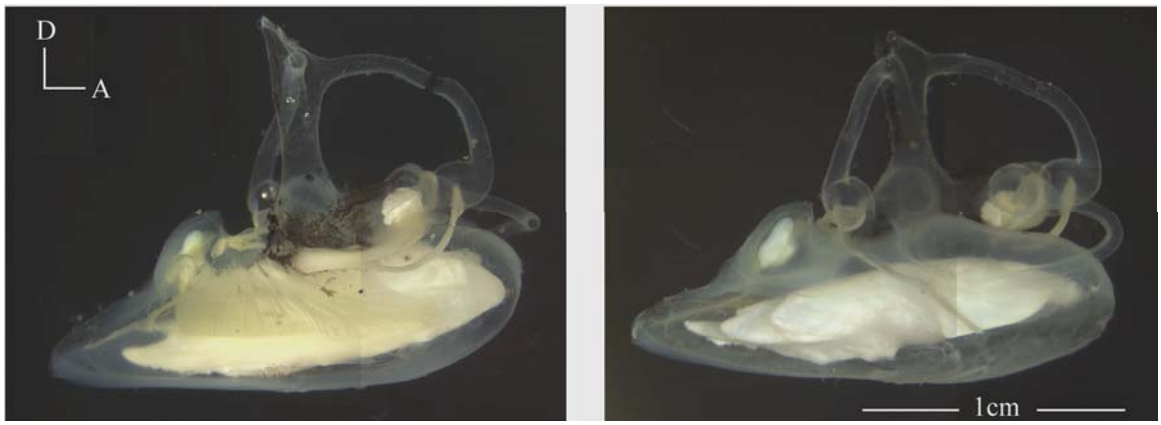

Figure 2.3 Left and right ears of a deep sea cod (image from http://www.life.umd.edu/biology/popperlab/research/deepsea.htm).

Each of the three otolithic endorgans (the utricle, saccule, and lagena) consist of a dense (specific gravity, S.G. ≈ 3) crystalline calcium carbonate mass, or otolith, supported by the otolithic membrane, surrounded by fluidic endolymph and contained within a sac, as shown in Figure 2.3. The complicated geometry of otoliths is specific both to the species and to the type of otolith. Although they maintain their characteristic shape, the otoliths and sensory epithelia grow as the fish grows, maintaining a relatively constant relationship between the size of the otolith and the size of the fish (Popper *et al.* 2005). Each otolith grows in layers, which when combined with their characteristic shapes may be used to determine the age and species of fish. In general, the oblate spheroid shaped utricular otolith tends to have the least variation. The lagenar otolith shows more geometric variation than the utricular otolith and is generally small and rounded, though those of fish in the goldfish family, the otophysans, have irregular edges. The saccular otolith is generally the largest and shows the most variation, resembling a compacted ellipsoidal shape with a trench-like portion (the sulcus) for the sensory epithelium, or sensory macula, where the otolithic membrane and hair cells are found (Platt and Popper 1981). The shape of the sulcus is "relatively invariant" amongst the studied species of fish (Popper *et al.* 2005). A sketch of the relative locations of the otolith and sensory macula is shown in Figure 2.4.

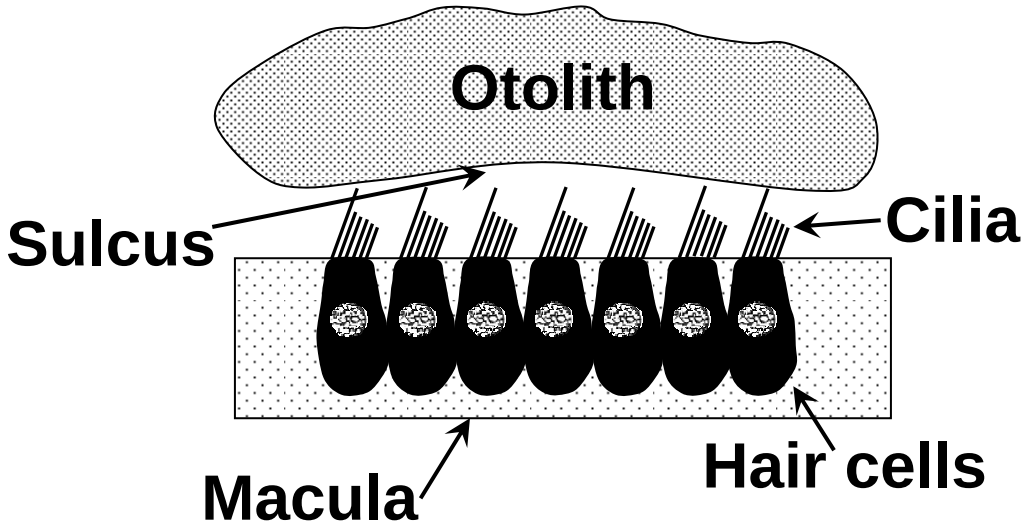

Figure 2.4 Schematic of a fish ear, showing relative positions of the otolith and sensory hair cells.

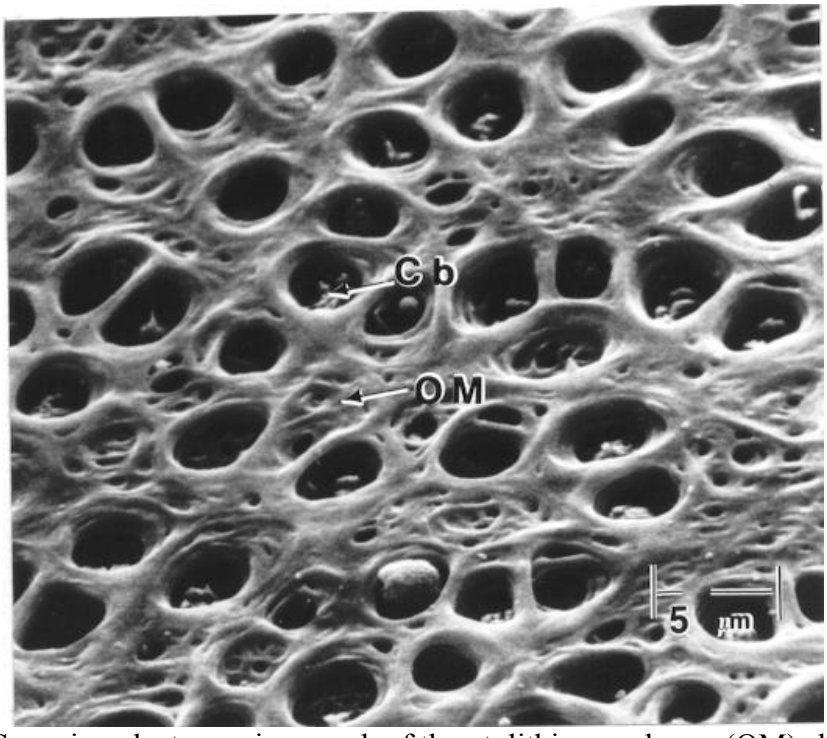

Figure 2.5 Scanning electron micrograph of the otolithic membrane (OM) showing the presence of hair cells (Cb) (from http://www.life.umd.edu/biology/popperlab/background/ultrastructuresurface.htm).

The otolith is supported by the subcupular meshwork, which consists of the gelatinous layer and the otolithic membrane. The hair cells of the sensory epithelium also extend into this layer (Dunkelberger et al. 1980). An electron micrograph of the otolithic membrane is shown in Figure 2.5, but the exact structure of the subcupular meshwork is unknown due to the difficulties in preserving and dissecting fish (Popper and personnel 2003). The sensory epithelium is the part of the otolithic endorgan containing the hair cells and connecting them the fish nervous system. A "watery" endolymph fills the rest of the ear. For a pike, the density and dynamic viscosity of the endolymph is 1.01 g/cm^3 and 1.2 cP, respectively (ten Kate and Kuiper 1970). To find the mechanical properties of the otolith and its attachments within the fish head, de Vries (1951) used X-rays to record the displacement of the otolith under a known force. He estimated that the "jelly like substance" surrounding the otolith had a dynamic viscosity of 0.45 $N \cdot s/m^2$, or 450 cP.

Fish use the sensory hair cells located on the epithelium of the otolithic endorgan to hear. The hair cells themselves, as illustrated in Figure 2.6, consist of a long kinocillium and an array of shorter sterocilia. The stereocilia are arranged in successively shorter rows moving away from the kinocilium, with a line from the shortest stereocilia to the kinocilium defining the principal axis of the hair cell (Popper *et al.* 2003). Movement of the surrounding fluid causes the fibers to bend which causes a change in the signals sent to the nervous system (Platt and Popper 1981). The afferents which send the signals to the nervous system may be associated with more than 100 hair cells each (Fay and Edds-Walton 1997).

Although these hair cells are generally located in the grooved area of the otolith known as the sulcus, they may extend beyond the otolith or appear in a separate region of the ear (the macula neglecta); the hair cells sample a wide area of acoustically induced fluid flows in the ear. The hair cells maximally respond to motion along the principal axis, with an overall cosine response pattern with respect to this axis (Flock 1971). The

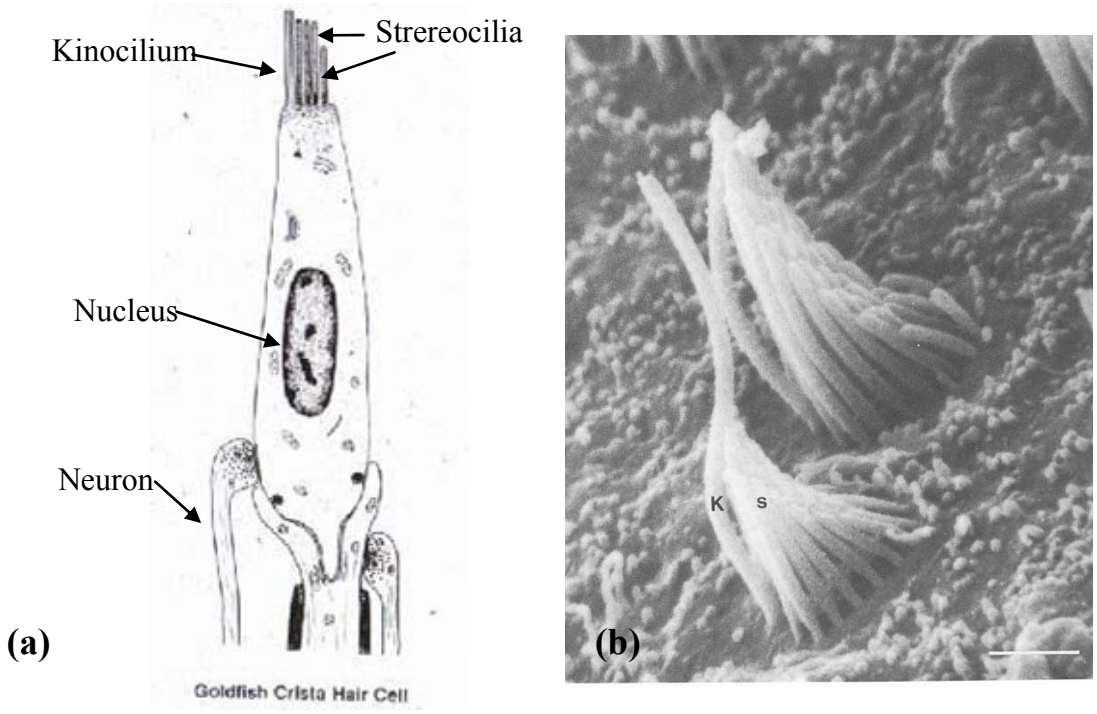

Figure 2.6 (a) Diagram of a hair cell (from http://www.life.umd.edu/biology/popperlab/research/hcheterogeneity.htm); (b) Scanning electron micrograph of the epithelial hair cells of a goldfish (Figure 1.3 from Platt and Popper 1981).

hair cells form patterns on the macula, with the most common having four groups of hair cells, as shown in Figure 2.7(a). Variations on this pattern exist primarily in hearing specialists (Popper and Fay 1993). A couple of hair cell pattern variations include the "dual" and "vertical" configurations, shown in Figure 2.7(b) and (c). The cod, a hearing generalist, has a "dual" pattern, as shown in Figure 2.7(d).

The lengths of typical kinocilia also vary from 2–10 μm (Platt and Popper 1981), with longer hair cells tending to be found at the edge of the macula. Hair cells of different lengths tend to have different "best response" frequencies, and may help fish to discriminate the frequencies of incident sound (Popper and Fay 1993).

The importance of the hair cells is emphasized by the fact that fish continue to add them throughout their lives. For instance, measurements of the number of hair cells

on the secular macula of a European hake range from about 8,000 hair cells in a 6 month old (7 cm) fish to nearly 1,000,000 hair cells in a 9 year old (75 cm) fish (Lombarte and Popper 1994). In addition, fish, like reptiles and birds, have the ability to repair damaged hair cells (Lombarte *et al.* 1993).

2.2.2 The Fish Ear's Response to Acoustic Stimulation

With the exception of the swimbladder and the otolith, fish are essentially transparent to incident sound. The fish moves with incident sound waves, but the otolith, due to its greater inertia, remains essentially stationary. Most biologists believe that the otolith functions like the proof mass of an accelerometer, however, a new model of the fish ear which treats the hair cells themselves as an accelerometer is proposed in Appendix F. Researchers who have attempted to measure the actual movement of the otolith inside of a vibrating fish, including de Vries (1951) and Sand and Michelson (1978), have also noted that the otolith's motion may have an out-of-plane, or torsional, component. Sand and Michelson found evidence suggesting that the out-of-plane components may be frequency dependent.

For hearing specialists, this "direct stimulation" of the otolith is augmented by the "indirect stimulation" from the pressure sensitive swimbladder resonating with the incident sound. Due to its high compliance, the swimbladder vibrates considerably in response to acoustic pressure. [The swim bladder also has a sharp low frequency (approximately 325/a Hz/cm where a is the radius of the swim bladder) but this resonance is generally above the fish's hearing range.] Since the swimbladder serves as an additional sound source, it will influence the motion of the fluid surrounding the otolith (Popper *et al.* 1988). However, by utilizing the swimbladder, fish are able to increase their hearing sensitivity and frequency range (Popper and Lu 2000).

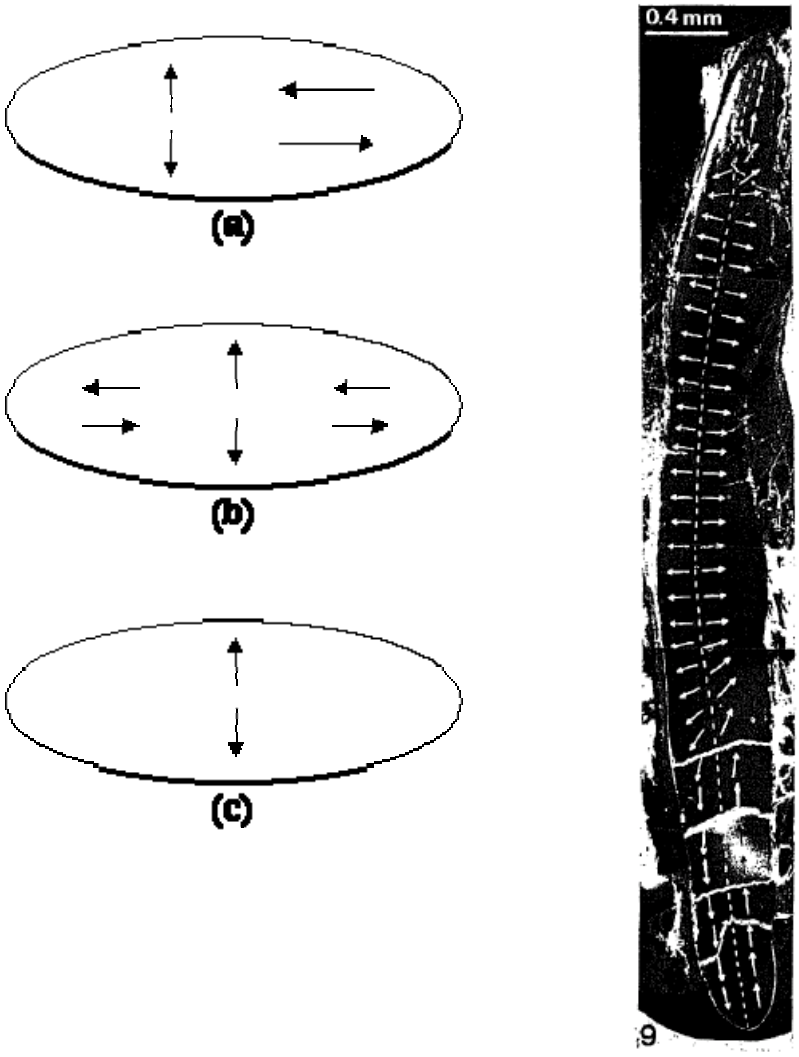

Figure 2.7 Generalized hair cell orientation patterns include (a) standard, (b) dual, and (c) vertical (after Schellart and Wubbels 1997), (d) saccular hair cell orientation pattern of a cod (Figure 9 from Dale 1976)

Fish without connections between the swimbladder and the ear are still capable of determining acoustic pressure, but have a reduced sensitivity. Instead, their ears must rely on the acoustic particle motion (either in terms of its displacement or acceleration) as their primary source. Their ears are sensitive enough to detect acoustic particle motions as small as 0.1 nm (Fay and Edds-Walton 1997).

These hearing trends are illustrated with the audiograms shown in Figure 2.8. As shown, the goldfish possesses noticeably more sensitivity and range than the dab (a flatfish without a swimbladder. The cod, which lacks the goldfish's specialized connections to the swimbladder, has a hearing range and sensitivity between that of the dab and the goldfish. The American shad, which like the cod does not have the specialized connections to the swimbladder, does not appear to hear frequencies below 100 Hz. However, the shad possesses a small gas-filled region near the ear which

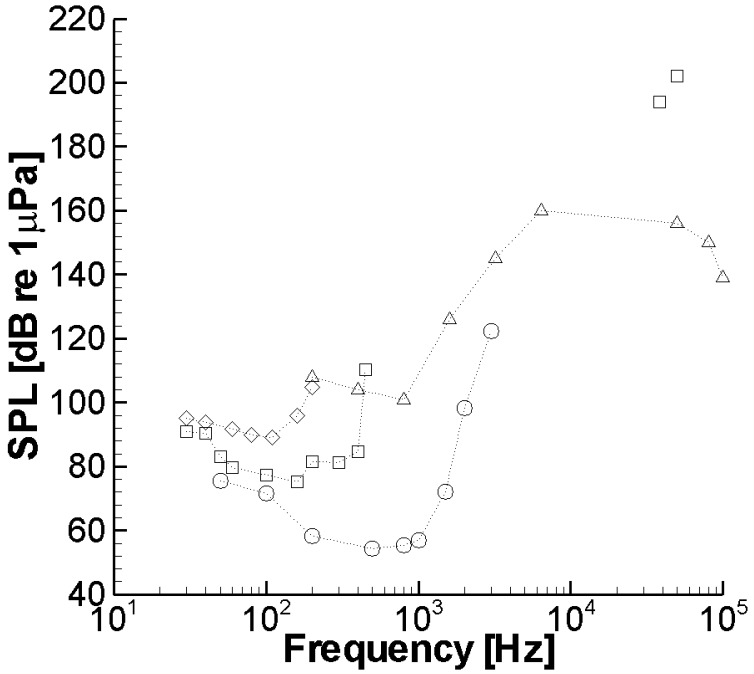

Figure 2.8 Audiograms of selected fish species, including the dab (*diamond*) (Chapman and Sand 1974), the cod (*square*) (Chapman and Hawkins 1973; Astrup and Møhl 1993, 1998), the goldfish (*circle*) (Jacobs and Tavolga 1967), and the American shad (*triangle*) (Mann *et al.* 1998).

contributes to their ability to hear ultrasound (Higgs *et al.* 2004). The cod has been also shown to hear ultrasound (Astrup and Møhl 1993, 1998), but it is unclear what mechanism is used.

Each otolith also seems to be sensitive to sound on a given plane. For example, Fay (1984) observes that the goldfish utricle responds primarily to sound in the horizontal plane, while the lagena responds to sounds in the vertical, corresponding to the orientations of the sensory macula. The goldfish saccula responds to sounds along a single axis, presumably related to the input from the swimbladder via the Weberian ossicles. How the individual ears work together to directionalize sound sources is still unknown, although several mechanisms have been hypothesized and are addressed below.

Fish are also capable of distinguishing one frequency from another. One way of expressing frequency discrimination is with the Weber ratio ($\Delta f/f$), which is about 0.04 for goldfish and at least 0.1 for hearing nonspecialists (Enger 1981; Popper *et al.* 2003). For comparison, the human ear would have a Weber ratio of 0.005–0.03, depending on the frequency (Roederer 1973). Enger (1981) theorized that fish perform at least some frequency discrimination in the ear itself. He validated this theory by submitting several fish to deafeningly loud sounds and then finding frequency-dependent patterns of hair cell destruction on the extracted the macula. This theory is supported as well by regional placement of hair cells with different fundamental frequencies on the macula and evidence that frequency sensitivity exists in individual neurons of the inner ear (Platt and Popper 1981). Although for fish it is unclear exactly how much frequency discrimination occurs in the ear itself or later during post-processing in the brain, the idea is based on human physiology. The human ear is known to be able to discriminate frequency in the ear itself based on the observed frequency dependence of the location where the incident sound causes the basilar membrane of the cochlea to have a maximal response (von Békésy 1960). This is referred to as the "place mechanism" for frequency discrimination.

The ability to differentiate sound intensities is also important for recognizing and localizing sound sources. For 500 ms tone bursts, goldfish have been shown to be sensitive to intensity differences of about 2 dB over a wide range of frequencies, which is similar to the sensitivity of other vertebrates (Fay 1988). Cod are also capable of discriminating sounds of different intensities, with experiments showing an approximately 6 dB just noticeable difference at 250 Hz (Chapman and Johnstone 1974). Similar sensitivity thresholds are expected for other species (Popper *et al.* 2003).

It is generally accepted that at least some fish are capable of directionalizing sound sources. For instance, sharks are also known to orient to sound sources that are 250 m away (Helfman *et al.* 1997), and Schuijf (1975) shows that cod are capable of discriminating sound sources to about 20° of separation in the acoustic far field. In addition, cod have been determined to be able to resolve the 180° ambiguity (Buwalda *et al.* 1983), meaning that if there are two sounds coming from opposite directions, the fish can tell the difference between them. This ability requires the fish to be able to determine more information about the sound source than just the direction of the acoustic particle displacement, most likely the phase of the acoustic pressure field relative to the acoustic particle displacement (van den Berg and Buwalda 1994). Goldfish have also been shown to be able to differentiate between clicks with variation in the initial polarity of the sound (Piddington 1972), an ability that may be useful in determining the direction of an impulsive sound source. However, due to the vast number of species that remain to be tested, it is difficult to generalize about sound localization abilities in fish.

The ability to directionalize sound has been tied to fish having two working ears (Schuijf 1975). Fay (2005) suggests that the reason both ears are required has to do with the inherent directional sensitivity of the fish ear, which resembles a cosine response pattern. Despite receiving the same input, the ears provide different responses because they are not oriented in the same direction. This binaural information improves the

sensitivity of the ear when determining the orientation of an incident sound, although it does not resolve the 180° ambiguity.

Although fish have demonstrated the ability to directionalize and localize sound sources, the methods that fish use to do so remain unresolved (Popper *et al.* 2003; Fay 2005). The most popular of the current theories are the phase model and Kalmijn's dipole model. Although primarily applicable to sound in the far field, the phase model suggested by Schuijf (1981) assumes that fish are able to detect the pressure and acoustic displacement vectors separately and use the acoustic intensity to resolve the 180º ambiguity in determining the sound direction. Buwalda (1981) provides evidence for the separate reception of pressure and acoustic particle motion in cod, a fish with a swimbladder but no direct connection between the ear and the swimbladder. Wubbels and Schellart (1997) also offer support for the phase model by measuring the response of directionally sensitive and non-directionally sensitive auditory neurons in rainbow trout. The phase model has some limitations, particularly since it cannot explain how fish without swimbladders (like sharks) are able to directionalize sound. The phase model is also restricted to monopole signals, where the direction of propagation is parallel to the direction of particle motion; however, monopole sources are uncommon in nature. The phase model has been expanded by van den Berg and Buwalda (1994) who point out that for other source types the direction of particle motion is in the direction of the source at the pressure null of the cycle.

Rogers *et al.* (1988) present a different method for localizing sound sources from the acoustic particle acceleration and the pressure. Their analysis assumes that motion of the saccular and lagenar otoliths on both sides of the fish is a combination of the direct and indirect stimulation from an acoustic signal. From these motions it is possible to derive matrix equations to decompose the otolithic motions into the acceleration and pressure of the driving signal.

Kalmijn's hypothesis (1997; 2003) is based on the mathematical similarity between the acoustic field of a dipole and the bioelectric field that sharks and rays use to detect prey. Since acoustically a swimming fish looks like a (low frequency) dipole, Kalmijn suggests that a predatory fish should be able to sense the acceleration field induced by a swimming prey fish. Then, by keeping a constant angle between its body and the lines of constant acceleration, the predatory fish can accurately approach his prey. However, it has done so without being able to determine its actual location from a distance. Kalmijn (2003) also suggests that this theory will be more applicable to low-frequency disturbances and for fish without swimbladders.

2.3 Steady Streaming Flows

2.3.1 Fluid Mechanics of Steady Streaming Flows

The previous sections have discussed the fish ear and its capabilities in interpreting its environment. In this section, consideration will be given to how the fish ear actually accomplishes these feats, with the focus being primarily on the behavior of the viscous fluid surrounding the otolith under acoustic stimulation.

Consider the behavior of an oscillating fluid. Under the linear assumptions used for most acoustic analysis, the particle movement induced by the acoustic waves is irrotational with no time-independent component of the flow. However, for strong, high frequency waves, frictional losses due to the viscosity of the fluid can induce variations in the momentum flux, or Reynolds stress gradients, that lead to time-independent motions, e.g. the "quartz wind" (Lighthill 1978a; Riley 1998). When the fluid is oscillating near a solid boundary, the boundary layer leads to the variations in the Reynolds stresses that cause steady motion (Lighthill 1978b; Riley 2001). It is this second type of streaming that could be important within the fish ear.

The inside of the fish ear (ignoring the otolithic membrane, hair cells, and surrounding structures) may be modeled as a sinusoidally oscillating body in an otherwise quiescent viscous fluid. (Although the physical situation is closer to that of an oscillating fluid around a stationary otolith, the Navier-Stokes equations possess extended Galilean invariance, *i.e.*, are invariant under rectilinear acceleration (Pope 2000). Therefore, the flow of a constant-density Newtonian fluid around the oscillating body is equivalent to that due to the fluid oscillating around a stationary body.) As the otolith oscillates, it induces fluid motion and generates vorticity at the boundary between the solid and the fluid. This vorticity is then convected away from the body and attenuated by the viscous forces. However, the attenuation leads to an imbalance in the Reynolds stresses which causes the development of a time-independent component of the flow, known as steady streaming (Lighthill 1978a, b; Riley 2001). Since the amplitude of oscillation is small, the fluid motion can then be divided into two portions: (1) a periodic flow that (to the first order) is proportional to the oscillation frequency of the body and (2) the steady streaming flow. Although small in magnitude, these steady streaming flows should not be neglected here since their magnitude is unknown. It is possible that over several oscillations these motions can have a significant effect on the displacement of the hair cells that the fish senses as sound. In determining which type of motion will be most important to the fish ear, it is necessary to consider the time scales over which the sounds occur and the ear responds since the displacements will be dominated by the periodic flows over short times and the streaming flows over longer times. Lesser and Berkley (1972) mention that longer time scales are needed for their numerical model of the human ear to capture the steady flows, or "eddies," observed by von Békésy's experimental model of the human ear.

2.3.2 Governing Fluid Mechanics Equations

The flow of an isothermal Newtonian fluid is described by the continuity and Navier-Stokes equations, which, with the appropriate boundary conditions, describe the pressure, density and velocity distributions of the flow field. When variations in pressure and body forces are negligible, and viscosity is constant, these equations are given by:

$$\frac{\partial \rho^*}{\partial t^*} + \nabla^* \bullet \rho^* \vec{V}^* = 0 \qquad 2.1$$

$$\frac{\partial}{\partial t^*}\vec{V}^* + \vec{V}^* \bullet \nabla^* \vec{V}^* = \nu \nabla^{*2} \vec{V}^* \qquad 2.2$$

Where ρ^*, $\vec{V}^*$ and t^* are fluid density, velocity and time in dimensional form and ν is the kinematic viscosity. If the equations are non-dimensionalized using the period of oscillation (ω^{-1}) as the time scale, a representative body dimension (L) as the length scale, and the maximum body velocity (ωs) as the velocity scale, the non-dimensionalized Navier-Stokes equation becomes:

$$\frac{\partial}{\partial t}\vec{V} + \varepsilon \vec{V} \bullet \nabla \vec{V} = \frac{\varepsilon}{Re} \nabla^2 \vec{V} \qquad 2.3$$

Here, $Re = \omega s L/\nu$ is the Reynolds number, and $\varepsilon = s/L$ is the amplitude ratio, or alternatively, the inverse of the Strouhal number; Re and ε are then the relevant dimensionless groups for this flow. For the cases considered here, $\varepsilon \ll 1$, as is the case for most analyses.

These equations are usually solved analytically by assuming that the flow is two-dimensional (axisymmetric) using a stream function approach. Following the derivation of Riley (1998), the stream function form of the Navier-Stokes equations is solved using asymptotic methods. To the first order, the nonlinear convective terms vanish, and the equations are those for unsteady Stokes flow, giving a first-order solution that is irrotational and linear. However, in order to satisfy the no-slip boundary condition at the solid surface, a shear layer must develop, with a thickness $O(\delta = (\omega/\nu)^{1/2})$. Fortunately,

solutions exist for the boundary problem represented by unsteady Stokes flows including numerical boundary integral method solutions (Pozrikidis 1989) and analytical Bessel function expansions (Venkatalaxmi *et al.* 2004).

At the second order, the solution involves both steady flows and flows that are proportional to twice the driving frequency (Riley 1966). The exact form of the steady flow depends on the relative magnitudes of the Reynolds number and normalized oscillation amplitude. For flows where $Re/\varepsilon << 1$, the Stokes layer is much larger than the length scale of the body, which means that the region where vorticity is important is relatively large. The flow in this case is seen to move towards the body along the axis of oscillation, as shown for a sphere in Figure 2.9. As *Re* increases, the boundary layer decreases in size and the outer flow becomes irrotational. A relatively thin boundary layer then contains the vorticity which leads to the steady streaming flows. The steady part of the streamfunction contains two counter-rotating regions in each quadrant, shown for a single quadrant of a sphere in Figure 2.10 (Riley 1966).

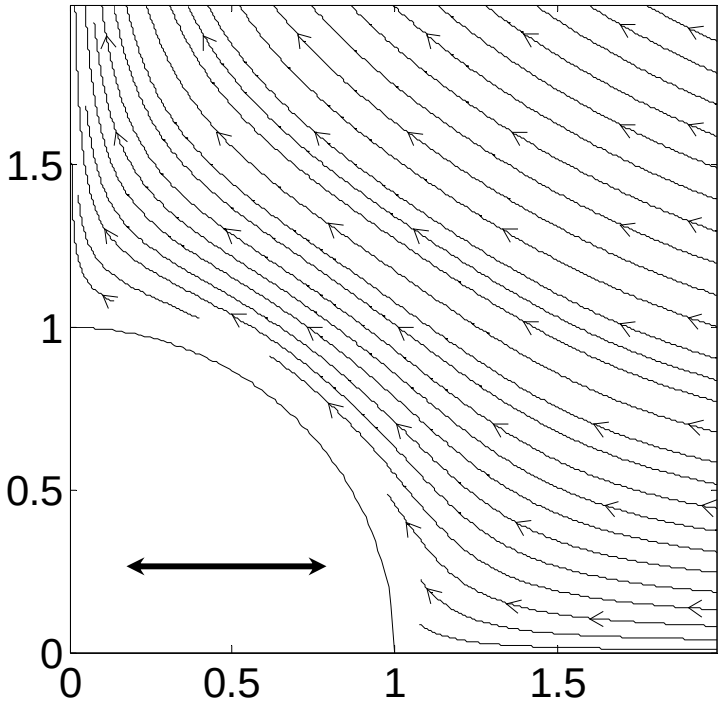

Figure 2.9 Steady streaming streamlines around a sphere for $Re_s << Re << Re_M << 1$. The solution is from Riley (1966). The direction of oscillation is marked with a double arrow.

Problems where steady streaming flows are generated by an oscillating boundary have been solved for a wide range of Reynolds numbers, oscillation amplitudes, and body geometries. Faraday (1859) first observed such flows in the motion of dust particles above a vibrating plate. Rayleigh (1883) derived the first theoretical model of this flow, using an informal perturbation analysis to show the effect of the nonlinear convective terms. He then expanded the derivation to include compressible flows and was able to explain the motion of particles in Kundt's dust experiments in a standing-wave tube. This type of steady streaming due to the attenuation of the oscillating motion at a boundary is therefore known as Rayleigh streaming.

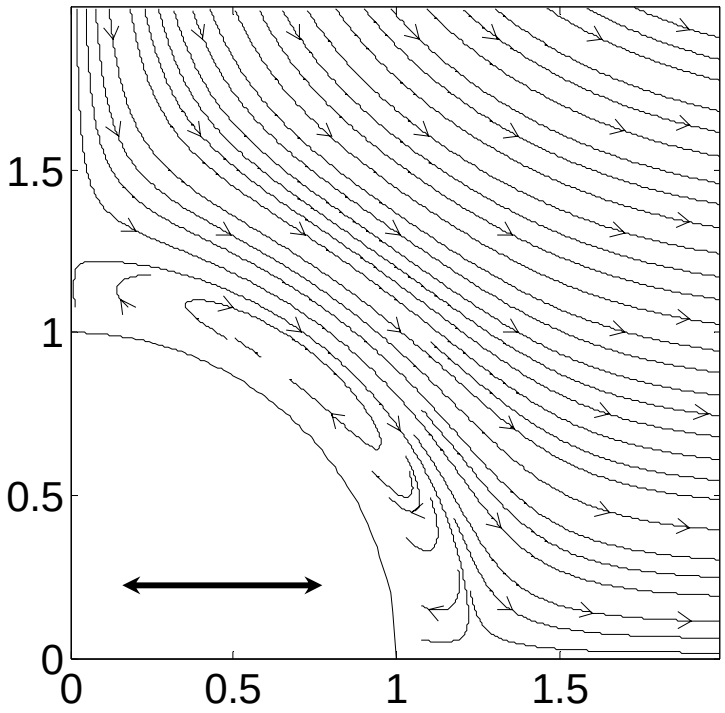

Figure 2.10 Steady streaming streamlines around a sphere for $Re_M >> 1$ and $Re_s << 1$. The solution is from Riley (1966). The direction of oscillation is marked with a double arrow.

2.3.3 Reynolds Number Definitions and Associated Flow Regimes

Since Rayleigh's time, steady streaming has been the subject of numerous analyses and experiments by a variety of researchers, as summarized in various review articles (Nyborg 1965; Riley 1967; Lighthill 1978a; Petit and Gondret 1992; Nyborg 1998; Riley 1998, 2001). These researchers (e.g. Riley 1967) have defined two additional Reynolds numbers based on the Stokes layer thickness, δ, in order to ease the analysis. These are the square of the ratio of the amplitude of oscillation, s, to δ, $Re_s = \varepsilon \cdot Re = \omega s^2/\nu$, and the square of the ratio of the body length scale, L, to δ, $Re_M = Re/\varepsilon =$

$\omega L^2/\nu$. Re_s is also known as the streaming Reynolds number, since it has a role analogous to the usual Reynolds number in the equations for steady streaming. When $\varepsilon < 1$ (as it is inside of the fish ear), the flow may be divided into five different regimes based on these parameters for the purposes of analysis:

1. $Re_s<Re<Re_M<<1$;
2. $Re_s<Re<<1$, $Re_M \sim O(1)$;
3. $Re_s<<1$, $Re \sim O(1)$, $1<<Re_M$;
4. $Re_s \sim O(1)$, $1<<Re<Re_M$;
5. $1<<Re_s<Re<Re_M$.

These five regimes can be viewed in terms of the thickness of the viscous shear layer relative to the size of the oscillating body, moving from the thickest to the thinnest Stokes layer.

The first flow regime, $Re_s<Re<Re_M<<1$, is mainly studied in terms of the first-order solution to the Stokes flow problem. By eliminating the nonlinear convective terms, the oscillating flow boundary value problem was first solved by Stokes (1850), but solutions can also be found for a variety of spheroids in terms of expansions of spheroidal functions (Kanwal 1955; Lai and Mockros 1972). Later researchers have expanded the solution to include more general boundaries by finding solutions in terms of series of Bessel functions (Venkatalaxmi *et al.* 2004). These solutions, however, do not include a steady flow component. It should also be noted that although some work in this regime has been done with Oseen approximations, they should only be used for an outer flow solution for the spherical case (Riley 1966).

If the shear layer thins a bit (either by decreasing the viscosity of the fluid or increasing the size of the oscillating body) such that $Re_s<Re<<1$ and $Re_M \sim O(1)$, then perturbation analyses can be used to extend the range of the solutions to larger Reynolds numbers, as used by Holtsmark *et al*. (1954) in their work with cylinders. From Holtsmark's solution, it is possible to see some of the characteristics of the steady flow,

including that the steady streaming flow has an inner rotating region whose thickness is a function of the size of the oscillating body [later experiments by Raney *et al.* (1954) tabulated the thickness as a function of $(Re_M)^{1/2}$]. Holtsmark presents solutions for both the bounded and unbounded vibrating cylinder, however the bounded solution assumes that the derivative of the steady streaming function is equal to 0, which Skavlem and Tjötta (1955) claim is unwarranted in their analysis. Lane (1955) has expanded Holtsmark's unbounded solution to spherical coordinates, though an omission in his results is corrected by Danilov (1984). Dōhara (1982) also completed analytical work in this flow regime by calculating the complete streamfunctions (including both the steady and unsteady streaming motions) to the second order around a sphere. These solutions were also explored experimentally for cases where $Re_M \sim O(100)$ by Holtsmark *et al.* (1954) for a cylinder in a standing wave tube filled with air and seeded with small MgO particles, Raney *et al.* (1954) and Bertelsen *et al.* (1973) for a cylinder oscillating in a seeded water/glycerin mixture, and Lane (1955) for a sphere in air. Except for Holtsmark's results, comparison between the experimental and theoretical results by including the velocity transform from the experimental Lagrangian velocities to the theoretical Eulerian velocities for their results. Results presented by Raney *et al.* (1954) also showed that while the inner layer thickness was a function of $(Re_M)^{1/2}$ for small values amplitudes of oscillation, this relationship ceased to hold as the amplitudes of oscillation were increased beyond $\varepsilon \approx 0.5$. Bertelsen *et al.*'s results show excellent agreement with theory and show how the thickness of the inner region is increased by the presence of an outer cylinder, though the effects level off for an outer cylinder approximately 7 times the size of the inner cylinder.

Qualitatively, the experiments above have already shown several aspects of the flow regime where $Re_s \ll 1$, $Re \sim O(1)$ and $Re_M \gg 1$, such as the thinning inner boundary region which confines the vorticity to the regions closer to the oscillating body. Analytical studies in this regime include the classic study by Schlichting (1932), who

used boundary layer theory to calculate the streaming motions near a cylinder. His work was later expanded by Andres and Ingard (1953) to larger values of the amplitude of oscillation. Although Andres and Ingard's solution shows a correlation between the thickness of the inner region and ε, they have not properly included the outer solution in their calculations, which limits their conclusions (Riley 1967). This flow regime has also been studied numerically by Chang and Maxey (1994) around spheres for Re = 0.1–17 and ε =0.1–10 using direct numerical simulations, and analytically assuming a solution in the form of a series of Legendre functions by Alassar and Badr for spheres (1997), prolate spheroids (1999b) and oblate spheroids (1999a). Rednikov and Sadhal (2004) have used asymptotic expansions to explore the effect of aspect ratio on the streaming around an oblate spheroid for a wide range of Re when $Re_M >> 1$ and $\varepsilon << 1$. Their results show that a more oblate spheroid has a larger effective slip velocity near the equator and a slightly thicker inner region, which is not necessarily constant around the body. Experimentally, Petit and Gondret (1992) use a seeded water/glycerin mixture to show the effect of increasing the frequency of oscillation (Re_M) on decreasing the inner layer thickness for a sphere. Odar and Hamilton (1964) have also used an instrumented oscillating sphere to relate the drag forces induced for Re =0–62 and ε = 0.8–3.2 to a sum of forces from the acceleration, velocity, history and inertia of the flow.

Solutions for flows in the regime for $Re_s \sim O(1)$ and $1 << Re < Re_M$ are really an extension of solutions flows in the regime where $1 << Re_s < Re < Re_M$, but that have extended the solutions to include higher order boundary layer effects so that Re_s can be expanded downward. This regime has been explored for spherical geometries by Wang (1965) and Riley (1966) using matched asymptotic expansions.

For the case where $1 << Re_s < Re < Re_M$, the Stokes shear layer is very thin and boundary layers exist for both the steady and unsteady flows. Solutions for this regime have been found using perturbation analyses for cylinders by Stuart (1966). Stuart's paper was instrumental in recognizing the important of Re_s in determining the boundary

layer characteristics of the steady flow. The flow was also explored using a slightly different method by Riley (1967), with similar findings. Bertelsen (1980) expanded these results analytically to improve their resolution in the azimuthal direction. Experimentally, Bertelsen (1974) measured the streaming velocities for Re_s = 60, 90, and 400 and found that although the agreement with Stuart's and Riley's solutions were good near the cylinder, discrepancies existed away from the body. Haddon and Riley (1979) performed a numerical approximation to solve the Navier-Stokes equations to eliminate effects of a finite Reynolds number, which significantly improved the agreement between theory and experiment. For spheres, Danilov (1985) sought a solution using a modified version of Lane's analysis and shows a good agreement between the measured and calculated thickness of the inner rotating region. Similarly, Amin and Riley (1990) present solutions for flow around a sphere near a pulsating source, which may seen as a sphere in an oscillating flow when the source moves into the far field. They also present a simple flow visualization of the jets formed along the axis of oscillation. Rednikov and Sadhal's (2004) results for an oblate spheroid also show the development of a thin boundary layer, the development of viscous fluid jets, and potential flow in the rest of the fluid.

2.3.4 Steady Streaming Generated by Multiple Frequency Oscillations

This section briefly reviews steady streaming flows around circular cylinders and spheres oscillated at multiple frequencies over a range of Re_s and $\varepsilon << 1$. Davidson and Riley (1972) used asymptotic analysis methods to analyze steady streaming flows at $Re_s \sim O(1)$ for a circular cylinder oscillated by a periodic waveform described by a Fourier series. To the second order, their results showed that the streaming solution was the sum of the streaming due to the individual components. Miyagi and Nakahasi (1975) expanded the solution to higher order for the specific case of a cylinder oscillating in jagged pattern described by the sum of a sinusoid and its first harmonic for $\varepsilon^2 << Re_s < 1$. Their results include a steady term of $O(\varepsilon^2)$ of the velocity solution infinitely far away

from the body. This term is from the asymmetric oscillation and results in a small steady flow across the flow field. Tatsuno (1981) studied this oscillation pattern experimentally for $\varepsilon = 0.17–0.44$, and $Re_s = 1.54–68.5$, suggesting that this analysis could be extended to somewhat higher ε values. Higa and Takahashi (1987) extended this analysis to the three-dimensional case of a sphere and reported similar behavior. These small steady bias flows at infinity are assumed to have a negligible effect near the body, and hence for the cases presented here. Similarly, Kubo and Kitano (1980) considered the flow created by a cylinder oscillated simultaneously along two orthogonal directions. To first order, their analytical study showed that the resulting elliptical motions created streaming patterns that were irrespective of the phase difference between the two oscillations. Again, these patterns were the superposition of the motions created by along each direction individually.

These multiple frequency flows also change the calculation of the Reynolds number of the oscillation. For the single frequency flows, the Reynolds number was defined in terms of the frequency of oscillation, the maximum body displacement and a body length scale. For multiple frequency flows, one possible Reynolds number is defined in terms of the maximum velocity of the oscillation, U_∞, and a body length scale, L (Davidson and Riley 1972). For a two frequency oscillation with a zero degree phase difference between them, this could be expressed as

$$Re = \frac{U_\infty L}{\nu} = \frac{2\pi L^2 \left(f_1 \varepsilon_1 + f_2 \varepsilon_2 \right)}{\nu}, \tag{2.4}$$

where the subscripts 1 and 2 refer to the two sinusoidal oscillation components oscillating at frequency f and normalized amplitude ε. A definition for the streaming velocity, V_s, can also be expressed in terms of the maximum body velocity as

$$V_s = \varepsilon^* U_\infty = \frac{U_\infty^2}{2\pi f_0 L} = \frac{2\pi L \left(f_1 \varepsilon_1 + f_2 \varepsilon_2 \right)^2}{f_0} \tag{2.5}$$

where ε^* is the normalized oscillation amplitude in terms of U_∞ defined by

$$\varepsilon^* \equiv \frac{U_\infty}{2\pi f_0 L} = \frac{f_1\varepsilon_1 + f_2\varepsilon_2}{f_0} \qquad 2.6$$

and f_0 is the fundamental frequency of the oscillation.

2.3.5 Other Studies of Steady Streaming Flows Related to the Fish Ear

This section summarizes more complex steady streaming flows relevant to this thesis. Experimental studies of more complex geometries include investigations of steady streaming over non-circular cylinders (Kim and Troesch 1989), arrays of cylinders (Yan *et al.* 1993) and cylinders near walls (Wybrow and Riley 1996; Wybrow *et al.* 1996). Secomb (1978) has looked at the streaming motions due to a vibrating tube wall (instead of a vibrating fluid) as a model for arterial flows; however these motions could also be applied to the ear.

Non-sinusoidal oscillations more consistent with the varied and noisy underwater acoustic environment have also been considered. For instance, Higa and Takahashi (1987) have considered the case of an asymmetrically oscillating sphere, while Lee and Wang (1989; 1990) considered a sphere placed between velocity node and anti-node of a standing wave. In addition, Karahalios and Sfetsos (1988) and Gopinath (1994) looked at the steady streaming flow due to combined torsional and linear oscillations of a sphere, which may provide a more complete model of the actual motion of the otolith in the presence of underwater sounds.

Steady streaming has also been demonstrated above permeable beds (Liu *et al.* 1996) and in viscoelastic fluids (James 1977; Bohme 1992), which may be important for understanding *in vivo* flows within the fish ear. It should also be noted that Riley (1967) suggests that the time scale for the flow to become fully developed is $O(\varepsilon^{-2}\omega^{-1})$, which for the relatively small oscillation amplitude ratios inside of the fish ear may be a relatively long time.

Most of the hair cells inside of the fish ear are located inside of the groove on the otolith known as the sulcus. Although flow in cavities and channels has been looked at by previous researchers, many of these studies consider the flow inside cavities driven by a lid translated at a constant velocity [*cf.* Taneda (1979); the review by Shankar and Deshpande (2000)], while the case of interest here is the flow inside a cavity driven by an oscillating shear flow (outside the cavity). A number of chaotic mixing studies have considered the flow inside cavities driven by an oscillating lid (e.g. Leong and Ottino 1989; Vogel *et al.* 2003), but the oscillation amplitude of the lid, typically 0.5–5 times the width of the cavity, is much greater than that for the case of interest here.

Perhaps the studies that are closest to the steady streaming flows inside the fish ear are for streaming flows driven by ocean waves over rough floors. Lyne (1971) and Kaneko and Honji (1979) considered oscillating flow over a wavy wall as a model of this situation, but their solutions are for cases where the shear layer is much thicker than the amplitude of the wall's "waviness," while the fish ear is likely (based on the currently available rough estimates of the constitutive properties of the fluids and tissues inside the fish ear) to have a very thin shear layer.

2.4 Steady Streaming Flows and Hearing

The oscillating flows that lead to steady streaming motions can come from a variety of sources, from ultrasonic quartz oscillators to ocean waves. There is even evidence to suggest that steady streaming generated by audible sounds may play a role in human hearing. Although streaming motions have not actually been observed in the human ear, streaming is usually associated with the part of the ear responsible for frequency discrimination, the cochlea. Physically, the cochlea is a fluid-filled spiraling chamber divided longitudinally by two membranes. Sound is transformed from a pressure wave by the mechanics of the ear into a traveling wave which travels down one

of these membranes, and the motion of this traveling wave should lead to steady streaming motions (Lighthill 1992).

Evidence for the presence of steady streaming is present in both experimental and theoretical explorations of the ear. Experimental models of the ear, beginning with the simple models used by von Békésy (1960) and Tonndorf (1958), show steady motions, which they refer to as "eddies." These models consisted of a box representing the human cochlea which has been divided by a rubber "basilar membrane." The vibrations are driven by a loudspeaker at one end. The more complete model used by Cancelli *et al*. (1985) also describes the presence of steady flows. Tonndorf (1986) discusses these eddies and describes them as depending on the square of the driving pressure amplitude, and appearing only after the drive signal large enough to overcome the fluid's viscosity. He suggests that these eddies are the result of (rather than caused by) the nonlinearities in the displacement of the basilar membrane (which lead to the vorticity generated in the boundary layer of the membrane). In order to demonstrate that the eddies he observed in his mechanical model could be caused by audible sounds, von Békésy (1960) used a temperature gradient across the ear drum to create a buoyancy driven streaming flow within the ear which caused the subject to tilt his head. When under the presence of a loud sound, the subject again tilted his head, thereby suggesting the presence of a similar streaming flow. Mathematical models, such as those developed by Holmes (1982), do not account for the steady streaming flow. Lesser and Berkeley (1972) mention that mathematical models must use longer time scales in order to account for the steady streaming flows, but leave the analysis for a future paper. Lighthill (1992) provides energy based arguments for acoustic streaming within the ear, and a formula to estimate its magnitude. However, many of the material properties of the ear are unknown, limiting the usefulness of the formula in actually predicting the steady streaming inside of the ear.

The role of steady streaming flows in the ear, however, is unknown. Several hypotheses have been suggested by the researchers who observed the flows. For instance, Tonndorf (1960) suggests that the appearance of steady streaming flows can be correlated to the perception of auditory distortions. Others, including Steele (1973) and Helle (1974), have suggested that the steady streaming flows may play a role in improving frequency sensitivity. Cancelli *et al*. (1985) hypothesized that the streaming flows could have an inhibitory effect on the basilar membrane. It could also be argued that von Békésy's tilting head study suggests that streaming flows in the ear would affect the subject's sense of balance. However, in order to understand the function of the cochlea, steady streaming flows must be accounted for, whatever their role.

In addition to human ears, Hassan (1985) has hypothesized that steady streaming could play a role in reptilian and mammalian ears. He notes that the steady streaming flows would explain higher harmonic and "DC" components in the measured electrical potentials of alligator lizards. For fish, Yoda *et al.* (2001) and Kotas *et al*. (2007) have suggested that the presence of steady streaming flows could play a role in their auditory retina hypothesis. This hypothesis suggests that the patterns formed by the fluid flows in the fish ear could be what the hair cell arrays are using to sense sound; much like the retina of the eyes recognizes patterns formed by incident light. One of the goals of this thesis is to evaluate the feasibility of the auditory retina hypothesis.

2.5 The Auditory Retina Hypothesis and Bio-mimetic Design

The auditory retina hypothesis is inspired in part by bio-mimetic and bio-inspired design, which seeks to understand biological sensors and use their underlying concepts to improve human sensing capabilities. Biologically inspired design has fascinated many researchers, including those who have worked to create a hair cell-like array mimicking the fish lateral line. These researchers have developed micromanufacturing techniques to construct hair cell-like sensors, then coat them with hydrogels to improve their sensitivity

while making them physically more like the neuromasts of the lateral line (Peleshanko *et al.* 2007). Such sensors, which may eventually be used on submarines to passively detect nearby objects like divers, are already capable of tracking dipole sources (like an oscillating sphere) in water (Gray 2006). If the auditory retina hypothesis is valid, making a sensor that mimics the auditory retina will require a similar effort to construct working mechanical models of the fish ear.

In addition to developing biologically inspired sensors, mechanical models have elucidated how rat whiskers can be used to form three-dimensional "images" of their surroundings and hence process sensory data (Solomon and Hartmann 2006; Gopal and Hartmann 2007). One of the unique features of this sensor is that the motion of the sensor (*i.e.*, the whisker array) itself provides part of the information. Understanding biological data-processing mechanisms can lead to new methods for processing large amounts of temporally and spatially varying data.

Perhaps the closest analog to these studies of how fish hear is the recent research on understanding how the tiny fly *Ormia* hears. This fly can determine the direction of incident sounds in air within 2° at a frequency of 5 kHz (= wavelength of 68 mm) using ears that are only 0.5 mm apart (Mason *et al.* 2001). These scales are similar to those found in the fish ear, which directionalizes sounds of $O(1–10^3$ m) wavelength using ears that are at most a few centimeters apart. The fly's ear is a demonstration of how biomechanics can be coupled with the neural apparatus that processes sensory data to create a high degree of sensitivity. Tiny directional microphones based on this fly's ears are being built that may eventually be suitable for use in hearing aids.

In a similar fashion, the auditory retina hypothesis proposes a new mechanism for how acoustic information may be sensed and processed by the fish ear, putting it in the initial stages of bio-inspired design. Before it could be used to design sensors, it must be established whether or not acoustical information is encoded in the steady and unsteady portions of the acoustically induced flows and whether the hair cells can sense this

information. Currently, it is unclear whether a biomimetic sensor based on the auditory retina concept is feasible or an improvement on current underwater acoustics sensors.

CHAPTER 3

EXPERIMENTAL DETAILS

Based on the acoustics, physiology and fluid mechanics of the fish ear (as discussed in Chapter 2), an experimental model of the fish ear was constructed. This model consists of a rigid body (representing the otolith) in a viscous fluid (representing the endolymph and surrounding tissues). The acoustic stimulation of the fish ear is expressed by oscillating the rigid body vertically in the fluid. The flow of a constant-density Newtonian fluid around the oscillating body is equivalent to that due to the fluid oscillating around a stationary body because the Navier-Stokes equations possess extended Galilean invariance, *i.e.*, are invariant under rectilinear acceleration (Pope 2000). Although these oscillations produce incompressible fluid motions that are larger than those produced by the compressible acoustic stimulation, the resultant fluid flows should have similar characteristics as long as the oscillations are small enough to keep the resulting flows in the linear regime.

The experimental setup for studying the steady streaming flows generated by oscillating spheroids in a viscous fluid was housed in the Love Building at the Georgia Institute of Technology. The setup is composed of four parts:

- the mechanism for oscillating the model otolith, consisting of:
  - the model otoliths;
  - the shaker;
  - an amplifier; and
  - a programmable attenuator;
- the tank and its support structure, consisting of:
  - a tank;

  - the working fluid consisting of tracer particles suspended in a water-glycerin mixture;
  - a vibration isolation table; and
  - the shaker mounting structure;
- the imaging optics, consisting of:
  - the laser;
  - optical components (lenses, mirrors, etc.);
  - the camera and zoom lens; and
  - the camera driver software and framegrabber;
- the coordinating computer code, consisting of:
  - the driver software for the shaker written in LabVIEW^{TM} v5.0; and
  - the data acquisition card.

As shown in Figure 3.1 and Figure 3.2, the experimental apparatus evolved over the course of this thesis, with the largest changes in the tank dimensions and the shaker mounting structure. Further details on the apparatus components and their evolution are given in the following sections.

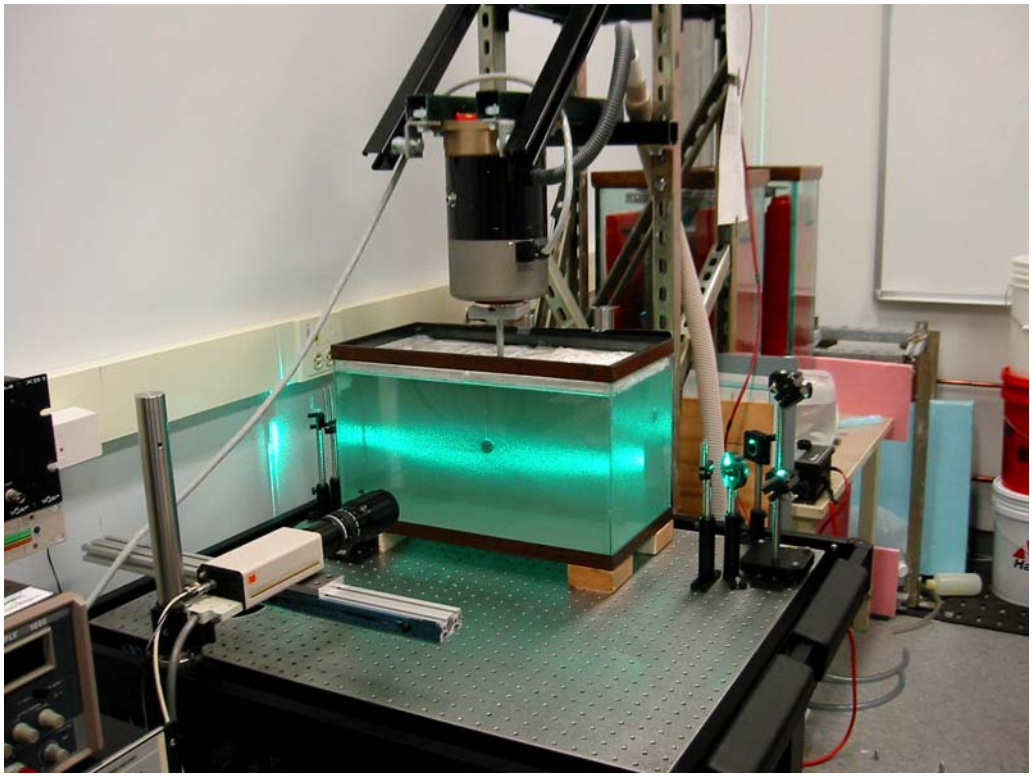

Figure 3.1 Initial apparatus configuration.

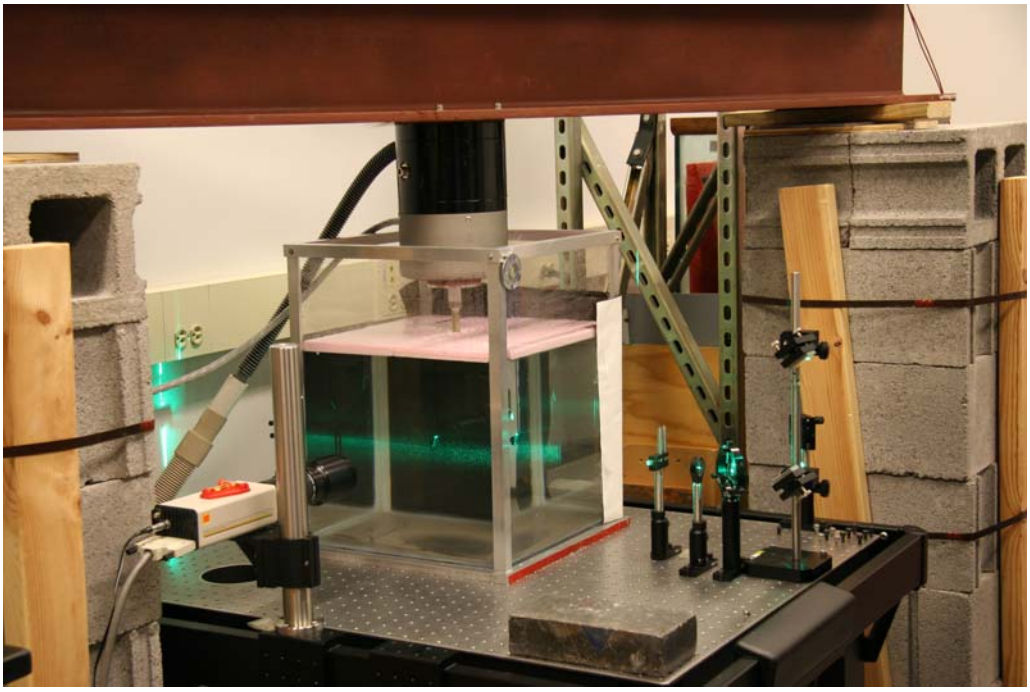

Figure 3.2 Final apparatus configuration (except for the displacement sensor).

3.1 Setup Components

3.1.1 Oscillating Mechanism

The otolith, or test body, was oscillated by a shaker controlled by software written in LabVIEW^{TM} via an amplifier and attenuator. Nearly all the bodies were spheroids constructed from a variety of materials. The first test bodies were acrylic spheres that were painted black with a solvent based enamel (Ace Flat Black) to reduce glare or spheroids molded from a nearly opaque dark brown polyurethane (Epoxical composite polymer 9130). Due to inconsistencies in the molding process, the bodies were later replaced by machined Delrin (an opaque white plastic) spheroids. However, due to concerns about local heating by the laser light sheet, the final set of bodies were clear acrylic spheres and spheroids. The spheres were purchased from Small Parts, Inc. (Acrylic Balls, BL-16), while the spheroids were machined by the Georgia Tech student machine shop using a computer numerically controlled (CNC) lathe. The bodies typically had a maximum dimension between 2 cm and 5 cm. In the latter stages of these studies, grooves were cut into a subset of the spheroids to approximate the sulcus of the fish ear. As shown in the sketch of a slotted oblate spheroid (Figure 3.3), a represents the maximum half-dimension of the body along the axis of symmetry, b is the maximum half-dimension of the body normal to the axis of symmetry, and c denotes the radius of the groove. The aspect ratio, AR, of all the spheroids is given by a/b; AR less than, equal to, and greater than unity correspond to a oblate spheroid, sphere and prolate spheroid, respectively. The equivalent radius, $r_{eq} \equiv (b^2 a)^{1/3}$, is the radius of a sphere with the same volume as the spheroid.

The spheroids were mounted on stainless steel rods of diameters ranging from 2 mm to 5 mm using a two part epoxy (DEVCON 5 Minute Fast Drying Expoxy); the thicker mounting rods were mainly used at frequencies greater than 16 Hz. The

mounting rods then were epoxied to a 12.7 mm diameter ½”-13 threaded rod, which was in turn rigidly mounted to the shaker table.

The flow around an oscillating 350%-scale model of a cod saccular otolith was also studied (Figure 3.4). These model otoliths were created from a microcomputer tomography (micro-CT) scan of an otolith extracted from a cod head (purchased at Your DeKalb Farmer’s Market, 3000 E. Ponce De Leon Avenue, Decatur, GA 30030). The micro-CT scans were performed by Angela Lin, Research Engineer I, at the Parker H. Petit Institute for Bioengineering and Bioscience of the Georgia Institute of Technology. Model otoliths were fabricated from these scans by stereolithography rapid prototyping of SL-5510 resin (supplied by Huntsman Specialty Chemicals) on a Viper Si2 at the

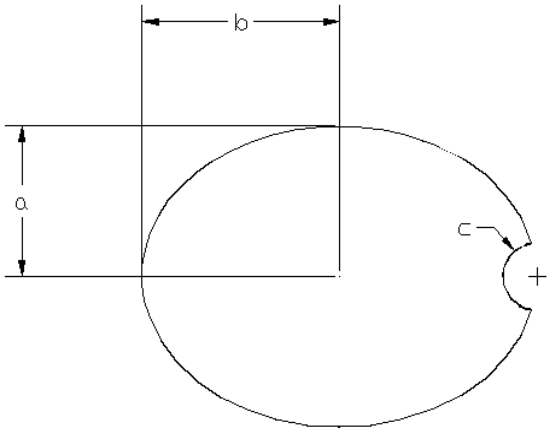

(a)

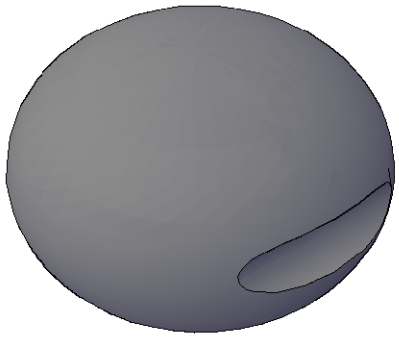

(b)

Figure 3.3 A slotted oblate spheroid (AR = 0.75) shown in a side view (a) and a shaded projection view (b).

Figure 3.4 350% scale cod otolith model.

Rapid Prototyping and Manufacturing Institute of the Georgia Institute of Technology. The scale model has a mass of 14.0 g, and dimensions of 69 mm in length, 36 mm in width, and 17 mm in height; the specific gravity is 1.2 and the volume is 12×10^3 mm^3. The sulcus on this model has a maximum width of about 1 cm and a length of about 6.8 cm.

The model otolith was mounted by press-fitting in a threaded insert into a small, shallow hole drilled in the side of the model otolith opposite the sulcus. An aluminum mounting block was then screwed into the insert and a 70 mm long 8-32 threaded stainless steel rod was attached to the mounting block. The threaded rod was screwed into a tapped hole in the end of a 12.7 mm diameter, 150 mm long stainless steel rod. The rod had ½”-13 threads cut into the other end which could then be mounted to the shaker table.

The shaker (Labworks Inc. ET-140) and its power supply (Labworks Inc. PA-141) are capable of a stroke of 2.54 cm stroke at a peak force of 490 N. The amplitude of the oscillation was controlled by a digital attenuator (Tucker Davis Technologies Model

PA4). The movement of the shaker was controlled by a signal created by a simple program written in LabVIEW™ v.5.0, which will be described later in this chapter. This signal was either a sine wave or the sum of two sine waves, as in:

$$y(t) = a_1 \sin(2\pi f_1 t) + a_2 \sin(2\pi f_2 t + \phi_2). \quad 3.1$$

The phase between the two given sine waves was adjusted so that the phase, ϕ_2, of the resulting displacement was zero. Because the shaker had a delay in its response, the camera trigger had to implement a variable phase offset in order to image the shaker at the center of its oscillation.

The trigger phase offset and the attenuator settings to produce the desired amplitude of oscillation were determined by monitoring the motion of the shaker using various techniques over the course of the experiments. Since the shaker was rigidly connected to the spheroid, it may be assumed that its oscillating motion is equal to that of the immersed body. The first method involved a linear variable displacement transducer, or LVDT (Sensotec 060-3621-01). The output voltage of the sensor is a function of the position of the core within the housing. Since the core is mechanically coupled to the tip of the sensor, the motion of the tip is easily monitored. The output voltage could be monitored with the input signal to determine the proper settings for the LabVIEW™ program to create the desired motion of the body. However, due to the size and shape of the sensor, it was difficult to mount to the apparatus without placing an uneven, and possibly unbalancing, load on the shaker table.

The next method employed to monitor the displacement of the spheroid and determine the appropriate phase offset and attenuator settings was an optical technique. The magnification of the camera was determined by imaging either a body of known dimension or a ruler. Then the body was oscillated at a range of attenuator settings and frequencies while the camera records a sequence of ninety-five images at a framing rate of *f*/1.025 covering nearly 2.5 cycles of motion. These images were acquired with the

lens at close to the maximum magnification of about 79,000 pixels/m (corresponding to an oscillation amplitude of 50 pixels at $\varepsilon = 0.05$). Using the acquired images, edge detection techniques were applied to a small (60 pixels wide) section of the lower edge of the spheroid to determine its location over the entire sequence. A least-squares curve-fit (in MATLAB® v7) to the appropriate waveform was then used to determine the oscillation amplitude(s). As before, the magnitude(s) of the signal driving the shaker and spheroid were then manually adjusted using the attenuator and LabVIEW™ until the oscillation amplitude(s) of the body reached its desired value. For multiple-frequency oscillations, the signal was also adjusted to ensure that the relative phase between the two sinusoidal waveforms was 0 or π. The images were phase-locked to the body oscillation by adjusting the delay in triggering the camera so that images of the body acquired an integral number of fundamental half-periods apart (*i.e.*, spaced by $N\pi$ in phase where N is an odd integer) were stationary. However, this technique did not allow the motion of the oscillating bodies to be monitored while data were being collected.

Finally, an induction displacement sensor was employed to monitor the motion of the shaker table. The digital displacement sensor (Sensor head: Keyence EX-422V; Controller: Keyence EX-V10) is capable of measuring 10 mm displacements, with 2 μm resolution, 0.075 ms response time, and 0.02 ms measuring time. The attenuator and LabVIEW™ phase settings were determined from these acquired data. As with the LVDT, the induction sensor can be used to measure the response of the shaker at the same time as the experimental test runs, but without actually contacting the shaker table.

3.1.2 Working Fluid, Tank, and Support Structure

The body was immersed in a viscous working fluid contained within a glass-walled tank. The initial experimental setup used a commercial 38 L glass fish tank (25 × 50 × 30 cm), which was replaced by a 63 L 37 × 37 × 46 cm glass tank of in-house manufacture. The working fluid was 10% water and 90% glycerin by weight with a

density of 1.23 g/cm^3 at 22°C. Pure glycerin absorbs water from the atmosphere, therefore a water/glycerin mixture was chosen because its properties are more stable (Petit and Gondret 1992). In general, 31 L of fluid was used for experiments in the 38 L tank while 34 L of fluid was used in the 63 L tank, giving a depth of about 250 mm of fluid. The fluid temperature varied between f 21°C and 25°C over the course of these experiments due to variations in room temperature, giving kinematic viscosities ranging from 130 cSt to 170 cSt. The temperature of the fluid was monitored during testing, initially using an immersion thermometer (SAMA CT15/Taylor 6332, accuracy of ±0.5°C) and later with two thermocouples (Omega Type T, error ±0.5°C) and digital reader (Omega HH806AU, error ±0.3°C).

The fluid was seeded with silver-coated 13 μm hollow glass bubbles (Potters Industries SH400S20) with a density ρ = 1.3 g/cm^3. The initial concentration of particles was nominally 27 ppm by weight. The fluid was filtered as required with a filter that removed particulates as small as 5 μm, and reseeded at 10 ppm by weight. Because the performance of the particles decreases over time, the lower seeding density was sufficient for the new particles that were added after the solution had been filtered.

The glass tank and optics were supported by a custom optical breadboard on a pneumatic vibration isolation mount (Newport LW Light Load Vibration Isolated Workstation 04SI62994, 76 × 91 cm table). The workstation had a support rail rigidly mounted to the table legs, but isolated from the table, which was used to mount the camera for most test cases. When high magnification required a shorter working distance (*e.g.* the slotted spheroid cases), the camera was mounted on the table itself.

The shaker was suspended above the fluid with its moving table facing the fluid. Initially, the shaker was mounted on a 41 mm (1.625 in) square profile UNISTRUT type steel frame bolted to the lab floor, as shown in Figure 3.1. However, due to the cantilevered mounting, vibration of the frame became a concern. To reduce these vibrations, the mount was redesigned to bolt the shaker to a larger mass. The shaker was

then centered on a steel I-beam (190 cm long, 25.4 cm wide, 25.4 cm tall, 1.4 cm flange thickness, 0.86 cm web thickness) supported on either side by columns of concrete blocks (Figure 3.2).

3.1.3 Illumination, Imaging and Optics

These experiments acquired a sequence of phase-locked images of the illuminated tracer particles convected by the steady streaming flow driven by the oscillating body. The illumination is from a light sheet with a thickness of about 1 mm formed by passing the beam from an argon-ion laser (Coherent Innova 90) with a typical output power of 1.2 W at a wavelength of 514 nm through a series of spherical and cylindrical lenses (Figures 3.5 and 3.6). The body was illuminated along the plane of symmetry, unless otherwise stated.

Two different illumination configurations were used in these studies. In the first, the oscillating body was imaged on both sides by dividing the light sheet using a beamsplitter and using mirrors to create two counterpropagating light sheets (Figure 3.5). This configuration eliminated any shadowing effects from opaque bodies. In the second configuration, the body was only illuminated from one side (Figure 3.6). This configuration was typically used for "close-ups" of the body, especially of the groove, when only one side of the body was visible in the image.

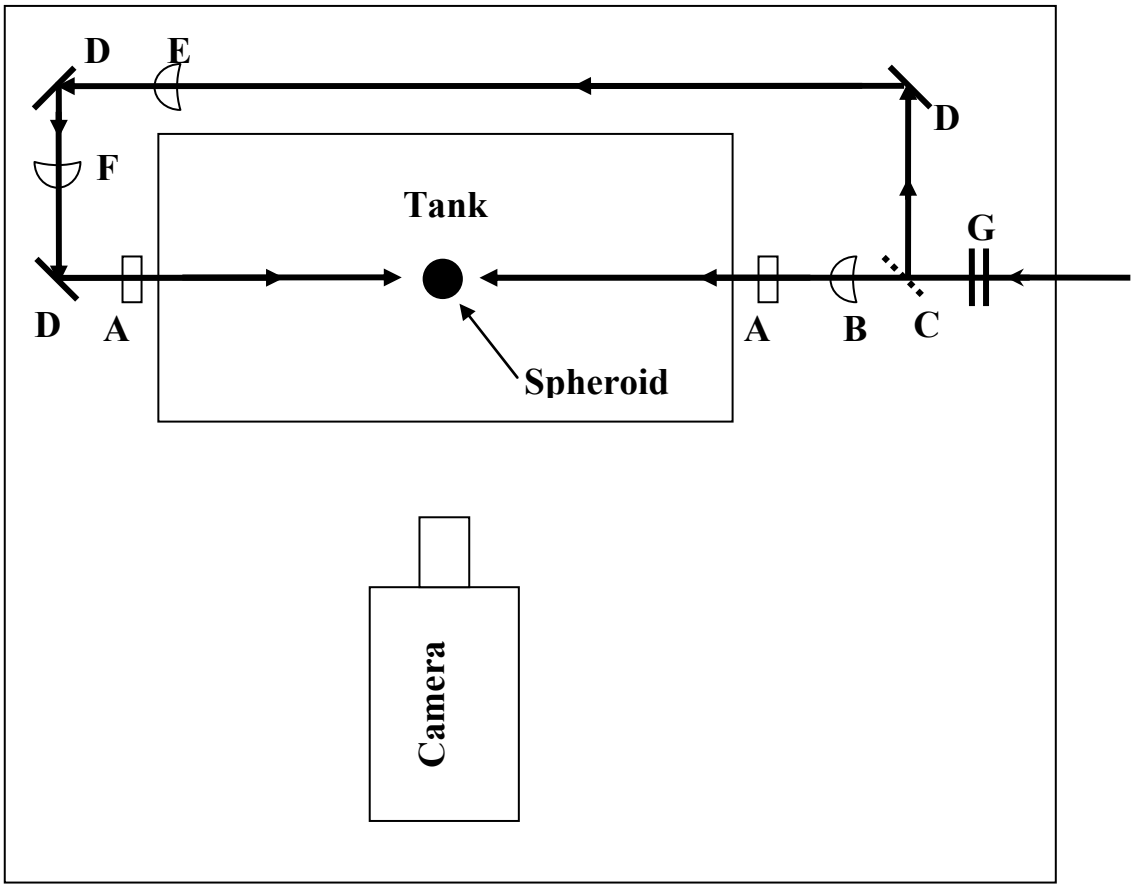

Figure 3.5 Schematic of a typical experimental layout on the optical table for illuminating the oscillating body from both sides. Entering laser light indicated by arrow on the right of the diagram. (A) Cylindrical lens (Thorlabs LK1087L2, f = -6.4 mm), (B) Spherical lens (Melles-Griot 01LPX313, f = -400 mm), (C) Beamsplitter/neutral density filter (Melles Griot 03FNG045, OD 0.3), (D) Plane mirror (various manufacturers), (E) Spherical lens (Newport KPX124, f = 1000 mm), (F) Spherical lens (Newport KPX 118, f = 500 mm), (G) Beam director (2 plane mirrors positioned to change the height of the laser beam)

The 1008 × 1000 pixel images were acquired with an 8-bit CCD camera (Kodak model ES 1.0) placed at a working distance of 25–50 cm from the front of the lens. Images were externally triggered and phase-locked to the oscillation up to the maximum camera framing rate of 27 Hz. The camera was equipped with a zoom lens (NAVITAR 7000, focal length 18–108 mm) with an adjustable aperture, which was fully open except

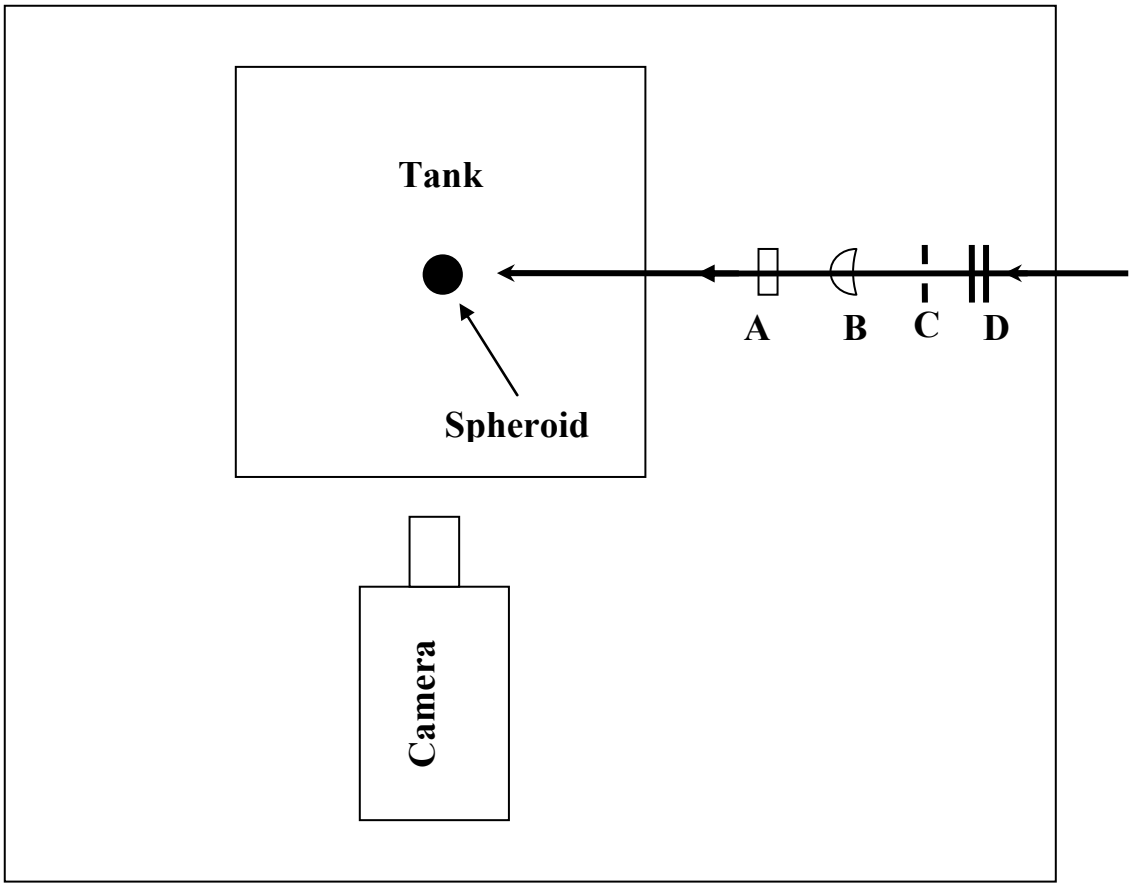

Figure 3.6 Schematic of a typical experimental layout on the optical table for illuminating the oscillating body from one side. Entering laser light indicated by arrow on the right of the diagram. (A) Cylindrical lens (Thorlabs LK1087L2, f = -6.4 mm), (B) Spherical lens (Melles-Griot 01LPX313, f = -400 mm), (C) Iris diaphragm (Thor Labs, Inc. SM1D12), (D) Beam director (2 plane mirrors positioned to change the height of the laser beam)

at the highest magnifications where a smaller aperture (generally reducing the aperture diameter by one half) was used to reduce spherical aberrations.

The LabVIEW^{TM} computer program generated an external trigger signal for each image of the sequence that was then recorded to the hard drive of a PC using a framegrabber card (Matrox Meteor II/DIG) and commercial image capture software (Video Savant v3.0, later upgraded to v4.0). The amount of light the images were exposed to was originally controlled by the exposure time of the camera. However, at high magnifications, concern over small convective motions due to heating of the

spheroid resulted in the need to control the laser light with an acousto-optic modulator (ISOMET model 1201E-1, controller model 521C-2). The acousto-optic modulator (AOM) was also controlled using LabVIEW™. Initially, LabVIEW™ generated a trigger signal which was sent to a function generator (Analogic polynomial waveform synthesizer model 2020) which then created a trigger for the camera and a TTL signal for the AOM. After the switch to Video Savant v4.0, the hardware configuration was changed to allow the camera to trigger off of the same signal as the AOM by using a weighted summer (Tucker Davis Technologies Model SM3) to invert and modify the signal for the framegrabber.

3.1.4 Coordinating Computer

A computer program written in LabVIEW™ v5.0 was used to control the oscillations, image capture, and AOM (where applicable). In addition, the program monitored and recorded the output signals and the readings from the displacement sensor (LVDT or induction sensor as described above). The program was run on a PC using a 12-bit data acquisition card (National Instruments PCI-MIO-16E-4) and a BNC terminal block (National Instruments BNC-2090). The LabVIEW™ code consisted of four major subroutines that:

1. gather the input data,
2. create the output waveforms in memory,
3. generate the waveforms on the terminal block, and
4. record the response of the system from the terminal block.

The input data used by the system includes the parameters used to generate the body's oscillation, image the body, and record the movement of the body. For single-frequency oscillations, the body's motion is described by the oscillation frequency, the oscillation amplitude (in Volts), and the number of points to use in defining the curve. The startup time, t_s, for the oscillation is also specified. In addition, for multiple frequency

oscillations it is necessary to specify the second oscillation frequency phase offset, ϕ_2, and relative amplitude ratio of the two sinusoids. To image the body, the trigger signal must be defined, including the trigger frequency, f_t, the trigger amplitude (in Volts), the trigger phase offset, ϕ_t, the length of the trigger signal, and the number of trigger signals to send. The code also allows the user to specify the parameters for recording the response of the system, including the data rate, trigger conditions, and the number of points to record. The relationship between several of these parameters is illustrated in Figure 3.7.

Based on the input parameters, the code created the waveforms that would be sent to the shaker and trigger the camera. A sinusoid of the appropriate length was created and stored, with a short start-up and die-out section of the requested length appended. The start-up and die-out sections were sinusoids that had been multiplied by an error function so that the amplitude of oscillation slowly increased and decreased to avoid sending a voltage with a very large slope to the shaker. The trigger signal is created as a modified square wave that has a "high" voltage value at the desired time and is "zero" for the remainder of the cycle. The signal also has a phase shift relative to the oscillation so that the camera is triggered at the desired position within the oscillation (generally when the body is at the center of its oscillation).

The created signals are then sent to the storage buffers and from there to the analog output of the data acquisition card. These signals from the card are transmitted to the BNC block, where they are connected to the inputs of the shaker, camera, and AOM as described above.

The response of the system is recorded from the analog inputs of the terminal block. The code records the shaker drive signal, the camera trigger, and the shaker displacement, if available. These readings are then saved to a text file along with the time from the start of the data sequence. The length of this data file is set independently of the

output of the system, and usually encompasses the first second of oscillation. (Screenshots of the graphical LabVIEW™ code may be found in Appendix D.)

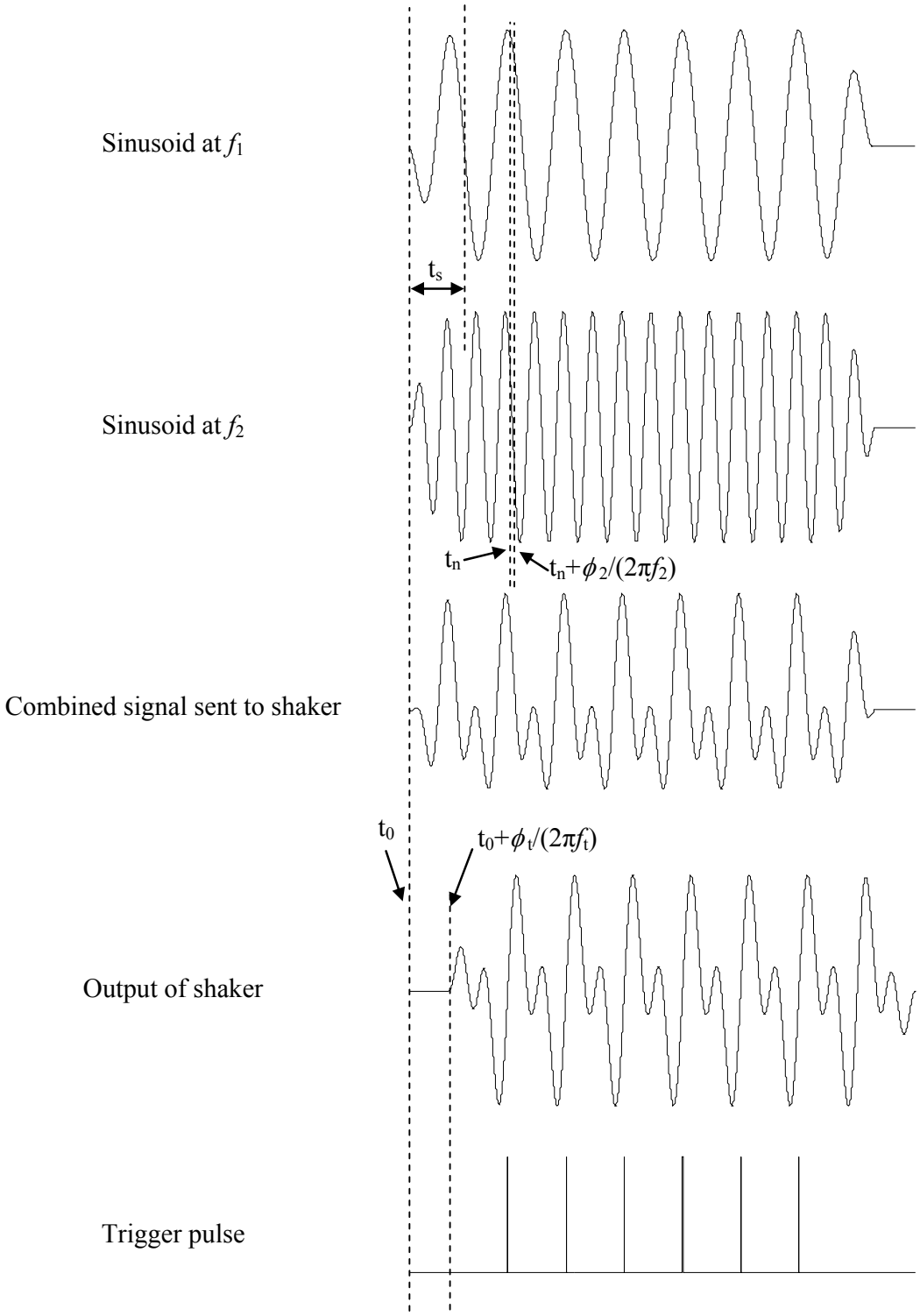

Figure 3.7 Timing diagram illustrating the relationship between various curves created or measured by the LabVIEW™ program.

3.2 Data Acquisition and Analysis

3.2.1 Acquired Data

Using the above methods, data were taken to characterize the steady streaming flow fields near oscillating bodies. The raw data collected consisted of sequences of 100–1000 equally spaced images illustrating the movement of the tracer particles within the working fluid due to the oscillation of the body. Data were taken for bodies of various geometries as described above, orientations from 0 to 75°, and oscillation patterns described by sinusoids of one frequency or the sum of two frequencies. A complete listing of test conditions can be found in Appendix C.

These data sets have been analyzed using a variety of techniques, which are summarized below. These include creating particle pathline images, measuring velocity fields using particle image velocimetry (PIV), locating stagnation points, and measuring the out-of-plane vorticity.

3.2.2 Particle Pathlines

Particle pathline images are created from the long image sequences by selecting an evenly spaced subset and averaging the grayscale values of the images. This composite image effectively creates a "long-time exposure" image which visualizes the flow patterns formed from the individual particle paths. Typically, the number of images averaged covers 75–100 oscillations; however, unusually slow particle motions may require longer sequences, up to the length of the test run (300–500 oscillations).

3.2.3 Body Location

The data analysis usually gives the results in terms of the body coordinate system. In general, this coordinate system was defined in terms of the body location, found by locating 10–15 roughly evenly spaced points along the edge of the body either visually or

using MATLAB®'s built in edge detection routines. A non-linear least squares curve fit to these points then determined the orientation and dimensions of the circular or elliptical body profile. Repeating these techniques usually provided estimates that varied by less than 1% for the body dimensions and at most 2° for the body orientation. In general, the results given are the average of several (typically five) test cases. The MATLAB® code for the circular and elliptical curve fit may be found in Appendices E.1.1–E.1.3.

3.2.4 PIV Analysis

The PIV analysis is based on the direct cross correlation methods with cross-correlation averaging described by Meinhart *et al*. (2000). Although the length of the image sequences taken varies between tests, the same general analysis procedure has been followed for the data presented in this thesis. Before computing the velocity vectors, the image sequence is averaged, and the average image is subtracted from the sequence in order to remove background noise. Then a 32×32 pixel computation grid is established relative to the images, with a 50 pixel border around the edge (for example, grid nodes in both the *x*- and *y*- directions were located at 50, 82,…, 946). In order to save computation time, grid nodes located within the body were not analyzed. For the spheroidal body cases, the grid nodes inside the body were found using the previously determined location of the spheroidal body. While for the otolith cases, the relatively bright body was located by taking a threshold of the averaged image, and locating the largest continuous area of bright pixels.

These image sequences were prepared for PIV processing by removing the first 25 images to minimize start-up effects. The remaining images were divided into 5 equal groups (if the remaining images were not evenly divisible by 5, the sequence was truncated). Within each of these sub-regions, the images are paired for analysis. The image separation varied between test runs and was adjusted for each test case to provide a maximum particle displacement between 4 and 12 pixels. The image pairs were then

processed using PIV with cross-correlation averaging. In general, the PIV processing calculated the cross-correlation plane of each image pair by moving a 16×16 interrogation window around a 48×48 pixel search window that is centered at the grid node. The individual cross-correlation planes of each node are then averaged, and the peak is used to determine the particle displacement. To determine the sub-pixel component of the displacement, a Gaussian curve is fit to the correlation plane. The PIV processing was then repeated using the entire image sequence. The computer code used for this processing was written by a Haifeng Li, a Ph.D. student in Mechanical Engineering at the Georgia Institute of Technology, as part of his doctoral studies.

The uncertainty in estimating the velocity fields comes from both the uncertainty in the PIV analysis and the repeatability of experimental setup. The uncertainty in the PIV processing can be estimated from the standard deviation of the velocity vectors found from the five sub-regions. The repeatability of the experiment can be found by considering stand deviation of the results of separate, but otherwise identical, test runs. The uncertainty, Δ, is then estimated from these standard deviations, δ, as

$$\Delta_{u,v} = \sqrt{(\delta_{u,v}^{P})^2 + (\delta_{u,v}^{E})^2} \qquad 3.2$$

where the subscripts represent the *u* and *v* velocity components. The superscripts *P* and *E* represent the standard deviation in the PIV analysis and experimental setup, respectively. The error in the experimental setup for the data taken with clear acrylic spheroids were found to be $\delta_u^E = 0.007$ mm/s and $\delta_v^E = 0.01$ mm/s (Kotas *et al.* 2008).

The velocity vector field from the entire image sequence was generally the smoothest and assumed to be the most accurate. These vectors were processed to remove spurious vectors, using the criterion suggested by Westerweel and Scarano (2005). The MATLAB® implementation of this calculation may be found in Appendix E.2. These filtered and unfiltered vector fields were then used for further analysis of the stagnation point locations and the out-of-plane vorticity, as described below.

3.2.5 Stagnation Point Location

Stagnation points in the steady streaming flow may be located using either the particle pathline images or the PIV data. Using the particle pathline images, stagnation points are located visually from the pathline patterns by looking for locations where the flow either "stops" or never enters. For example, the particles never enter the center of the rotating "vortical" regions or the point where the regions meet. It is also possible to visually follow the particle pathlines which delineate the flow regions near the body to locate the stagnation points along the body surface.

The stagnation points may also be found from the PIV vector field using bilinear interpolation to locate positions within the flow where the velocity goes to zero. The MATLAB® code used for these calculations may be found in Appendix E.3.1.

Near the body, where the PIV vector field is less reliable, two assumptions are made in order to estimate the location of the stagnation points. The first is that the stagnation point lies on the elliptical body outline, which has been determined as described above. The second is that a stagnation point should be approximated by the intersection of the body and a line drawn through points where the velocity tangential to the body goes to zero. (The tangential direction was approximated using polar coordinates for the circular profiles and spheroidal coordinates for the elliptical, with the tangential direction along the circular or elliptical curves.) These points are located by creating an ordered list of the grid locations adjacent to the body and determining the sign of the tangential velocity at each of these grid locations. Locations where the velocity component changes sign imply that the flow has changed directions, and should be near a stagnation point. To improve the estimation of the stagnation point, PIV is used to find additional velocity vectors on a finer 8×8 pixel grid in the immediate 32×32 or 48×48 pixel region surrounding the grid node closest to where the velocity changed sign. It is then possible to take the velocity component that changed sign and locate the three

"zeros" closest to the body using linear interpolation. The stagnation point is then estimated by a line fit to these points and its the intersection with the body. If the line fails to intersect the body, the closest zero to the ellipse is used to locate the closest point on the ellipse, and that is used as the stagnation point estimate. The work on the near body stagnation points was done in collaboration with Ehsan Maleki (GT BSME 07). The MATLAB® code used for locating the stagnation point near a spheroidal body is given in Appendix E.3.2.

3.2.6 Vorticity

As discussed in Kotas *et al.* (2008), the out-of-plane vorticity component Ω_z is found from the PIV velocity vectors describing the steady streaming velocities. At a location (x_0, y_0) on a grid with spacing Δx and Δy in the x- and y- directions, respectively, Ω_z can be found from the nearest 8 neighboring points using the circulation method (Abrahamson and Lonnes 1995):

$$\Omega_z = \frac{\Gamma}{A} = \frac{-\int_{x_0-\Delta x}^{x_0+\Delta x} u\Big|_{y_0+\Delta y} dx + \int_{x_0+\Delta x}^{x_0-\Delta x} u\Big|_{y_0-\Delta y} dx - \int_{y_0+\Delta y}^{y_0-\Delta y} v\Big|_{x_0+\Delta x} dy + \int_{y_0-\Delta y}^{y_0+\Delta y} v\Big|_{x_0-\Delta x} dy}{4(\Delta x)(\Delta y)} \qquad 3.3$$

Here A is the area enclosed by the 8 neighboring points surrounding x_0 and y_0, Γ is the circulation, u and v are the x- and y-components of the velocity, respectively. If the circulation method cannot be used because of spurious velocity vectors, the out-of-plane vorticity component can be found using its definition

$$\Omega_z = \frac{\partial v}{\partial x} - \frac{\partial u}{\partial y}, \qquad 3.4$$

where the derivatives are determined using the highest-order finite difference scheme possible based on the available velocity vectors. These expressions assume that Ω_z is positive for a counter-clockwise rotation. The MATLAB® code used for these calculations may be found in Appendix E.4.

CHAPTER 4

AXISYMMETRIC TEST CASES

4.1 Results

4.1.1 General Features of the Steady Streaming Flow Patterns

A typical example of the particle pathlines visualizing the steady streaming flow driven by a spheroidal body oscillated sinusoidally in a viscous fluid otherwise at rest for moderate Reynolds numbers is shown in Figure 4.1. In the figures shown in this thesis, the direction of oscillation is denoted by a double-headed arrow and is, unless otherwise stated, along the vertical. As shown in the diagram, the orthogonal body-fixed coordinate system has its origin at the center of the body, an x-axis along the horizontal pointing to the right, and a y-axis along the vertical pointing downwards. Since the body is

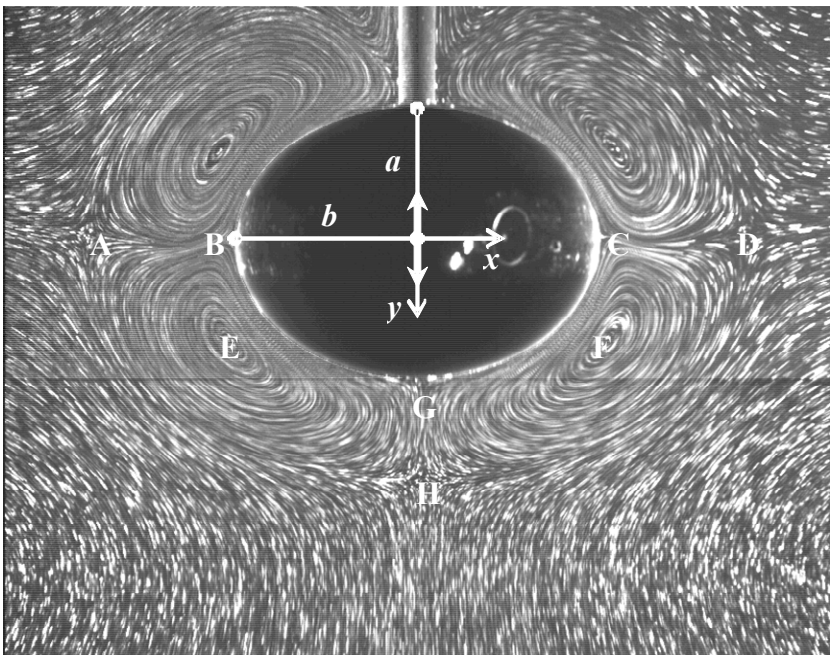

Figure 4.1 Definition sketch for axisymmetric steady streaming about a spheroid. (Re_M = 42, ε = 0.15, AR = 0.74)

axisymmetric, it is not necessary to explicitly define a third spatial dimension. However, a z-axis orthogonal to the x-y plane or an angular coordinate defined by the rotation of the y-axis (as in cylindrical coordinates) could be used. As described in Chapter 2, the body half-dimension along the axis of oscillation is denoted by a, while the equatorial radius is denoted by b (where the polar axis is defined by the axis of oscillation (the y-axis), and the aspect ratio $AR = a/b$.

Since the top-bottom symmetry of the flow pattern shown in Figure 4.1 is broken by the presence of the mounting rod, the results presented here are all determined from the presumably less disturbed flow near the lower half of the body. In order to describe the flows, the locations where the streaming velocity is zero are labeled in the image by the letters A through H. For simplicity, this thesis will refer to these locations as "stagnation points," though they are, strictly speaking, only the where the streaming velocity (*vs.* the time-dependent velocity) is zero. In addition, only G and H are likely to be "points." As the body is rotated, the "points" in this slice of the body become lines.

Since the image shows a diametric slice of a flow that is axisymmetric about the y-axis, the lower rotating regions adjacent to the body are part of the same "toroidal" rotating eddy. These stagnation points on the lower half of the body divide this rotating region into the counter-rotating regions shown. Stagnation points (B, G) are on the body, and will be referred to as the "on-surface stagnation points," while stagnation points (A, D, H) divide the so-called inner and outer flow regions, as discussed in the Literature Review. Points (E, F) represent the center of the inner rotating region. The inner rotating region is divided along the line connecting stagnation points G and H, where the flow turns and approaches the body. The inner rotation region to the left and right of the body centered about E and F, respectively, rotate counter-clockwise and clockwise, respectively. Conversely, in the outer region the flow approaches point A from the left and point D from the right, leading to a clockwise and counter-clockwise rotation to the left and right, respectively, of the body. Although not shown in the Figure, the mean

horizontal distance between A and D and the edge of the body is denoted by T, while the minimum distance from the centers of the rotating regions (E and F) and the nearest surface of the body is denoted by h.

The flow patterns around spheroids of various aspect ratio are qualitatively similar, with the inner flow region essentially mimicking the shape of the body. As shown in Figure 4.2 for the steady streaming flows around a prolate spheroid of AR = 1.33 (a), a sphere (b), and an oblate spheroid of AR = 0.74 (c), all at Re_M =42 and ε =0.15, the particle pathlines around sinusoidally oscillated spheroids retain their left–right symmetry and the inner and outer flow regions. The steady streaming flow within the inner region along the axis of oscillation is inwards towards the body in all cases. These three images are all at different magnifications so that they have a consistent length scale L; the largest physical dimension of each of the bodies is approximately 25.4 mm. With this scaling, the radial extent of the inner region normalized by L appears to be similar for all of these bodies, as will be discussed in more detail subsequently. It should also be noted that the radial extent of this inner region is not constant over the surface of the body; the analytical solution of Rednikov and Sadhal (2004) shows that for an oblate spheroid of AR = 0.5, the thickness of the inner region along the y-axis (*i.e.*, the axis of oscillation) is approximately 90% less than that along the x-axis.

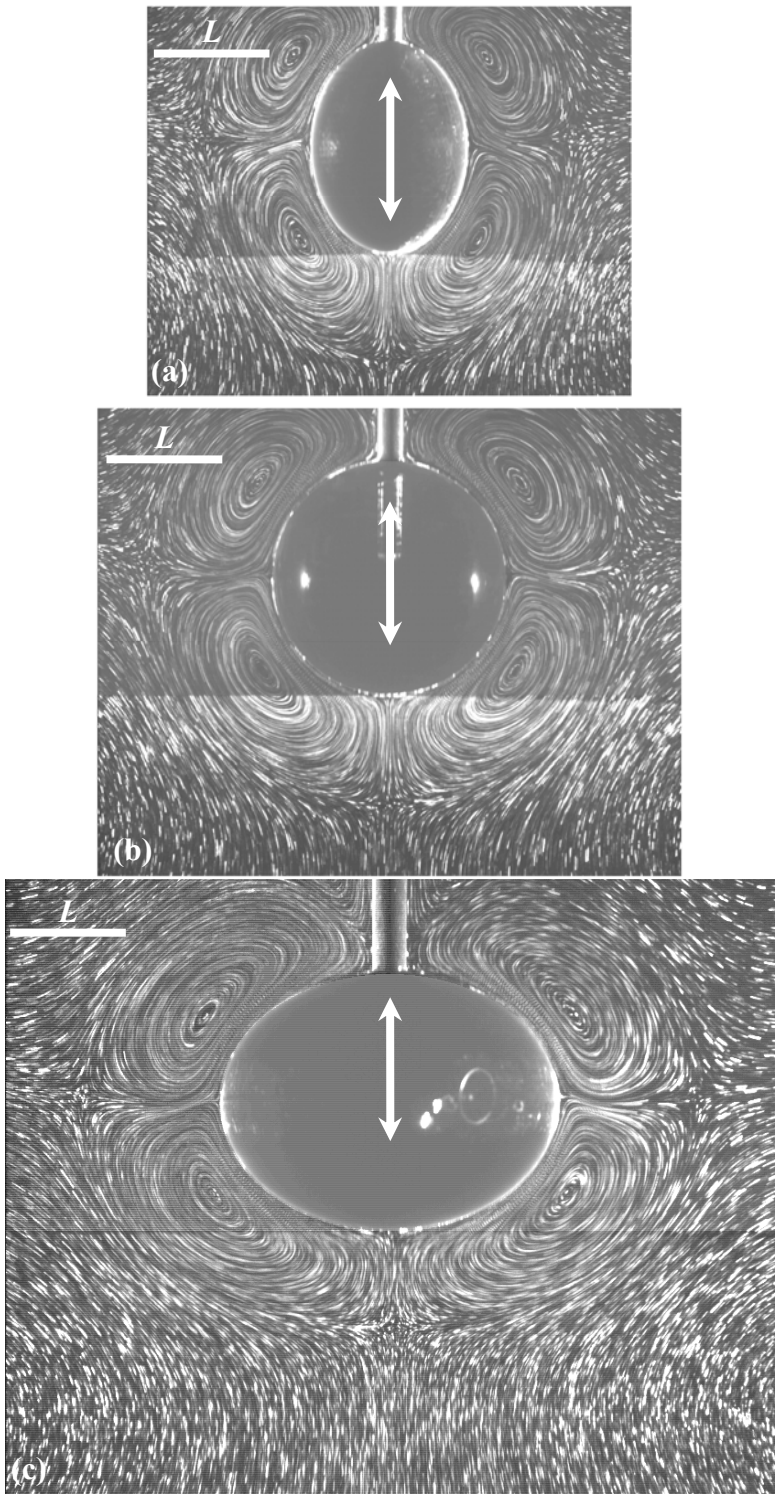

Figure 4.2 Particle pathlines at $Re_M = 42$, $\varepsilon = 0.15$ for aspect ratios of (a) $AR = 1.33$ (62 oscillations), (b) $AR = 1$ (68 oscillations), (c) $AR = 0.74$ (100 oscillations). The images have a magnification that ensures that L is consistent in each image. The double arrow indicates the axis of symmetry and the direction of oscillation.

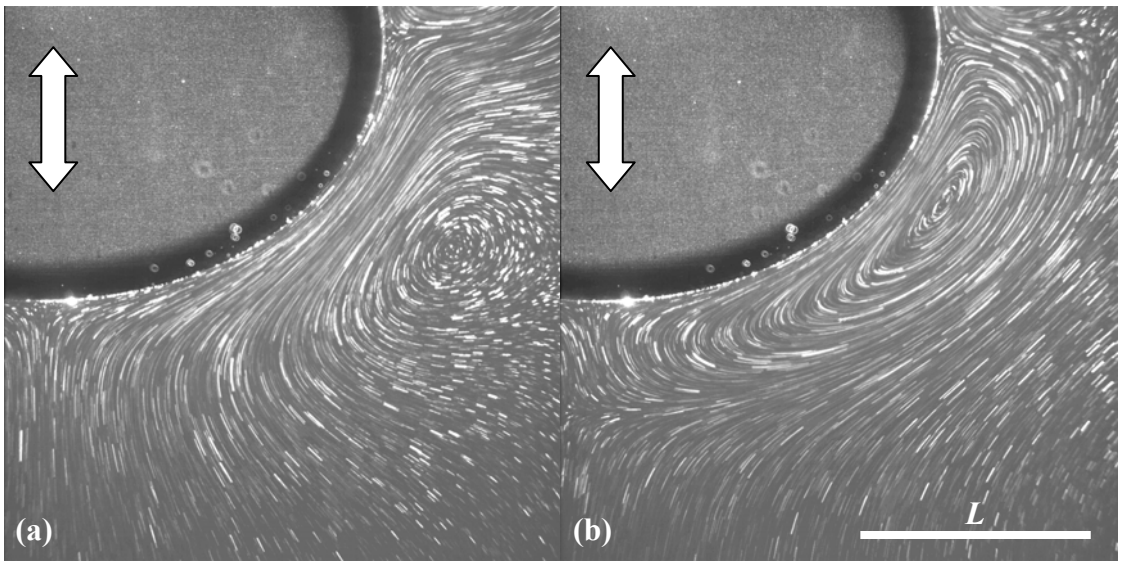

Figure 4.3 Steady streaming pathlines over 100 oscillation periods of an oblate spheroid (AR = 0.76, ε = 0.05) at (a) Re_M = 26 and (b) Re_M = 78.

The extent of the inner region decreases as the Reynolds number of the steady streaming flow increases, as shown in Figure 4.3 for an oblate spheroid (AR = 0.76) at Re_M = 26 (a) and 78 (b) and ε =0.05; note that both images are shown at the same magnification. Here, the outer edge of the inner region goes from being completely outside of the field of view to within 0.7L of the body surface.

The normalized oscillation amplitude, ε, appears to have almost no effect on the flow patterns. Presumably, this is due to the studied steady flow being in the linear regime where terms of higher order in epsilon are small enough to be ignored. Figure 4.4 shows particle pathlines near a sphere at Re_M =60 and ε = 0.05 (a) and ε = 0.18 (b) over 75 oscillation periods. The flow patterns visualized by the pathlines are qualitatively nearly identical, although the actual length of the pathlines is less for the lower ε case because of the resultant reduction in the streaming flow speeds.

4.1.2 Outer Stagnation Points/Inner Vortex Limits

As discussed above, the extent of the inner rotating region is clearly a function of both the body geometry and the Reynolds number. Raney *et al.* (1954), who studied the steady streaming around circular cylinders, suggested that inner layer thickness became a self-similar function of Reynolds number when the radius was used as the length scale. To the best of the author's knowledge, previous studies of spheroids have not reported a specific correlation relating the extent of the inner region to the Reynolds number. In addition, several different length scales have been suggested by different studies, including the equatorial radius, the equivalent radius, and the focal distance of the spheroid (Alassar and Badr 1999a; Rednikov and Sadhal 2004), with relatively little justification. After evaluating all of these suggested length scales, the results from the steady streaming flows in this study indicate that the length scale that best reduces the extent of the inner region to a self-similar function of Re_M is

$$L \equiv (AR)\, r_{eq} = \left(\frac{a}{b}\right)\left(b^2 a\right)^{1/3} = \left(\frac{a^4}{b}\right)^{1/3}, \qquad 4.1$$

where r_{eq} is the radius of a sphere with a volume equal to that of the body. The depth of

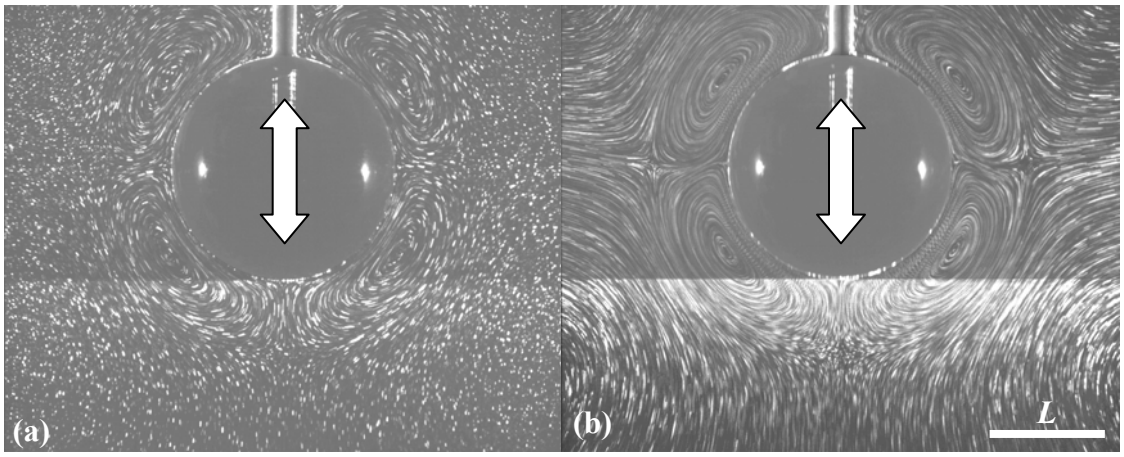

Figure 4.4 Steady streaming pathlines over 75 oscillation periods of a sphere for Re_M = 60 at (a) ε = 0.05 and (b) ε = 0.18.

the inner layer, T, was defined to be the average horizontal distance from the surface of the body to the side stagnation points (A and D in Figure 4.1). Figure 4.5 shows a log-log plot of T/L as a function of Re_M for spheroids of AR = 0.76 (triangle), 1 (circle), 1.35 (diamond) and 2 (square) for ε values ranging from 0.04 to 0.3. The plot suggests that T/L is essentially independent of ε and is related to Reynolds number as follows:

$$\frac{T}{L} = \frac{44}{Re_M} \Rightarrow T = 44\frac{\nu}{\omega L}$$

over the range of Re_M studied here. Only the side stagnation points were used due to the presence of the mounting rod and previous analyses suggesting that the thickness of the layer is not uniform (Rednikov and Sadhal 2004). The test cases used to create this plot are listed under "Axisymmetric Data" in Appendix C.

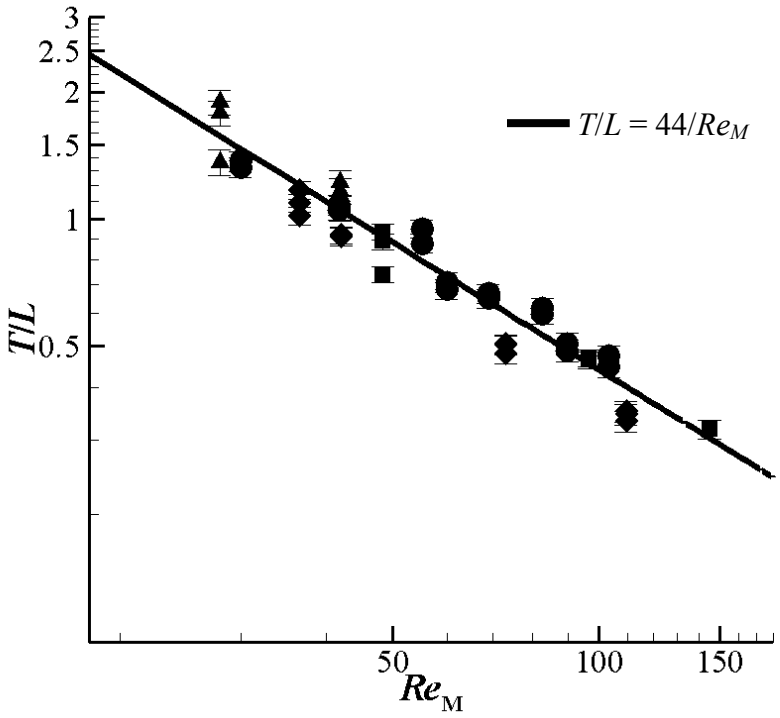

Figure 4.5 Log-log plot of the extent of the normalized inner region as a function of Reynolds number for AR = 0.76 (*triangle*), 1 (*circle*), 1.35 (*diamond*), and 2 (*square*).

4.1.3 Center of the Inner Rotating Region

The extent of the inner region can also be described by the shortest distance, *h*, from the body to the center of the inner rotating region, denoted by E and F in Figure 4.1. The streaming velocities within this region will be along the same direction relative to the body, suggesting that the hair cell cilia, which would measure the fluid displacement in the auditory retina hypothesis, would need to be within this distance of the body to have a consistent deflection along their entire length.

The asymptotic analysis of Rednikov and Sadhal (2004) for steady streaming near oblate spheroids at large Reynolds numbers suggests that for the axisymmetric case, the center of the inner rotating region is a function of the aspect ratio and Reynolds number. Their solution is defined in terms of modified oblate spheroidal coordinates (μ, λ). As defined in their paper, the orthogonal coordinate system consists of confocal ellipsoids centered at the origin, denoted by λ, and hyperboloids of revolution, denoted by μ. These coordinates can be related to standard cylindrical polar coordinates *z* and *r*, where *z* is aligned with the body's axis of symmetry and *r* is the distance from the *z*-axis, as follows

$$z = c_e \lambda \mu \tag{4.2}$$

$$r = c_e \left(1+\lambda^2\right)^{1/2} \left(1-\mu^2\right)^{1/2} \tag{4.3}$$

or

$$\mu^2 = -\frac{1}{2}\left(\frac{r^2}{c_e{}^2}+\frac{z^2}{c_e{}^2}-1\right) \pm \frac{1}{2}\left[\left(\frac{r^2}{c_e{}^2}+\frac{z^2}{c_e{}^2}-1\right)^2 + 4\frac{z^2}{c_e{}^2}\right]^{1/2} \tag{4.4}$$

$$\lambda = \frac{z}{c_e \mu} \tag{4.5}$$

where $c_e{}^2 = b^2 - a^2$ is the focal length of the ellipse. As defined by the above equations, λ monotonically increases from λ_0 at the surface of the body to ∞, while μ varies from ±1 along the axis of oscillation to 0 at the "equator." The relationship between the (*r*, *z*) and

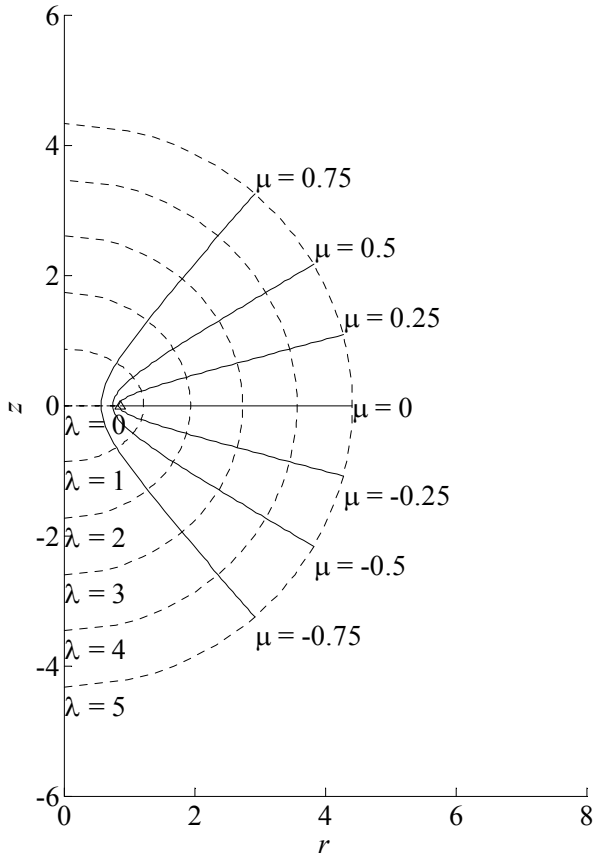

Figure 4.6 Sketch of the oblate ellipsoidal coordinate system with $c_e = 0.866$.

(λ, μ) coordinate systems is shown graphically in Figure 4.6 Because c_e must be a real number, this coordinate system definition does not apply to spheres and prolate spheroids. However, similar coordinate systems exist for these cases. For comparison, the value of μ will be taken as cos(θ), where θ is the polar angle, for spherical coordinates, and

$$\mu^2 = \frac{1}{2}\left(\frac{r^2}{c_e^{\,2}} + \frac{z^2}{c_e^{\,2}} + 1\right) \pm \frac{1}{2}\left[\left(\frac{r^2}{c_e^{\,2}} + \frac{z^2}{c_e^{\,2}} + 1\right)^2 - 4\frac{z^2}{c_e^{\,2}}\right]^{1/2} \qquad 4.6$$

for prolate coordinates (where the focal length is now $c_e^{\,2} = a^2 - b^2$). These relationships are derived from the standard spherical and modified prolate coordinate systems (for example, Happel and Brenner 1965).

The measured μ location of the center of the inner rotating region is compared with the asymptotic value for oblate spheroids (Rednikov and Sadhal 2004) and spheres (Lane 1955) for the sphere in Figure 4.7. Although both the experimental and analytical results predict that the center of the rotating region will approach the equator as the AR decreases, the analytical results predict a much faster approach than the experimental results, which predict $\mu \approx 0.5$ for $AR < 1$. The discrepancy between the experimental and analytical results is most likely due to the relatively low Reynolds numbers ($Re_M < 80$) for the experimental data compared with the Reynolds numbers for the asymptotic analysis; $Re_M = 2$ for the $AR = 0.25$ case. The experimental data used to generate this graph are taken from the "single frequency" part of the multiple frequency data set and from the "Axisymmetric" data taken on May 21, 2008, as described in Appendix C. Results for the other axisymmetric cases used in this chapter were not included because their experimental errors led to significant uncertainty in the imaged oscillation phase, and thus the r and z coordinates. The error bars are calculated assuming an uncertainty of 5 pixels in locating the position of the body center, body dimensions, and location of the center of the vertical region, as discussed in Appendix A.

The distance from the body to the center of the inner rotating region, h, is shown normalized by the length scale L in the log-log graph of Figure 4.8. Like T/L, h/L decreases as Re_M increases and is essentially independent of ε. The values in this figure come from the "Axisymmetric" data set, including those omitted in Figure 4.7. If both stagnation points E and F are visible, then the average distance is used. The error calculation assumes 1 pixel uncertainty in the location and sizing of the body in the images, as well as 1 degree uncertainty in the orientation of the body. The error calculation is discussed further in Appendix A.

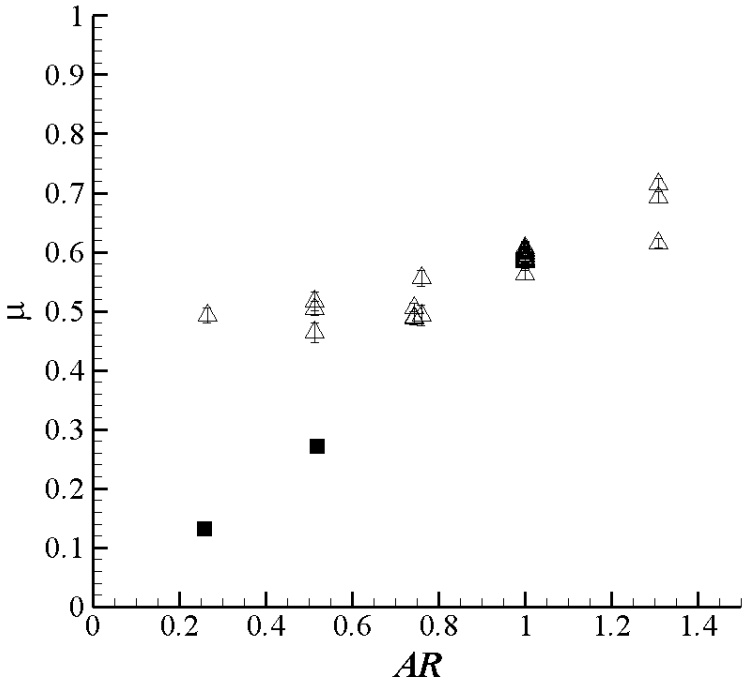

Figure 4.7 Comparison of the spheroidal angular location of the experimental data (*triangle*) and asymptotic theory (*square*) at various aspect ratios using the single frequency "multiple frequency" and May 21, 2008 data.

Rednikov and Sadhal suggested that the flow in the inner region for different *AR* should scale as the square root of the Reynolds number (dashed line), and hence scaled their streamfunction in the inner region by $Re_M^{1/2}$, c_e, and λ_0. Curve-fits of the form $h/L \propto Re_M^{N}$ through these experimental data give exponents N ranging from -0.4–0.6 for $AR = 0.5$–2; although the $AR = 0.25$ case again had anomalous behavior, with N = 0.2. This suggests that the scaling suggested by Rednikov and Sahal for h/L is valid for these data, even though their analysis was only applied to oblate spheroids at $Re_M >> 1$. Note, however, that the measured distance h is more than triple that predicted by Rednikov and Sadhal, which, as before, is most likely an effect of the smaller Reynolds number values for these experiments.

A curve-fit instead through all of the data for h/L at all aspect ratios suggests instead N = 2/3 (solid line) over the range of Reynolds numbers studied here. This

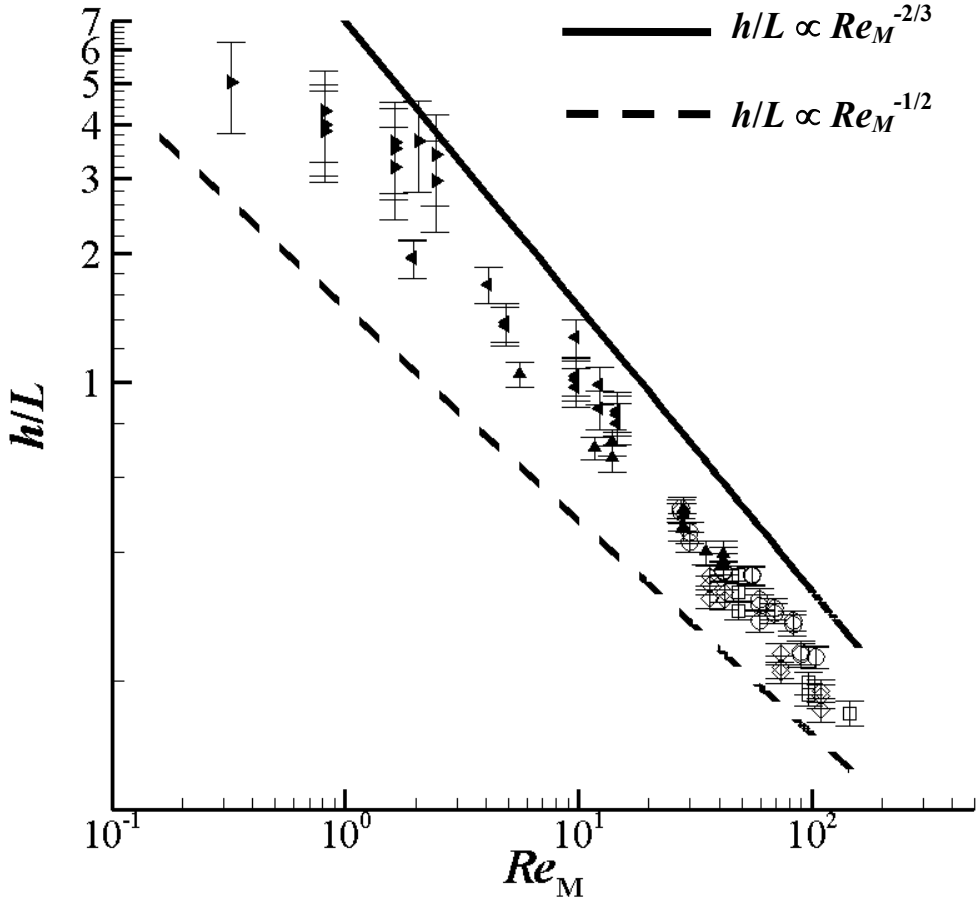

Figure 4.8 Log-log plot of the normalized distance to the center of the inner rotating region as a function of Reynolds number for AR = 0.26 (*left facing triangle*), 0.52 (*right facing triangle*), 0.76 (*triangle*), 1 (*circle*), 1.35 (*diamond*), and 2 (*square*).

observation comes with a caveat against further generalization. Since the data for different AR were obtained over different Reynolds number ranges—and several of these data sets have Re_M ranges that do not overlap—this scaling may be an artifact of the chosen test cases and the aspect ratio dependent parameters. In other words, there may not be a coherent trend for all values of AR, it might just look that way because of the spread in Re_M of our data.

4.1.4 Effect of Phase

Although phase-locked images were obtained to visualize only the steady streaming portion of the flow, the effect of the oscillation phase on these patterns was also investigated, in part to evaluate the errors associated with imaging the body out of phase, which was a concern in some of the early experiments. Figure 4.9 shows the particle pathlines for a sphere at $Re_M = 60$ and $\varepsilon = 0.1$ at the top (a), middle (b), and bottom (c) of its oscillation. The five stagnation points C, D, F, G, and H (as labeled in Figure 4.1), change their locations relative to the body with oscillation phase. For instance, as the body descends, the distance from G to H decreases, presumably due to fluid inertia. Similarly, D moves upward relative to body, as the body moves downward, while F shifts to the right. Meanwhile, the on-surface stagnation points (C, G) are essentially fixed in a body-centered frame of reference.

To help visualize the displacement of the stagnation points, the point of view is shifted from the observer, or Eulerian, to the body-fixed, or Lagrangian, frames, as shown in Figure 4.10(a) and (b), respectively. From the Eulerian perspective, it is apparent that the displacement of the off-body stagnation points at D and H are primarily vertical, while F moves primarily in the horizontal. The displacement of the off-body stagnation points is also far less than the movement of the body, $0.04L$–$0.06L$, *vs.* the displacement of the body of $0.2L$. In Lagrangian coordinates, the shift in these stagnation points is even greater, $0.15L$–$0.25L$. Finally, note that the measured variation in these stagnation point locations was 14–20 pixels, which is greater than our experimental uncertainty in locating the stagnation points.

From these results, it is shown that the steady streaming flow patterns vary with phase. Although this result is not unexpected, given the finite inertia of the fluid, the authors are unaware of previous studies demonstrating this effect (Kotas *et al.* 2008). It

should be noted that this case has a relatively large Stokes layer thickness, $(\nu/\omega)^{1/2}$, of about 0.14*L*, or 2 mm, which is comparable to the displacement of the body.

Because the steady streaming flow patterns vary with phase, some care must be taken in choosing the identifying characteristics of these flow fields. The angular location of the stagnation points (*e.g.* D and F) shows a greater variation with phase than the distance from the stagnation points to body. For instance, the horizontal distance between stagnation points C and D shows less variation than the variations in the total distance [about 0.006*L* (2 pixels) *vs.* 0.02*L* (6 pixels), respectively]. In this case, both measures of the inner region thickness are (nearly) within experimental error. However, the angular location of the side stagnation point varies by nearly 7°, making it a less reliable indicator of the stagnation point location. The location of the center of the inner rotating region (stagnation point F) shows much greater variability with phase. Its angular location moves by nearly 10° ($\mu = 0.14$), while *h* varies by 0.04*L* (12 pixels). This variation in angular position is the primary reason why the axisymmetric data from cases obtained before 2007 (mostly listed under Axisymmetric test cases in Appendix C.1) were omitted from Figure 4.7. The relative error measured here when $\varepsilon = 0.1$ provides a guideline to the errors that can be expected in the earliest axisymmetric data, where $\varepsilon = 0.05$–0.2.

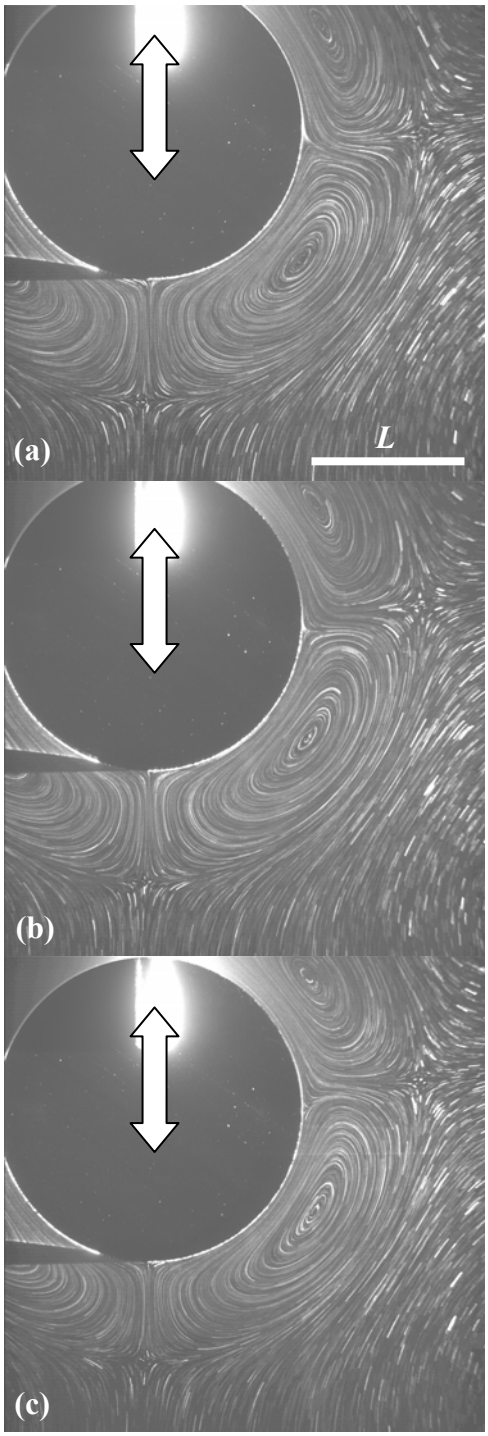

Figure 4.9 Steady streaming flow near a sphere ($Re_M = 60$, $\varepsilon = 0.1$) at the (a) top, (b) middle, and (c) bottom of its oscillation.

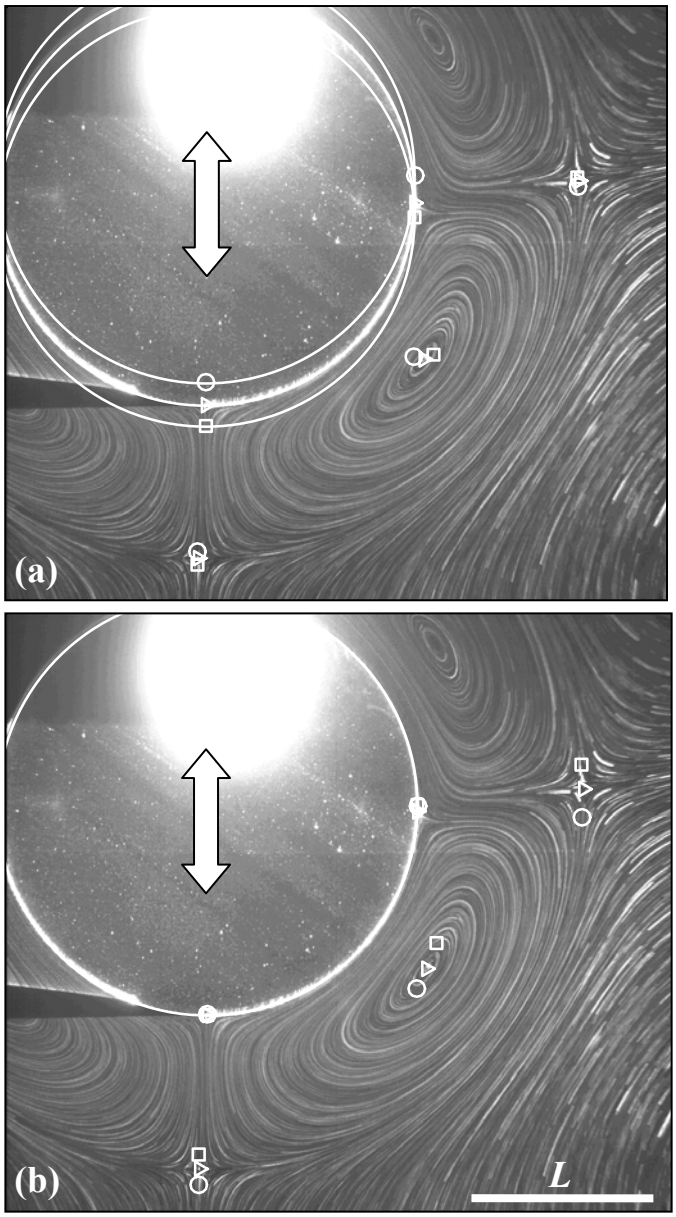

Figure 4.10 Steady streaming pathlines for a sphere oscillating at $Re_M = 57$ and $\varepsilon = 0.1$. Symbols denote the stagnation point locations at the top (*circle*), middle (*triangle*), and bottom (*square*) of the sphere oscillation translated to Eulerian (a) and Lagrangian coordinates (b). The arrow denotes the direction of oscillation.

4.1.5 Velocity Fields

The two in-plane velocity components were determined from the particle visualizations using PIV. These velocity fields were used to establish the appropriate velocity scale for the steady streaming flows at various ε and to locate the maximum streaming speeds as a function of *AR*.

Figure 4.11 shows the scaled velocity along the *y*-axis at $x = 0$ for a sphere at $Re_M = 60$ and $\varepsilon = 0.05$ (*gray triangle*), 0.1 (*black triangle*), and 0.18 (*open triangle*). Note that the *y*-coordinate is that shown in Figure 4.1, and increases along the downward direction. The velocity scale is given by

$$V_s = \varepsilon s \omega \,, \tag{4.7}$$

as suggested by Stuart (1963) for the streaming at the edge of the boundary layer for cases where $Re_M >> 1$ and $\varepsilon << 1$. The error bars are calculated as described in Chapter 3. As shown in the Figure, with this scaling, the velocity profile becomes a self-similar

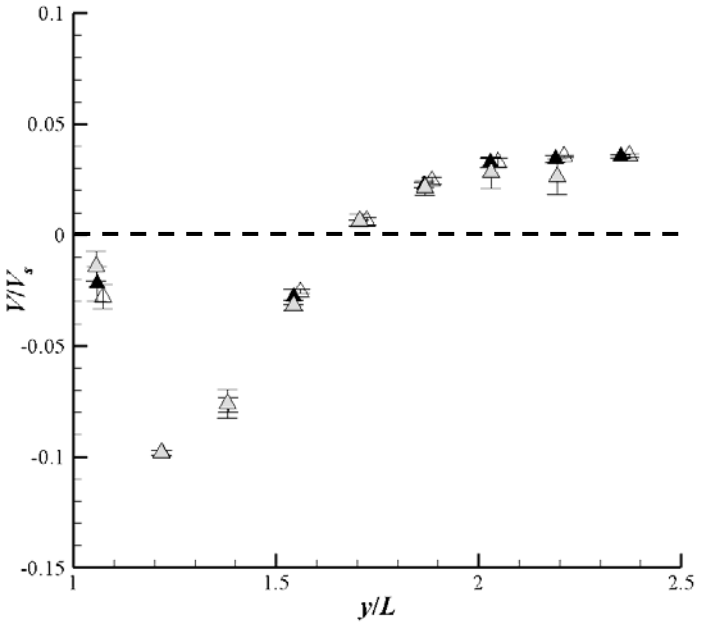

Figure 4.11 Scaled velocity along the axis of oscillation for a sphere at $Re_M = 60$ and $\varepsilon = 0.05$ (*gray triangle*), 0.1 (*black triangle*), 0.18 (*open triangle*).

curve for the range of Reynolds numbers shown, and since the flow is presumed to be linear at small ε values, this scaling should hold for the smaller ε values typical of underwater sounds. This is supported by the observations of Raney *et al.* (1954) who noted that the thickness of the inner region around a cylinder was independent of ε for ε < 0.5. It is also supported by asymptotic analysis of Riley (1966) for oscillating spheres at ε << 1.

The scaled velocity does, however, vary with Re_M changes, as shown in Figure 4.12 for Re_M = 28 (*square*), 55 (*triangle*), 83(*diamond*), 100 (*circle*) and 30 (*larger circle*) with ε = 0.1 (*filled symbol*) and 0.2 (*open symbol*). As in Figure 4.11, Figure 4.12 shows the velocity along the *y*-axis at *x* = 0 for a sphere. The thickness of the inner region can be seen on the graph as the region where the scaled velocity is negative (*i.e.*, moving towards the body along the axis of oscillation). As Re_M increases, the thickness of the inner region decreases.

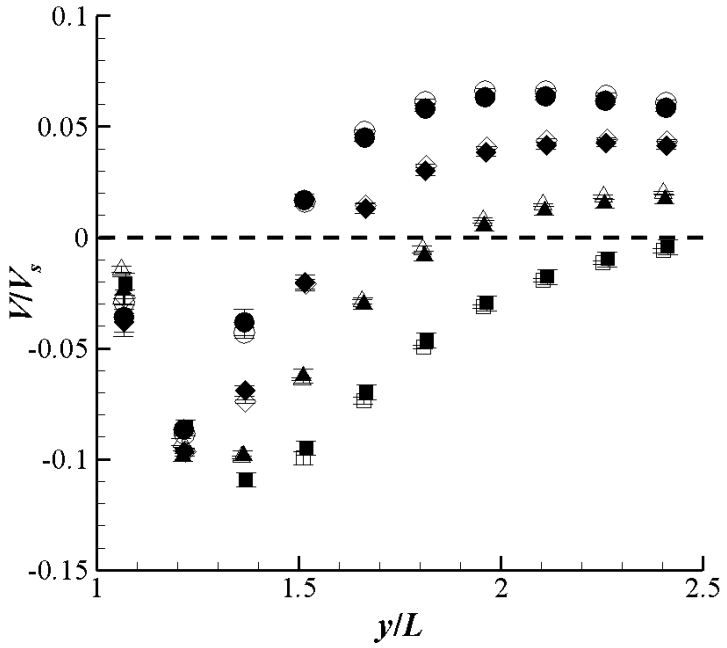

Figure 4.12 Scaled velocity along the axis of oscillation for a sphere at Re_M = 28 (*square*), 55 (*triangle*), 83(*diamond*), and 100 (*circle*) with ε = 0.1 (*filled symbol*) and 0.2 (*open symbol*).

Figure 4.13 shows a velocity vector plot for the lower right quadrant of a prolate spheroid of $AR = 1.33$ (a), a sphere (b), and an oblate spheroid of $AR = 0.74$ (c) at $Re_M = 42$ and $\varepsilon = 42$. These are the cases shown in Figure 4.2. Stagnation points are marked with black circles and points the algorithm described in Chapter 3 deemed to be spurious are marked with a square. Although points with a large velocity in the strong velocity gradient near the body were identified as spurious, they do not appear to be spurious based on visual inspection. As can be seen in the figure, the largest velocities occur near the body in the inner rotating region, with the scaled velocities decreasing and nearly vanishing going away from the body. The figure also shows that the location of maximum velocity near the body moves away from the axis of symmetry as the aspect ratio decreases. A similar trend was noted by Rednikov and Sadhal (2004) for the maximum streaming velocity at the outer edge of the inner layer.

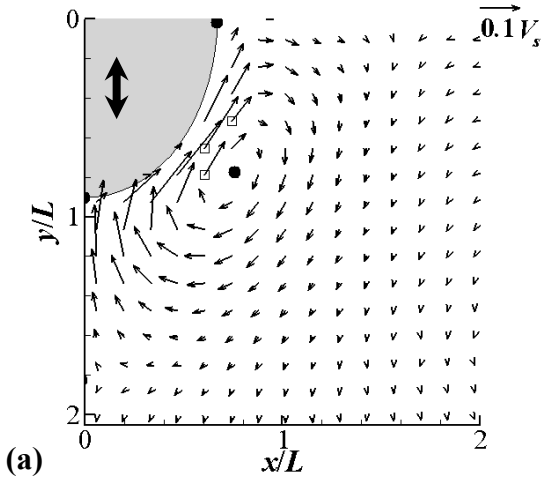

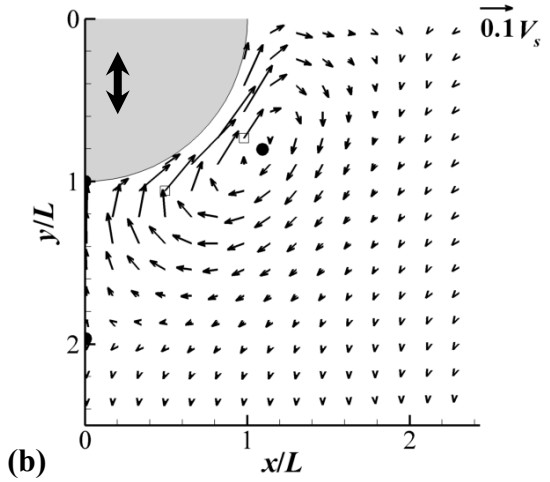

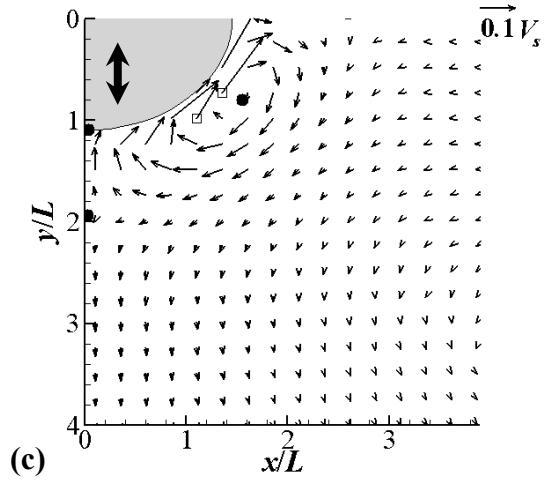

Figure 4.13 PIV velocity vectors for $Re_M = 42$, $\varepsilon = 0.15$ for aspect ratios of (a) $AR = 1.33$, (b) $AR = 1$, (c) $AR = 0.74$. The double-headed arrow indicates the direction of oscillation.

4.1.6 Vorticity

The in-plane component of the vorticity was calculated from the PIV data. Three typical examples are shown in Figure 4.14 for the lower right quadrant of a prolate spheroid of $AR = 1.33$ (a), a sphere (b), and an oblate spheroid of $AR = 0.74$ (c) at $Re_M = 42$ and $\varepsilon = 42$. These cases correspond to the velocity data shown in Figure 4.2 and Figure 4.13. Here, the vorticity has been scaled by V_s/L, which produces vorticity values of $O(1)$. As can be seen from the Figures, the vorticity generated by the streaming flows on the right lower quadrant of the body shows a region of negative vorticity adjacent to the body and positive vorticity away from the body. The signs of the vorticity are then reversed for the left lower quadrant of the body on the other side of the y-axis. It should be noted that the vorticity changes sign at the edge of the Stokes layer (here, $0.15L$ from the body surface), which is well within the distance to the center of the inner rotating region. Like the maximum velocity, the location of the maximum vorticity shifts away from axis of symmetry as the aspect ratio decreases, and appears, based on visual inspection, to move towards the region of the minimum radius of curvature of the body.

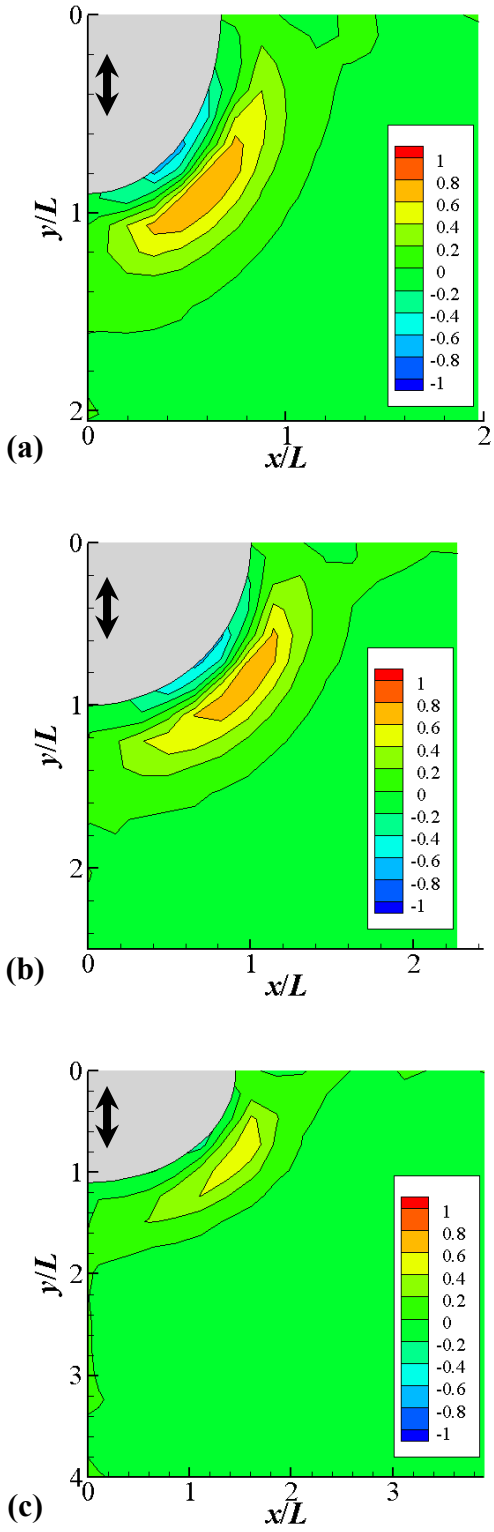

Figure 4.14 Scaled vorticity at $Re_M = 42$, $\varepsilon = 0.15$ for aspect ratios of (a) $AR = 1.33$, (b) $AR = 1$, (c) $AR = 0.74$. The double-headed arrow indicates the direction of oscillation.

4.1.7 Transient Effects

The basic flow patterns develop relatively quickly inside the inner region, suggesting that such flow patterns will be established even by short "pulses" of sound. The development of steady streaming flows was analyzed by processing PIV image pairs separated by the smallest time interval possible, namely a single oscillation period. Cross-correlation averaging obviously cannot be used for these analyses because the flow is likely to be unsteady. Standard cross-correlation-based PIV processing was performed instead on a 24×24 pixel interrogation region and an 8 pixel search radius along the axis of symmetry. Despite the noise in the PIV results, a comparison of these data (points) with their steady-state value (lines) as a function of the total number of oscillations of the body at the locations marked on the particle pathline image of a sphere oscillated at $\varepsilon = 0.2$ and $Re_M = 90$ (Figure 4.15a) shown in Figure 4.15(b) suggests that the flow reaches its steady-state value in less than 10 oscillations in the inner region (astericks). In the outer region, the flow appears to reach steady-state within 50 oscillation periods at the farthest distance shown (squares at $y/L = 3.8$). A curve-fit through the points indicates that the velocity reaches 95% of its final value in 27, 36, and 47 oscillations for $y/L = 2.1$, 3.0, and 3.8, respectively.

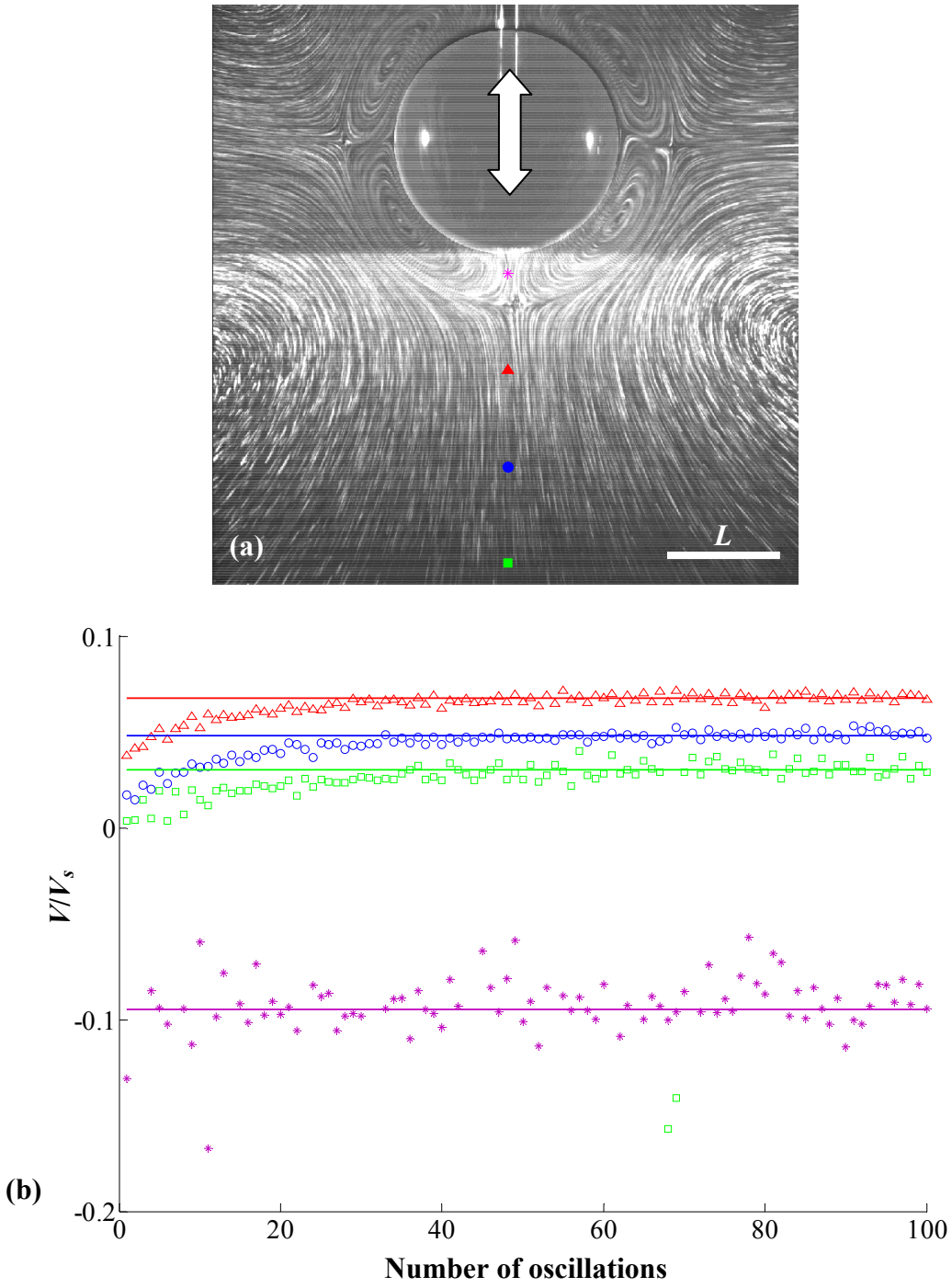

Figure 4.15 Development of steady streaming flow for a sphere oscillating at ε = 0.2 and Re_M = 90. Each symbol in the particle pathline image (a) shows the location of the velocity plot (b). Velocity profiles are shown for y/L = 1.2 (*astericks*), 2.1 (*triangles*), 3.0 (*circles*), 3.8 (*squares*).

4.2 Discussion

4.2.1 Data Validation

The experimental pathline visualizations were also compared to the streamlines from the numerical solution of Chang and Maxey (1994) for a vertically oscillated sphere at $Re_M = 84$ and $\varepsilon = 0.1$. As shown in Figure 4.16, the experimental results (a) and the numerical simulations (b) give qualitatively similar flow patterns, although the pathlines separating the upper and lower regions in the experimental results are not completely horizontal, either from asymmetries introduced by the mounting rod or from imaging the body at a phase slightly off the center of its oscillation. The experimental result also predicts a slightly thinner inner layer when compared to the numerical simulation ($\approx 0.6L$ compared to $0.7L$). For comparison, the results presented above suggest that $Re_M = 65$ would be required to achieve the larger inner region thickness. This discrepancy may be due to difficulties in achieving steady-state in the numerical simulation; numerical results of steady streaming around spheres at $Re_M = 18$ and $\varepsilon = 0.2$ show that the inner region after 10 oscillations is about 10% larger than that after 100 oscillations (R S Alassar 2005, private communication). The experimental results show the steady streaming pathlines for the 25^{th}–100^{th} oscillation cycle.

The reproducibility of the experimental results was evaluated by comparing three independent runs of otherwise identical test cases. As shown in Figure 4.17, the scaled vertical streaming flow velocity along the axis of oscillation for $Re_M = 50$ and $\varepsilon = 0.1$ for cases are identical within experimental error. The variations between these three cases may be due to slight variations in the viscosity of the working fluid due to variations in its temperature. For a 90% glycerine mixture at these temperatures a 1°C change in temperature changes the viscosity by about 5%; day-to-day variations of a few °C in room (and hence fluid) temperature were common. The variations may also be due to

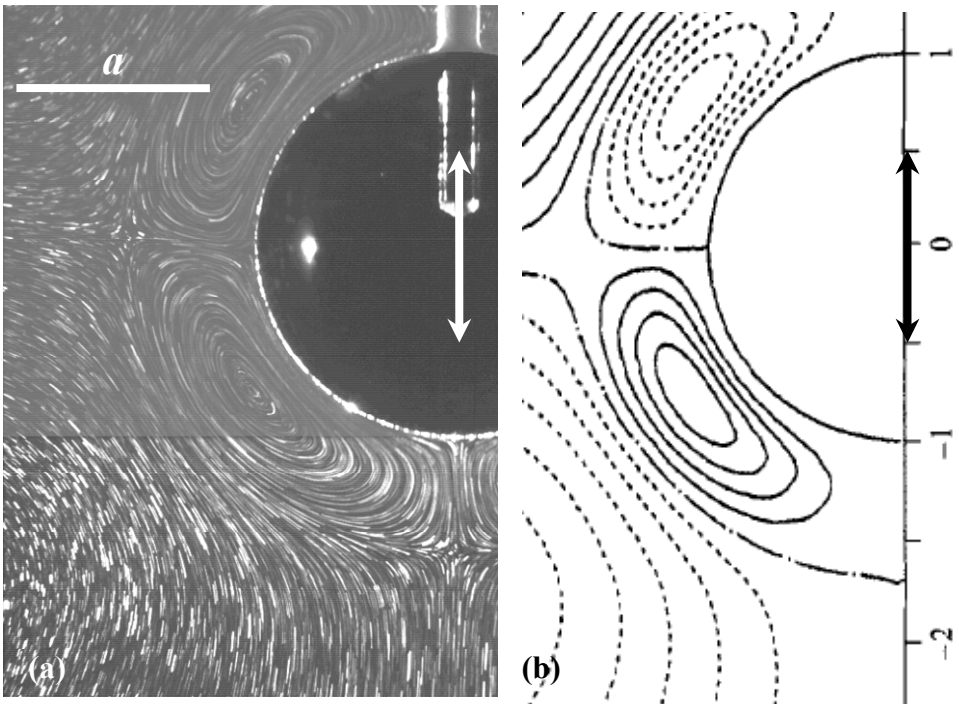

Figure 4.16 Steady streaming flows around a vertically oscillated sphere at $Re_M = 84$, $\varepsilon = 0.1$: experimental (a) and numerical simulation (b) results. Numerical simulation from Figure 16 of Chang and Maxey (1994). The images have been scaled so that the sphere dimensions are the same. The arrow denotes the direction of oscillation, and the white bar is the radius of the sphere, a = 12.7 mm.

slight differences in the phase of the oscillation for these visualizations, which can affect the thickness of the inner region (as discussed above).

4.2.2 Relevance to the Fish Ear

The information on axisymmetric steady streaming flows gained from these studies can provide some preliminary estimates relating to the auditory retina hypothesis. First, these studies establish that the flow is linear even at the quite large oscillation amplitudes (compared with those expected in the acoustically induced flows near the otoliths in fish ears) studied hereof $\varepsilon \leq 0.1$. The experimental studies reported here should therefore still be qualitatively relevant to those in the fish ear. For example, these studies indicate that the maximum streaming velocity is $\approx 0.1\ V_s$. A typical underwater

sound might have a sound pressure level of 93 dB re 20 μPa; for a plane wave at a frequency of 100 Hz this translates into an amplitude of 1 nm. The streaming velocity near a 1 cm otolith can then be estimated from $0.1\ \varepsilon\ \omega\ s$, or 6 fm/s. This streaming flow is most likely too small for the fish hair cells to use effectively, since typical amphibian hair cells are generally assumed to be able to sense tip displacements on the order of 0.1 nm (Hudspeth 2005). If fish are instead sensitive to displacements on the order of particle motion at their threshold of hearing, they would be able to detect particle motions of ≈8 pm (based on the cod's threshold of 52 dB re 20 μPa at 100 Hz) (Chapman and Hawkins 1973). Even this level of sensitivity is at least three orders of magnitude too large for the estimated streaming flow, particularly when it is considered that most natural sound sources are generally not a second long. This does not mean that streaming flows are not important, but it does imply that in order for them to be important at this frequency range ε will have to increase, either by decreasing the body length scale or increasing the amplitude of motion. Since the sulcus has a complicated geometry, it is certainly possible that the appropriate length scale may not be the maximum length of the otolith, but should instead be defined in terms of the sulcus width, equivalent radius, or some other prominent feature in the vicinity of the sensory macula.

Recent studies have shown that some fish, including some clupeids and the cod, are capable of responding to ultrasound. At 38 kHz, the cod has a threshold of about 194 dB re 1 μPa (Astrup and Møhl 1993). The streaming velocity near a 1 cm otolith in this case is then $O(10^{-10}$ m/s). If the sensitivity of the ear is on the order of picometers, as suggested by their hearing thresholds, it is possible that steady streaming flows may provide a mechanism for cod to detect ultrasound. For the American shad, who has been shown to be more sensitive to ultrasonic sounds than the cod, a typical threshold at 80 kHz is 150 dB re 1 μPa (Mann *et al.* 1998), which gives a streaming velocity of $0.1\ \varepsilon\ \omega\ s = 9$ fm/s. However, the American shad is hypothesized to make use of specializations in a bulla (a gas-filled body) near their utricle to allow for the detection of

ultrasound (Higgs *et al.* 2004). This suggests that cod (who do not have this specialization) should use a different method to detect ultrasound.

The thickness of the inner region in the fish ear can also be estimated from these studies. As an illustration, a 1 cm otolith oscillating at 100 Hz can be estimated to operate at Reynolds numbers of 140–52000, using the density of water and dynamic viscosity values 4.5 P (de Vries 1951) and 0.012 P (ten Kate and Kuiper 1970), respectively, giving an inner region thickness of 3 mm–8 μm. Since kinocilia on the macula have lengths on the order of 10 μm, the macular hair cells should sample only the flow within the inner region of the flow. For comparison, a 38 kHz sound would be at Reynolds numbers from 50×10^3–20×10^6, and have an inner region thickness from 20 nm–8 μm, depending on the viscosity estimate and assuming that these scalings hold at the higher Reynolds numbers. Although the ultrasonic frequencies will only be in the inner region of the flow if the surrounding fluid's viscosity is closer to the larger estimate, these flows should not be discounted without further exploration.

The shape of the body also shapes the flow patterns, with regions of stronger vorticity near regions of greater curvature. The shape of the otolith may therefore localize the stronger shear flows in particular portions of the macula, and it may well be that the taller hair cells (*i.e.*, those with longer cilia) are placed towards the edge of the macula to sense regions of greater shear.

These initial results provide some insight into the steady streaming flow patterns and indicate that they may contain acoustic information. Considering the usefulness of these patterns, they are worthy of further study. As more data are collected, its impact on fish hearing will be be discussed, particularly at the end of Chapter 8.

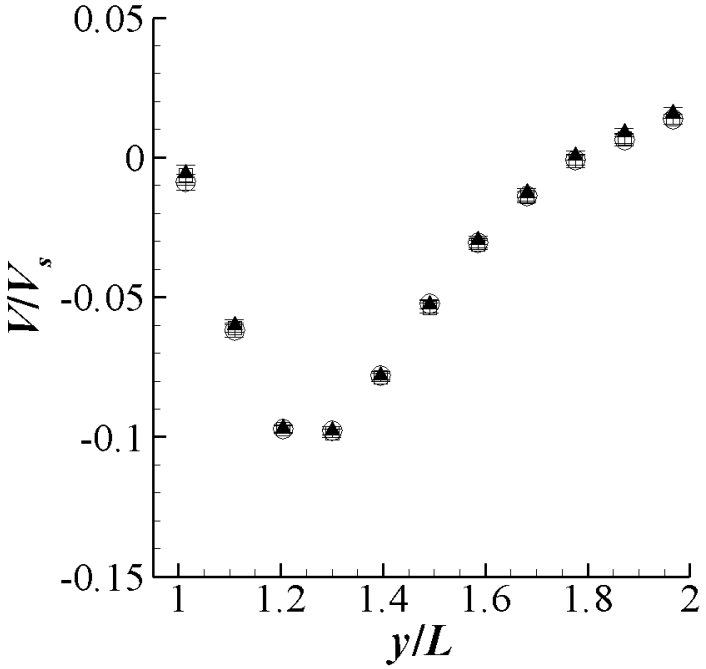

Figure 4.17 Scaled velocity along the axis of oscillation for a sphere at $Re_M = 50$ and $\varepsilon = 0.1$ for three distinct test runs, represented by a *circle*, *triangle*, and *square*.

CHAPTER 5

MULTIPLE FREQUENCY TEST CASES

5.1 Multiple Frequency Data Analysis

The underwater environment in which fish live is a noisy place, and few if any of the underwater sounds heard by fish correspond to the single-tone pure sinusoidal plane waves modeled in these studies. Nevertheless, any periodic signal typical of underwater sounds can be decomposed into the superposition, or sum, of many such sine waves of varying frequency, amplitude and phase, *e.g.* a Fourier series. In this section we discuss the behavior of steady streaming flows due to a sound wave and hence oscillation comprised of the sum of two in-phase sine waves

$$y(t) = a_1 \sin(2\pi f_1 t) + a_2 \sin(2\pi f_2 t), \tag{5.1}$$

where a_i and f_i are the oscillation amplitude and frequency, respectively, of the i^{th} component (i = 1, 2). In all cases, the two frequencies are defined so that $f_1 < f_2$.

The asymptotic analysis by Davidson and Riley (1972) for the two-dimensional case of an oscillating cylinder in an infinite medium suggests that the steady streaming flow is, to first order, equal to the sum of the component frequencies. In other words, the streaming velocity field may be approximated as the sum of the velocity field generated by each of the component frequencies individually as long as

$$\varepsilon^* = \frac{U_\infty}{2\pi f_0 L} \ll 1, \tag{5.2}$$

where U_∞ is the maximum streaming velocity and f_0 is the fundamental frequency. For the purposes of this study, the fundamental frequency may be considered to be the greatest common denominator of the component oscillation frequencies. Although U_∞ is

in general a function of the relative phase of the oscillation, for two in-phase oscillations, ε* becomes

$$\varepsilon^* = \frac{f_1\varepsilon_1 + f_2\varepsilon_2}{f_0}. \tag{5.3}$$

The appropriate multiple frequency velocity scale is then given by

$$V_s = \varepsilon^* U_\infty = \frac{U_\infty^2}{2\pi f_0 L} = \frac{2\pi L\left(f_1\varepsilon_1 + f_2\varepsilon_2\right)^2}{f_0}, \tag{5.4}$$

while the single-frequency velocity scale is identical to that discussed in Equation 4.7.

Comparing the single and multiple frequency velocity fields requires appropriate scaling of the component velocity fields. First, the single frequency results are scaled so that they represent the same oscillation amplitudes as the multiple frequency case. The measured component velocity V_c is rescaled to give the rescaled velocity

$$V_{rs} = V_c\left(\frac{s_m}{s_c}\right)^2, \tag{5.5}$$

where s_m is the amplitude of the appropriate component of the multiple frequency oscillation, and s_c is the amplitude of the single frequency oscillation. The oscillation amplitudes are squared because the streaming velocity is proportional to the square of the amplitude: $\varepsilon U_o = \varepsilon\omega s = \omega s^2/L$. The scaled single frequency velocities can then be superposed for comparison with the multiple frequency results. The uncertainty in their sum is assumed to be

$$\Delta_{u,v}^c = \sqrt{(\Delta_{u,v}^1)^2 + (\Delta_{u,v}^2)^2}, \tag{5.6}$$

where $\Delta_{u,v}$ is the uncertainty as defined in Chapter 3 and the superscripts 1 and 2 denote the individual frequency components. The uncertainty in the multiple frequency cases, $\Delta_{u,v}^m$, is defined in Chapter 3.

If the experimental results are in agreement with the linear theory, they are said to "superpose." For the purposes of this experiment, the vectors will be said to "superpose"

if twice the sum of the uncertainty is greater than the difference in the measurements. In other words, if for a given vector location

$$(u,v)_{rs,1}+(u,v)_{rs,2}-(u,v)_m < M\sqrt{\left(\Delta^c_{u,v}\right)^2+\left(\Delta^m_{u,v}\right)^2}\,, \qquad 5.7$$

where $M = 2$, then that vector is defined to superpose. When the data are assumed to have a normal distribution, the choice of $M = 2$ on the right hand side of the inequality defines a 95% confidence interval for the measurement. The inequality then represents the difference in the measurements falling within the confidence interval. If for the entire flow field, 90% of the non-spurious vector locations superpose in both u and v, then the test case will be said to superpose, *i.e.*, it is concluded that superposition is successful for that test case. Setting M =2 in the above comparison allows for some experimental uncertainty due to variations in timing the images, temperature changes, and convective motion induced by the laser heating the body.

5.2 Results Near Spheres and Spheroids at Small Amplitudes

In general, the flow patterns formed by the multiple frequency oscillations are qualitatively similar to those from the single frequency oscillations. More specifically, the inner and outer rotating regions with the same directions of rotation (as those observed for single frequency flows) are observed in the multiple frequency flows. The physical extent of these regions lies between those for the component single frequency flows, and is greater than that generated by the oscillation due only to the higher-frequency (higher Re_M) excitation and less than that generated by the lower-frequency (lower Re_M) oscillation. Figure 5.1(a) shows a typical flow pattern near an oscillating oblate spheroid ($Re_{M1} = 26$, $\varepsilon_1 = 0.05$ and $Re_{M2} = 52$, $\varepsilon_2 = 0.05$). Comparing the extent of the inner region with that shown in Figure 4.3(a), it is clear that the inner region of the multiple frequency case is thinner than that for the lower Reynolds number component. This observation agrees with the linearity of the flow at small Reynolds number predicted

by Davidson and Riley (1972). Figure 5.1(b) shows a typical velocity profile from the PIV results. The profile is taken at $x/L = 1.55$ (denoted by the dashed line to the right of the body). The y-velocity profiles shows u/V_s as squares and v/V_s as triangles, while filled symbols denote the sum of two single frequency velocity cases and open symbols denote the multiple simultaneous oscillation case. As can be seen, there is generally good agreement between the summed and the multiple frequency results.

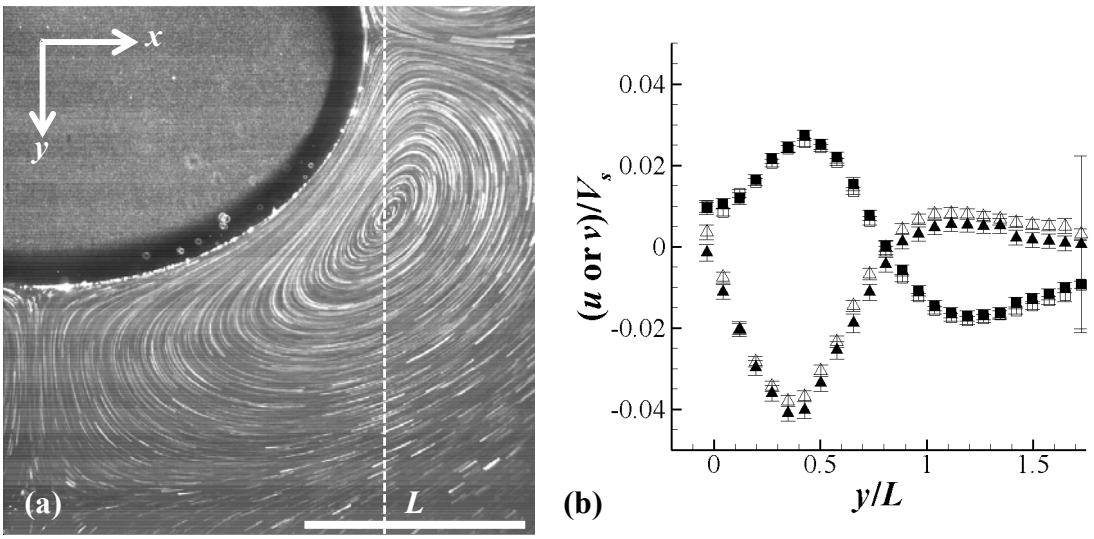

Figure 5.1 Particle pathlines for an oblate spheroid ($AR = 0.74$) oscillating vertically at two frequencies, $Re_{M1} = 26$, $\varepsilon_1 = 0.05$ and $Re_{M2} = 52$, $\varepsilon_2 = 0.05$ (a). A representative normalized velocity profile is shown at $x/L = 1.55$ for u/V_s (*squares*) and v/V_s (*triangles*) (b). The multiple frequency case is denoted by *open* symbols and the sum of the two component cases is denoted by the *filled* symbols. Error bars are calculated as described in the text.

Similarly, results for a prolate spheroid oscillating at $Re_{M1} = 26$, $\varepsilon_1 = 0.05$ and $Re_{M2} = 51$, $\varepsilon_2 = 0.06$ are shown in Figure 5.2, while results for a sphere oscillating at $Re_{M1} = 30$, $\varepsilon_1 = 0.05$ and $Re_{M2} = 61$, $\varepsilon_2 = 0.05$ are shown in Figure 5.3. In general, good agreement is seen, and the velocity vectors appear to superpose. The PIV vectors for the entire flow field for the sphere case shown in Figure 5.3 is shown in Figure 5.4. Vectors that are considered to superpose are shown in black, vectors that do not superpose in u only are shown in blue, and vectors that do not superpose in v only are shown in red. Spurious vectors are omitted.

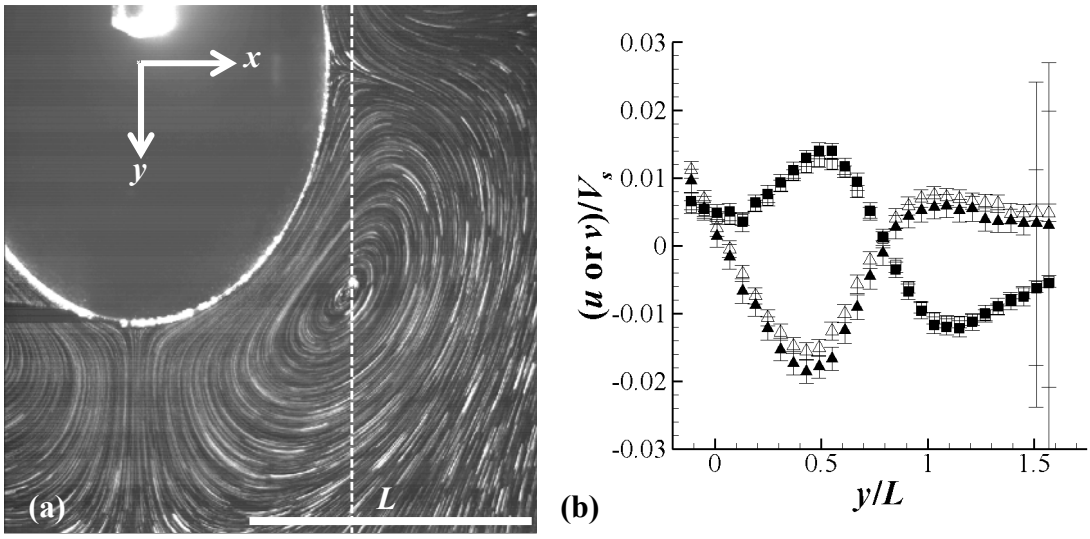

Figure 5.2 As in Figure 5.1, for a prolate spheroid ($AR = 1.31$) oscillating vertically at two frequencies, $Re_{M1} = 26$, $\varepsilon_1 = 0.05$ and $Re_{M2} = 51$, $\varepsilon_2 = 0.06$. Velocity profile shown along $x/L = 0.76$.

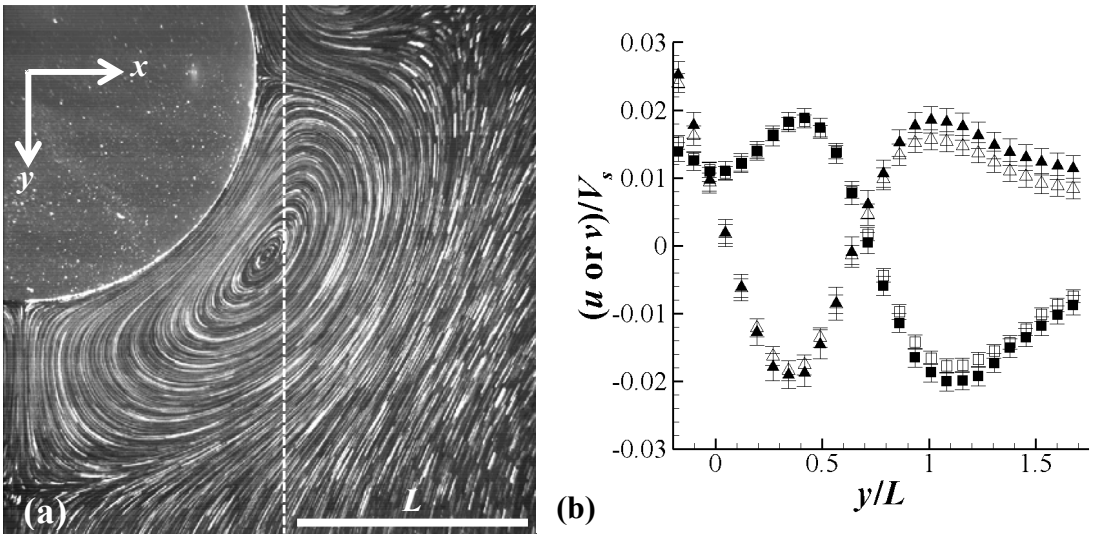

Figure 5.3 As in **Figure 5.1**, for a sphere oscillating vertically at two frequencies Re_{M1} = 30, ε_1 = 0.05 and Re_{M2} = 61, ε_2 = 0.06. Velocity profile shown along x/L = 1.13.

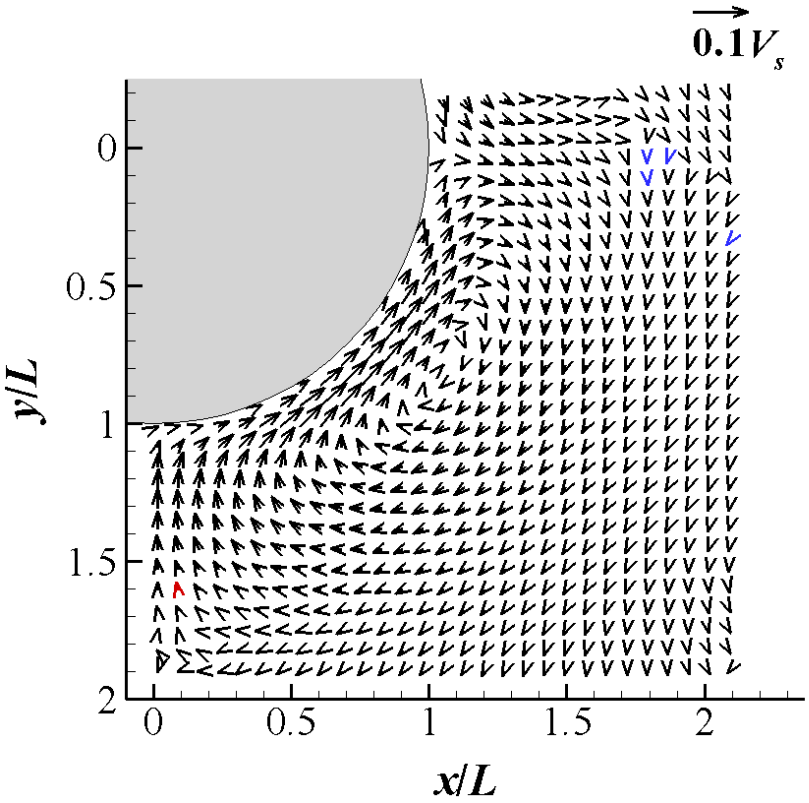

Figure 5.4 Velocity vector field for a sphere oscillating vertically at two frequencies, Re_{M1} = 30, ε_1 = 0.05 and Re_{M2} = 61, ε_2 = 0.05. Vectors that are considered to superpose are shown in *black*, vectors that do not superpose in u only are shown in *blue*, and vectors that do not superpose in v only are shown in *red*. Spurious vectors are not shown.

5.3 Results at Large Oscillation Amplitudes

The agreement between the multiple frequency experiments and the sum of the single frequency experiments breaks down as the amplitude of the oscillation increases. In the above cases where the superposition is successful, ε_1 and ε_2 are about 0.05. However, as ε_1 and ε_2 approach 0.1, superposition begins to fail. Figure 5.5 shows the particle pathlines (a) and velocity profiles (b) for a sphere vertically oscillated at $\varepsilon_1 = \varepsilon_2 = 0.1$, $Re_{M1} = 30$ and $Re_{M2} = 60$. Although the summed velocity field is qualitatively similar to that due to the multiple frequency oscillation, discrepancies in the measured velocity are particularly noticeable in the vertical direction (triangles representing v/V_s) near $y/L = 0.5$, which is just above the center of the inner rotating region.

Figure 5.6 shows the entire velocity field for the case shown in Figure 5.5. In this figure, the velocity vectors are colored to mark the spatial locations where the velocities do not superpose. Locations where superposition is successful are marked in black, and locations where u/V_s, v/V_s, and both u/V_s and v/V_s do not superpose are marked in blue,

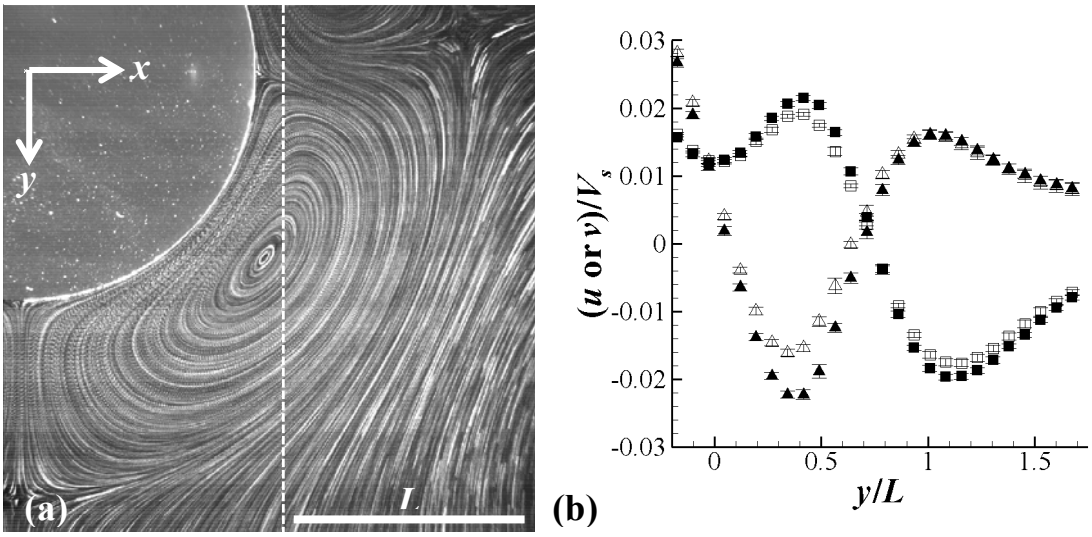

Figure 5.5 As in **Figure 5.1**, for a sphere oscillating vertically at two frequencies, $Re_{M1} = 30$, $\varepsilon_1 = 0.1$ and $Re_{M2} = 61$, $\varepsilon_2 = 0.1$. Velocity profile shown along $x/L = 1.13$.

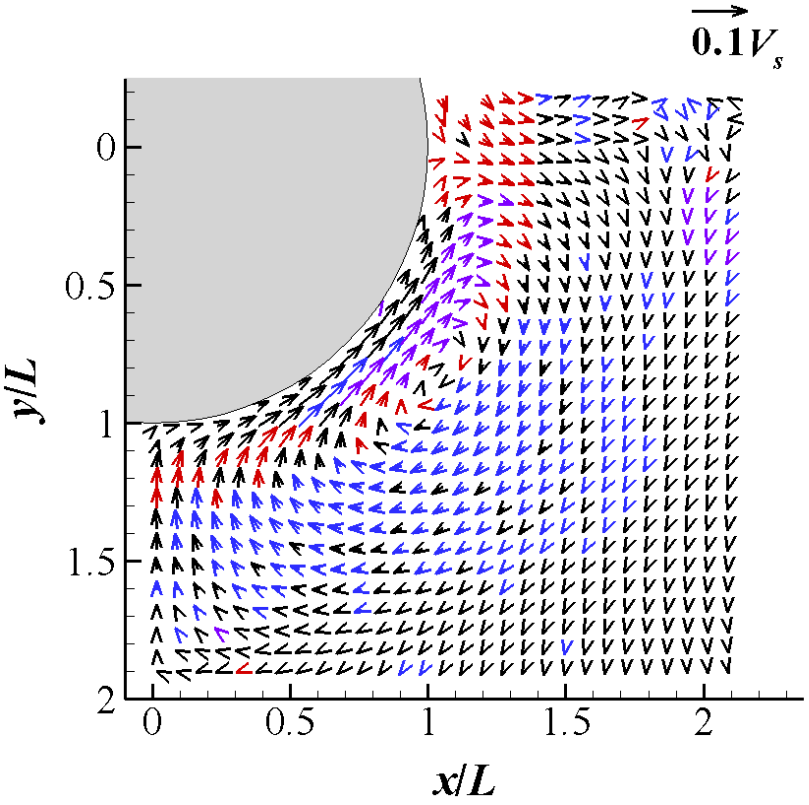

Figure 5.6 Velocity vector field for a sphere oscillating vertically at two frequencies, $Re_{M1} = 30$, $\varepsilon_1 = 0.1$ and $Re_{M2} = 61$, $\varepsilon_2 = 0.1$. Vectors that are considered to superpose are shown in *black*, vectors that do not superpose in u only are shown in *blue*, vectors that do not superpose in v only are shown in *red*, and vectors that do not superpose in both u and v are shown in *purple*. Spurious vectors are not shown.

red, and purple, respectively. This two-dimensional vector field exhibits similar characteristics to the one-dimensional profile shown in Figure 5.5, with most of the "bad" (*i.e.*, non-superposing) vectors occurring in the inner region. It is clear that the velocity field does not superpose over large regions of the flow, with velocities where u/V_s do not superpose particularly common on the outer side of the inner rotating region. In total, 41% of the vector locations had at least one component which did not superpose. This result is not surprising given that the theory is based on the linearized form of the basic equations, and is therefore only valid for small amplitudes of oscillation, or $\varepsilon^* << 1$. Since $\varepsilon^* = 0.3$ for this case, it is hardly unexpected that the linearized analysis is no longer valid.

5.4 Summary

The experimental results are summarized in Table 5.1, which describes the multiple frequency test cases and whether the component frequencies superpose or not, based on the criteria given in Section 5.1. The Table gives the percentages of u/Vs and v/Vs values and locations where superposition is successful, omitting spurious vectors and those in the shadow to the left of the body. Cases with slight variations in Re_M for the same body were generally conducted at the same oscillation frequency, but had temperature-induced variations in the viscosity of the fluid. As can be seen from the Table, cases where $\varepsilon^* \leq 0.25$ generally superpose.

These results can also be summarized in the form of a "flow regime map," as shown in Figure 5.7. In this Figure, the test cases are plotted as a function of the streaming Reynolds number of each component, Re_{s1} and Re_{s2}, respectively. Filled symbols indicate successful superposition, or test cases in the linear regime, while open symbols indicate unsuccessful superposition, or cases in the nonlinear regime. When the streaming Reynolds number for both oscillations is less than about 0.2, the flow appears to be in the linear regime, with a few exceptions. This suggests that the criterion for superposition is likely to be a function of the streaming Reynolds numbers of *both* component frequencies.

Table 5.1 Summary of multiple frequency test case results. For a more complete list of tests and test conditions, refer to Appendix C.4.

File	Folder	AR	ε*	Re_{M1}	Re_{s1}	ε_1	Re_{M2}	Re_{s2}	ε_2	Percent spurious vectors	Percent u vectors superposed	Percent v vectors superposed	Percent u and v vectors superposed
march212007	4and8Hza	0.75	0.16	26	0.07	0.05	52	0.15	0.05	0.00	99.15	86.15	*85.81*
march212007	4and12Hza	0.75	0.21	26	0.07	0.05	78	0.23	0.05	0.00	97.61	99.15	96.92
march212007	8and12Hza	0.75	0.27	52	0.15	0.05	78	0.23	0.05	0.17	87.67	95.03	*83.73*
march052007	4and8Hza	1.00	0.16	29	0.08	0.05	57	0.16	0.05	0.16	98.53	99.84	98.37
march082007	4and8Hza	1.00	0.30	30	0.31	0.10	61	0.59	0.10	0.15	67.94	85.28	*58.90*
march082007	4and8Hzb	1.00	0.15	30	0.08	0.05	61	0.16	0.05	0.00	99.39	99.85	99.23
february222007	4and8Hza	1.00	0.21	30	0.31	0.10	59	0.16	0.05	0.92	97.58	95.16	92.92
february222007	4and12Hza	1.00	0.31	30	0.70	0.15	89	0.25	0.05	1.29	92.90	91.40	*86.36*
march012007	4and8Hz1	1.00	0.32	27	0.29	0.10	54	0.60	0.11	0.72	70.94	66.06	*51.62*
march012007	4and8Hz2	1.00	0.32	27	0.29	0.10	54	0.60	0.11	1.43	64.00	74.73	*49.27*
march012007	4and8Hz3	1.00	0.32	27	0.29	0.10	54	0.60	0.11	1.43	69.82	70.55	*52.91*

(continued).

march062007	4and8Hza	1.00	0.31	29	0.31	0.10	57	0.62	0.10	0.84	53.57	80.10	*38.95*
march062007	4and8Hzb	1.00	0.31	29	0.31	0.10	57	0.62	0.10	1.01	57.07	78.02	*44.12*
march142007	4and12Hza	1.00	0.20	26	0.07	0.05	79	0.20	0.05	0.33	95.73	98.36	95.24
march142007	6and12Hza	1.00	0.15	40	0.10	0.05	79	0.20	0.05	0.16	94.10	96.72	92.30
march142007	6and12Hzb	1.00	0.07	40	0.03	0.03	79	0.05	0.02	0.00	94.44	94.27	94.11
march142007	6and12Hzc	1.00	0.10	40	0.10	0.05	79	0.05	0.02	0.16	94.10	94.59	93.93
march192007	4and8Hza	1.30	0.16	26	0.08	0.05	51	0.16	0.06	0.18	99.46	98.03	97.67
march192007	4and12Hza	1.30	0.22	26	0.08	0.05	77	0.23	0.06	0.18	98.92	99.10	98.38
march192007	8and12Hza	1.30	0.28	51	0.16	0.06	77	0.23	0.06	0.72	84.84	77.80	*66.06*

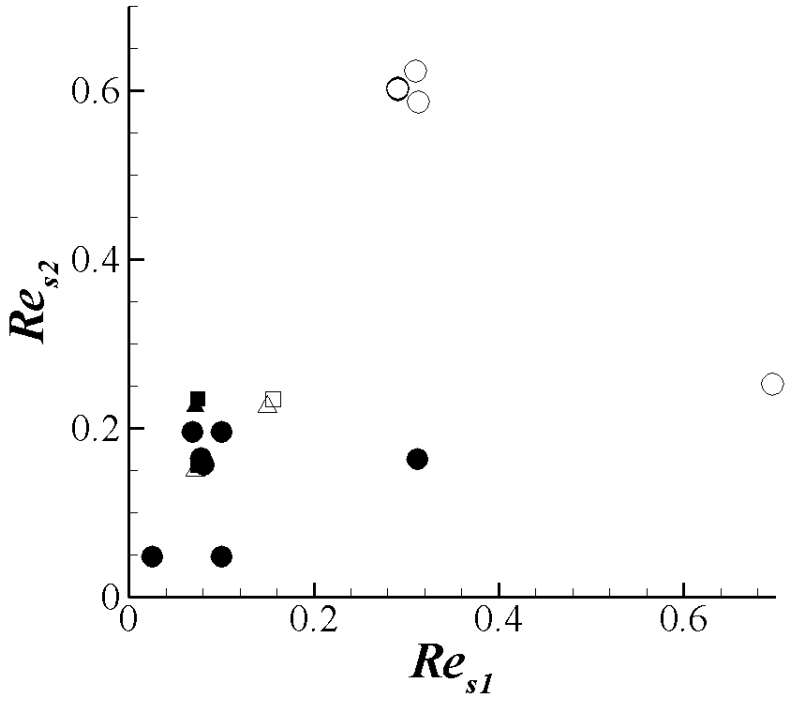

Figure 5.7 Flow map summarizing the studies of multiple frequency oscillations in terms of the streaming Reynolds numbers of the two component frequencies $Re_{s2} = \varepsilon_2^2 Re_{M2}$ (*vertical axis*) and $Re_{s1} = \varepsilon_1^2 Re_{M1}$ (*horizontal axis*) for spheres (*circle*), prolate spheroids (*square*), and oblate spheroids (*triangle*). Filled symbols denote cases where the multiple frequency results are the superposition of the individual component frequency velocities within experimental error; open symbols denote cases in the nonlinear regime where the velocity fields do not superpose.

The criteria for superposition can also be expressed in terms of the amplitude ratio, ε*, of Davidson and Riley (1972). Figure 5.8 shows the percent of superposed vectors locations as a function of ε* for values of the multiplier, $M = 1$ (filled squares), 2 (open triangles), and 3 (filled circles), where M is as defined in Equation 5.7. (In Figure 5.8 the triangles are denoted by open symbols in order to make the graph easier to read.) As can be seen from the figure, again nearly all the cases where $\varepsilon^* \leq 0.25$ superpose for M = 2, and as is especially evident for M = 1 (squares), the fraction of superposed vector locations increases as ε* decreases. Note that when M = 3, most of the cases where ε* <

0.3 have more than 90% of their vector locations matched (data above the dotted line); for M = 1, the fraction of superposed vectors has not reached 90% even at the lowest value of ε* of 0.1. Unfortunately, experimental difficulties precluded experiments at smaller oscillation amplitudes and hence smaller ε*.

5.5 Implications for the Fish Ear

The observation that the velocity fields from multiple frequency flow patterns are the sum of the velocity fields of the component flow patterns suggests a mechanism by which fish ears could decompose the measured flow fields into their component frequencies. At the small amplitudes of oscillation present in the fish ear, the resultant

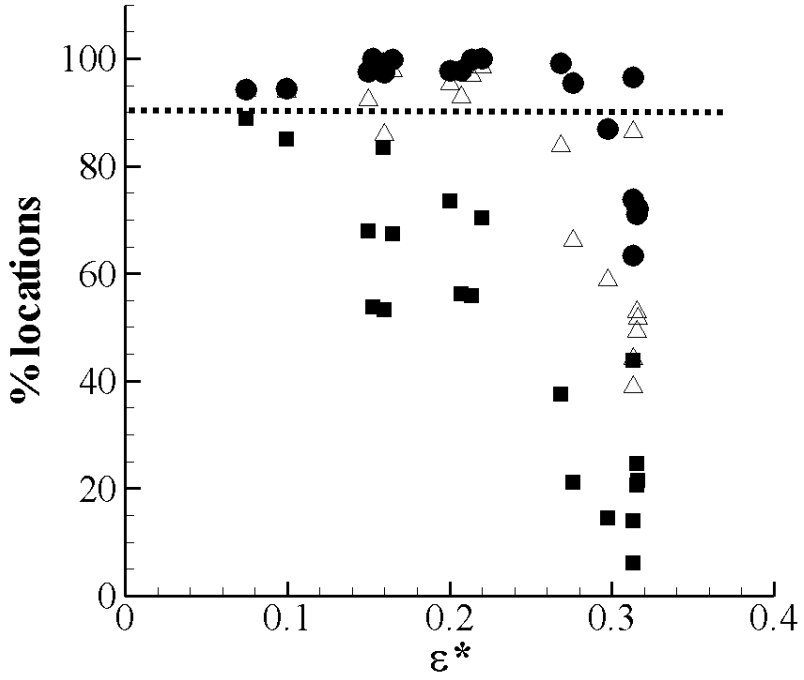

Figure 5.8 Flow map illustrating the percent of total vector locations where both u and v are considered to superpose as a function of ε* for superposition test error multipliers of 1 (*square*), 2 (*triangle*), and 3 (*circle*).

flow patterns should be a simple linear superposition of the component flow patterns (assuming that flows from multiple directions also superpose). Fish should be able to deconstruct these flow patterns to determine the direction, frequency, and amplitude of the incident flow field. Actual underwater sounds are usually comprised of many single-frequency components. If the fish can compare a given sound (*e.g.* that from a school of prey) to several "prototypical" sounds (*e.g.* that from a single prey), it can use the linearity of these flow patterns to determine which combination of the prototypes would most likely generate the actual sound heard by the fish. However, these techniques do not resolve the 180° ambiguity inherent in directionalizing the oscillating sound waves.

Enger (1981) suggests that fish may use a place mechanism to determine the frequency of incident sounds. Fish were placed in a standing-wave tube and exposed to high-powered sound for a few hours. The macula of these fish were then visually examined to determine if there destroyed hair cells were localized in any specific regions, under the assumption that such damaged regions were preferentially sensitive to the driving frequency. These studies suggest that for a sound coming from a single direction, streaming flows may be set up which would be faster in some areas of the macula than others, leading to larger displacements of (and a greater chance of damage to) the hair cell cilia. Since the geometry of the sulcus is not constant along its length, it is conceivable that the locations of maximum streaming velocity are frequency dependent. Although this observation does not mean that fish are capable of using this information to determine the incident sound frequency, it does suggest an explanation for Enger's results.

Although this model omits many features of the fish ear, like the variation in the surrounding tissue and the effect of the otolith geometry, the equations of motion will remain linear at the small amplitudes of oscillation typical of the relative motion of the otolith in the presence of underwater sounds. The specifics of the flow patterns may change as the model is made more complete, but the streaming patterns and the linearity represented by the superposition of multiple frequency sounds should remain valid.

CHAPTER 6

ANGLED TEST CASES

6.1 General Features of the Steady Streaming Flow Patterns

Since fish may be exposed to incident sounds from essentially any direction, it is useful to have an understanding of how the orientation of the ersatz otolith (*i.e.*, spheroid) oscillations (in the otolith-fixed reference frame) affects the steady streaming flow fields. This chapter describes studies of the steady streaming flow fields resulting from the sinusoidal oscillation of spheroids along directions that were tilted relative to the axis of symmetry of the spheroid (as described in Chapter 3). As shown in Figure 6.1, the oscillation angle, θ, is defined to be the angle between the axis of oscillation and the axis of symmetry of the spheroidal body. In all cases, as before, the oscillation direction is vertical. Figure 6.1(a) shows the steady streaming pattern near a prolate spheroid (AR = 2.0) oscillating 1 mm in amplitude at 15 Hz, while Figure 6.1(b) shows an oblate spheroid (AR = 0.5) oscillated at the same frequency and amplitude; note that both images are at the same magnification. The steady streaming flow patterns near these two bodies with the same cross-section but differing volumes (because they have different axes of symmetry) have similar length scales, at least in the region adjacent to the body. If the axisymmetric length scale ($L = (a^4/b)^{1/3}$), is used, then the distance to the center of the lower right rotating region (denoted A_p and A_o on the prolate and oblate images, respectively) is 0.22 for the prolate case and 0.76 for the oblate case. This observation suggests that L as defined above may not be the appropriate length scale for these experimental data. The length scale for the flows near a body oscillated at various angles measured with respect to the body axis of symmetry (referred to as the "angled test cases") was therefore defined as

$$L^* = \sqrt{ab} \tag{6.1}$$

namely, the equivalent radius of the elliptical cross-section (*vs.* the entire volume) of the body. This definition results in a normalized distance to A_p and A_o of 0.38 and 0.43, respectively. The Reynolds number (Re_M*) and the oscillation amplitude ratio (ε*) are then also defined in this Chapter in terms of L*, *i.e.*

$$Re_M^* = \frac{\omega L^{*2}}{\nu}; \varepsilon^* = \frac{s}{L^*} \tag{6.2}$$

Figure 6.1 also shows the angular location of the stagnation point on the lower half of the body, φ, which is defined as the angle between a line from the body center to the stagnation point and the body axis of symmetry. Both θ and φ are taken to be positive measured counter-clockwise from axis of symmetry (giving negative values for the prolate spheroid).

Oscillations along directions other than the body axis of symmetry also break the axisymmetry of the flow field, and while the flows are imaged in their plane of symmetry, the steady streaming flow patterns are clearly a strong function of the oscillation direction, as shown in Figure 6.2. As θ changes from 0° (a) to 15° (b) to 30° (c) to 45° (d), the

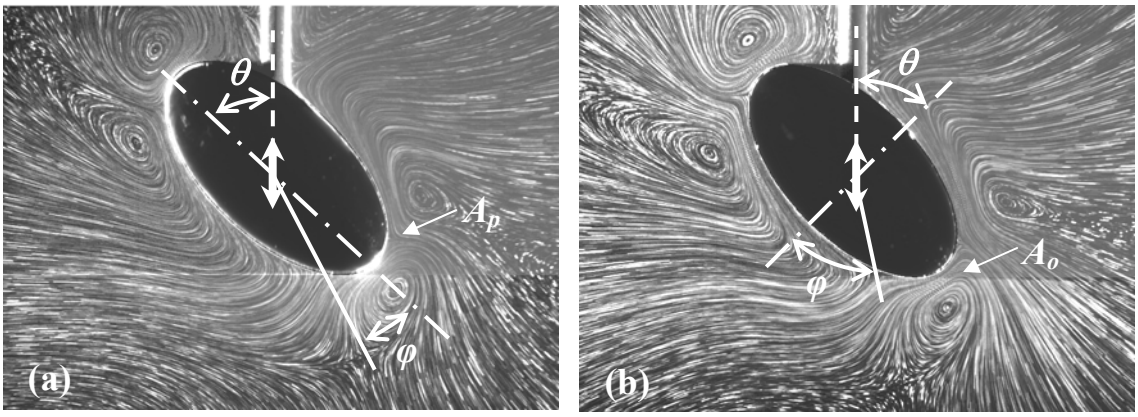

Figure 6.1 Particle pathline images for prolate (AR = 2, L* = 9 mm) (a) and oblate (AR = 0.5, L* = 9 mm) (b) spheroids oscillated sinusoidally at θ = 45° at 15 Hz, s = 1 mm, Re_M* ≈ 50, ε ≈ 0.1. Note that the orientation angle, θ, is defined in terms of the axis of oscillation (*dashed line*) and the axis of symmetry of the body (*dashed-dotted line*).

counter-rotating regions adjacent to the body change their position and size. To characterize these changes, consider an imaginary line drawn through the centers of the two counter-rotating regions adjacent to the lower half of the body. At $\theta = 0°$, this line defines the orientation of the toroidal structure formed by the lower rotating regions and is essentially horizontal. As θ increases to 15° and 30°, the lines (and, presumably, the associated toroidal structures) rotate 10° and 20° clockwise with respect to the horizontal, respectively. The lower right rotating region also appears to shrink as θ increases, complicating the three dimensional structures. At $\theta = 45°$, the lower right rotating region appears to form a small closed region, bounded below by what appears to be an additional stagnation point. It should be noted that although the flow should be two-fold rotationally symmetric, the mounting rod clearly disrupts this symmetry and introduces additional rotating regions in its vicinity.

As already observed for the "baseline" axisymmetric flow case of $\theta = 0°$ (Chapter 4), varying the frequency of oscillation has a marked effect on the flow patterns adjacent to the oscillating bodies. Decreasing the frequency causes the rotating regions to move away from the oscillating body, as shown in Figure 6.3(a), which is at an oscillation frequency half that of Figure 6.2(c). Comparing the two test cases, the rotating region to the lower right moves from $\approx L^*$ away from the body to $1.7L^*$ as the Re_M decreases from 30 to 15. Decreasing the amplitude of oscillation has little effect on the qualitative features of the steady streaming flows, but does of course increase the steady streaming velocity magnitudes, as can be seen by comparing Figure 6.2(c) and Figure 6.3(b), which both show 169 oscillation periods at $\varepsilon = 0.14$ and 0.07 for $\theta = 30°$ and $Re_M = 30$. Although the flow patterns are qualitatively similar, the particle pathlines are much shorter in Figure 6.3(b) due to the smaller velocity magnitudes, especially near the edge of the images.

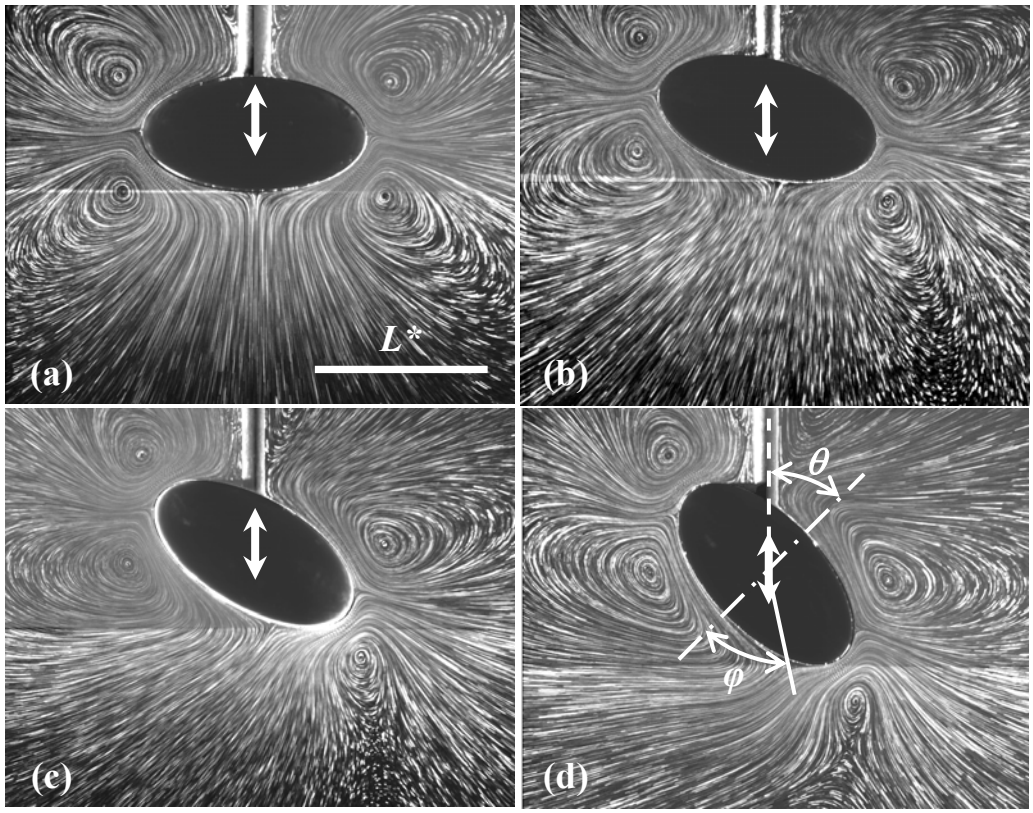

Figure 6.2 Particle pathline images for an angled oblate spheroid (AR = 0.5, L^* = 9 mm) oscillating at Re_M^* =30 and ε ≈ 0.1 for θ = 0° (a), 15° (b), 30° (c), and 45°(d). The oscillation angle θ is measured from the axis of oscillation of the body to the body's axis of symmetry. The angular location of the surface stagnation point, φ, is measured from the body's axis of symmetry.

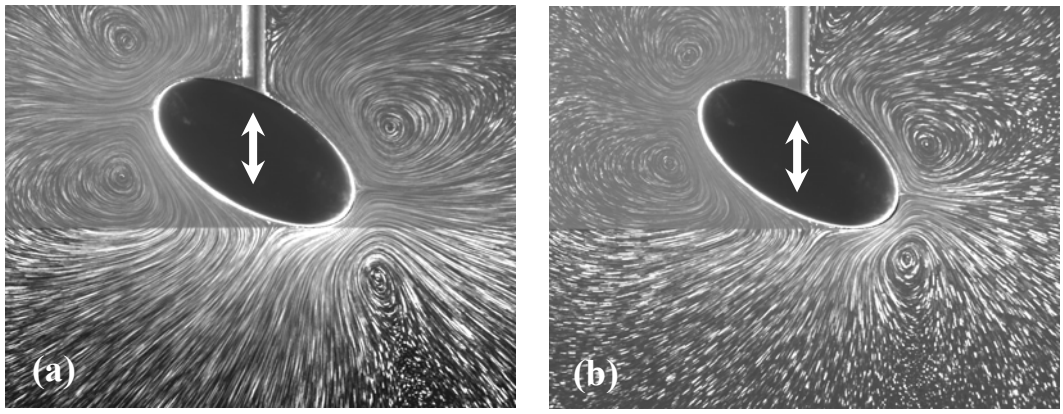

Figure 6.3 Particle pathline images for an angled oblate spheroid (AR = 0.5, L^* = 9 mm) oscillating at θ = 30° for Re_M^* =15 and ε ≈ 0.1 (a) and Re_M^* =30 and ε ≈ 0.07 (b). The images shown here, and in Figure 6.2, are obtained over 169 oscillation periods.

6.2 Velocity Fields

As before, PIV is used to determine the velocity of the steady streaming flow fields around the angled oscillating bodies. Figure 6.4 shows the velocity vector field for the cases shown in Figure 6.2, where $Re_M^* = 30$ and $\varepsilon^* = 0.1$. The streaming velocity scale, $V_s = \varepsilon^* \omega s$, is identical over all of these images. Black circles denote stagnation point locations and squares are used to label the vectors that were found to be "spurious" using the algorithm described in Chapter 3. The typical streaming velocities around the body at each orientation are $0.1V_s$–$0.2V_s$. The maximum velocity occurs near the body, approximately halfway between the body and the center of the rotating regions.

Figure 6.5, which shows scaled streaming velocity vectors at $Re_M^* = 50$ and $\varepsilon^* = 0.1$ for two bodies with different shapes but the same elliptical cross section, namely: (a) a prolate ($AR = 2.0$) spheroid; and (b) an oblate ($AR = 0.5$) spheroid (these are the same cases as are shown in Figure 6.1.). Note that the maximum velocity magnitudes scaled using L^* for the oblate and prolate cases shown in the Figure are 0.35 and 0.23, respectively, *vs.* 0.20 and 0.41, respectively for the same velocities scaled using L. A comparison of the two scales in terms of maximum velocity versus Reynolds number is found in Figure 7.6.

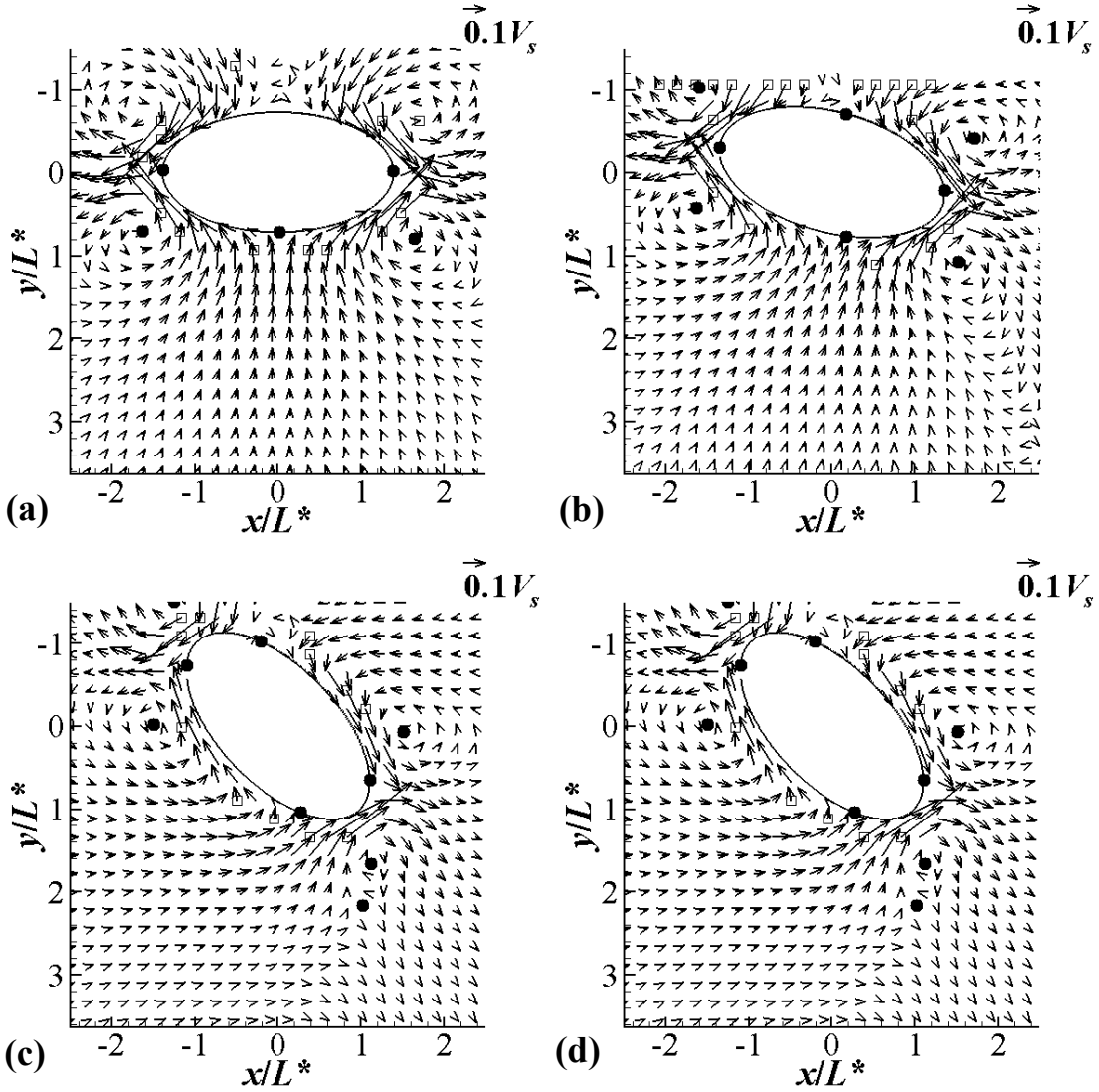

Figure 6.4 Velocity vector fields for an angled oblate spheroid (AR = 0.5, L^* = 9 mm) oscillating at Re^* =30 and ε ≈ 0.1 for θ = 0° (a), 15° (b), 30° (c), and 45°(d). The vectors are from the test cases shown in Figure 6.2

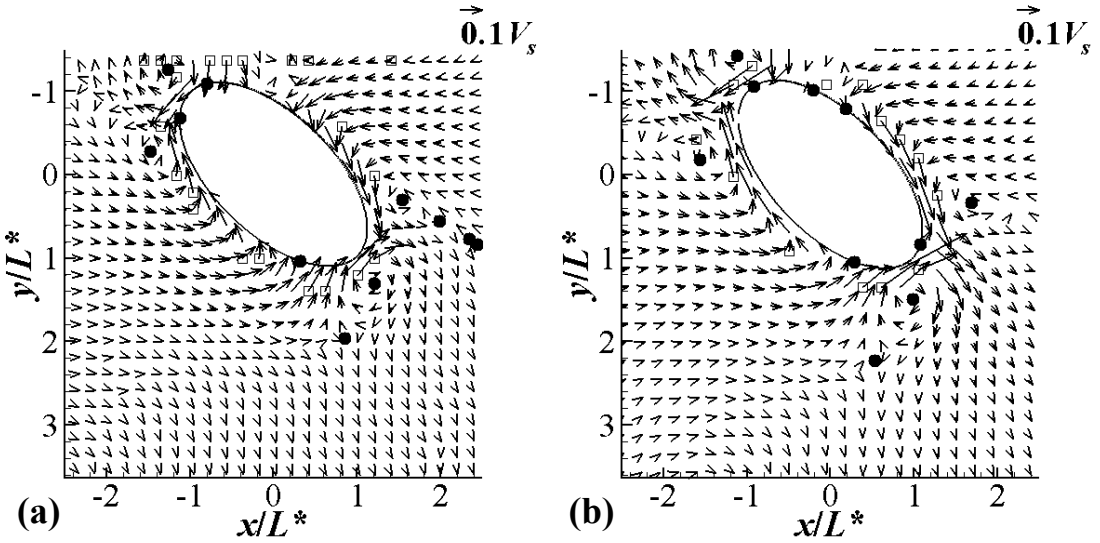

Figure 6.5 Velocity vectors for prolate (AR = 2.0, L* = 9 mm) (a) and oblate (AR = 0.5, L* = 9 mm) (b) spheroids oscillated sinusoidally at θ = 45° at 15 Hz, s = 1 mm, Re^* ≈ 50, ε ≈ 0.1. Test cases presented are those shown in Figure 6.1.

6.3 Vorticity Fields

The z-component of the vorticity Ω_z near an oblate spheroid (AR = 0.5) was calculated from the PIV data of Figure 6.4 and shown in Figure 6.6; note that the particle pathlines for these cases are given in Figure 6.2. The vorticity values are normalized by the vorticity scale Ω_s, defined as the streaming velocity divided by the Stokes layer thickness

$$\Omega_s = \frac{V_s}{\delta} = \frac{\dfrac{\omega s^2}{L^*}}{\sqrt{\dfrac{\nu}{\omega}}}. \qquad 6.3$$

The Stokes layer thickness, δ, was chosen as the length scale because the vorticity generation is essentially confined to this region. For the test cases shown in Figure 6.6, the Stokes layer thickness is approximately 0.2 L^*, which corresponds to the distance

from the body to where the vorticity changes sign for the first time. The vorticity field consists of paired positive and negative regions, with a thin layer adjacent to the body and a thicker region of opposite sign farther away from the body. The locations of these paired regions roughly correspond to the rotating regions observed in the "inner region" of the flow (*cf.* Figure 6.2). The qualitative changes in the vorticity as θ increases are similar to those observed in the PIV results and particle pathline visualizations, with the regions of positive and negative vorticity near the ends of the body that "lead" the oscillation shrinking as θ increases

The effect of changing the body shape from: (a) oblate (AR = 2.0) to (b) prolate (AR = 0.5), while maintaining the same cross-sectional shape, is shown in Figure 6.7, corresponding to the PIV data of Figure 6.5 and the flow visualizations of Figure 6.1. The line on the Figure denotes the $\Omega_z = 0$ contour. An estimate of the "extent" of the vorticity using the zero contour-lines shown in the images suggests that there is a thin, but noisy, region of vorticity near the body. The second time that the vorticity changes sign (moving away from the body), the vorticity near the oblate case appears to have a greater extent. Given the greater volume of the oblate spheroid, it is not surprising that the oscillation of this body has a larger impact on the flow field.

It should be noted that the thin layer of vorticity adjacent to the body is likely to be real, but under-resolved due to the coarseness of the PIV data used to generate the vorticity plots. The spatial resolution is one reason that the region appears to be so "noisy". In fact, due to the proximity of the hair cells to the otolith and their comparatively small length, this inner vorticity region is probably what the hair cells are sensing.

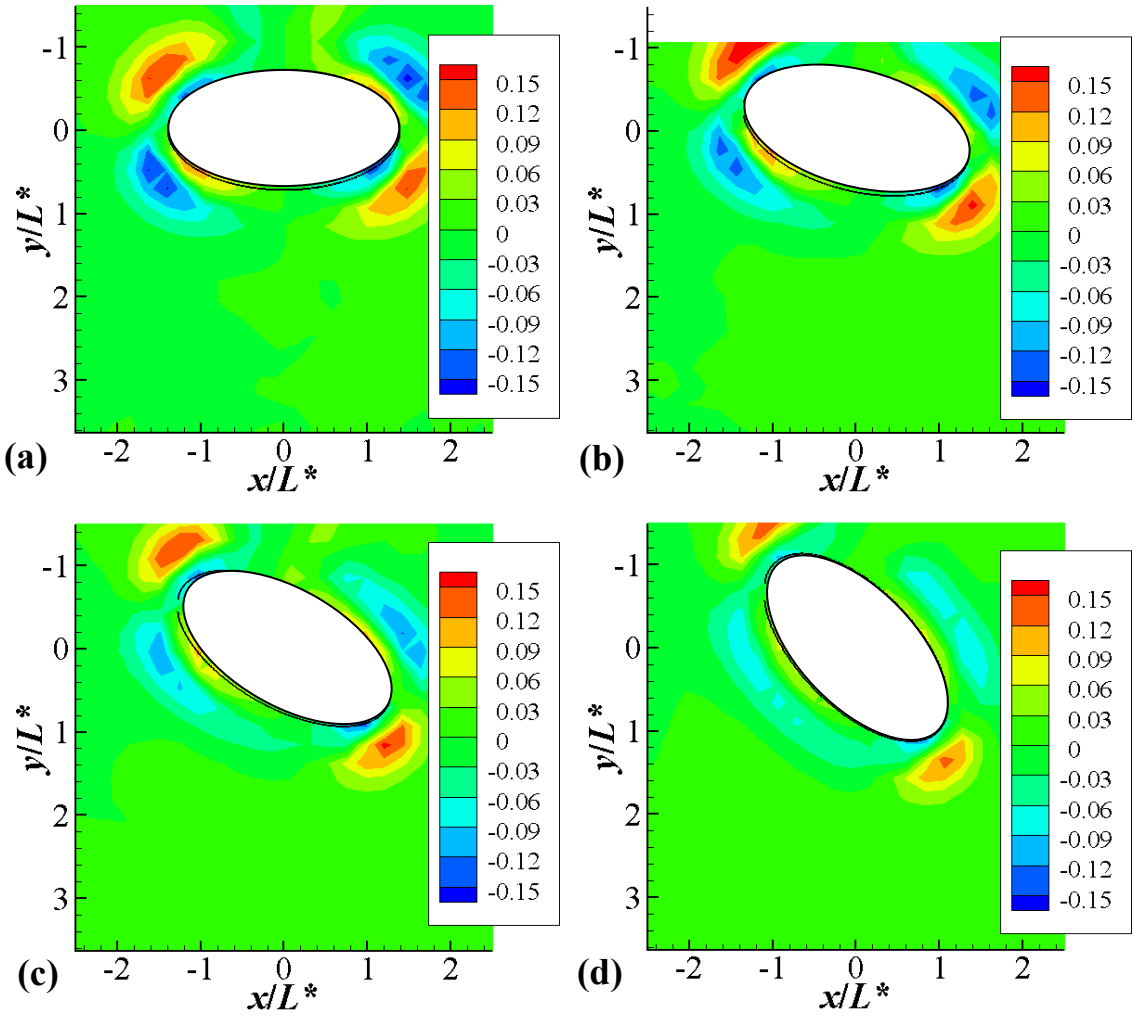

Figure 6.6 Scaled vorticity fields for an angled oblate spheroid ($AR = 0.5$, $L^* = 9$ mm) oscillating at $Re^* = 30$ and $\varepsilon \approx 0.1$ for $\theta = 0°$ (a), 15° (b), 30° (c), and 45°(d). Vorticity scaling as described in the text. The test cases presented are those shown in Figure 6.2.

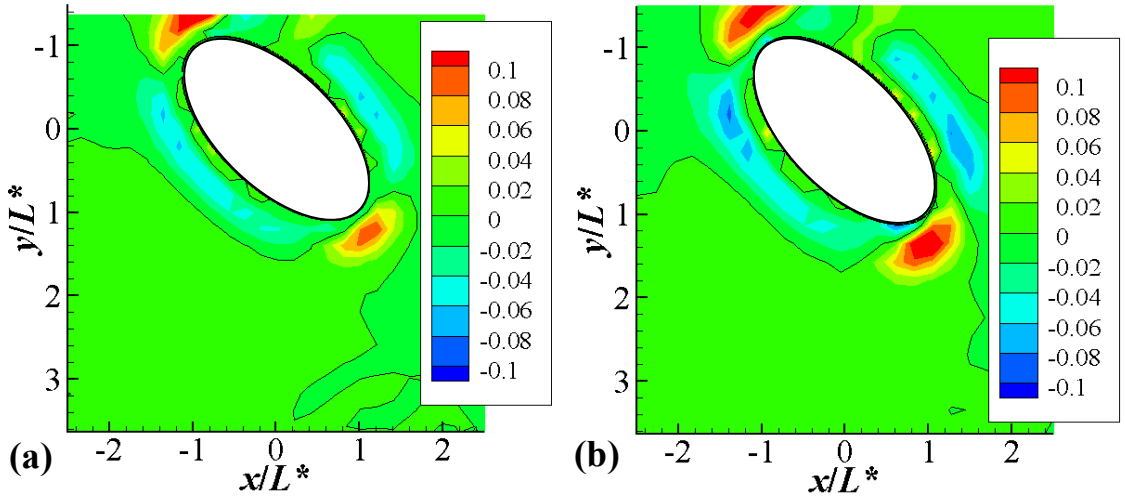

Figure 6.7 Scaled vorticity field for prolate (AR = 1.33, L^* = 9 mm) (a) and oblate (AR = 0.5, L^* = 9 mm) (b) spheroids oscillated sinusoidally at θ = 45° at 15 Hz, s = 1 mm, $Re^* \approx 50$, $\varepsilon \approx 0.1$ (*i.e.*, the test cases presented in Figure 6.1). The lines represent the $\Omega_z = 0$ contour.

6.4 Stagnation Point Location

The location of the stagnation points in the flow field near the body are qualitatively similar to those for the axisymmetrical cases, appearing in the middle of the counter-rotating regions and along the body where the rotating regions meet. The stagnation points on the surface of the oscillating body are of primary interest because they are the most likely to be sensible to the fish ear. (The hair cells can only sample the area of the fluid adjacent to the otolith; therefore, of the stagnation points locations, the points along the body are the most likely to be sensible). Again, only the two on-surface stagnation points for the lower half of the body are considered here because of disturbances due to the mounting rod on the upper half of the body.

First, consider the stagnation point at the center of the lower surface of the body at $\theta = 0°$. Its angular position is quantified in terms of φ, the angle (measured counterclockwise) from the axis of symmetry to a line drawn from the center of the body to the stagnation point (*cf.* Figure 6.1). Figure 6.8 shows $AR \tan(\varphi)$ as a function of $\tan(\theta)$ over a range of Reynolds numbers and amplitude ratios; clearly, φ increases with

increasing θ. The error bars shown in the figure are determined using standard propagation of error analysis, discussed in Appendix A. A curve-fit of these data gives

$$\frac{\tan(\theta)}{\tan(\varphi)} = AR \qquad 6.4$$

where φ is independent of the oscillation frequency and amplitude for the values studied here. This equation is reminiscent of that for steady flow over an elliptical cylinder, which produces two stagnation points along the surface of the cylinder at angular locations given by the same relationship (Batchelor 1967).

Next, consider the stagnation point that begins on the right side of the body at θ = 0°. Although the mounting rod may interfere with the location of the stagnation points on the side of the body, the data suggest that the location of these stagnation points also

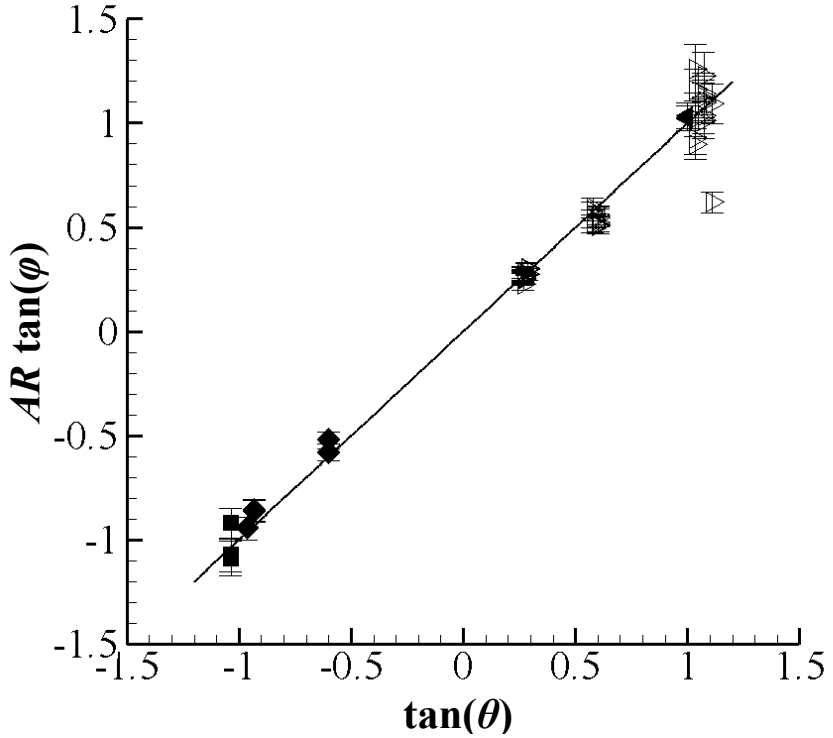

Figure 6.8 Graph of $AR\tan(\varphi)$ as a function of $\tan(\theta)$ for AR = 0.5 (*open triangle*), 0.76 (*closed triangle*), 1.3 (*filled diamond*), and 2 (filled square) at Re_M* = 6–76 and ε* = 0.07–0.3.

varies with θ in body-fixed coordinates. These stagnation points generally appear near the rightmost position of the spheroid, *i.e.*, the location where the surface of the spheroid is nearly parallel to the vertical. However, there is some spread to the data. The mean tangent to elliptical outline at these side points is 96°, with a standard deviation of 16°. Although not shown, the positions of these stagnation points also appear to be independent of the frequency or amplitude of oscillation.

6.5 Implications for Fish Hearing

The angled oscillating spheroids produce flow patterns that vary significantly with the orientation and aspect ratio of the body, suggesting that fish may be able to use these patterns to determine the direction of incident sounds (or at least the direction of the acoustic particle velocity). Since the body geometry (*e.g.* the aspect ratio) is essentially constant for a given otolith with respect to time, fish may be able to infer the direction of travel for an incident plane wave by locating the stagnation points on the otolith. Given that the steady streaming flow changes direction near the stagnation points, the hair cells will sense a much greater range of displacements in these flow regions. These stagnation point locations could be particularly useful in determining the direction of incident sound since they appear to be independent of frequency and amplitude on the "ungrooved" body. Although the hair cells will oscillate with the time-dependent flow, the steady coherent portion of the flow should nevertheless create a sensible bias that the fish may be able to exploit.

CHAPTER 7

GROOVED TEST CASES

7.1 General Features of the Steady Streaming Flow Patterns

Initial studies of the flow inside of a groove were conducted to determine how a recessed surface (like that of the sulcus) affects the steady streaming flow patterns. An oblate spheroid (AR = 0.75, a = 14 mm, b = 18.6 mm) was modified by cutting a 6 mm diameter slot into one side, as shown in Figure 3.3. Since the flow of interest here is shaped by the oscillating slot, the body length scale is taken to be the slot radius, c. Therefore, the Reynolds number and oscillation amplitude ratio are calculated from

$$Re_M = \frac{\omega c^2}{\nu} \tag{7.1}$$

and

$$\varepsilon = \frac{s}{c} \tag{7.2}$$

For several test cases, the body was angled relative to the oscillation. The oscillation angle θ is defined as in Chapter 6; since the slot remains at a constant position in body-fixed coordinates, θ describes the orientation of the slot relative to the oscillation.

As shown in Figure 6.1, two counter-rotating regions form inside of the slot. As θ varies from 0° (a) to 15° (b), 30° (c), and 45° (d), the fluid inside the slot becomes more exposed to motion along the vertical, *i.e.*, the direction of oscillation. The direction of fluid motion is such that the flow moves towards the body along the pathlines in the middle of the slot, resulting in a clockwise motion in the upper rotating region and a counter-clockwise motion in the lower rotating region. These two regions are (essentially) identical at θ=0° but as θ increase from 15° to 45°, the upper rotating region begins to dominate the slot, becoming rounder and larger than the lower rotating region.

The stagnation point occurring where the streamline dividing the upper and lower rotating regions intersects the slot (which is the center of the slot when $\theta = 0°$) also shifts counter-clockwise away from the center of the slot as the body and slot rotate clockwise.

As before, the Reynolds number, or normalized oscillation frequency, determines the extent of the inner rotating regions. As shown in the Figures, the lower inner rotating region elongates as the Reynolds number increases from 1.7 [Figure 7.2(a)]to 3.4 [Figure 7.2(b)] to 5 [Figure 7.1(c)]. At the same time, the upper rotating region becomes more defined, with the center of the upper eddy appearing and drawing closer to the body while the eddy structure becomes more circular. As the body tilts, the relative positions of the rotating regions appear to tilt in the same direction as the body, although this trend is not consistent over all Reynolds numbers and orientations. Figure 7.3(a) gives the distance from the top "tip" of the slot (as shown on Figure 7.1(a), the "tip" of the slot refers to the intersection of the body's overall elliptical outline and the circular groove) to the center of the upper rotating region as a function of θ for a range of Reynolds numbers from two to seven and $\varepsilon = 0.1$, 0.2 and 0.4. This distance is essentially constant for $Re_M = 3$ (*triangles*), 5 (*circles*), and 7 (*diamonds*); however, at $Re_M = 2$ (*squares*), the upper rotating region moves away from the body as the orientation angle increases. It should be noted that at $Re_M = 2$, the upper rotating region did not have a well defined center for the lower oscillation amplitude of $\varepsilon = 0.1$. Figure 7.3(b) shows a similar measurement for the distance from the lower "tip" of the slot to the center of the lower rotating region. Here, the lower rotating regions at both $Re_M = 2$ and 3 appear to approach the body as the orientation angle increases. Although the distance appears to remain constant at $Re_M = 5$, the results at $Re_M = 7$ are inconclusive since the "center" of the lower rotating region was not well-defined at $\theta = 30°$ and 45°. Note that the rotating regions near the groove have an extent comparable to c , which is much smaller than the corresponding regions for the axisymmetric and angled test cases.

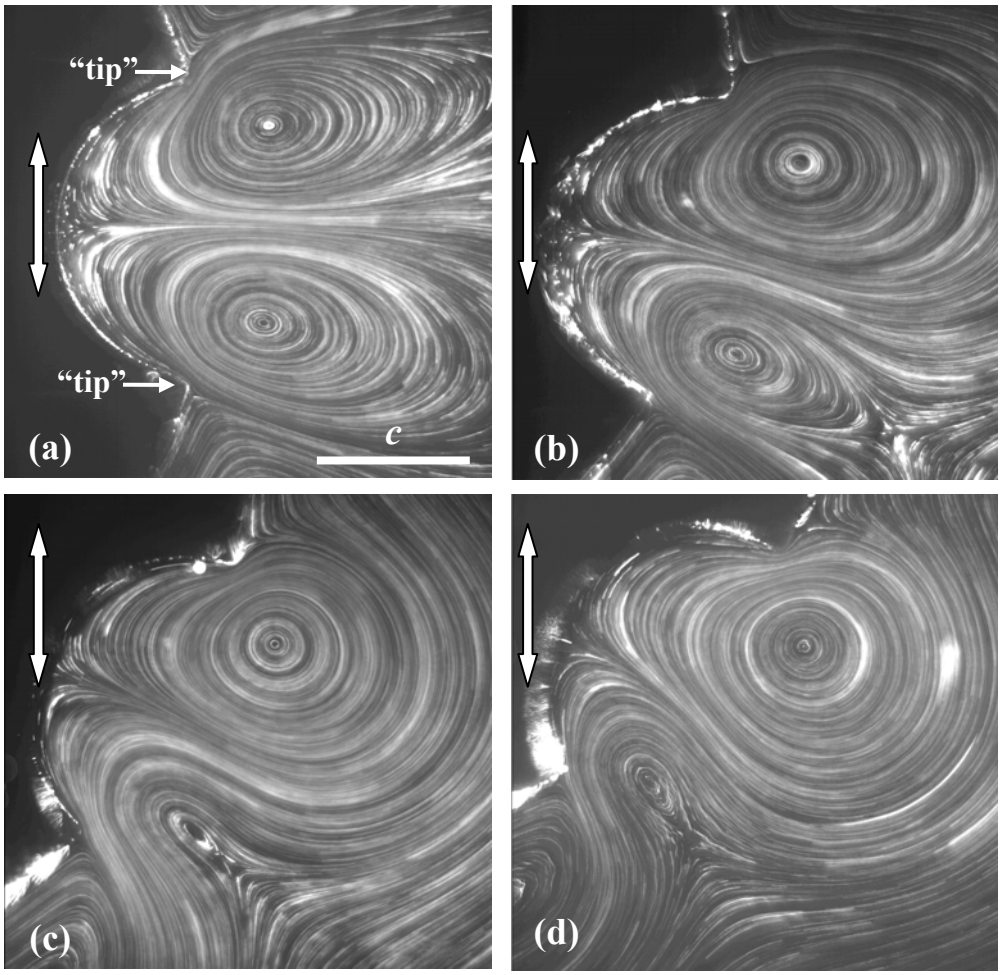

Figure 7.1 Sequence of particle pathline images illustrating the effect of tilting the slotted body 0° (a), 15° (b), 30° (c) and 45° (d) from the axis of oscillation for $Re_M = 5$ and $\varepsilon = 0.1$. As described in the text, the body is an oblate spheroid with $AR = 0.75$, $a =$ 14 mm, $b = 18.6$ mm, $c = 3.2$ mm.

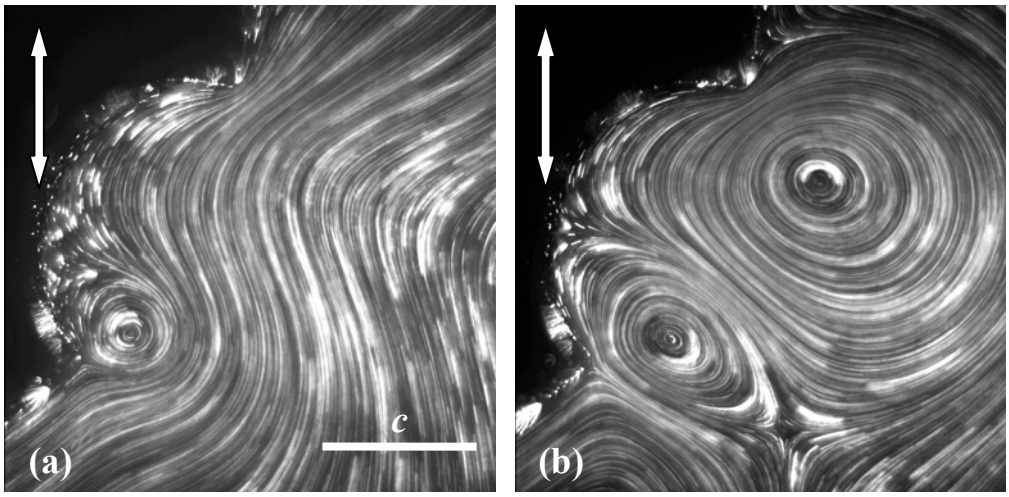

Figure 7.2 Particle pathline images for a slotted oblate spheroid oriented 30° from the horizontal position, oscillating at $Re_M = 1.7$ (a) and 3.4 (b) with $\varepsilon = 0.1$. As described in the text, the body is an oblate spheroid with $AR = 0.75$, $a = 14$ mm, $b = 18.6$ mm, $c = 3.2$ mm.

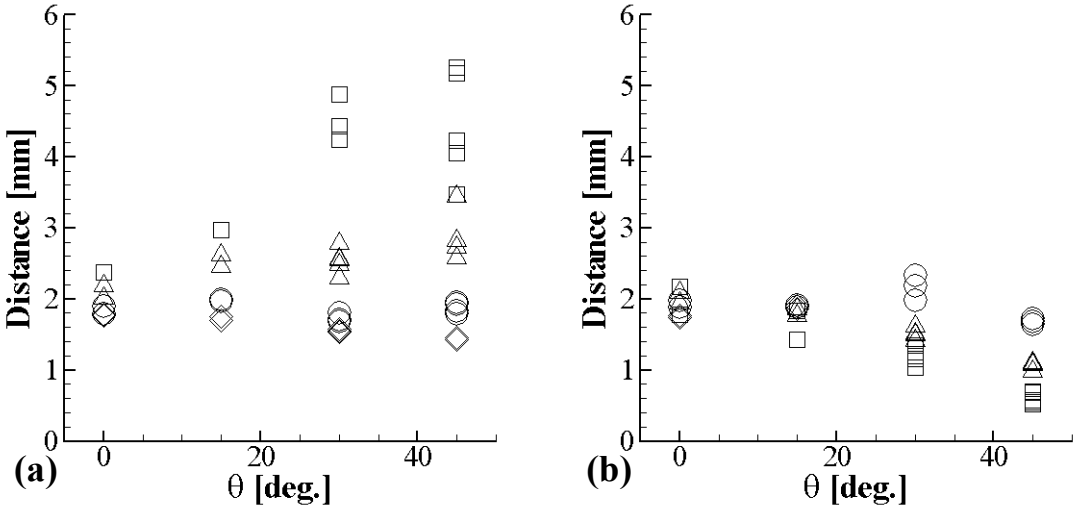

Figure 7.3 Distance from the "tip" of the slot to the center of the rotating region for the top tip to the upper rotating region (a) and the bottom tip to the lower rotating region (b) for $Re_M = 2$ (*squares*), 3 (*triangles*), 5 (*circles*), and 7 (*diamonds*).

7.2 Velocity Fields

The streaming velocity near the groove was studied with PIV as described in Chapter 3. The velocity scale is defined using the slot radius, c:

$$V_s = \varepsilon U_0 = \frac{\omega s^2}{c} \tag{7.3}$$

Because c = 3.2 mm is one-fourth of the length scale for the ungrooved axisymmetric body (L = 12.7 mm) and one-fifth the scale of the ungrooved angled body (L^* = 16.2 mm), the scaled velocities should not be compared directly with those presented for the previous tests.

Typical examples of the steady streaming velocity field are shown in Figure 7.4 for body orientation angles of (a) 0° and (b) 30° at Re_M = 5 and ε = 0.1 (note that $Re_M = \omega c^2 / \nu$.) In the Figure, squares denote locations of spurious vectors, while circles denote stagnation point locations. Only every other vector is shown in the Figure for clarity. As can be seen in the Figure, the algorithm for detecting stagnation points works

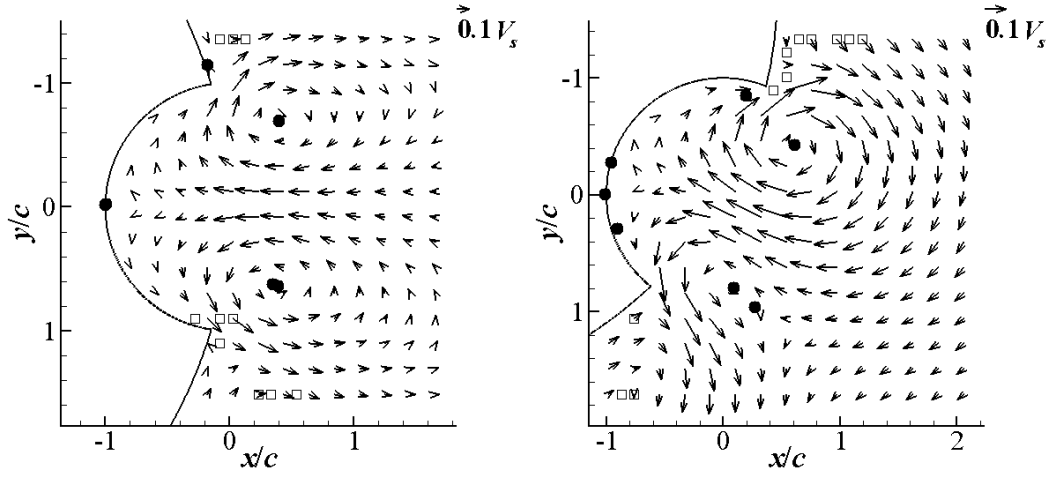

Figure 7.4 Scaled PIV vectors for Re_M = 5 and ε = 0.1 at 0° (a) and 30° (b), showing every other vector for clarity. Stagnation points are shown as *circles* while "bad vectors" are shown as *squares*. The position of the body is shown by the black outline.

reasonably well within the flow field, but it occasionally locates "false positives" inside the groove due to spurious vectors in PIV data. The "false positives" are subsequently identified and removed by visual inspection. The maximum speed is generally located near the upper "tip" of the groove, specifically between the tip of the groove and the center of the upper rotating region. The presence of the groove increases the maximum speed of the streaming flow near the body. Figure 7.5 shows particle pathlines obtained over the entire extent of the grooved spheroid with a = 11.9 mm, b = 15.7 mm, c = 3.2 mm, and θ = 15°. Although it may seem counter-intuitive, the very short, almost "dot-like" pathlines near the groove on the right hand side indicate that the flow in this region is faster than in the "smooth" flow at the corresponding location on the other side of the body. In traditional pathlines, where the image is formed from a continuous exposure, a short path line indicates a particle that does not travel very far over the time of the exposure (or moves out of the focal plane). Here, the pathlines are formed by averaging individual images numerically, and the dot-like pattern to the right is formed from the particle moving more than its diameter between exposures. Essentially, rather than getting the long smooth streak from the slower particles, the faster particles generate a "dotted" streak. The PIV results for this case suggest that the velocity near the groove is at least three times larger than that on the other side of the body. However, this preliminary result has a relatively large oscillation amplitude of 0.3 relative to the dimension of the groove, and therefore, may not be in the linear regime. This suggests that although the flows are certainly faster near the groove, it is uncertain how much faster they would be at a lower oscillation amplitude. As shown in Figure 7.4, the flows inside of the groove near the body stagnation points are much slower than the flow at the "tips" of the groove.

The maximum scaled velocity is plotted as a function of Reynolds number in Figure 7.6 using L as the length scale in Figure 7.6(a) and L^* in Figure 7.6(b). Note that each plot uses a consistent choice of length scale for calculating V_s as well as the

Reynolds number. In the Figure, colors denote the orientation of the body and shapes denote the aspect ratio, as described in the caption. The filled symbols are the grooved cases discussed in this chapter. For the test cases studied, it appears that L provides a more consistent velocity scaling over a range of Reynolds numbers and orientations. However, the maximum velocity for the grooved test cases appears to increase with Re_M for all values of θ regardless of the choice of length scale.

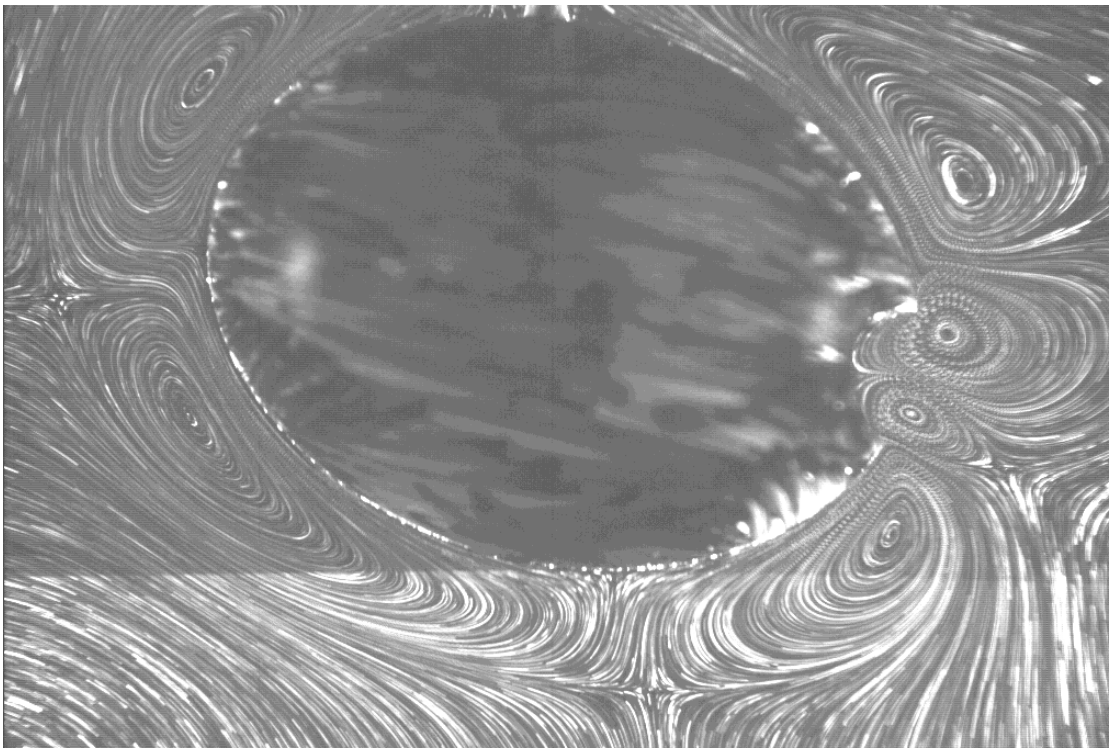

Figure 7.5 Grooved oblate spheroid (a = 11.9 mm, b = 15.7 mm, c = 3.2 mm, θ = 15°) oscillated 1 mm in amplitude at 20 Hz. Based on the slot, the nondimensional parameters are Re_M = 8 and ε = 0.3.

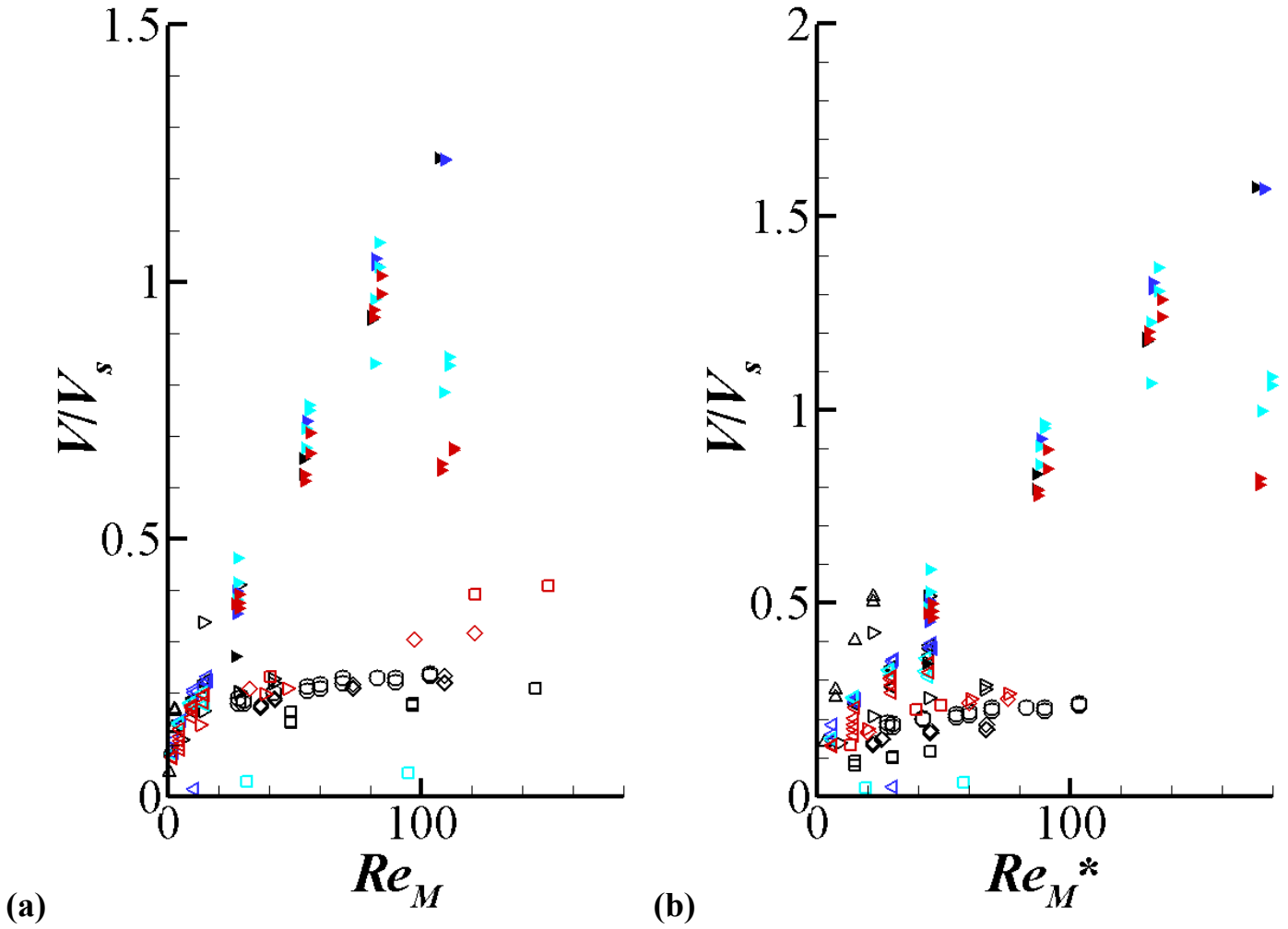

Figure 7.6 Scaled velocity values *vs.* Reynolds number using L (a) and L^* (b) for AR = 2 (*square*), 1.3 (*diamond*), 1 (*circle*), 0.75 (*right triangle*), 0.5 (*left triangle*), 0.25 (*delta*) and $|\theta|$ = 0° (*black*), 15° (*dark blue*), 30° (*light blue*), 45° (*red*). Filled symbols denoted grooved bodies while unfilled symbols denote ungrooved bodies.

7.3 Vorticity Fields

The vorticity component normal to the plane is concentrated at the tips of the grooves, as shown in Figure 7.7 for $Re_M = 5$ and ε = 0.1 at 0° (a) and 30° (b). These vorticity values are calculated from the velocity vectors shown in Figure 7.4. As before, the vorticity is scaled using the Stokes layer thickness:

$$\Omega_s = \frac{V_s}{\delta} = \frac{\frac{\omega s^2}{c}}{\sqrt{\frac{\nu}{\omega}}} \qquad 7.4$$

As can be seen in the Figure, small regions of negative and positive vorticity can be observed at the upper and lower "tips" of the groove, respectively, with a larger region of vorticity of the opposite sign farther away from the body. For the $\theta = 0°$ case, the vorticity magnitude near the upper and lower ends of the groove are roughly equal; for the $\theta = 30°$ case, however, the breakdown in the top-bottom symmetry of the flow inside the slot leads to a larger vorticity magnitude near the upper end of the groove.

The vorticity near the groove is expected to have a larger magnitude than that near the ungrooved axisymmetric and angled bodies since the flow is faster near the groove and the Stokes layer thickness, $\delta = \sqrt{\frac{\nu}{\omega}}$, remains unchanged. When the scaling given above is used, the maximum scaled vorticity values for the grooved case are approximately 0.5. For comparison with the ungrooved cases, it is necessary to use the same vorticity scale for each case. Recall that in Chapter 6 the vorticity was scaled by

$$\Omega_s = \frac{V_s}{\delta} = \frac{\frac{\omega s^2}{\sqrt{ab}}}{\sqrt{\frac{\nu}{\omega}}} \qquad 7.5$$

which is used to scale the vorticities for the grooved and ungrooved cases in the following comparisons. Figure 7.8 illustrates the maximum scaled vorticity values over the same range of test cases as Figure 7.6; *cf.* the caption of Figure 7.6 for the legend. For the cases studied, the typical maximum ungrooved axisymmetric angled scaled vorticity values are about 0.1, while those for the grooved cases are generally between 1.5 and 3, and increase with Reynolds number. The presence of the groove clearly increases the magnitude of the out-of-plane vorticity component, particularly at the tips of the groove.

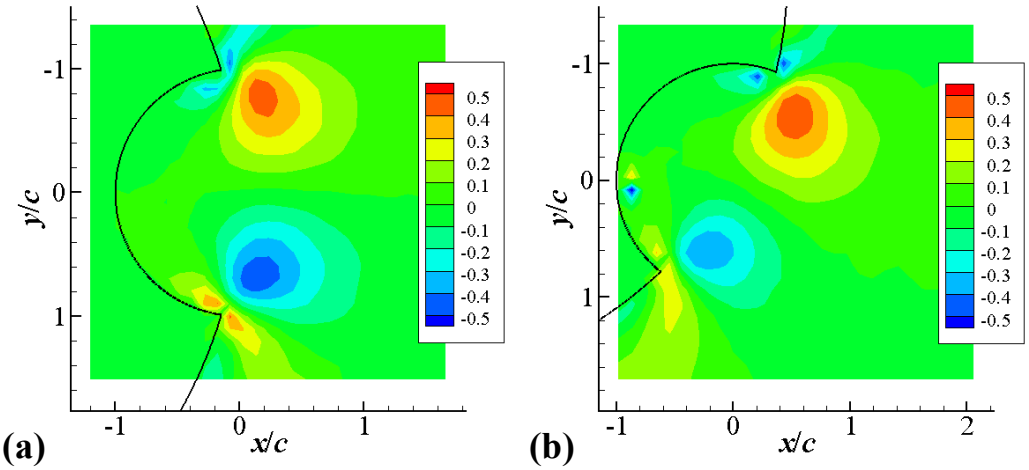

Figure 7.7 Contour map of the vorticity scaled by Ω_s for $Re_M = 5$ and $\varepsilon = 0.1$ at 0° (a) and 30° (b). The position of the body is shown by the black outline.

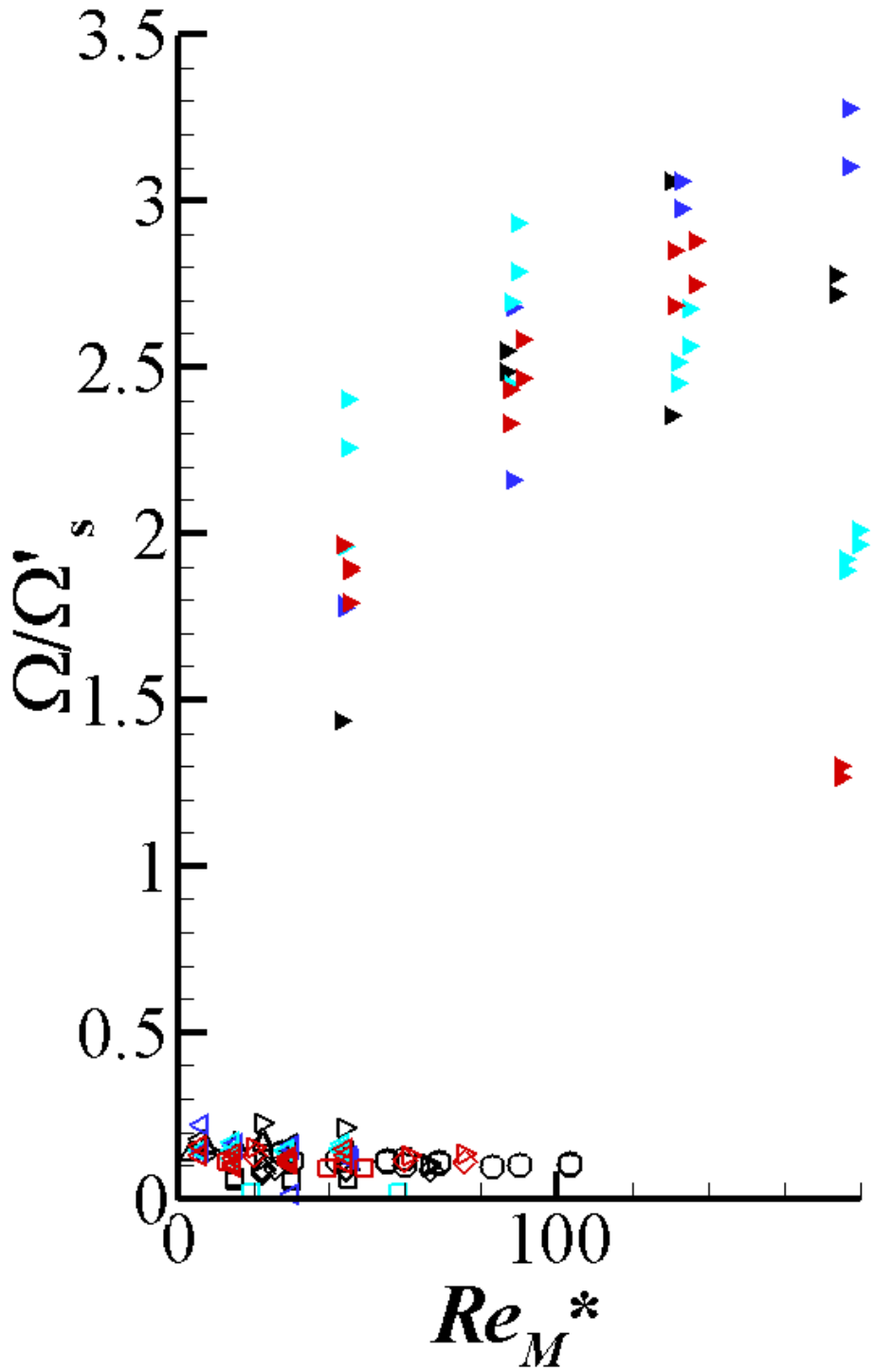

Figure 7.8 Vorticity values scaled by Ω_s' *vs.* Re_M* for AR = 2 (*square*), 1.3 (*diamond*), 1 (*circle*), 0.75 (*right triangle*), 0.5 (*left triangle*), 0.25 (*delta*) and $|\theta| = 0°$ (*black*), 15° (*dark blue*), 30° (*light blue*), 45° (*red*). Filled symbols denoted grooved bodies while unfilled symbols denote ungrooved bodies.

7.4 Stagnation Point Location

In most cases, the steady streaming flow inside the groove has three stagnation points: one at the center of each of the two counter rotating regions and one on the groove surface. Because the groove in these studies models the sulcus, and the macular hair cells should primarily sample the flow immediately adjacent to the surface of the sulcus, this thesis focuses on the on-surface stagnation point inside the groove. The angular location of this stagnation point is defined in terms of its angular location, A, measured clockwise from a line through the groove's center of curvature perpendicular to the axis of oscillation (*i.e.*, along the horizontal) and a line from the stagnation point to the groove's center of curvature, as illustrated in Figure 7.9(a). Unlike the "un-grooved" case, the surface stagnation point angular location is a function of the Reynolds number, but it appears to still be independent of the oscillation amplitude. As can be seen from Figure 7.9(b), for Reynolds numbers of 3 and 7 (triangles and diamonds, respectively) and for cases where $\theta = 0°$, A is approximately 0° (the error bars on this plot are found through standard propagation of error analysis, similar to that used for the stagnation point analysis on the ungrooved case). As defined, A would be equal to θ if the stagnation point were to be fixed in body fixed coordinates; for the stagnation point to be fixed relative to the slot's center of curvature, $A = 0°$. Although A appears to vary linearly θ for a given Reynolds number, there is no clear trend evident over all Re_M* and these initial results are inconclusive. The very small streaming velocity magnitudes at the lowest Reynolds number could be affected by convective currents in the fluid. These data may also be affected by the relatively thick Stokes layer at these Re_M*, since the Stokes layer thicknesses of 1.2–2.4 mm in these cases is comparable to the overall extent of the groove, or c.

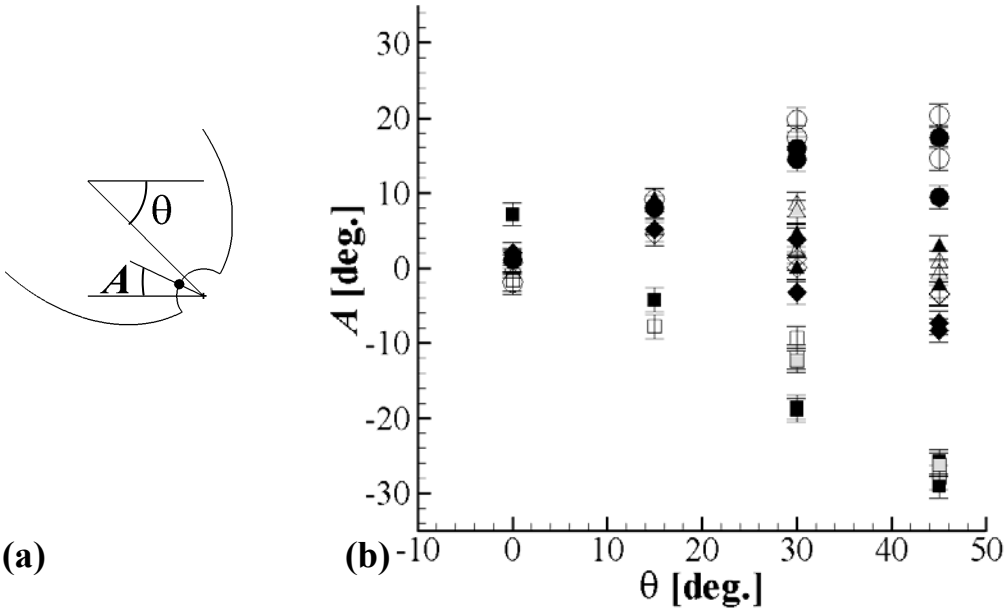

Figure 7.9 (a) Schematic showing the definition of A and θ. (b) A *vs.* θ for Reynolds numbers of 2 (*squares*), 3 (*triangles*), 5 (*circles*), and 7 (*diamonds*) at amplitudes of oscillation of 0.1 (*filled symbols)*, 0.2 (*open symbols*), and 0.4 (*gray symbols*).

7.5 Implications for Fish Hearing

The study of the grooved oscillating spheroid reveals several facets of steady streaming flows that are of interest to the fish ear. First, the groove appears to increase the scaled velocity magnitude of the steady streaming flows. (This is partly because the groove shrinks the length scale of the rotating steady streaming regions, increasing the oscillation amplitude ratio for the same oscillation, which in turn decreases the streaming velocity scale, since $V_s = \varepsilon U_0$.) However, comparing the streaming flows from the grooved and ungrooved side of the same spheroid clearly indicates that the groove increases the streaming velocity. Second, the geometry of the groove appears to have a strong impact on the location of the local maximum of the steady streaming flows, implying that the presence of the groove may serve to "focus" or shape the fluid flows so that they are more (or less) apparent along the area of the otolith where the hair cells are

located. Although the relatively deep groove used here increased the streaming velocity near the "tips" of the groove, the flow was very slow along the surface towards the center of the slot. If the groove/sulcus is too deep, then the streaming along the surface of the groove near the stagnation points will be very small. Depending on the depth of the groove, the hair cells could be shielded from the streaming flows at some locations. Although there is some species dependent variation in the sulcus depth, it is typically a relatively shallow groove or indentation in the otolith. Therefore, the ideal depth for the sulcus is likely far shallower than what was shown here, particularly considering the biological pressures that have shaped its design.

For the groove used in this study, it should also be noted that the stagnation point location for the grooved flow is not independent of Reynolds number (or frequency) for the cases studied. This result, if true for an actual sulcus, suggests that fish would have to determine the frequency of incident sounds by other means before they could determine the direction of the sound sources from the location of the stagnation point in the sulcus. Indeed, fish may well be able to determine the sound frequency by other means. For instance, studies show that hair cells of varying lengths have frequency-dependent responses; also, some hair cells are capable of phase-locking to the incident sounds, providing a time-domain technique for frequency analysis (Popper *et al.* 2003).

CHAPTER 8

OTOLITH TEST CASES

8.1 Steady Streaming Flow Patterns

A 350% scale model of a cod otolith was fabricated (as described in Chapter 3) to investigate whether steady streaming flows could encode acoustical information in a geometry that was more representative of an actual fish ear. Otoliths from the cod, a deep-sea species, were chosen because cod have relatively well studied hearing abilities as discussed in Chapter 2. In particular, cod are sensitive to a wide range of frequencies (Sand and Enger 1973; Sand and Karlsen 1986; Astrup and Møhl 1993), can directionalize sounds (Schuijf 1975; Hawkins 1981; Schuijf 1981; Buwalda *et al.* 1983), and are capable of discriminating sounds of different intensities(Chapman and Johnstone 1974). Given that the steady streaming flow patterns around "ersatz" otoliths (*i.e.*, spheroids) clearly vary with the frequency and direction of incident sound, cod appear to be a good candidate species for further study.

The 350% scale model, as shown in Figure 3.4, has a maximum width of about 3.6 cm (y-direction) and a length of about 6.9 cm (z-direction). Since the studies discussed here focus on the region near the sulcus as the region of the flow sensed by the macular hair cells, the maximum width of the sulcus of 1 cm was taken to be the length scale L. A sketch of the model otolith is shown in Figure 8.1. The flow was visualized over three planes: the two x-y planes denoted by the dashed and solid lines near the center of the sulcus, and the x-z' plane denoted by the dotted line near the left end of the sulcus. The x-axis points out of the page. The orientation angle, θ, is defined as before for data taken along the x-y planes: the angle represents the orientation of the body relative to the axis of oscillation. However, $\theta = 0°$ refers to the location where the plane

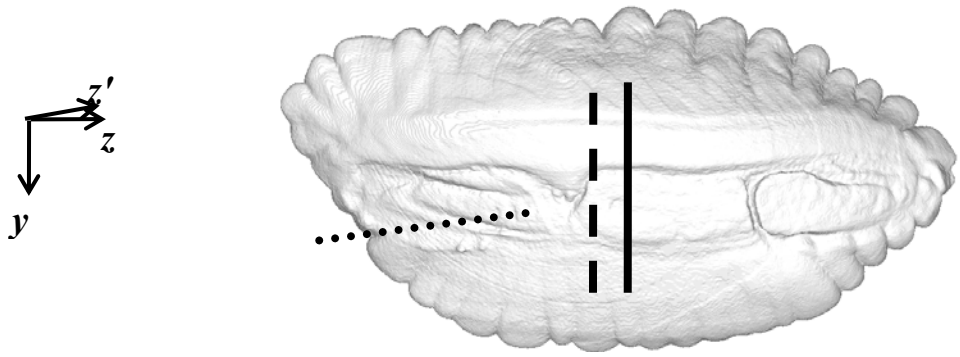

Figure 8.1 Sketch of the scale model otolith with a line denoting the position of the laser light sheet for Figures discussed in this chapter. The *x*-axis is coming out of the page.

of the sulcus is (for the data taken) closest to the being aligned to the *x*-axis, and θ increases as the sulcus rotates counterclockwise to become more vertical. The body orientation for data taken along the dotted location will be referred to as α, where α is the relative angle between the z'-axis and the axis of oscillation. Again, α has been arbitrarily set as 0° when the sulcus is at its most horizontal position (of the data taken), and increases as the body rotates counterclockwise.

Near the otolith, the steady streaming flow patterns vary primarily with the oscillation frequency and the body orientation. These variations are illustrated using particle pathline images over 200 oscillations with the laser light sheet along the solid line shown in Figure 8.2. In the sequence of pathline images shown in this Figure, each column represents a different oscillation frequency (increasing from left to right) or Re_M, while each row represents a different otolith orientation (or, alternatively, oscillation direction) θ, where θ increases going down the page. As before, all oscillations are along the vertical in these images, which is denoted by the double-headed arrow. In the steady streaming flow patterns in the area near the sulcus (marked with a white line in images a, d, h, and k), each particle pathline is that of an individual particle moving along the sulcus in the plane of the laser light sheet over all 200 oscillation periods. (Individual particles were visually tracked over the time sequence of the flows used to create the

averaged pathline images.) This observation suggests that there is very little motion normal to the plane of the image since the particles remain within the light sheet, which is nearly normal to the axis of the sulcus. Near the sulcus, the number of rotating regions, or eddies (estimated here by counting the number of times the flow changes direction along the sulcus and adding one for the "incomplete" eddy), varies depending on the orientation of the body, from one eddy at $\theta = 0°$ to three eddies at $\theta = 30°$, 45°, and 75°. Note that only the lower two surface stagnation points in Figure 8.2 (e) (marked by blue circles) are on the sulcus. Similarly, as θ increases from 0° to 75°, the number of stagnation points increases from zero to two along the sulcus, and the distance between the points increases with the angle of oscillation.

The eddy size near the sulcus also depends upon the oscillation frequency, or Re_M. If we consider the $\theta = 45°$ case (Figure 8.2g-i), the eddy next to the surface of the sulcus (denoted by the red arrow in h) grows with Re_M. Similar behavior can also be observed for the row of images at $\theta = 30°$ (Figure 8.2d-f); although, the eddy, if present, is so small that it cannot be discerned in Figure 8.2d. The eddy at the bottom of the images, marked with the blue arrows in Figure 8.2e and h, also appears to grow with oscillation frequency at $\theta = 30°$ and 45°. The particle pathlines in the rotating region in the upper right-hand corner (marked with the black arrow in Figure 8.2h) change drastically as Re_M increases. At $Re_M = 30$, the rotating region is nearly circular, but it elongates as the Reynolds number increases. At $Re_M = 90$, the region scarcely appears to rotate as the flow dips towards the body. However, it is unlikely that this portion of the flow can be sensed by the macular hair cells directly. Finally, the center of the primary eddy at $\theta = 0°$ moves closer to the sulcus as the Reynolds number increases.

The steady streaming flow near the sulcus also consists of eddies if the otolith is oscillated and observed along the z-axis (dotted line shown in Figure 8.1), as shown in Figure 8.3. Again, the body orientation affects the number and extent of the rotating

regions near the body. At $\alpha = 15°$ (b), the flow changes directions 7 times along the sulcus in this image, while at $\alpha = 0°$ (a) the flow has essentially one rotating region (there may also be some additional very small eddies near the bottom of the image along the body). These rotating regions appear to mimic the bumps and grooves on the sulcus.

The amplitude of oscillation affects the flow patterns in the bulk of the flow only slightly and has a minor impact on the patterns near the body surface. A comparison of the particle pathlines shown in Figure 8.4 at $\varepsilon = 0.025$ (a) and 0.05 (b) at $Re_M = 80$ suggests that although the pathlines are qualitatively very similar (neglecting the change in the length of the particle pathlines associated with the increase in streaming speeds), there are some minor differences between the images. In particular as the amplitude of oscillation increases, the upper rotating region goes from a "c-shaped" pattern with an undefined center to a pattern with a small, but complete, circular rotation path.

Figure 8.5 shows the flow patterns for $Re_M = 90$ and $\varepsilon = 0.05$ at two different z-positions denoted by the solid (a) and dashed (b) lines are shown in Figure 8.1. The variations in the flow pattern are relatively small and are comparable to the variations associated with changes in the oscillation amplitude, suggesting that the steady streaming flow patterns in the center of the sulcus are nearly independent of z-position.

In summary, the visualizations of the steady streaming flows around the magnified cod otolith demonstrate that the flow patterns encode information about the oscillation parameters. The shape and the extent of the rotating eddies are clearly a strong function of the frequency of the oscillation, while the number and location of the surface stagnation points are determined by the orientation of the body (and hence the oscillation direction). The flow patterns are, however, not significantly affected by the amplitude of the oscillation (although the amplitude is related to the flow speeds). These observations are in qualitative agreement with those for the steady streaming flow patterns around (ungrooved and grooved) spheroids.

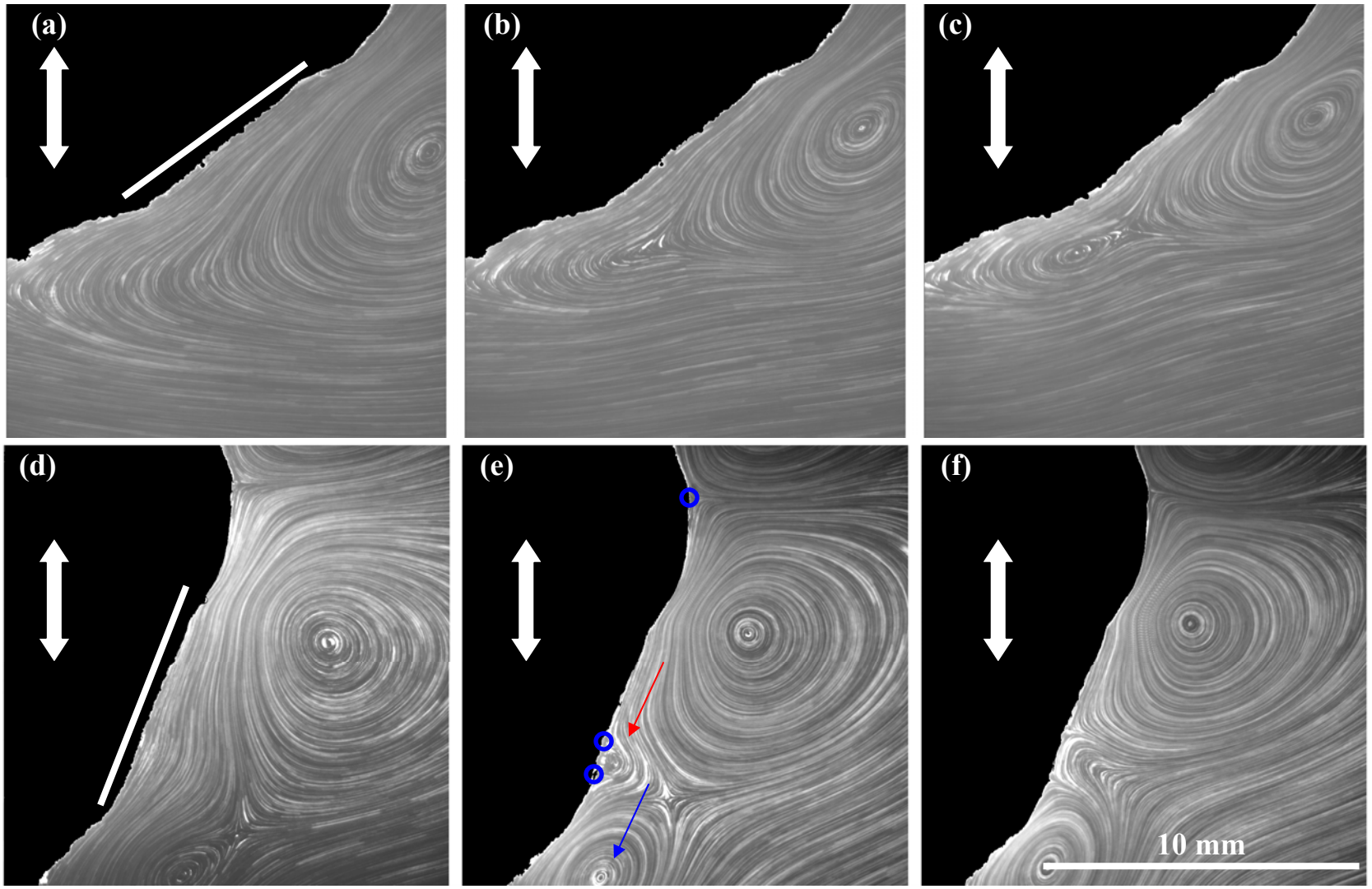

Figure 8.2 Particle pathlines near the model cod otolith oriented along the solid line at $\theta = 0°$ (a, b, c), 30° (d, e, f), 45° (g, h, i), and 75° (j, k, l), oscillating at $Re_M = 30$ (a, d, g, j), 60 (b, e, h, k), and 90 (c, f, i, l) and $\varepsilon = 0.05$. Images show 200 oscillations.

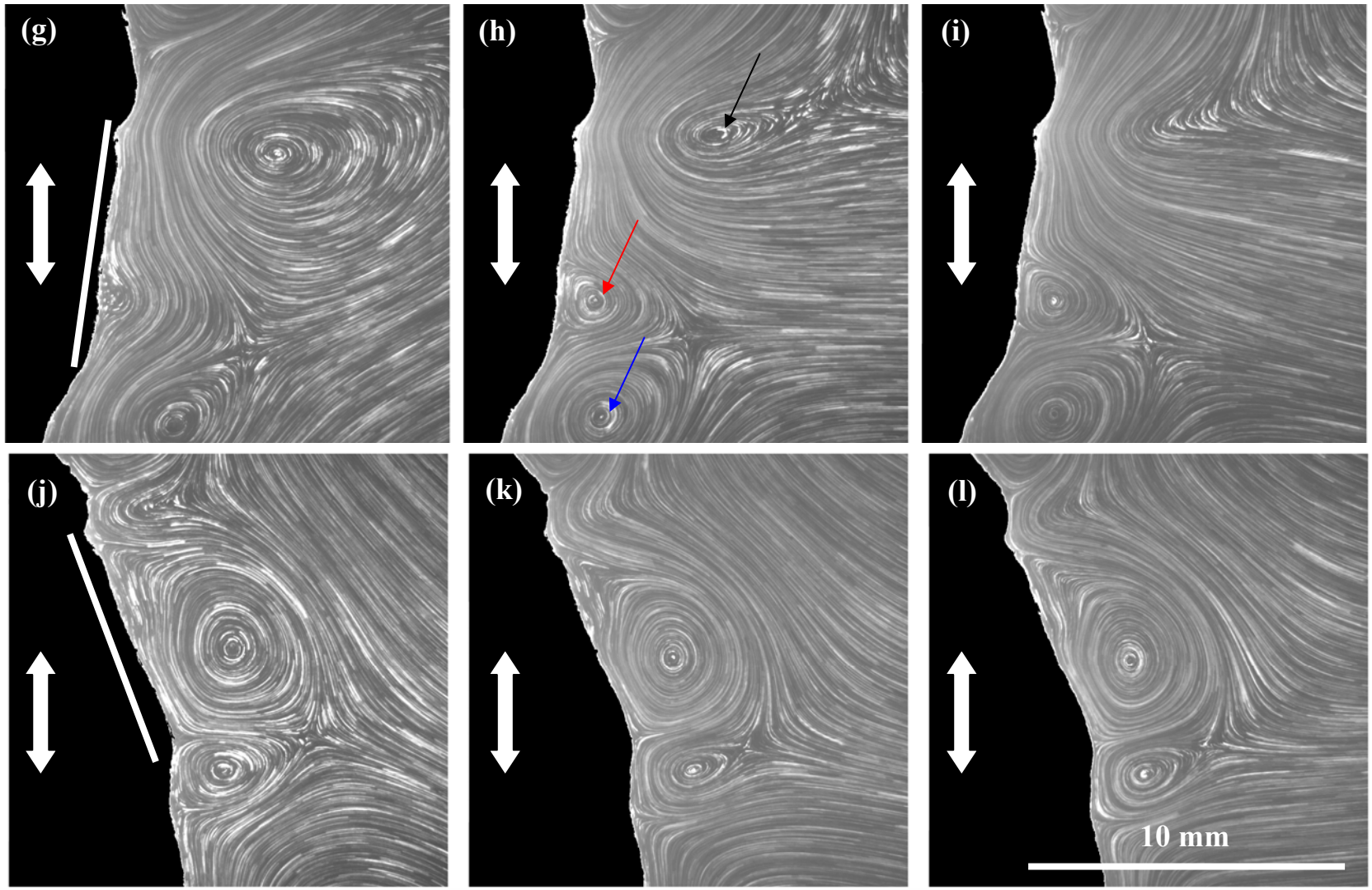

Figure 8.2 (continued).

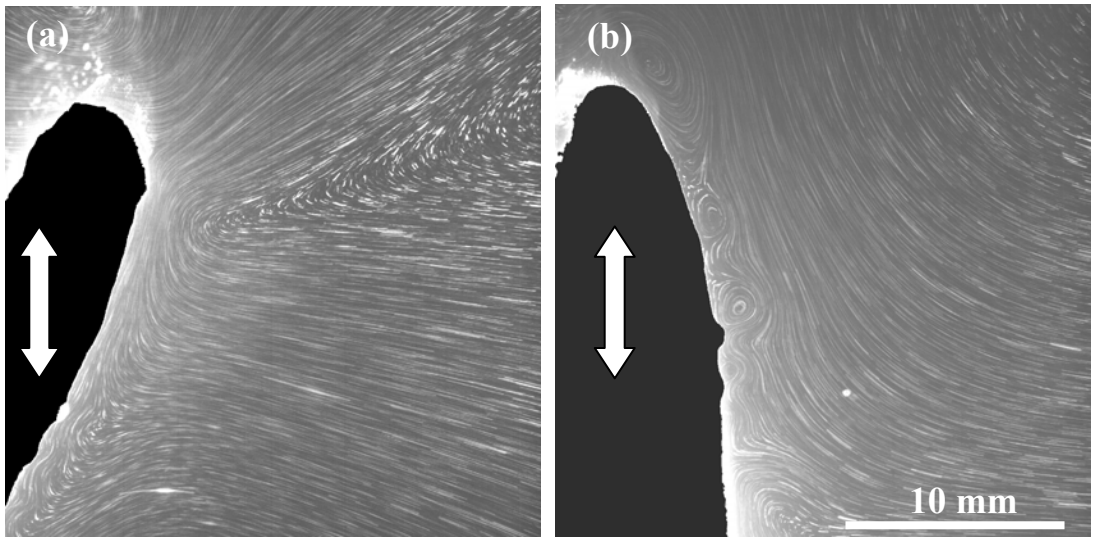

Figure 8.3 Particle pathlines near the model cod otolith oriented along the dotted line at $\alpha = 0°$ (a) and 15° (b) and oscillating at $Re_M = 90$ and $\varepsilon = 0.05$. Images show 400 oscilations.

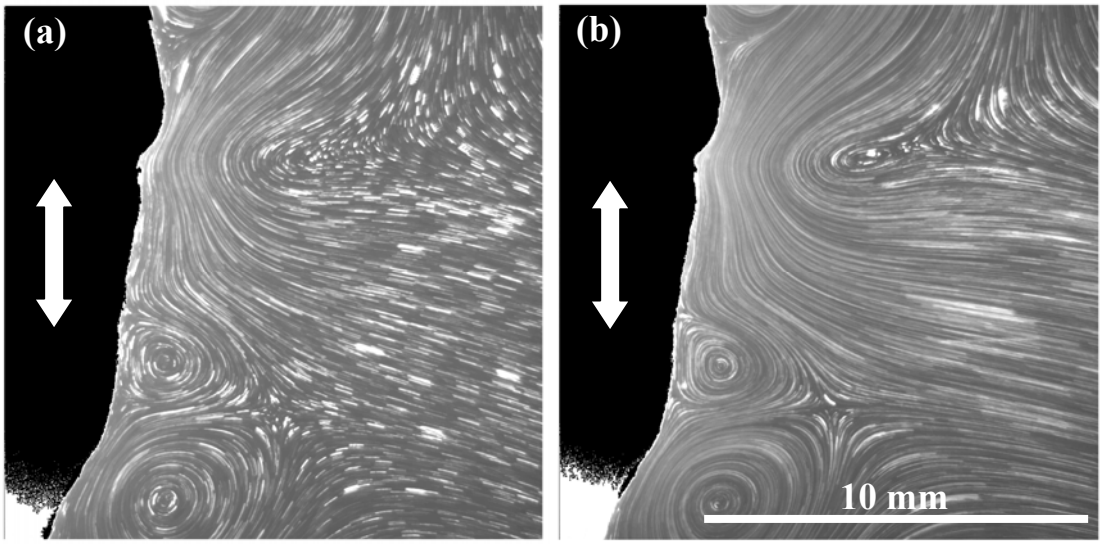

Figure 8.4 Particle pathlines representing 200 oscillations around a model otolith oscillating at ε = 0.025 (a) and 0.05 (b) at Re_M = 79 and θ = 45°.

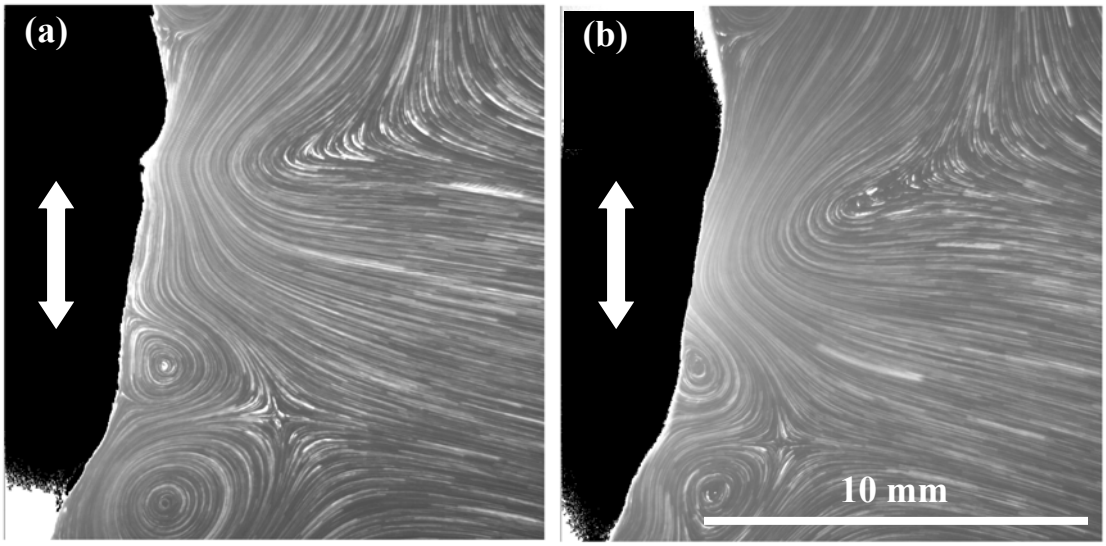

Figure 8.5 Particle pathlines representing 200 oscillations around a model otolith with the images taken at the solid line (a) and the dashed line (b) of Figure 8.1. The model otolith is oscillating at ε = 0.05, Re_M = 85, and θ = 45°.

8.2 Velocity Fields

The steady streaming flow velocities near the model otolith were measured using PIV. Figure 8.6 gives typical velocity vector plots at $Re_M = 60$ and $\varepsilon = 0.05$ for $\theta = 0°$ (a), 30° (b), 45° (c), and 75° (d), corresponding to the particle pathlines shown in Figure 8.2(b, e, h, k). (As noted in Figure 8.1, the oscillation is always along the y-axis, which points downward, while the x-axis points away from the body. However, the axes are not fixed to the body, and are defined such that $(x,y) = (0,0)$ corresponds to the upper left corner of the image. This is different than the spheroidal cases where $(x,y) = (0,0)$ represented the center of the body, regardless of the field of view of the camera.) The maximum speed obtained with PIV in each image varied from about 10% to 60% of $V_s = \varepsilon \omega s$. A plot of the maximum speed as a function of the Reynolds number is shown in Figure 8.7. Different orientations, θ, are denoted by different symbols, while the filled and open symbols denote data obtained along the planes corresponding to the "solid" and "dashed" lines, respectively, of Figure 8.1. Identical symbols at a given Reynolds number represent cases obtained at different ε; for the most part, the scaling appears to "remove" oscillation amplitude effects, giving maximum scaled speeds within 4% (with a standard deviation of 6%) for cases obtained at different ε values. The maximum speed is greater along the plane corresponding to the solid line near the center of the sulcus (filled symbols) than that along the plane corresponding to the dashed line (open symbols), except at $\theta = 75°$. In general, the normalized maximum speed increases with Reynolds number for a given orientation and location near the sulcus. The normalized speed also appears to decreases as θ increases.

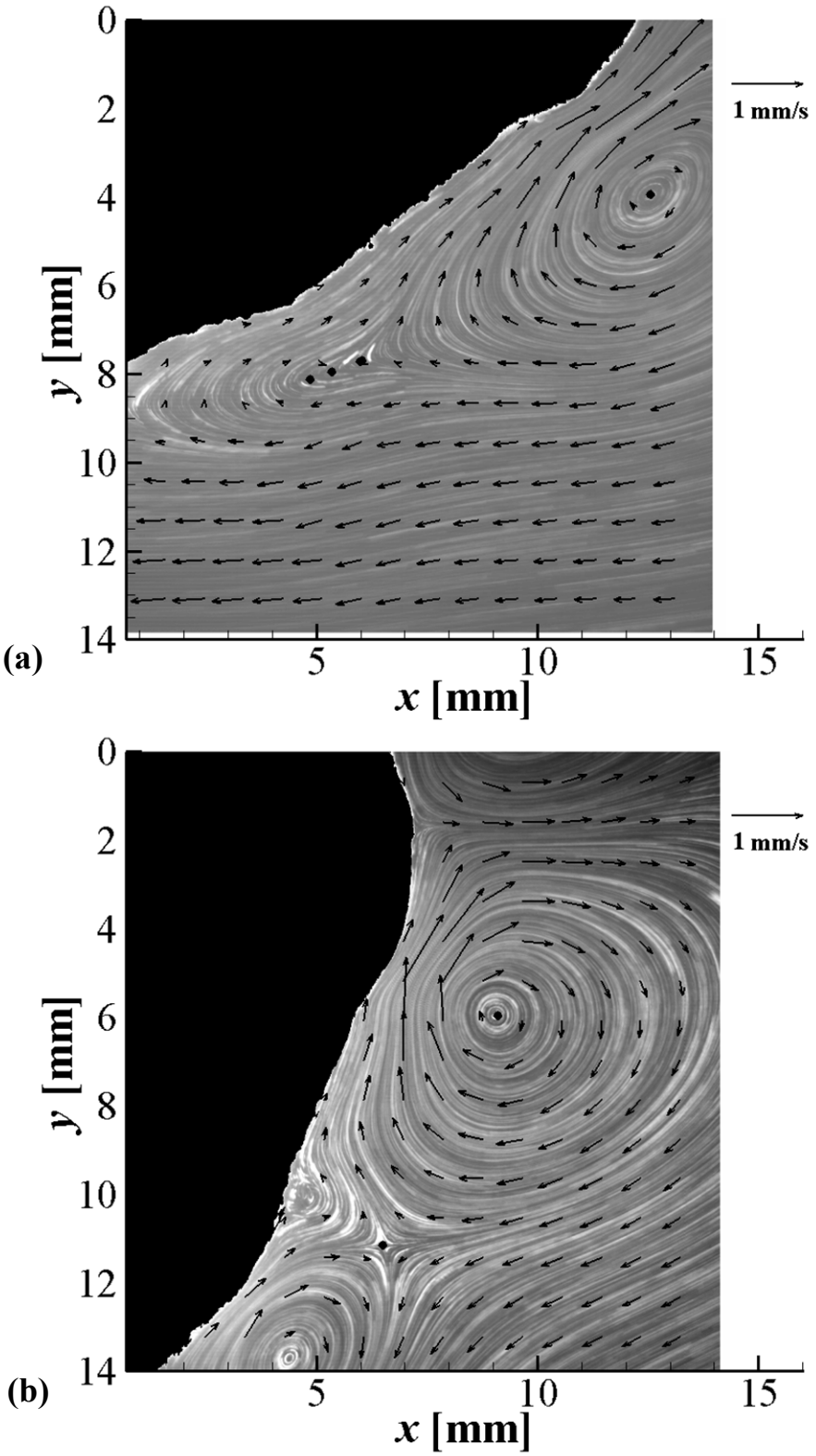

Figure 8.6 Velocity vectors for $Re_M = 60$ and $\varepsilon = 0.05$ for $\theta = 0°$ (a), 30° (b), 45° (c), and 75° (d). The oscillation is along the y-axis. Black circles denote stagnation points. Every other vector omitted for clarity.

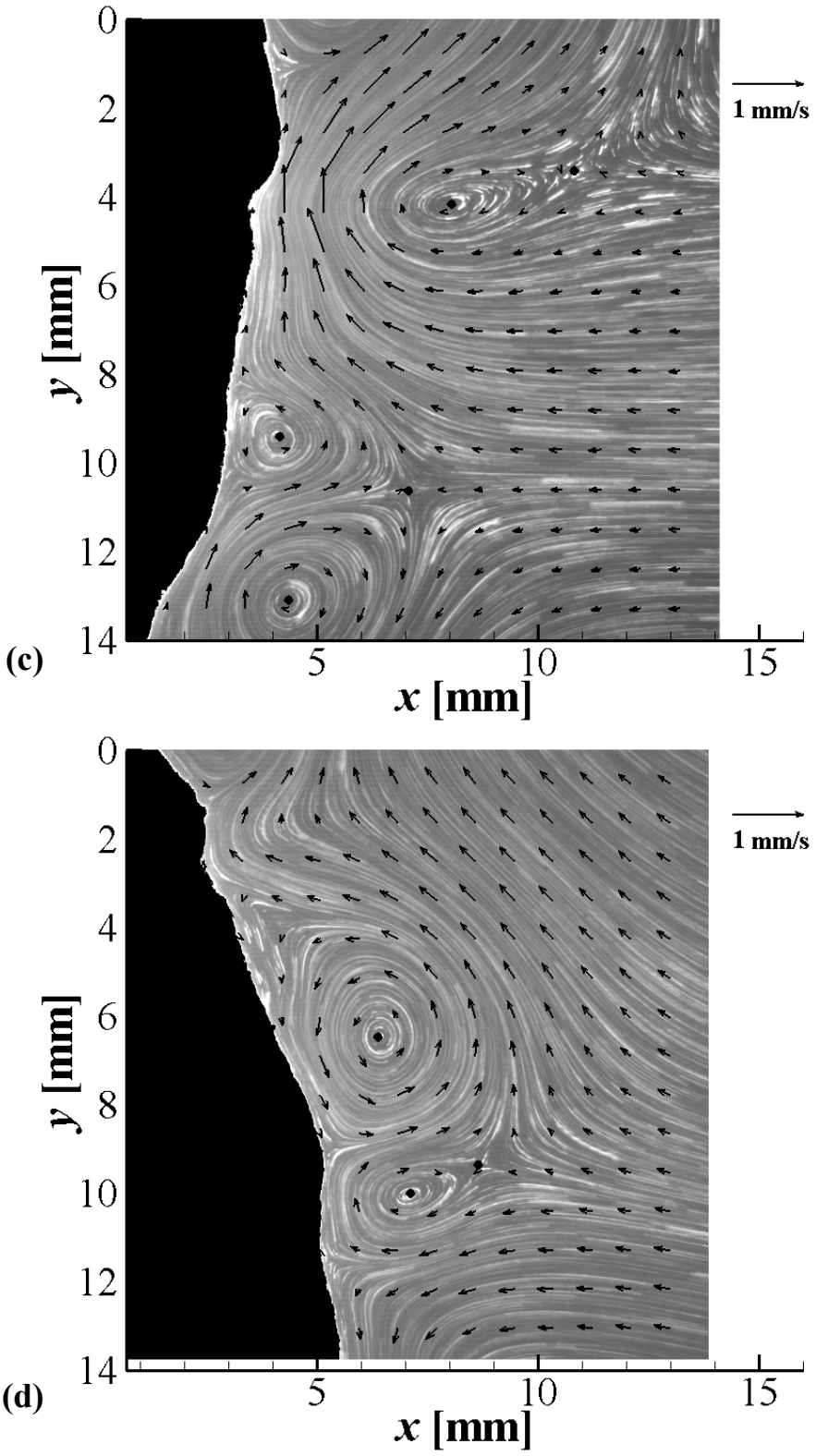

Figure 8.6 (continued).

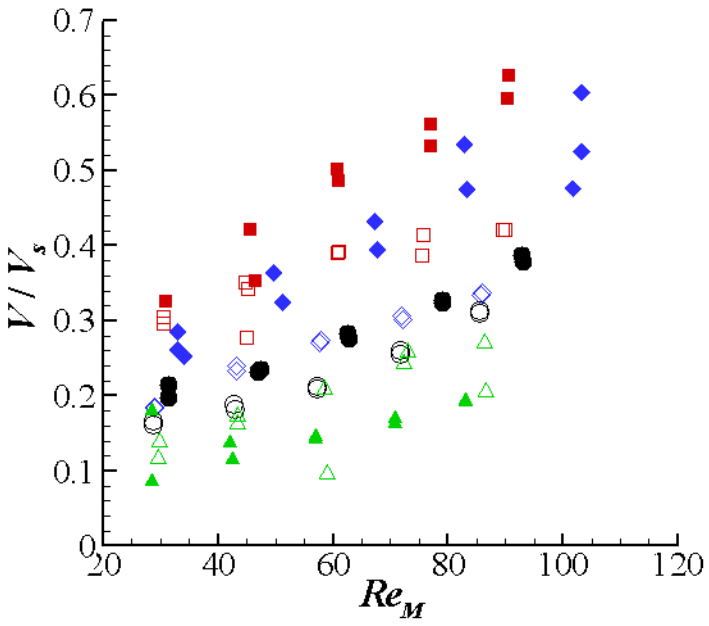

Figure 8.7 Maximum scaled streaming flow speed as a function of Reynolds number for $\theta = 0°$ (*square*), 30° (*diamond*), 45° (*circle*) and 75° (*triangle*). Filled and open symbols represent data taken along the "solid" and "dashed" lines of Figure 8.1, respectively.

8.3 Vorticity Fields

Contour plots of the vorticity calculated from the PIV data for several typical cases are shown in Figure 8.8 at $Re_M = 60$ and $\varepsilon = 0.05$ for $\theta = 0°$ (a), 30° (b), 45° (c), and 75° (d); these cases correspond to the cases shown in Figure 8.6. The axes are defined as in Figure 8.1, so the vorticity is positive in the clockwise direction because the z-axis is going into the page. The largest vorticity magnitudes are observed near the bumps on the sulcus surface, much like the tips of the grooved spheroids in Chapter 7. Moving downwards (along the positive y-direction) from the protrusion in the upper right-hand corner of Figure 8.8(a) and (b), a region of strongly negative vorticity, then a region of strongly positive vorticity, are evident.

The maximum absolute vorticity values ranged from 0.2–4.5 s^{-1} in these studies. Figure 8.9 shows the maximum absolute vorticity scaled by

$$\Omega_s = \frac{V_s}{\sqrt{\nu / \omega}} \qquad 8.1$$

using the same legend as that used in Figure 8.7. The maximum scaled vorticity values (like those for the maximum velocity) are greater in the plane near the center of the otolith (filled symbols, solid line in Figure 8.1) than those in the plane to the side of the otolith (open symbols, dashed line in Figure 8.1), except at $\theta = 75°$. No vorticity results are presented for the data taken along the plane denoted by the dashed line at $\theta = 0°$ because the maximum vorticity occurred at a location beyond the field of view of the image. Although results are presented at different ε under otherwise identical conditions using the same symbols, the results at $\theta = 45°$ (black filled circles) suggest that the scaling used here for the maximum vorticity magnitude is not as effective at "removing" the effects of oscillation amplitude as the scaling used for the maximum velocity magnitudes. For the $\theta = 45°$ case, the maximum scaled vorticity values appear to increase with ε, especially at higher Re_M. In general, the normalized maximum vorticity increases with Reynolds number for a given orientation and location near the sulcus. The trends for the normalized vorticity with changing orientation are much less clear; although the vorticity appears to increase slightly with θ up to $\theta = 45°$, the scaled values at $\theta = 75°$ are much less than those at $\theta = 45°$.

The vorticity values presented here are estimated, as in the previous chapters, from velocity vectors obtained over interrogation regions 16 pixels square. Since the interrogation regions are spaced 32 pixels apart, the velocity derivatives are then obtained using central differencing over two grid squares, or over a 64 pixels square region. Given that central differencing is effectively equivalent to a weighted convolution over this region, it is very likely that the vorticity values presented here underestimate the true vorticity values.

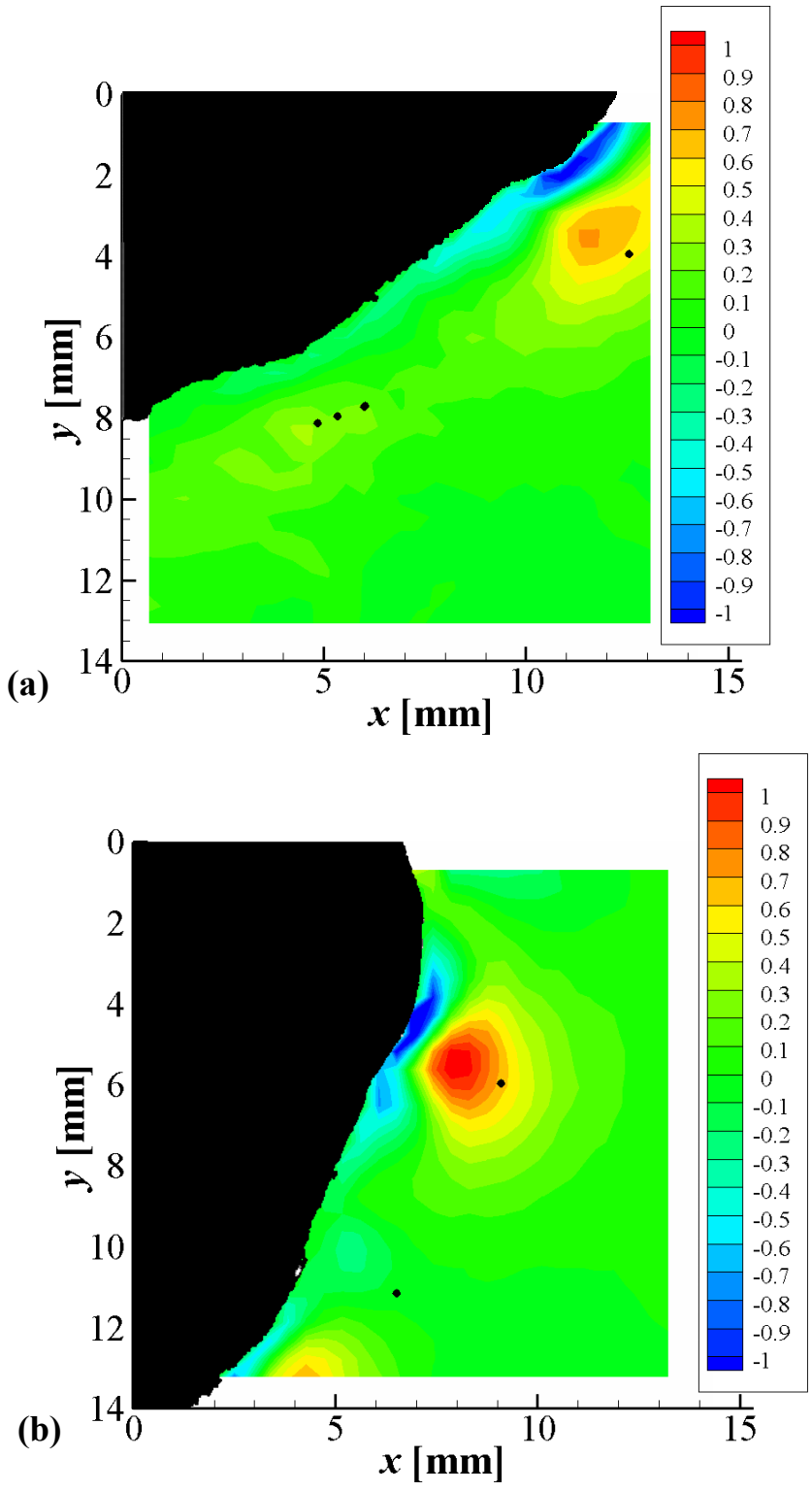

Figure 8.8 Unscaled vorticity contours of the flow near model otolith (units of s^{-1}) for $Re_M = 60$ and $\varepsilon = 0.05$ for $\theta = 0°$ (a), 30° (b), 45° (c), and 75° (d). Filled black circles represent stagnation point locations. The bodies are all oscillated along the vertical.

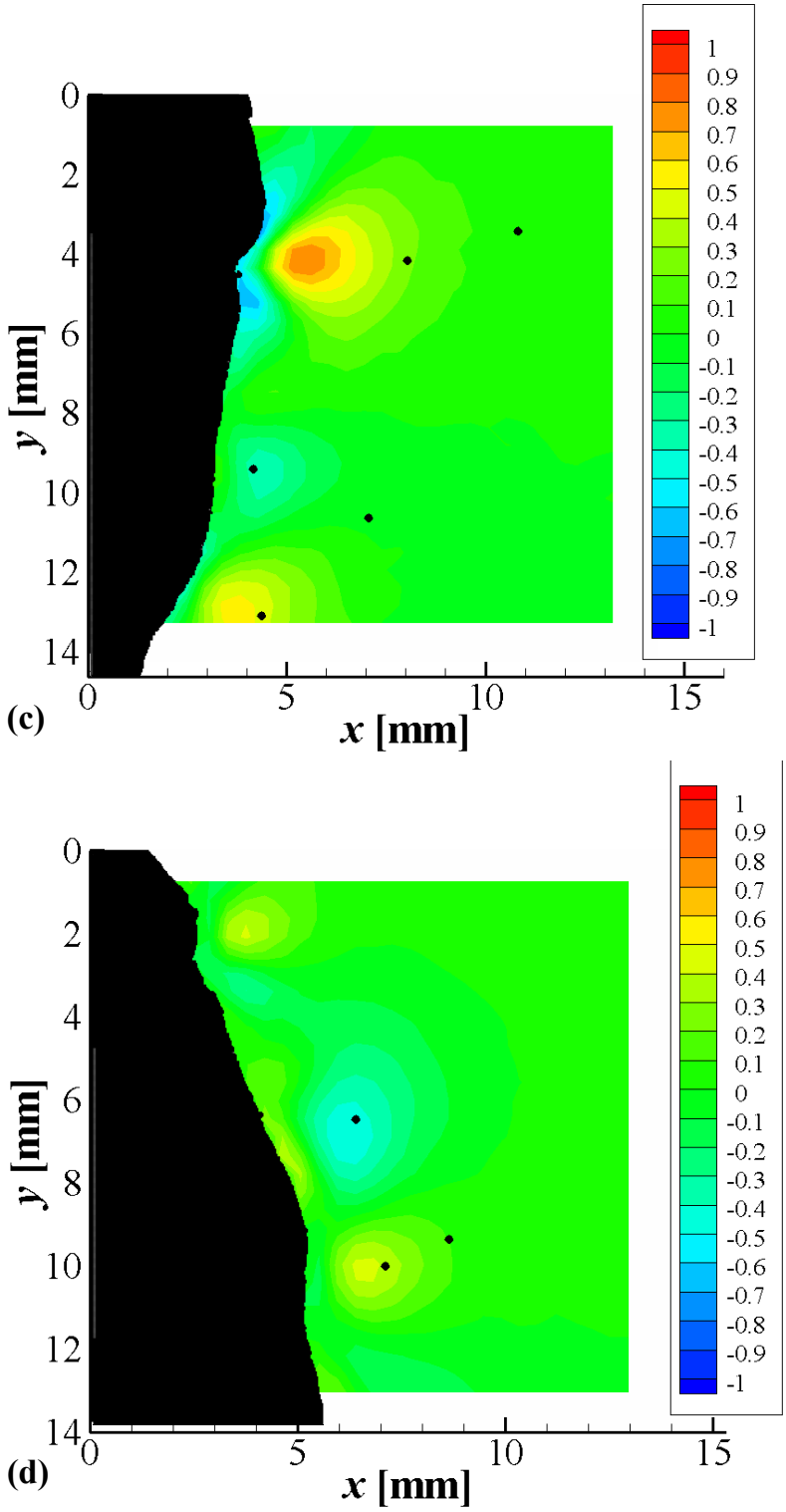

Figure 8.8 (continued).

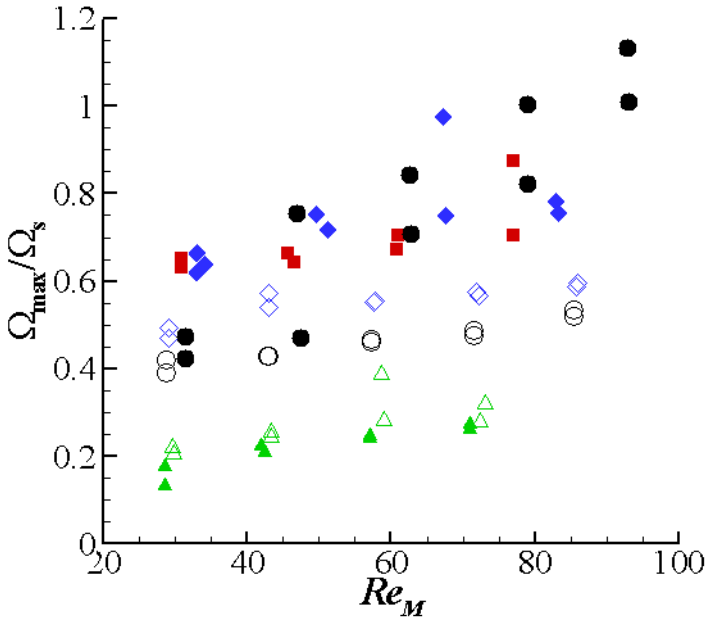

Figure 8.9 Maximum scaled absolute value of the vorticity as a function of Reynolds number for $\theta = 0°$ (*square*), 30° (*diamond*), 45° (*circle*) and 75° (*triangle*). Filled and open symbols represent data taken along the planes corresponding to the "solid" and "dashed" lines of Figure 8.1, respectively.

8.4 Stagnation Point Locations

The PIV data were used to estimate the stagnation point positions along the surface of the sulcus. As discussed previously, both the number and positions of the stagnation points vary with otolith orientation. As can be seen in Figure 8.2, the number of stagnation points that can be detected by the macular hair cells on the surface of the sulcus increases from 0 at $\theta = 0°$ to 2 at $\theta = 30°$ and 45°, then decreases to 0 at $\theta = 75°$. The Reynolds number also appears to have an effect on the stagnation point locations, particularly at $\theta = 30°$ and 45° [Figure 8.2 (d-f) and (g-i), respectively], where a rotating region appears to grow "outwards" from the body as the Reynolds number increases.

For the ungrooved angled spheroids (Chapter 6), it was observed that a stagnation point occurred to the side of the body near the locations where the body was essentially parallel to the axis of oscillation. For the model otolith, several of the cases are also

observed to have stagnation points when the body is essentially parallel to the direction of motion, *e.g.* in the $\theta = 75°$ case. Although this trend does not hold for all of the orientations (for instance, the $\theta = 45°$ does not have a stagnation point in one of its grooves), the presence of the grooves and bumps does appear to increase the number of stagnation points along the sulcus and affect their locations.

8.5 Implications for Fish Hearing

8.5.1 Surrounding Tissue Modeled as a Single Fluid

The oscillating otolith produces complex steady streaming flow patterns that encode acoustic information on the frequency and orientation (and, to a limited extent, the amplitude) of the incident sound that could be useful to fish. In particular, the variations in stagnation point location and flow direction with orientation of the otolith (and hence the direction of oscillation) could provide a way for fish to directionalize incident sound waves.

To visualize the effects of the steady streaming flow, consider the array of "pseudo-hair cells" depicted in Figure 8.10. The array of lines adjacent to the sulcus represent the cilia on each hair cell, with the lines ending in circles representing hair cells oriented with their primary excitation axis towards the top of the image and the lines ending in diamonds representing hair cells oriented with their primary excitation axis towards the bottom of the image. (It should be noted that the hair cell cilia scaled to the size of the model otolith would be about 2 pixels long in the original 1008×1000 pixel image, far smaller than length of the pseudo-hair cells shown.) The tilting of the "pseudo-hair cells" reflects their expected displacement by the streaming flow (only the mean displacement of the hair cells is shown here, since the hair cells would also be oscillating with the acoustic particle motion). In Figure 8.10(a) the "circle" hair cells are excited by the streaming flows while the uppermost and bottom three "diamond" hair

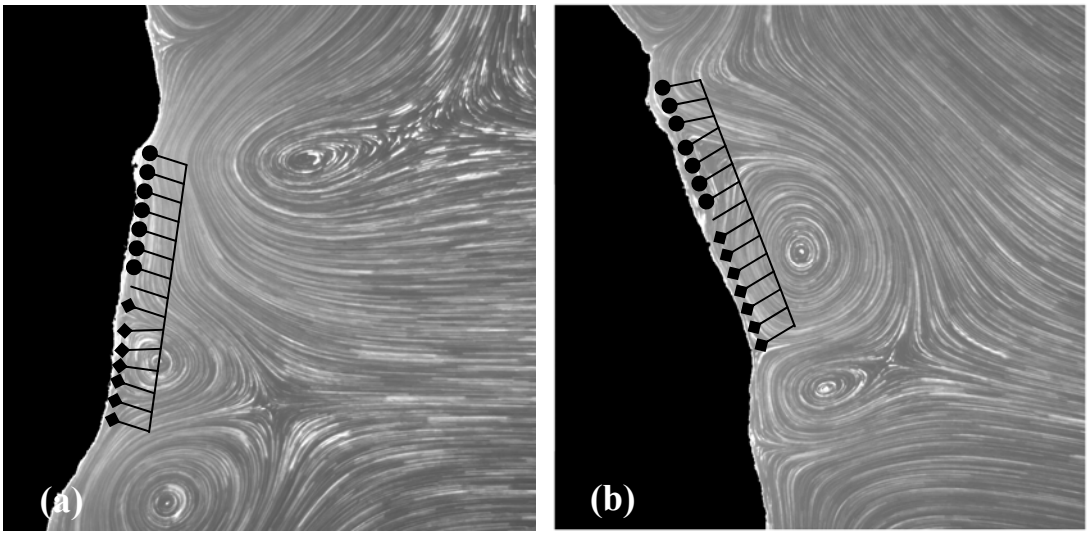

Figure 8.10 Illustration of hair cell motions using particle pathlines near the model cod otolith oriented along the solid line of Figure 8.1 at $\theta = 45°$ (a) and 75° (b), oscillating at $Re_M = 60$ and $\varepsilon = 0.05$. Images show 200 oscillations.

cells are inhibited. The pattern changes at $\theta = 75°$ in Figure 8.10(b), where most of the flow is moving "down" the sulcus, which excites all the "diamond" hair cells, as well as the top three circle hair cells. Obviously, these streaming patterns (over many oscillations) will produce relatively large changes at the level of the hair cells. If the ear is sensitive enough to sense these patterns, they contain a wealth of information about the oscillation characteristics, and hence the sound driving this oscillation. The most important remaining question is then, *are these flows sensible to the fish ear?*

Appendix F discusses a model of the fish ear based on the finite density of the otolith and the accelerometer-like response of the audiogram which suggests that the actual displacement at the tip of the hair cell cilia is less than the acoustic particle displacement by a factor of

$$\left(\frac{S.G.-1}{S.G.+0.5}\right)\left(\frac{f}{f_n}\right)^2 \qquad 8.2$$

which, for an otolithic specific gravity ($S.G.$) of 3, results in a factor of $O(10^{-2})$ for a

natural frequency (f_n) of 1 kHz and $O(10^{-4})$ for a natural frequency of 10 kHz. If this model is correct, the cod ear, which can hear sounds with particle displacements of $O(10^{-11}$ m) at 100 Hz, would actually have hair cells that are able to distinguish tip displacements as small as $O(10^{-13}$–10^{-15} m), or in terms of the angular displacement of a 10 μm hair cell, 10^{-8}–10^{-10} rad = 10^{-6}–10^{-8}°. It should be emphasized that the individual hair cells are unlikely to be responding to such small motions, but that (under this model) the ensemble of $O(10^5$–$10^6)$ hair cells need to sense motions of this order of magnitude to detect sounds (though fewer would be available to discriminate spatial features).

The relative motion between the otolith and the (fluid-like) surroundings is less than the acoustic particle motion by a factor of

$$\left(\frac{S.G.-1}{S.G.+0.5}\right) \tag{8.3}$$

due to the finite inertia of the body. This means that the estimate of the otolith displacement relative to its surroundings is not the acoustic particle motion, but is instead 60% of the acoustic particle motion (for an otolith *S.G.* of 3). In addition, the acoustically induced streaming motions are unlikely to explain how fish hear at their threshold, but they may play a role in how fish directionalize sound. Evidence suggests that in order for sounds to be directionalized they need to be at least 6 dB above threshold; in other words, the sound needs to have an amplitude that is twice the acoustic particle motion at threshold in order to be directionalized (Schuijf 1975).

The deflection of the hair cell cilia due to the steady streaming flows can be estimated from the streaming patterns observed near the otolithic body. Since the 350% model was assumed to have a length scale of 1 cm, the cod's length scale should be 2.9 mm, assuming that the length scale of the body scales linearly. However, as mentioned in Chapter 4, it is difficult to determine the Reynolds number for these flows because there is very little data on the viscosities of viscoelastic soft tissue in general, and particularly that surrounding the otolith (Chen *et al.* 2004). Considering that viscosity

estimates of human muscle tissue are on the order of 150 P for frequencies of 500–5000 Hz (Oestreicher 1951), this section will assume that the viscosity of the tissue surrounding the otolith is close to the larger of the viscosity measurements mentioned in Chapter 2, namely 4.5 P (de Vries 1951). This means that the flows in the ear of a cod, which typically hear sounds from about 50–500 Hz, have Re_M of about 30–300, assuming that the density of the surrounding fluid is 1 g/cm^3. Because this range is similar to that of the experimental studies presented here, typical experimental values for the streaming velocity are assumed to represent typical values within the fish ear.

Assuming that the hair cell cilia deflection can be estimated by the shear rate of the fluid near the near the body, $\dot{\gamma}$, the relative speed between the body and the base of the hair cell is given by

$$\dot{\gamma} l_{cilia} \approx \frac{\partial v}{\partial s} l_{cilia} \qquad 8.4$$

where s is the spatial coordinate measured along the sulcus (*i.e.*, the z-axis), v is the z-component of the velocity, and $l_{cilia} \approx 10$ μm is the length of the cilia. The sulcus was approximated by a line and the velocity component was found by projecting the velocity vectors in the direction of the line. Estimates from the experimental data give $\dot{\gamma} = 0.2$–$8\ \varepsilon^2\omega$. For example, at $\theta = 45°$, $Re_M = 60$ and $\varepsilon = 0.05$, $v \approx 0.055$ mm/s about 0.2 mm from the body. These values give $\dot{\gamma} = 0.2$ Hz^{-1}, corresponding to a normalized shear of $0.9\ \varepsilon^2\omega$. The shear rate is mainly a function of the oscillation direction and Re_M, and it is nearly independent of the oscillation amplitude. In most cases, $\dot{\gamma} < 4\ \varepsilon^2\omega$ and increases with Re_M.

In order to relate these displacements to those inside the fish ear, recall that a cod can hear acoustic particle displacements of 10^{-11} m at 100 Hz, corresponding to a relative motion of 6×10^{-12} m, and a "directional" sound amplitude of 1.2×10^{-11} m. If the fish ear experiences shear rates similar to those observed in these experiments, the steady

streaming motions would produce maximum tip deflections of

$$4\varepsilon^2\omega l_{cilia} = 4\left(\frac{1.2\times10^{-11}\ \text{m}}{2.9\times10^{-3}\ \text{m}}\right)^2 (2\pi 100\ \text{rad/s})\left(10\times10^{-6}\ \text{m}\right) = 4\times10^{-19}\ \text{m/s}. \qquad 8.5$$

For goldfish, hearing improves with signal length up to about 400 ms (Popper *et al.* 2003), implying that the temporal filters are no longer than a few hundred ms. This means that the fish ear would need to be able to detect displacements on the order of 2×10^{-19} m in order for this streaming to be sensible. Hence this streaming velocity is too small to be of practical use in fish hearing, even considering the improved estimates of fish ear sensitivity given above.

Alternatively, one could ask the question, *how strong would the sound need to be in order to produce a sensible streaming flow?* Assuming that a 100 Hz sound pulse 200 ms long needs to displace the tip of the hair cell 10^{-13} m, the required relative motion between the otolith and its surroundings is:

$$\left(\frac{\frac{10^{-13}\ \text{m}}{0.2\ \text{s}}L^2}{4\omega l_{cilia}}\right)^{\frac{1}{2}} = 1\times10^{-8}\ \text{m} \qquad 8.6$$

which is 60% less than the acoustic particle motion of the surroundings (2×10^{-8} m). The rms pressure is then 14 Pa, or 143 dB re 1 μPa. Although this is a loud underwater sound, it is still within the range of sounds experienced by fish in their natural environment Many species of whales produce sounds in this range, such as the gray whale whose 20–1200 Hz moans have been recorded at 185 dB re 1 μPa at 1 m (Thomson and Richardson 1995). If the fish ear can detect displacements of 10^{-15} m, then the required rms pressure would be 1 Pa or 123 dB re 1 μPa. This sound level is about 30 dB over the sea noise level at 100 Hz and could be biologically relevant considering that fish choruses have been recorded at sound levels of about 150 dB re 1 μPa at 1 m (McCauley and Cato 2000). For persperctive, in deep water where sound may be

assumed to decrease in intensity following spherical spreading, a fish capable of hearing 143 dB re 1 μPa (or 123 dB re 1 μPa) would be able to detect the 150 dB re 1 μPa fish chorus 2.2 m (or 22 m) away.

Streaming flows inside of the fish ear could, however, explain how cod detect ultrasound. Cod are able to hear ultrasonic frequencies on the order of 194 dB re 1 μPa at 38 kHz (Astrup and Møhl 1993), which results in an acoustic particle displacement amplitude of 1×10^{-7} m and a relative motion between the otolith and its surroundings of 6×10^{-8} m. Based on the analysis presented previously, the cilia's tip velocity is then 4×10^{-9} m/s. This streaming velocity should be sensible to the fish ear. In fact, if the hair cells are able to detect streaming motions of $O(10^{-13}$ m), then the sound pulse would only need to be 20 μs long to be sensible. Considering that dolphin echolocation clicks are typically between 40 and 600 μs in length (Akamatsu *et al.* 1998), such sensitivity would provide a biological advantage. However, the data for cod were acquired with 3 ms pulses (Astrup and Møhl 1993), which implies that if this model is correct, the cod should have responded to much lower intensity levels. The most likely explanation for the discrepancy is that the steady streaming analysis discussed above does not apply at the ultrasonic Reynolds numbers ($Re_M = 4\times10^3$, $Re_s = 3\times10^{-6}$). Steady streaming may explain how cod hear ultrasound, but the predicted streaming velocities discussed in this chapter were designed for lower Reynolds numbers and are not directly applicable to the ultrasonic case. It should also be noted that the Stokes layer is only 40 μm thick at this frequency, suggesting that the hair cells sample a significant portion of the inner region of the streaming flow, which may decrease the shearing forces on the cilia.

8.5.2 Surrounding Tissue Modeled as Two Fluids

The presence of lower-viscosity endolymph near the otolith could greatly affect the shear rates due to the flow. Since the otolith is immersed in endolymph, which

permeates the otolithic membrane; a better model might have the otolith surrounded by a low viscosity fluid which is surrounded by the higher viscosity tissue, as shown in the cross-sectional view of Figure 8.11. If the endolymph is assumed to have a viscosity that is approximately that of water, namely 1 cP, then the shear will be higher in the endolymph (where the hair cells are) than in the tissue itself.

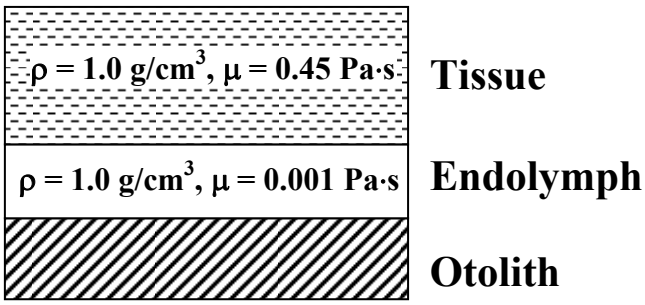

Figure 8.11 Illustration of the relationship between the tissue, endolymph, and otolith.

In order to understand the fluid behavior in the endolymph, consider the classic problem of two-fluid Couette flow, where two layers of immiscible and incompressible fluids are sandwiched between two infinite plates and driven by the motion of the upper plate, which is moving to the right at a constant speed U_0, as shown in Figure 8.12. The problem is defined in Cartesian coordinates, with the spatial coordinates and corresponding velocity components of (x,y) and (u,v), respectively. It is assumed that there is no flow in the z-direction normal to the page and that all the flow parameters are independent of the z-coordinate. The endolymph and tissue are denoted by the subscripts 1 and 2, respectively. The shear stresses must be continous across the endolymph-tissue interface, which gives the boundary condition:

$$\mu_1 \left.\frac{\partial u_1}{\partial y}\right|_{y=h_1} = \mu_2 \left.\frac{\partial u_2}{\partial y}\right|_{y=h_1} \qquad 8.7$$

where μ_i is the dynamic viscosity. At the endolymph-tissue interface and the interfaces between the endolymph and the top plate and the tissue and the bottom plate, the velocity tangential to the interface must be continuous to ensure that there is "no-slip" across these three interfaces. Assuming that the flow is fully developed along the *x*-direction (because the plates have a large *x*-dimension), the velocity is independent of *x*. The incompressible Continuity Equation then becomes:

$$\frac{\partial v_i}{\partial y} = 0 \tag{8.8}$$

where the subscript *i* refers to the fluids 1 and 2. As there is no flow through the top or bottom plates, $v_i(y) = 0$. The velocity in the *x*-direction is found from the momentum equation, which reduces to

$$\mu_i \frac{\partial^2 u_i}{\partial y^2} = 0 \tag{8.9}$$

The solution for the flow between the plates is linear, and of the form:

$$\begin{aligned} u_1 &= Ay + B \\ u_2 &= Cy + D \end{aligned} \tag{8.10}$$

Applying the boundary conditions to solve for the constants A, B, C and D gives:

$$\begin{aligned} u_1 &= \frac{\mu_2 U_0}{\mu_2 h_1 + \mu_1 h_2} y \\ u_2 &= \frac{\mu_1 U_0}{\mu_2 h_1 + \mu_1 h_2}\left(y - h_1 - h_2\right) + U_0 \end{aligned} \tag{8.11}$$

From this solution, it is clear that slopes of the linear velocity profiles are related by

$$\mu_1 \frac{\partial u_1}{\partial y} = \mu_2 \frac{\partial u_2}{\partial y} \tag{8.12}$$

or, by the ratio of their dynamic viscosities. If the lower viscosity fluid was not present, the velocity would change linearly from 0 to U_0 over the fluid between the plates.

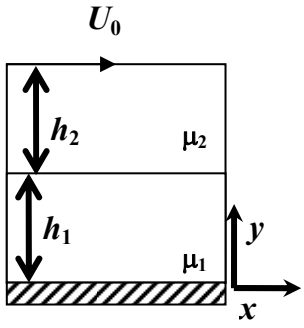

$$\frac{\partial}{\partial x} = \frac{\partial}{\partial t} = 0$$

Boundary Conditions:

$$u_2\left(h_1 + h_2\right) = U_0$$

$$u_1\left(0\right) = v_1\left(0\right) = 0$$

$$v_2\left(h_1 + h_2\right) = 0$$

$$\mu_1 \left.\frac{\partial u_1}{\partial y}\right|_{y=h_1} = \mu_2 \left.\frac{\partial u_2}{\partial y}\right|_{y=h_1}$$

$$u_1\left(h_1\right) = u_2\left(h_1\right)$$

Figure 8.12 Two layer Couette flow.

This result shows that the slope of the velocity in the endolymph will be larger than the slope of the velocity in the surrounding tissue, resulting in a higher shear rate in the endolymph. Since the hair cell cilia are deflected by this shear rate, the presence of the lower-viscosity fluid near the otolith will increase the angular deflection of the hair cells. For the steady case above, assume μ_1 = 0.01 P, μ_2 =4.5 P, h_1 = 10 μm and h_2 = 90 μm. Then, $u(h_1)$ =0.98U_0. Essentially, the tissue is more "solid-like" than the endolymph, and the fluid velocity increases linearly in y, nearly reaching its maximum value at the edge of the endolymph (*vs.* the tissue).

The velocity profile in the tissue is therefore nearly uniform. For simplicity, the tissue will be assumed to move with the maximum fluid velocity, and the velocity at the edge of the endolymph will be taken to be the maximum streaming velocity. If the depth of the endolymph layer is comparable to the length of the hair cell cilia, the maximum shear seen by the hair cells can then be approximated by

$$\frac{U_{max}}{l_{cilia}} \qquad 8.13$$

For cases studied here, the maximum streaming velocity was approximately 0.6εω*s* and

the length of the cilia is assumed to be on the order of 10 μm. For a cod listening to $O(10^{-11}$ m) particle displacements at 100 Hz, this gives a maximum shear of 8×10^{-13} s^{-1}. If the cod is capable of discriminating displacements of 10^{-8} rad, then it would require a continuous sound lasting 200 min, or over 3 h, to produce a noticeable streaming flow. However, if the cod can sense 10^{-10} rad, the sound pulse would only need to be 2 min long. As the sound would need to be detected in less than a second, this is still at least two orders of magnitude too long to be useful within the fish ear.

For completeness, the sound pressure level for a sensible displacement should also be considered for this two-fluid model. Here, in order to produce a 10^{-8} rad displacement, a 100 Hz, 200 ms sound would need to have an amplitude of

$$\left(\frac{\left(\frac{10^{-8}}{0.2} \right) l_{cilia} L}{0.6\omega} \right)^{\frac{1}{2}} = 2\times10^{-9} \text{ m}$$

or a rms pressure of 1.3 Pa (122 dB re 1 μPa). For a 10^{-10} rad displacement, the rms sound level would be 102 dB re 1 μPa. Both of these sound pressure levels are found in nature from biological sources.

The two-fluid model incorporating a layer of lower-viscosity endolymph increases the shear rate experienced by the hair cells compared with the model for the single layer of tissue. Nevertheless, the estimates from this model suggest that the streaming flow displacements are still too weak to be responsible for the fish ear's abilities at threshold levels for normal sound frequencies (less than 600 Hz for cod). However, steady streaming flows could be strong enough to be sensible at levels that are found in nature. Steady streaming could lead to sound being distorted within the fish ear, or to hair cells being deflected far enough to cause damage. At ultrasonic frequencies, the lower viscosity endolymph would have a Stokes layer thickness of only 2 μm, which

is less than the length of typical hair cell kinocilia. If the hair cells are not contained within the Stokes layer, the hair cells may not be displaced in a consistent direction by the streaming flows. Since most of the data in this thesis are only valid in the inner region, it is unclear if these results are applicable to steady streaming flows created by ultrasound.

CHAPTER 9

CONCLUSIONS

9.1 Summary of Results

This thesis has studied the characteristics of steady streaming flows and their possible applications to fish hearing. Over the course of the experimental studies, it was found that steady streaming flows contain information about the parameters of the oscillation that drives such flows. These parameters—namely the oscillation frequency and direction—are acoustically relevant and could be used by fish to determine, for example, the direction of incident sounds. However, these flows are generally very weak, and unless the hair cells of the fish ear are far more sensitive than is currently believed, it is unlikely that fish can sense the extremely small displacements due to these flows. For this reason, it is unlikely that steady streaming flows form the flow patterns that the auditory retina hypothesis would require inside of the fish ear.

These experiments have shown that the characteristics of steady streaming flows near a sinusoidally oscillating body are functions of the oscillation frequency, direction (angle), and, to a lesser extent the oscillation amplitude, as well as the geometry of the body. The oscillation frequency affects the extent of and the flows within the inner region. As shown for the oscillating spheroids, the extent, or thickness, of the inner rotating region T decreases as the frequency, or Re_M, increases. For the spheroids mounted along their axis of symmetry, this relationship was found to be (Equation 4.2)

$$\frac{T}{L} = \frac{44}{Re_M}$$

Here, the length scale, L, is equal to the equivalent radius times the aspect ratio, or (Equation 4.1)

$$L = \left(\frac{a^4}{b} \right)^{1/3}$$

where a is the half dimension of the spheroid along its axis of symmetry and b is the maximum half dimension normal to the axis of symmetry. As shown in Figure 4.8, a similar relationship is observed for the distance, h, between the center of the inner rotating regions and the surface of the oscillating body which is:

$$\frac{h}{L} \propto Re_M^{-1/2}$$

The constant of proportionality is a function of the aspect ratio of the body. The center of the rotating eddies also approach the body with increasing Reynolds number for the angled, grooved and "otolithic" geometries. Although these changes in the size of the rotating region cannot be directly sensed by the hair cells, which typically sample only a small fraction of the inner region of about one eightieth of the Stokes layer thickness at 100 Hz (assuming a viscosity of 450 cP), these changes do affect the strength of the shear and thus the deflection of the hair cell cilia.

The oscillation angle determines the location of the stagnation points on the body surface and the position of the rotating regions relative to the body. Changing the oscillation angle shifts the rotating region relative to the body and affects the extent of the rotating region. As shown in Figure 6.8, the angular shift, quantified in terms of the location of the stagnation point on the lower surface of the spheroids is given by:

$$\frac{\tan(\theta)}{\tan(\varphi)} = AR$$

where θ is the angle between the axis of oscillation and the body's axis of symmetry and φ is the angle between the body's axis of symmetry and a line from the center of the body to the on surface stagnation point. The angular shift of the on-surface stagnation point was found to be a function of both the orientation angle and the oscillation frequency for the grooved spheroids. For the model cod otolith, changing the oscillation direction

changed both the angular position and the number of eddies from essentially one very large eddy in the vicinity of the hair cells at $\theta = 0°$ to three smaller eddies at $\theta = 30–75°$, with corresponding changes in both the number and location(s) of the on-surface stagnation points between the eddies (for the otolith model the angle θ is defined as the relative angle of oscillation, with 0° the most horizontal orientation). These stagnation point locations, if sensible to the fish, may provide a means for the fish to determine the oscillation direction of incident sounds.

The rotating regions "mimic" the body geometry for the spheroid cases. In the grooved spheroid and otolith cases, the largest values of the out-of-plane component of vorticity were observed in the locations with the smallest radius of curvature.

Finally, the oscillation amplitude was found to have little if any effect on the steady streaming flow patterns. It did, however, affect the speed of the streaming flow.

This thesis also studied the steady streaming flows due to simultaneously oscillating a spheroid at two frequencies along the same direction. The streaming velocity was found to be the superposition, or sum, of the streaming velocity associated with oscillating the body at each frequency individually for these multiple frequency cases. Given the linearity of such flows at small oscillation amplitudes, it seems likely that the flow fields due to the streaming flows from two different sounds in the fish ear would also superpose.

From these experiments, it is clear that there is acoustic information encoded in the steady streaming flow patterns. If fish are able to sense it, they could use various flow characteristics to determine the properties of the sound, such as the angle of incidence based upon the locations of the on-surface stagnation points, which should be sensible to the hair cells. However, even if the hair cells can detect displacements as small as 10^{-15} m for a 10 μm hair cell (as suggested by Appendix F) the streaming flows are still orders of magnitude too small to be sensed by the hair cells at the fish ear's hearing threshold. The analyses presented here have explored the effects of the finite

inertia of the otolith and of a thin, low viscosity layer between the tissue and the otolith. The acoustic particle motion is not equal to the relative motion between the otolith and its surroundings due to the finite inertia of the body. The relative motion can be found by multiplying the acoustic particle motion by a factor of (Equation 8.3)

$$\left(\frac{S.G.-1}{S.G.+0.5}\right),$$

where *S.G.* is the specific gravity of the otolith. The lower-viscosity endolymph adjacent to the otolith could increase the fluid shear experienced by the hair cell cilia to its maximum value of (Equation 8.13):

$$\frac{U_{max}}{l_{cilia}}$$

where U_{max} is the maximum streaming velocity in the tissue and l_{cilia} is the length of the hair cell cilia.

The analyses do suggest that the steady streaming flows are sufficiently strong enough at ultrasonic frequencies to provide useful information. However, the Stokes layer is considerably thinner at high frequencies, and is on the order of the length of the hair cell cilia (~2 μm for water/endolymph at this frequency). In addition, it is not clear that the scaling discussed here would extend to this Reynolds number range. Given these caveats, the estimated cilia tip velocity (based on the shear in the tissue without the endolymph layer) is then 4×10^{-4} rad/s, or 4 nm/s for a 10 μm hair cell. This streaming velocity should produce particle displacements on the order of the acoustic particle motion within a few milliseconds, and should therefore be sensible to the fish ear.

Based upon these results, it appears unlikely that the patterns predicted by auditory retina hypothesis and sensed by the hair cells are a result of the streaming flows. Because the fish ear is clearly capable of detecting auditory features like the direction and frequency of incident sound, other mechanisms should be considered, including the oscillatory component of the incident sound. The oscillatory component produces larger

displacements than the streaming flows over acoustically relevant time scales, as shown by this thesis, and for this reason should be considered the most likely candidate for demonstrating the auditory retina hypothesis's flow patterns.

9.2 Contributions

The contributions of these studies to fluid dynamics and fish bioacoustics include:

- Defining a new length scale, $L = (a^4/b)^{1/3}$, that makes the distance from the flow stagnation points to the body (*e.g. T* and *h)* directly proportional to Re_M for a variety of aspect ratios and oscillation amplitudes.
- Showing that the component steady streaming velocities superpose for multiple frequency sinusoidal oscillations along the same direction for $Re_M \sim O(10)$ and $\varepsilon^* \leq 0.25$.
- Demonstrating the angular location of the stagnation points on the lower surface of an angled oscillating spheroid is a function of the aspect ratio and orientation of the body, and not the amplitude or frequency of oscillation, as in

$$\frac{\tan(\theta)}{\tan(\varphi)} = AR$$

- New insights into the role of steady streaming flows and fish hearing, including evidence that steady streaming is not important at frequencies less than 1000 Hz but may play a role at ultrasonic frequencies.
- Illustration of the role a thin, low viscosity region adjacent to the otolith could play in increasing the shear of the hair cells.
- A novel vibrational model of the fish ear, which models the hair cell itself as the limiting spring/mass system of the accelerometer-like otolith and predicts a sensitivity for the hair cells that is three to five orders of

magnitude less than the previously suggested displacement sensitivity of 0.1 nm.

9.3 Model Limitations

The idealized "model" of the fish ear discussed here is clearly missing a number of important physical features present in the actual fish ear. Working from the otolith outward, this model omits:

1. the actual motion of the oscillating otolith (which may not be linear);
2. the observed variations in the otolith geometry;
3. the structure of the otolithic membrane (including the gelatinous layer and subcupular meshwork);
4. the distance between the hair cell cilia and the otolith;
5. the macula and surrounding tissue; and
6. the oscillatory portion of the flow.

Obviously, omitting these components could greatly affect the accuracy of the conclusions drawn here. The most important omission is likely to be neglecting the oscillatory portion of the flow. The objective of this thesis was to explore the effects of the time-independent steady streaming component of the flowfield on the cilia displacement, but these have been shown to be too small to be responsible for hearing in the fish ear. Therefore, the larger oscillatory components of the flow (which must be detectable by the fish at threshold) should be explored in more detail to determine its acoustically relevant characteristics and patterns. Although such information may be sensible by the individual hair cells, it is quite possible that sensing this information in the form of a spatially distributed pattern by the many hair cells on the macula enhances acoustic sensitivity in some fashion.

The streaming flow that has been studied here may provide some insight into the characteristics of the oscillatory flow. For instance, the stagnation point locations found

for the streaming flow may correspond to locations where the oscillatory flow would produce either its maximum or minimum shear with respect to the body. As an illustration, consider an oscillating spheroid. At the stagnation points along the axis of oscillation, the hair cells would not be deflected, but would instead be elongated or compressed during the oscillation. This type of motion would not enervate the hair cell, since the stereocilia are not displaced relative to the kinocilium. At the side of the spheroid, the body moves while surrounding fluid is essentially still, which would produce the maximum hair cell response.

This research was limited by our lack of knowledge of the tissue and fluids surrounding the otolith. For instance, biologists do not know exactly how the hair cells are positioned within the otolithic membrane due to difficulties in preserving, dissecting, or otherwise measuring the fish ear. It is unknown how close the hair cells are to the otolith, or even if they are touching or otherwise connected to its surface. Although hair cells have different lengths across the macula, it is unknown if the tips or the base of the cilia maintain a constant distance from the otolith's surface. Clearly, these details need to be understood in order to understand which parts of the flow are sampled by the hair cells.

In addition, the structure of the otolithic membrane itself is unclear. It touches the otolith on one side and the macula on the other, but how either is attached or coupled to the otolithic membrane is unknown. If it is rigidly connected, how much does the otolithic membrane deform with the oscillating surroundings and what happens to the embedded hair cells? If the otolith or the surrounding tissue can move relative to the membrane's structure, how are they connected and what provides the "suspension" in the otolithic system? How permeable is the gelatinous layer? Does the endolymph have pathways to flow across the otolith? How strongly anisotropic and viscoelastic are the properties of the membrane? Although this thesis assumed that the endolymph would be free to move as a fluid near the hair cells at the small displacements relevant to the fish

ear, this may not be true throughout the membrane due to the various fibers that support the otolith.

Many of the uncertainties about the otolithic membrane also apply to the surrounding tissues and the macula. Although the tissue is assumed to be viscoelastic, it is unclear what would be appropriate values for its stiffness and viscosity. These tissues will shape and contain the flows that set up in the endolymph adjacent to the otolith. In general, this will serve to increase the shear rate of the fluid adjacent to the otolith, and thus increase the sensitivity of the system.

Finally, there is some evidence that the actual otolith motion under acoustic stimulation contains frequency-dependent rotational as well as translational components (Sand and Michelsen 1978). Although this research only considered translational oscillations, rotational components might serve to shape steady streaming flows. If these rotational motions are also frequency dependent, it would result in frequency dependent flow patterns. These patterns might be part of a "place mechanism," where different areas of the macula have responses that vary with frequency.

The variations in the otolith geometry may play a role in shaping the flow patterns. Although this was partially addressed by looking at the patterns along the cod otolith at different locations, there are as many otolith geometries as there are fish species. The variations in geometry will affect the flow patterns, and may serve to filter or amplify various signals for fish ears as required.

9.4 Future Research Directions

This research explores the question of how fish hear and directionalize sound, which has implications for both biologists and engineers who seek to mimic the fish's auditory capabilities. The compactness of the fish ear makes it an attractive model for novel underwater sensors that do not rely on time-of-arrival differences or multipole

directivity to directionalize sounds. However, there remain many unresolved questions about the fish ear and how it detects underwater sounds.

This doctoral thesis suggests numerous future research directions, including:

1. The analyses presented here were limited by our lack of understanding of the structure and properties of the tissue surrounding the otolith. Very little is known about the properties of these tissues *in vivo*, including the location of the hair cell cilia with respect to the otolith, the viscoelastic properties of the surrounding tissues, and the natural frequency of the system formed by the otolith and surrounding tissue. In order to accurately model the fish ear, the morphology and tissue properties of the ear need to be better understood.
2. This study of the fish ear concentrated on the time-independent steady streaming components of the fluid motion inside of the fish ear. However, the time-varying oscillatory components that drive the steady streaming flows should also contain acoustically relevant information. These flows should be examined to see if they form acoustically relevant patterns in the sulcus that vary with the oscillation orientation, frequency, and amplitude, for example. Unlike the steady streaming flows studied here, the fish ear must be able to sense the oscillatory flow.
3. Both the streaming and oscillatory components of the flow will be affected by the properties of the surrounding tissue and bones, and in general these materials will confine these flows. Studying how flow confinement affects the shear rate near the otolith (and thus the hair cells) could improve our understanding of how sound experienced by the fish ear affects the hair cell ciliary deflections.
4. The superposition of the steady streaming flows for multiple frequency oscillations along a single direction should be expanded to include bodies oscillating in multiple directions (and frequencies) simultaneously and to oscillation amplitudes comparable to those due to underwater sounds.

5. This research suggests that steady streaming flows at ultrasonic frequencies may be significant and play a role in how cod and other fish detect and directionalize sound. It would be useful to perform experiments that visualize the flows near model otoliths in ultrasonic sound fields.
6. The morphology of the fish ear is known for only a small fraction of the identified teleost species, and the hearing capabilities of only a small fraction of those species have in turn been characterized. What is known about fish hearing capabilities, including the available fish audiograms, should be compared to the otoliths of the appropriate species in order to learn which morphological characteristics are most correlated with which hearing capabilities.
7. These analyses assumed that the length scale for the streaming flow near the model otolith was the width (y-dimension) of the sulcus, and that this length scale scaled linearly with the dimensions of the otolith. Both of these assumptions should be verified by, for example, performing similar experiments with model otoliths at various magnifications. It is unlikely, however, that a new length scale would be sufficient to change the conclusions of this study regarding the very small displacements associated with the steady streaming flows in the fish ear.

APPENDIX A

ERROR ANALYSIS

A.1 Axisymmetric Body Stagnation Point Location

The error in calculating the normalized location off the stagnation point measured with respect to the surface of the body T/L is determined by considering the uncertainty in locating the surface of the body and the appropriate stagnation points. If the off-surface stagnation points on both sides of the spheroid are visible, then

$$\frac{T}{L} = \frac{x_R - x_L - 2r_x}{2LM_{\text{px}}} = f\left(x_R, x_L, r_x, L, M_{\text{px}}\right) \tag{A.1}$$

where r_x is the axis of the body in the x-direction, L is the critical length based on measurements of the body, M_{px} is the magnification of the image (measured in pixels/mm), and x_R and x_L are the stagnation points to the right and left of the spheroid, respectively. The uncertainty (taken here to be a standard deviation) can be found from the square root of the variance, σ_f^2, which is given by

$$\sigma_f^2 = \sum_i \left(u_{x_i} \frac{\partial f}{\partial x_i} \right)^2 \tag{A.2}$$

$$\sigma_f^2 = \left(u_{x_R} \frac{\partial f}{\partial x_R} \right)^2 + \left(u_{x_L} \frac{\partial f}{\partial x_L} \right)^2 + \left(u_{r_x} \frac{\partial f}{\partial r_x} \right)^2 + \left(u_L \frac{\partial f}{\partial L} \right)^2 + \left(u_{M_{\text{px}}} \frac{\partial f}{\partial M_{\text{px}}} \right)^2 \tag{A.3}$$

where u_i is the uncertainty in the i^{th} component of f. The partial derivatives in this expression can be determined from Eq. A.1:

$$\frac{\partial f}{\partial x_R} = \frac{1}{2LM_{\text{px}}} \tag{A.4}$$

$$\frac{\partial f}{\partial x_L} = -\frac{1}{2LM_{\text{px}}} \tag{A.5}$$

$$\frac{\partial f}{\partial r_x} = \frac{1}{LM_{\text{px}}} \tag{A.6}$$

$$\frac{\partial f}{\partial L} = -\frac{x_R - x_L - 2r_x}{2L^2 M_{\text{px}}} \tag{A.7}$$

$$\frac{\partial f}{\partial M_{\text{px}}} = -\frac{x_R - x_L - 2r_x}{2LM_{\text{px}}^2} \tag{A.8}$$

The uncertainty is then

$$u_f = \sqrt{\sigma_f^2}$$

If only the stagnation point to the right of the body is visible, T/L is:

$$\frac{T}{L} = \frac{x_R - x_0 - r_x}{LM_{\text{px}}} = g\left(x_R, x_0, r_x, L, M_{\text{px}}\right) \tag{A.9}$$

where x_0 is the x-direction location of the center of the body. The variance is then:

$$\sigma_f^2 = \left(u_{x_R}\frac{\partial g}{\partial x_R}\right)^2 + \left(u_{x_0}\frac{\partial g}{\partial x_0}\right)^2 + \left(u_{r_x}\frac{\partial g}{\partial r_x}\right)^2 + \left(u_L\frac{\partial g}{\partial L}\right)^2 + \left(u_{M_{\text{px}}}\frac{\partial g}{\partial M_{\text{px}}}\right)^2 \tag{A.10}$$

where the partial derivatives are:

$$\frac{\partial g}{\partial x_R} = \frac{1}{LM_{\text{px}}} \tag{A.11}$$

$$\frac{\partial g}{\partial x_0} = \frac{\partial g}{\partial r_x} = -\frac{1}{LM_{\text{px}}} \tag{A.12}$$

$$\frac{\partial g}{\partial L} = -\frac{x_R - x_0 - r_x}{L^2 M_{\text{px}}} \tag{A.13}$$

$$\frac{\partial g}{\partial M_{\text{px}}} = -\frac{x_R - x_0 - r_x}{LM_{\text{px}}^2} \tag{A.14}$$

For the chart shown in Chapter 4, the uncertainty in locating the stagnation points and the body surface was taken to be 2 pixels, while the uncertainty in L was taken to be 0.5 mm, and the uncertainty in M_{px} was taken to be 0.5 px/mm.

A.2 Spheroidal Coordinate

The modified oblate spheroidal coordinate, μ, represents the angular position relative to the positive *z*-axis. In terms of the polar coordinates (*r*, *z*), it is given by:

$$\mu^2 = -\frac{1}{2}\left(\frac{r^2}{c_e{}^2}+\frac{z^2}{c_e{}^2}-1\right)\pm\frac{1}{2}\left[\left(\frac{r^2}{c_e{}^2}+\frac{z^2}{c_e{}^2}-1\right)^2+4\frac{z^2}{c_e{}^2}\right]^{1/2} \quad \text{A.15}$$

where c_e, the focal length, is:

$$c_e{}^2 = b^2 - a^2 \quad \text{A.16}$$

Here, *a* and *b* are the radii along the *z*- and *r*-axes, respectively. For prolate spheroidal coordinates Eq. A.15 becomes:

$$\mu^2 = \frac{1}{2}\left(\frac{r^2}{c_e{}^2}+\frac{z^2}{c_e{}^2}+1\right)\pm\frac{1}{2}\left[\left(\frac{r^2}{c_e{}^2}+\frac{z^2}{c_e{}^2}+1\right)^2-4\frac{z^2}{c_e{}^2}\right]^{1/2} \quad \text{A.17}$$

where $c_e{}^2 = a^2 - b^2$. The variables $r = x_v - x_0$ and $z = y_v - y_0$ are found from the coordinates of the center of the ellipse (x_0, y_0) and the center of the rotating region (x_v, y_v). The coordinate μ is then

$$\mu = \mu\left(x_0, y_0, x_v, y_v, a, b\right) \quad \text{A.18}$$

The uncertainty in μ can be calculated from

$$\sigma_\mu^2 = \left(u_{x_0}\frac{\partial\mu}{\partial x_0}\right)^2+\left(u_{x_v}\frac{\partial\mu}{\partial x_v}\right)^2+\left(u_{y_0}\frac{\partial\mu}{\partial y_0}\right)^2+\left(u_{y_v}\frac{\partial\mu}{\partial y_v}\right)^2+\left(u_a\frac{\partial\mu}{\partial xa}\right)^2+\left(u_b\frac{\partial\mu}{\partial b}\right)^2 . \quad \text{A.19}$$

However, considering the complexity of the analytical solution, the partial derivatives were found numerically using centered finite difference approximations. For example:

$$\frac{\partial\mu}{\partial y_0} = \frac{\mu\left(x_0, y_0+\zeta, x_v, y_v, a, b\right)-\mu\left(x_0, y_0-\zeta, x_v, y_v, a, b\right)}{2\zeta} \quad \text{A.20}$$

where ζ should be a small value because the error in the central-difference approximation is $O(\zeta^2)$.

A.3 Minimum Distance

The minimum distance from the body surface to the center of the inner rotating region, h, was calculated by minimizing the distance between a set of points on the edge of the body and the center of the rotating region, (x_v, y_v). Since

$$h = h\left(x_0, y_0, a, b, \theta, x_v, y_v\right), \tag{A.21}$$

the variance is

$$\begin{aligned}\sigma_h^2 = &\left(u_{x_0}\frac{\partial\mu}{\partial x_0}\right)^2 + \left(u_{y_0}\frac{\partial\mu}{\partial y_0}\right)^2 + \left(u_a\frac{\partial\mu}{\partial xa}\right)^2 + \\ &\left(u_b\frac{\partial\mu}{\partial b}\right)^2 + \left(u_\theta\frac{\partial\mu}{\partial\theta}\right)^2 + \left(u_{x_v}\frac{\partial\mu}{\partial x_v}\right)^2 + \left(u_{y_v}\frac{\partial\mu}{\partial y_v}\right)^2\end{aligned} \tag{A.22}$$

As with μ, the partial derivatives were calculated using a centered finite difference approximation. For example:

$$\frac{\partial h}{\partial y_0} = \frac{h\left(x_0, y_0+\zeta, a, b, \theta, x_v, y_v\right) - h\left(x_0, y_0-\zeta, a, b, \theta, x_v, y_v\right)}{2\zeta} \tag{A.23}$$

where ζ should be a small value because the error in the central-difference approximation is $O(\zeta^2)$. The uncertainty in h is then found from

$$u_h = \sqrt{\sigma_h^2} \tag{A.24}$$

Assuming that h and L are both given in the same dimensions, the error in h/L can be estimated as follows:

$$u_{h/L} = \sqrt{\left(\frac{u_h}{L}\right)^2 + \left(\frac{u_L h}{L^2}\right)^2} \tag{A.25}$$

where the uncertainty in L is from

$$u_L = \sqrt{\left(u_{L_{mm}} M_{\text{px}}\right)^2 + \left(u_{M_{\text{px}}} L_{mm}\right)^2} \tag{A.26}$$

where L_{mm} is the measurement of the critical length in millimeters, M_{px} is the

magnification of the image in pixels per millimeters, and u_i is the uncertainty in these quantities.

A.4 Angular Location of Surface Stagnation Point

The angular location of the surface stagnation point on the angled spheroidal body is quantified in terms of the function *f*. The function *f* is given by:

$$f = AR\tan(\varphi) = \frac{r_y}{r_x}\tan(\varphi) \tag{A.27}$$

The uncertainty in *f* is then given by the square root of the variance, σ_f^2:

$$\sigma_f^2 = \left(u_{r_y}\frac{\partial f}{\partial r_y}\right)^2 + \left(u_{r_x}\frac{\partial f}{\partial r_x}\right)^2 + \left(u_{\varphi}\frac{\partial f}{\partial \varphi}\right)^2 \tag{A.28}$$

where r_x and r_y are the axes of the elliptical profile of the spheroidal body, φ is the angular location of the stagnation point as described in the text, u_i is the uncertainty in the *i*th component, and

$$\frac{\partial f}{\partial r_y} = \frac{\tan(\varphi)}{r_x} \tag{A.29}$$

$$\frac{\partial f}{\partial r_x} = \frac{r_y\tan(\varphi)}{r_x^2} \tag{A.30}$$

$$\frac{\partial f}{\partial \varphi} = \frac{r_y}{r_x}\sec^2(\varphi) \tag{A.31}$$

Although the uncertainty in the dimensions of the body can be estimated from the body dimensions in the images (or from physical measurements of the body), the uncertainty in the angular location of the stagnation is calculated instead. The error in the angular location of the body stagnation point, φ, is found from the expression:

$$\varphi(x_s, y_s, x_0, y_0, \theta) = \tan^{-1}\left(\frac{y_s - y_0}{x_s - x_0}\right) + \theta \tag{A.32}$$

where (x_s, y_s) are the coordinates of the stagnation point on the surface of the elliptical

cross-section of the body, (x_0, y_0) are the coordinates of the center of elliptical cross-section of the body, and θ is the body's orientation angle. The error is then estimated from the square root of the variance σ_φ^2

$$\sigma_\varphi^2 = \left(u_{y_s}\frac{\partial\varphi}{\partial y_s}\right)^2 + \left(u_{y_0}\frac{\partial\varphi}{\partial y_0}\right)^2 + \left(u_{xs}\frac{\partial\varphi}{\partial x_s}\right)^2 + \left(u_{x_0}\frac{\partial\varphi}{\partial x_0}\right)^2 + \left(u_\theta\frac{\partial\varphi}{\partial\theta}\right)^2 \quad \text{A.33}$$

where u_i is the uncertainty in the i^{th} variable of φ and the partial derivatives are given by:

$$\frac{\partial\varphi}{\partial y_s} = \frac{(x_s - x_0)}{(x_s - x_0)^2 + (y_s - y_0)^2} \quad \text{A.34}$$

$$\frac{\partial\varphi}{\partial y_0} = \frac{-(x_s - x_0)}{(x_s - x_0)^2 + (y_s - y_0)^2} \quad \text{A.35}$$

$$\frac{\partial\varphi}{\partial x_s} = \frac{-(y_s - y_0)}{(x_s - x_0)^2 + (y_s - y_0)^2} \quad \text{A.36}$$

$$\frac{\partial\varphi}{\partial x_0} = \frac{(y_s - y_0)}{(x_s - x_0)^2 + (y_s - y_0)^2} \quad \text{A.37}$$

The uncertainty in locating the body parameters x_0, y_0, r_x, and r_y was taken to be 2 pixels, while the uncertainty in locating the angle of the ellipse was estimated to be 1°. Given the difficulty in locating the stagnation points near the body, the uncertainty in x_s and y_s is taken to be 4 pixels.

APPENDIX B

PLOTTED DATA TABLES

The data for many of the "*x*-*y*" style plots are presented in this Appendix. These graphs were plotted using Tecplot 360. The tables presented here are taken from the *.dat files read by Tecplot to create the graphs. This data file has a format that presents the "Title" of the data set on the first line, the "Variables" included in the file on the second line, and information about the "Zone" on the third line. The Zone line includes information on the "Title" (T), the number of points in the "Zone" (I and J), and the format of the data supplied in the "Zone" (Datapacking). For these files, the data are provided in "Point" format, which means that each line of the zone presents each of the named variables in the order given in the "Variables" list. An attempt was made to give the variables intuitive names, such as ReM for Re_M and "err ReM" for the "error" or uncertainty in Re_M.

Notes:

1.) In Appendix B.14 and B.17, "W" is meant to stand in for Ω (the vorticity).

2.) In Appendix B.16 and B.17, the Zone title in the form "Angle Location," so T="0A" means that this is in location "A" on the otolith oriented at 0°. Location A is the more central location and location B is the location closer to the side of the otolith.

B.1 Data for Figure 4.5

```
TITLE = "T/L vs ReM"
VARIABLES = "ReM", "T/L", "err ReM", "err T/L"
ZONE T="AR=2", I=6, J=1, DATAPACKING=POINT
145.18      0.318      8.87       0.0158
96.79       0.465      5.91       0.0212
96.79       0.469      5.92       0.0214
48.40       0.887      2.96       0.0317
48.40       0.934      2.96       0.0307
```

```
48.40      0.741      2.96       0.0316
ZONE T="AR=1.35", I=11, J=1, DATAPACKING=POINT
109.71     0.332      6.70       0.0193
109.71     0.351      6.70       0.0201
109.71     0.345      6.70       0.0198
73.12      0.481      4.47       0.0255
73.12      0.507      4.47       0.0266
73.13      0.503      4.47       0.0264
36.57      1.018      2.23       0.0498
36.56      1.093      2.23       0.0533
36.56      1.169      2.23       0.0420
42.04      0.916      2.57       0.0440
42.05      0.910      2.57       0.0437
ZONE T="AR=1", I=17, J=1, DATAPACKING=POINT
89.97      0.488      5.50       0.0288
89.97      0.507      5.50       0.0297
29.98      1.372      1.83       0.0615
29.98      1.325      1.83       0.0171
103.44     0.446      18.96      0.0247
103.44     0.476      18.96      0.0260
82.70      0.595      15.16      0.0314
82.70      0.617      15.16      0.0324
68.95      0.648      12.64      0.0339
68.95      0.666      12.64      0.0347
55.16      0.876      10.11      0.0446
55.16      0.949      10.11      0.0480
41.80      1.079      2.55       0.0562
41.80      1.050      2.55       0.0548
59.96      0.683      3.66       0.0369
59.96      0.709      3.66       0.0381
59.96      0.710      3.66       0.0382
ZONE T="AR=0.76", I=6, J=1, DATAPACKING=POINT
41.93      1.064      2.56       0.0737
41.93      1.165      2.56       0.0802
41.93      1.218      2.56       0.1043
27.95      1.783      1.71       0.1208
27.95      1.890      1.71       0.1409
27.95      1.362      1.71       0.0931
```

B.2 Data for Figure 4.7

```
TITLE = "Mu vs AR"
VARIABLES = "AR", "Mu", "err Mu"
ZONE T="Experimental Data", I=34, J=1, DATAPACKING=POINT
0.27       0.341      0.0105
0.51       0.358      0.0126
0.51       0.398      0.0106
0.51       0.309      0.0129
0.76       0.476      0.0130
0.76       0.392      0.0152
0.74       0.413      0.0073
```

```
0.74       0.373      0.0083
0.74       0.360      0.0086
1.00       0.608      0.0098
1.00       0.589      0.0108
1.00       0.599      0.0090
1.00       0.607      0.0093
1.00       0.603      0.0101
1.00       0.600      0.0101
1.00       0.594      0.0125
1.00       0.603      0.0124
1.00       0.597      0.0139
1.00       0.584      0.0149
1.00       0.583      0.0115
1.00       0.595      0.0116
1.00       0.594      0.0115
1.00       0.593      0.0129
1.00       0.589      0.0129
1.00       0.585      0.0130
1.00       0.591      0.0096
1.00       0.587      0.0108
1.00       0.587      0.0080
1.00       0.600      0.0085
1.00       0.600      0.0094
1.00       0.563      0.0096
1.31       0.615      0.0083
1.31       0.693      0.0093
1.31       0.716      0.0097
ZONE T="Asymptotic Theory", I=4, J=1, DATAPACKING=POINT
0.26       0.131      0.0000
0.52       0.271      0.0000
0.76       0.416      0.0000
1.00       0.577      0.0000
```

B.3 Data for Figure 4.8

```
TITLE = "h/L vs ReM"
VARIABLES = "ReM", "h/L", "err h/L"
ZONE T="AR=2", I=6, J=1, DATAPACKING=POINT
145.18     0.168      0.011
96.79      0.186      0.011
96.79      0.198      0.012
48.40      0.292      0.015
48.40      0.322      0.016
48.40      0.356      0.017
ZONE T="AR=1.35", I=11, J=1, DATAPACKING=POINT
109.71     0.171      0.011
109.71     0.184      0.012
109.71     0.190      0.012
73.12      0.209      0.012
73.12      0.231      0.013
73.13      0.216      0.013
```

```
36.57      0.311      0.017
36.56      0.335      0.018
36.56      0.353      0.018
42.04      0.310      0.016
42.05      0.323      0.017
ZONE T="AR=1", I=19, J=1, DATAPACKING=POINT
89.97      0.233      0.015
89.97      0.230      0.014
29.98      0.423      0.024
29.98      0.445      0.025
103.44     0.227      0.013
103.44     0.228      0.013
82.70      0.270      0.015
82.70      0.277      0.015
68.95      0.288      0.016
68.95      0.295      0.016
55.16      0.354      0.019
55.16      0.351      0.019
27.57      0.497      0.025
27.57      0.506      0.026
41.80      0.362      0.020
41.80      0.359      0.020
59.96      0.276      0.016
59.96      0.300      0.017
59.96      0.311      0.018
ZONE T="AR=0.76", I=11, J=1, DATAPACKING=POINT
41.93      0.368      0.028
41.93      0.382      0.029
41.93      0.395      0.030
27.95      0.459      0.034
27.95      0.485      0.035
27.95      0.504      0.036
13.97      0.663      0.046
13.97      0.725      0.050
5.59       1.044      0.071
11.75      0.701      0.044
35.24      0.400      0.026
ZONE T="AR=0.26", I=10, J=1, DATAPACKING=POINT
2.44       2.959      0.719
2.44       3.414      0.828
1.62       3.182      0.773
1.62       3.525      0.855
1.62       3.656      0.886
0.81       3.872      0.939
0.81       4.015      0.973
0.81       4.326      1.047
0.32       5.050      1.222
2.05       3.667      0.881
ZONE T="AR=0.52", I=15, J=1, DATAPACKING=POINT
9.75       1.272      0.131
1.95       1.947      0.198
14.62      0.804      0.087
```

```
14.62      0.859      0.092
14.62      0.840      0.090
9.75       0.977      0.104
9.75       1.012      0.107
9.75       1.038      0.110
4.87       1.359      0.142
4.87       1.388      0.145
4.87       1.359      0.142
1.95       1.958      0.203
4.12       1.696      0.170
12.36      0.866      0.089
12.36      0.985      0.100
```

B.4 Data for Figure 4.11

```
TITLE = "ReM = 60, x/L = 0"
VARIABLES = "Y/L", "V/Vs", "err V/Vs"
ZONE T="eps = 0.18", I=13, J=1, DATAPACKING=POINT
1.07261    -0.02785   0.005609
1.56018    -0.0256    0.001501
1.72271    0.006383   0.001926
1.88523    0.024534   0.000391
2.04776    0.032724   0.000728
2.21028    0.035414   0.000525
2.37281    0.035778   0.000729
2.53533    0.034944   0.000851
2.69786    0.033794   0.000736
2.86038    0.031949   0.000889
3.0229     0.029608   0.001224
3.18543    0.027238   0.096071
3.34795    0.024951   0.034418
ZONE T="eps = 0.1", I=12, J=1, DATAPACKING=POINT
1.0585     -0.02189   0.007838
1.22005    -0.09837   0.00131
1.38161    -0.07651   0.003273
1.54317    -0.02802   0.003396
1.70472    0.00549    0.00129
1.86628    0.022442   0.001299
2.02783    0.032628   0.002189
2.18939    0.034302   0.001637
2.35095    0.035437   0.000874
2.5125     0.034379   0.001015
2.67406    0.033557   0.002052
2.83562    0.031633   0.357916
ZONE T="eps = 0.05", I=13, J=1, DATAPACKING=POINT
1.05536    -0.01417   0.006703
1.2179     -0.09837   0.001107
1.38043    -0.07612   0.006383
1.54297    -0.03167   0.002273
1.7055     0.006502   0.002805
1.86804    0.021177   0.003305
```

```
2.03058    0.028093   0.006982
2.19311    0.026263   0.008135
2.68072    0.035349   0.019103
2.84325    0.03397    0.039723
3.00579    0.034802   0.048333
3.16832    0.029539   0.343703
3.33086    0.033203   0.081589
```

B.5 Data for Figure 4.12

```
TITLE = "Sphere along axis"
VARIABLES = "Y/L", "V/Vs", "err V/Vs"
ZONE T="ReM=103, eps=0.2", I=15, J=1, DATAPACKING=POINT
1.07       -0.0292    0.0030
1.22       -0.0885    0.0010
1.37       -0.0430    0.0023
1.51       0.0161     0.0019
1.66       0.0477     0.0008
1.81       0.0614     0.0010
1.96       0.0660     0.0011
2.11       0.0662     0.0011
2.26       0.0642     0.0012
2.41       0.0609     0.0013
2.56       0.0576     0.0014
2.71       0.0539     0.0015
2.85       0.0501     0.0014
3.00       0.0471     0.0017
3.15       0.0434     0.0015
ZONE T="ReM=103, eps=0.1", I=15, J=1, DATAPACKING=POINT
1.07       -0.0360    0.0086
1.22       -0.0868    0.0013
1.36       -0.0381    0.0059
1.51       0.0169     0.0027
1.66       0.0452     0.0016
1.81       0.0582     0.0014
1.96       0.0633     0.0012
2.11       0.0635     0.0015
2.26       0.0616     0.0015
2.41       0.0586     0.0016
2.56       0.0550     0.0017
2.71       0.0511     0.0019
2.85       0.0475     0.0016
3.00       0.0441     0.0015
3.15       0.0417     0.0016
ZONE T="ReM=83, eps=0.2", I=15, J=1, DATAPACKING=POINT
1.07       -0.0271    0.0034
1.22       -0.0965    0.0010
1.37       -0.0739    0.0009
1.52       -0.0210    0.0021
1.67       0.0145     0.0011
1.81       0.0322     0.0007
```

```
1.96       0.0406     0.0006
2.11       0.0437     0.0009
2.26       0.0444     0.0008
2.41       0.0436     0.0007
2.56       0.0416     0.0008
2.71       0.0393     0.0009
2.86       0.0374     0.0007
3.01       0.0354     0.0009
3.16       0.0334     0.0010
ZONE T="ReM=83, eps=0.1", I=15, J=1, DATAPACKING=POINT
1.07       -0.0384    0.0043
1.22       -0.0967    0.0017
1.37       -0.0691    0.0023
1.52       -0.0204    0.0037
1.66       0.0131     0.0021
1.81       0.0299     0.0018
1.96       0.0382     0.0016
2.11       0.0414     0.0016
2.26       0.0425     0.0017
2.41       0.0416     0.0017
2.56       0.0399     0.0019
2.71       0.0390     0.0017
2.86       0.0370     0.0018
3.01       0.0352     0.0020
3.15       0.0327     0.0593
ZONE T="ReM=55, eps=0.2", I=15, J=1, DATAPACKING=POINT
1.06       -0.0143    0.0015
1.21       -0.0921    0.0016
1.36       -0.0991    0.0006
1.51       -0.0640    0.0006
1.66       -0.0288    0.0010
1.81       -0.0052    0.0016
1.96       0.0077     0.0012
2.10       0.0147     0.0006
2.25       0.0185     0.0006
2.40       0.0202     0.0007
2.55       0.0209     0.0007
2.70       0.0207     0.0007
2.85       0.0204     0.0007
3.00       0.0199     0.0007
3.15       0.0188     0.0008
ZONE T="ReM=55, eps=0.1", I=15, J=1, DATAPACKING=POINT
1.06       -0.0238    0.0061
1.21       -0.0986    0.0024
1.36       -0.0983    0.0022
1.51       -0.0625    0.0031
1.66       -0.0298    0.0024
1.81       -0.0083    0.0022
1.96       0.0054     0.0023
2.11       0.0121     0.0020
2.26       0.0153     0.0020
2.41       0.0173     0.0021
```

```
2.55       0.0179     0.0025
2.70       0.0175     0.0021
2.85       0.0175     0.0024
3.00       0.0161     0.0021
3.15       0.0156     0.1390
ZONE T="ReM=28, eps=0.2", I=12, J=1, DATAPACKING=POINT
1.51       -0.0995    0.0030
1.66       -0.0735    0.0015
1.81       -0.0493    0.0008
1.96       -0.0312    0.0008
2.10       -0.0192    0.0008
2.25       -0.0112    0.0009
2.40       -0.0059    0.0009
2.55       -0.0023    0.0010
2.70       0.0000     0.0009
2.84       0.0010     0.0011
2.99       0.0022     0.0011
3.14       0.0031     0.0011
ZONE T="ReM=28, eps=0.1", I=15, J=1, DATAPACKING=POINT
1.07       -0.0211    0.0050
1.22       -0.0859    0.0036
1.37       -0.1093    0.0032
1.52       -0.0950    0.0033
1.67       -0.0698    0.0033
1.82       -0.0465    0.0033
1.97       -0.0296    0.0034
2.11       -0.0178    0.0035
2.26       -0.0098    0.0033
2.41       -0.0043    0.0034
2.56       -0.0021    0.0049
2.71       0.0015     0.0033
2.86       0.0030     0.0035
3.01       0.0041     0.0033
3.16       0.0039     0.0035
```

B.6 Data for Figure 4.17

```
TITLE = "Validation"
VARIABLES = "Y/L", "V/Vs", "err V/Vs"
ZONE T="ReM = 54, eps = 0.11, A", I=11, J=1, DATAPACKING=POINT
1.01       -0.0064    0.0036
1.11       -0.0609    0.0016
1.21       -0.0971    0.0014
1.30       -0.0986    0.0015
1.40       -0.0787    0.0016
1.49       -0.0538    0.0018
1.59       -0.0313    0.0017
1.68       -0.0141    0.0019
1.78       -0.0014    0.0022
1.87       0.0068     0.0017
1.97       0.0138     0.0018
```

```
ZONE T="ReM = 54, eps = 0.11, B", I=11, J=1, DATAPACKING=POINT
1.01       -0.0058    0.0032
1.11       -0.0602    0.0023
1.21       -0.0970    0.0014
1.30       -0.0977    0.0014
1.40       -0.0779    0.0015
1.49       -0.0526    0.0015
1.59       -0.0297    0.0016
1.68       -0.0127    0.0017
1.78       0.0006     0.0016
1.87       0.0089     0.0016
1.97       0.0159     0.0019
ZONE T="ReM = 54, eps = 0.11, C", I=11, J=1, DATAPACKING=POINT
1.01       -0.0088    0.0029
1.11       -0.0620    0.0023
1.21       -0.0973    0.0015
1.30       -0.0978    0.0015
1.40       -0.0781    0.0015
1.49       -0.0524    0.0015
1.59       -0.0307    0.0017
1.68       -0.0139    0.0016
1.78       -0.0009    0.0019
1.87       0.0062     0.0021
1.97       0.0138     0.0018
```

B.7 Data for Figure 5.1(b)

```
TITLE = "Oblate: 4and8Hza_march212007.dat"
VARIABLES = "X/L","Y/L","U/Vs ","V/Vs","err U/Vs","err V/Vs"
ZONE T="Sum" I=1 J=29 DATAPACKING=POINT
1.55       -0.03      0.0094     -0.0014    0.0015     0.0020
1.55       0.04       0.0106     -0.0111    0.0013     0.0018
1.55       0.12       0.0119     -0.0203    0.0014     0.0018
1.55       0.20       0.0164     -0.0297    0.0013     0.0018
1.55       0.27       0.0217     -0.0361    0.0013     0.0018
1.55       0.35       0.0245     -0.0410    0.0012     0.0018
1.55       0.43       0.0274     -0.0402    0.0013     0.0021
1.55       0.50       0.0252     -0.0336    0.0013     0.0021
1.55       0.58       0.0220     -0.0255    0.0014     0.0022
1.55       0.66       0.0154     -0.0188    0.0016     0.0023
1.55       0.73       0.0077     -0.0112    0.0013     0.0020
1.55       0.81       0.0002     -0.0044    0.0014     0.0018
1.55       0.89       -0.0058    0.0012     0.0013     0.0018
1.55       0.96       -0.0109    0.0031     0.0013     0.0018
1.55       1.04       -0.0145    0.0047     0.0013     0.0018
1.55       1.12       -0.0162    0.0055     0.0013     0.0018
1.55       1.19       -0.0170    0.0053     0.0013     0.0018
1.55       1.27       -0.0167    0.0051     0.0013     0.0018
1.55       1.35       -0.0163    0.0051     0.0013     0.0018
1.55       1.42       -0.0139    0.0022     0.0015     0.0018
1.55       1.50       -0.0128    0.0017     0.0013     0.0018
```

```
1.55       1.57       -0.0117    0.0014     0.0013     0.0018
1.55       1.65       -0.0100    0.0009     0.0013     0.0018
1.55       1.73       -0.0093    0.0006     0.0108     0.0218
1.55       1.80       -0.0080    0.0004     0.0013     0.0018
1.55       1.88       -0.0071    -0.0014    0.0571     0.0611
1.55       1.96       -0.0066    -0.0026    0.0582     0.0412
1.55       2.03       -0.0045    0.0000     0.0414     0.0724
1.55       2.11       -0.0027    0.0022     0.0016     0.0022
ZONE T="Mult" I=1 J=29 DATAPACKING=POINT
1.55       -0.03      0.0099     0.0035     0.0015     0.0018
1.55       0.04       0.0085     -0.0075    0.0009     0.0013
1.55       0.12       0.0131     -0.0203    0.0010     0.0014
1.55       0.20       0.0158     -0.0283    0.0009     0.0013
1.55       0.27       0.0206     -0.0343    0.0010     0.0013
1.55       0.35       0.0240     -0.0379    0.0009     0.0014
1.55       0.43       0.0256     -0.0368    0.0010     0.0014
1.55       0.50       0.0243     -0.0305    0.0009     0.0015
1.55       0.58       0.0208     -0.0234    0.0009     0.0014
1.55       0.66       0.0136     -0.0146    0.0009     0.0013
1.55       0.73       0.0063     -0.0067    0.0011     0.0015
1.55       0.81       -0.0011    -0.0003    0.0012     0.0016
1.55       0.89       -0.0077    0.0043     0.0009     0.0013
1.55       0.96       -0.0123    0.0068     0.0009     0.0013
1.55       1.04       -0.0156    0.0080     0.0009     0.0013
1.55       1.12       -0.0174    0.0083     0.0009     0.0013
1.55       1.19       -0.0181    0.0081     0.0009     0.0013
1.55       1.27       -0.0177    0.0074     0.0009     0.0013
1.55       1.35       -0.0168    0.0067     0.0010     0.0013
1.55       1.42       -0.0157    0.0060     0.0009     0.0013
1.55       1.50       -0.0145    0.0055     0.0009     0.0013
1.55       1.57       -0.0132    0.0052     0.0009     0.0013
1.55       1.65       -0.0119    0.0051     0.0016     0.0018
1.55       1.73       -0.0093    0.0031     0.0009     0.0013
1.55       1.80       -0.0084    0.0029     0.0009     0.0013
1.55       1.88       -0.0073    0.0025     0.0009     0.0014
1.55       1.96       -0.0069    0.0023     0.0009     0.0016
1.55       2.03       -0.0064    0.0013     0.0010     0.0013
1.55       2.11       -0.0058    0.0002     0.0010     0.0016
```

B.8 Data for Figure 5.2(b)

```
TITLE = "Prolate: 4and8Hza_march192007.dat"
VARIABLES = "X/L","Y/L","U/Vs ","V/Vs","err U/Vs","err V/Vs"
ZONE T="Sum" I=1 J=29 DATAPACKING=POINT
0.76       -0.11      0.0065     0.0096     0.0012     0.0017
0.76       -0.05      0.0054     0.0055     0.0013     0.0018
0.76       0.01       0.0048     0.0014     0.0012     0.0017
0.76       0.07       0.0050     -0.0016    0.0013     0.0018
0.76       0.13       0.0035     -0.0067    0.0014     0.0018
0.76       0.19       0.0063     -0.0088    0.0012     0.0017
0.76       0.25       0.0076     -0.0122    0.0013     0.0017
```

```
0.76       0.31       0.0093     -0.0153    0.0012     0.0017
0.76       0.37       0.0111     -0.0174    0.0012     0.0017
0.76       0.43       0.0129     -0.0186    0.0012     0.0017
0.76       0.49       0.0140     -0.0179    0.0012     0.0017
0.76       0.55       0.0139     -0.0167    0.0012     0.0017
0.76       0.61       0.0117     -0.0125    0.0012     0.0019
0.76       0.67       0.0094     -0.0090    0.0013     0.0018
0.76       0.73       0.0051     -0.0045    0.0013     0.0019
0.76       0.79       0.0013     -0.0011    0.0012     0.0018
0.76       0.85       -0.0036    0.0027     0.0012     0.0017
0.76       0.91       -0.0068    0.0044     0.0012     0.0017
0.76       0.97       -0.0096    0.0052     0.0012     0.0017
0.76       1.03       -0.0117    0.0057     0.0012     0.0017
0.76       1.09       -0.0120    0.0059     0.0012     0.0017
0.76       1.15       -0.0122    0.0052     0.0012     0.0017
0.76       1.21       -0.0112    0.0054     0.0012     0.0019
0.76       1.27       -0.0100    0.0039     0.0012     0.0017
0.76       1.33       -0.0090    0.0036     0.0012     0.0017
0.76       1.39       -0.0081    0.0036     0.0013     0.0017
0.76       1.45       -0.0076    0.0033     0.0013     0.0017
0.76       1.51       -0.0063    0.0033     0.0175     0.0209
0.76       1.57       -0.0055    0.0030     0.0254     0.0239
ZONE T="Mult" I=1 J=29 DATAPACKING=POINT
0.76       -0.11      0.0057     0.0112     0.0009     0.0012
0.76       -0.05      0.0052     0.0069     0.0009     0.0012
0.76       0.01       0.0041     0.0027     0.0009     0.0012
0.76       0.07       0.0040     -0.0005    0.0009     0.0012
0.76       0.13       0.0038     -0.0041    0.0009     0.0012
0.76       0.19       0.0058     -0.0074    0.0008     0.0012
0.76       0.25       0.0067     -0.0106    0.0008     0.0012
0.76       0.31       0.0088     -0.0127    0.0008     0.0012
0.76       0.37       0.0104     -0.0148    0.0008     0.0012
0.76       0.43       0.0116     -0.0155    0.0008     0.0012
0.76       0.49       0.0124     -0.0151    0.0008     0.0013
0.76       0.55       0.0121     -0.0126    0.0009     0.0013
0.76       0.61       0.0109     -0.0100    0.0009     0.0013
0.76       0.67       0.0080     -0.0057    0.0009     0.0014
0.76       0.73       0.0049     -0.0021    0.0008     0.0012
0.76       0.79       0.0011     0.0011     0.0010     0.0014
0.76       0.85       -0.0029    0.0040     0.0010     0.0015
0.76       0.91       -0.0061    0.0059     0.0009     0.0013
0.76       0.97       -0.0091    0.0070     0.0009     0.0013
0.76       1.03       -0.0107    0.0075     0.0009     0.0012
0.76       1.09       -0.0112    0.0072     0.0009     0.0012
0.76       1.15       -0.0113    0.0070     0.0009     0.0013
0.76       1.21       -0.0109    0.0066     0.0008     0.0012
0.76       1.27       -0.0103    0.0064     0.0008     0.0012
0.76       1.33       -0.0094    0.0062     0.0008     0.0013
0.76       1.39       -0.0080    0.0048     0.0009     0.0014
0.76       1.45       -0.0069    0.0048     0.0009     0.0012
0.76       1.51       -0.0060    0.0049     0.0009     0.0013
0.76       1.57       -0.0053    0.0048     0.0008     0.0013
```

B.9 Data for Figure 5.3(b)

```
TITLE = "Sphere: 4and8Hzb_march082007.dat"
VARIABLES = "X/L","Y/L","U/Vs ","V/Vs","err U/Vs","err V/Vs"
ZONE T="Sum" I=1 J=29 DATAPACKING=POINT
1.13       -0.18      0.0138     0.0252     0.0014     0.0019
1.13       -0.10      0.0125     0.0177     0.0014     0.0019
1.13       -0.03      0.0109     0.0097     0.0014     0.0019
1.13       0.05       0.0110     0.0019     0.0014     0.0020
1.13       0.12       0.0122     -0.0062    0.0014     0.0019
1.13       0.19       0.0140     -0.0127    0.0014     0.0019
1.13       0.27       0.0162     -0.0179    0.0015     0.0020
1.13       0.34       0.0183     -0.0190    0.0014     0.0020
1.13       0.42       0.0188     -0.0188    0.0014     0.0020
1.13       0.49       0.0174     -0.0146    0.0014     0.0021
1.13       0.57       0.0136     -0.0085    0.0015     0.0024
1.13       0.64       0.0078     -0.0010    0.0017     0.0023
1.13       0.71       0.0004     0.0061     0.0016     0.0021
1.13       0.79       -0.0059    0.0107     0.0014     0.0020
1.13       0.86       -0.0114    0.0152     0.0014     0.0019
1.13       0.94       -0.0165    0.0177     0.0014     0.0019
1.13       1.01       -0.0187    0.0186     0.0014     0.0019
1.13       1.08       -0.0201    0.0183     0.0014     0.0019
1.13       1.16       -0.0199    0.0176     0.0014     0.0020
1.13       1.23       -0.0193    0.0163     0.0014     0.0020
1.13       1.31       -0.0173    0.0148     0.0014     0.0020
1.13       1.38       -0.0151    0.0138     0.0014     0.0020
1.13       1.45       -0.0136    0.0130     0.0013     0.0019
1.13       1.53       -0.0119    0.0124     0.0014     0.0020
1.13       1.60       -0.0102    0.0118     0.0013     0.0019
1.13       1.68       -0.0088    0.0114     0.0015     0.0020
1.13       1.75       -0.0069    0.0115     0.0014     0.0020
1.13       1.82       -0.0058    0.0111     0.0013     0.0020
1.13       1.90       -0.0047    0.0110     0.0014     0.0020
ZONE T="Mult" I=1 J=29 DATAPACKING=POINT
1.13       -0.18      0.0153     0.0240     0.0010     0.0014
1.13       -0.10      0.0128     0.0162     0.0010     0.0014
1.13       -0.03      0.0112     0.0094     0.0012     0.0014
1.13       0.05       0.0108     0.0018     0.0009     0.0014
1.13       0.12       0.0121     -0.0062    0.0011     0.0014
1.13       0.19       0.0139     -0.0121    0.0010     0.0014
1.13       0.27       0.0164     -0.0163    0.0009     0.0014
1.13       0.34       0.0180     -0.0184    0.0009     0.0015
1.13       0.42       0.0183     -0.0176    0.0009     0.0015
1.13       0.49       0.0168     -0.0135    0.0010     0.0014
1.13       0.57       0.0138     -0.0086    0.0010     0.0014
1.13       0.64       0.0079     -0.0014    0.0010     0.0014
1.13       0.71       0.0017     0.0046     0.0010     0.0016
1.13       0.79       -0.0044    0.0099     0.0010     0.0016
1.13       0.86       -0.0098    0.0134     0.0011     0.0016
1.13       0.94       -0.0142    0.0152     0.0010     0.0015
```

```
1.13       1.01       -0.0166    0.0157     0.0010     0.0015
1.13       1.08       -0.0177    0.0154     0.0010     0.0015
1.13       1.16       -0.0176    0.0148     0.0010     0.0015
1.13       1.23       -0.0168    0.0137     0.0010     0.0015
1.13       1.31       -0.0156    0.0124     0.0010     0.0016
1.13       1.38       -0.0143    0.0110     0.0010     0.0015
1.13       1.45       -0.0123    0.0102     0.0010     0.0016
1.13       1.53       -0.0102    0.0092     0.0010     0.0015
1.13       1.60       -0.0087    0.0088     0.0010     0.0015
1.13       1.68       -0.0074    0.0084     0.0009     0.0016
1.13       1.75       -0.0066    0.0081     0.0010     0.0016
1.13       1.82       -0.0054    0.0078     0.0010     0.0015
1.13       1.90       -0.0045    0.0075     0.0010     0.0015
```

B.10 Data for Figure 5.5(b)

```
TITLE = "Sphere: 4and8Hza_march082007.dat"
VARIABLES = "X/L","Y/L","U/Vs ","V/Vs","err U/Vs","err V/Vs"
ZONE T="Sum" I=1 J=29 DATAPACKING=POINT
1.13       -0.18      0.0157     0.0267     0.0004     0.0006
1.13       -0.10      0.0132     0.0190     0.0004     0.0005
1.13       -0.03      0.0118     0.0113     0.0004     0.0005
1.13       0.05       0.0124     0.0019     0.0004     0.0007
1.13       0.12       0.0134     -0.0064    0.0004     0.0005
1.13       0.19       0.0158     -0.0138    0.0004     0.0005
1.13       0.27       0.0185     -0.0195    0.0004     0.0005
1.13       0.34       0.0206     -0.0223    0.0004     0.0005
1.13       0.42       0.0215     -0.0223    0.0004     0.0007
1.13       0.49       0.0204     -0.0189    0.0004     0.0010
1.13       0.57       0.0164     -0.0124    0.0004     0.0007
1.13       0.64       0.0107     -0.0051    0.0005     0.0008
1.13       0.71       0.0038     0.0017     0.0006     0.0010
1.13       0.79       -0.0038    0.0079     0.0007     0.0008
1.13       0.86       -0.0104    0.0123     0.0005     0.0007
1.13       0.94       -0.0154    0.0149     0.0004     0.0006
1.13       1.01       -0.0184    0.0160     0.0005     0.0007
1.13       1.08       -0.0196    0.0160     0.0004     0.0006
1.13       1.16       -0.0196    0.0151     0.0004     0.0006
1.13       1.23       -0.0187    0.0138     0.0004     0.0006
1.13       1.31       -0.0172    0.0123     0.0005     0.0007
1.13       1.38       -0.0151    0.0111     0.0004     0.0006
1.13       1.45       -0.0134    0.0103     0.0004     0.0006
1.13       1.53       -0.0113    0.0093     0.0004     0.0007
1.13       1.60       -0.0095    0.0088     0.0004     0.0007
1.13       1.68       -0.0079    0.0081     0.0004     0.0007
1.13       1.75       -0.0064    0.0077     0.0004     0.0007
1.13       1.82       -0.0052    0.0073     0.0004     0.0006
1.13       1.90       -0.0042    0.0074     0.0004     0.0007
ZONE T="Mult" I=1 J=29 DATAPACKING=POINT
1.13       -0.18      0.0161     0.0282     0.0003     0.0005
1.13       -0.10      0.0137     0.0208     0.0003     0.0005
```

```
1.13       -0.03      0.0122     0.0123     0.0003     0.0005
1.13       0.05       0.0121     0.0040     0.0003     0.0004
1.13       0.12       0.0130     -0.0039    0.0003     0.0004
1.13       0.19       0.0151     -0.0099    0.0005     0.0006
1.13       0.27       0.0168     -0.0146    0.0004     0.0005
1.13       0.34       0.0188     -0.0161    0.0003     0.0005
1.13       0.42       0.0191     -0.0154    0.0003     0.0005
1.13       0.49       0.0174     -0.0115    0.0003     0.0007
1.13       0.57       0.0136     -0.0062    0.0006     0.0011
1.13       0.64       0.0086     -0.0001    0.0003     0.0005
1.13       0.71       0.0028     0.0046     0.0006     0.0011
1.13       0.79       -0.0038    0.0102     0.0005     0.0006
1.13       0.86       -0.0092    0.0132     0.0003     0.0006
1.13       0.94       -0.0135    0.0155     0.0004     0.0006
1.13       1.01       -0.0164    0.0161     0.0005     0.0007
1.13       1.08       -0.0175    0.0158     0.0005     0.0007
1.13       1.16       -0.0176    0.0148     0.0005     0.0009
1.13       1.23       -0.0168    0.0133     0.0005     0.0009
1.13       1.31       -0.0155    0.0123     0.0005     0.0008
1.13       1.38       -0.0137    0.0110     0.0005     0.0008
1.13       1.45       -0.0118    0.0100     0.0006     0.0010
1.13       1.53       -0.0100    0.0090     0.0006     0.0010
1.13       1.60       -0.0085    0.0085     0.0004     0.0010
1.13       1.68       -0.0072    0.0080     0.0005     0.0009
1.13       1.75       -0.0056    0.0076     0.0005     0.0010
1.13       1.82       -0.0046    0.0073     0.0004     0.0011
1.13       1.90       -0.0037    0.0070     0.0004     0.0011
```

B.11 Data for Figure 5.8

```
TITLE = "Multiple Frequency Superposition"
VARIABLES = "eps","%matched"
ZONE T="Multiplier 1" I=1 J=20 DATAPACKING=POINT
0.16       53.2
0.21       55.9
0.27       37.5
0.16       83.4
0.30       14.6
0.15       53.8
0.21       56.2
0.31       43.7
0.32       21.5
0.32       20.5
0.32       24.5
0.31       6.1
0.31       14.0
0.20       73.4
0.15       67.9
0.07       88.9
0.10       84.9
0.16       67.3
```

```
0.22       70.4
0.28       21.1
ZONE T="Multiplier 2" I=1 J=20 DATAPACKING=POINT
0.16       85.8
0.21       96.9
0.27       83.7
0.16       98.4
0.30       58.9
0.15       99.2
0.21       92.9
0.31       86.4
0.32       51.6
0.32       49.3
0.32       52.9
0.31       38.9
0.31       44.1
0.20       95.2
0.15       92.3
0.07       94.1
0.10       93.9
0.16       97.7
0.22       98.4
0.28       66.1
ZONE T="Multiplier 3" I=1 J=20 DATAPACKING=POINT
0.16       97.4
0.21       99.8
0.27       99.1
0.16       99.2
0.30       87.0
0.15       100.0
0.21       97.8
0.31       96.4
0.32       72.0
0.32       72.4
0.32       71.1
0.31       63.4
0.31       73.8
0.20       97.7
0.15       97.5
0.07       94.3
0.10       94.4
0.16       99.8
0.22       100.0
0.28       95.5
```

B.12 Data for Figure 6.8

```
TITLE = "tan(theta) vs AR*tan(phi)"
VARIABLES = "tan(theta)", "AR*tan(phi)",  "err AR*tan(phi)"
ZONE T="AR=0.5", I=38, J=1, DATAPACKING=POINT
0.287      0.303      0.030
```

```
0.268      0.262      0.028
0.268      0.283      0.029
0.287      0.298      0.030
0.268      0.277      0.029
0.268      0.285      0.029
0.287      0.273      0.029
0.268      0.259      0.028
0.268      0.269      0.029
0.268      0.253      0.028
0.268      0.251      0.028
0.268      0.226      0.027
0.601      0.522      0.042
0.601      0.508      0.041
0.577      0.577      0.046
0.577      0.518      0.042
0.577      0.592      0.047
0.601      0.544      0.044
0.601      0.513      0.041
0.601      0.556      0.044
0.601      0.554      0.044
0.577      0.541      0.043
1.072      1.108      0.097
1.036      1.260      0.116
1.072      1.037      0.088
1.036      1.020      0.087
1.072      1.228      0.112
1.036      0.928      0.076
1.036      1.022      0.087
1.072      1.014      0.086
1.036      0.900      0.073
1.036      1.158      0.103
1.111      1.093      0.095
1.072      1.139      0.101
1.072      1.141      0.101
1.072      1.098      0.096
1.072      1.127      0.099
1.111      0.620      0.049
ZONE T="AR=0.76", I=3, J=1, DATAPACKING=POINT
1.000      1.024      0.060
1.000      1.022      0.060
1.000      1.036      0.061
ZONE T="AR=1.3", I=5, J=1, DATAPACKING=POINT
-0.966     -0.946     0.056
-0.933     -0.859     0.052
-0.933     -0.865     0.052
-0.601     -0.580     0.042
-0.601     -0.523     0.040
ZONE T="AR=2", I=3, J=1, DATAPACKING=POINT
-1.036     -0.921     0.074
-1.036     -1.071     0.081
-1.036     -1.090     0.082
```

B.13 Data for Figure 7.3

```
TITLE = "Distance to vortical centers"
VARIABLES = "Body orientation [deg.]", "Bottom [mm]", "Top [mm]"
ZONE T="4Hz, Re=2", I=10, J=1, DATAPACKING=POINT
0          2.37       2.17
15         2.97       1.84
30         4.43       1.16
30         4.88       1.19
30         4.24       1.35
45         3.48       0.70
45         5.25       0.52
45         5.18       0.55
45         4.05       0.57
45         4.22       0.68
ZONE T="8Hz, Re=3", I=13, J=1, DATAPACKING=POINT
0          2.19       1.95
0          2.00       2.09
15         2.61       1.77
15         2.45       1.86
30         2.30       1.61
30         2.55       1.51
30         2.77       1.42
30         2.56       1.49
30         2.48       1.62
45         2.57       1.07
45         2.81       1.09
45         3.44       0.98
45         2.73       1.11
ZONE T="12Hz, Re=5", I=12, J=1, DATAPACKING=POINT
0          1.90       1.88
0          1.80       1.99
15         1.98       1.92
15         2.00       1.89
30         1.72       2.19
30         1.68       2.34
30         1.80       1.98
30         1.71       2.18
45         1.92       1.64
45         1.80       1.68
45         1.95       1.68
45         1.83       1.72
ZONE T="16Hz, Re=7", I=4, J=1, DATAPACKING=POINT
0          1.79       1.73
0          1.77       1.77
15         1.75       1.86
15         1.70       1.91
```

B.14 Data for Figure 7.6 and 7.8

B.14.1 Scaling with *L*

```
TITLE="Max Velocity/Vorticity Chart for L"
VARIABLES="ReM","V/Vs","W/Ws"
ZONE T="AR=2, Th=0", I=6, J=1, DATAPACKING=POINT
145.3      0.209      0.106
96.8       0.177      0.099
96.9       0.181      0.102
48.4       0.143      0.098
48.4       0.146      0.101
48.4       0.164      0.110
ZONE T="AR=1.3, Th=0", I=11, J=1, DATAPACKING=POINT
109.6      0.221      0.109
109.6      0.222      0.112
109.6      0.235      0.112
73.1       0.210      0.115
73.1       0.212      0.111
73.1       0.218      0.115
36.5       0.171      0.100
36.5       0.174      0.116
36.5       0.179      0.112
42.0       0.186      0.114
42.0       0.190      0.116
ZONE T="AR=1, Th=0", I=18, J=1, DATAPACKING=POINT
90.0       0.230      0.103
90.0       0.221      0.103
30.0       0.187      0.111
30.0       0.180      0.115
103.4      0.239      0.106
103.4      0.234      0.102
82.7       0.230      0.098
68.9       0.230      0.111
68.9       0.221      0.104
55.2       0.214      0.117
55.2       0.205      0.111
27.6       0.192      0.139
27.6       0.180      0.133
41.8       0.200      0.117
41.8       0.202      0.116
60.0       0.218      0.120
60.0       0.217      0.103
60.0       0.210      0.122
ZONE T="AR=0.75, Th=0", I=9, J=1, DATAPACKING=POINT
41.9       0.220      0.084
41.9       0.220      0.078
41.9       0.228      0.085
27.9       0.202      0.089
27.9       0.202      0.088
27.9       0.410      0.170
14.0       0.165      0.093
14.0       0.337      0.181
5.6        0.110      0.110
ZONE T="AR=0.5, Th=0", I=12, J=1, DATAPACKING=POINT
9.7        0.163      0.095
```

```
1.9         0.076       0.103
14.6        0.209       0.073
14.6        0.219       0.079
14.6        0.224       0.079
9.7         0.191       0.079
9.7         0.189       0.081
9.7         0.188       0.085
4.9         0.137       0.079
4.9         0.141       0.091
4.9         0.140       0.093
1.9         0.082       0.084
ZONE T="AR=0.3, Th=0", I=8, J=1, DATAPACKING=POINT
2.4         0.171       0.054
2.4         0.166       0.058
1.6         0.134       0.056
1.6         0.133       0.053
0.8         0.091       0.053
0.8         0.085       0.051
0.8         0.085       0.052
0.3         0.046       0.044
ZONE T="AR=0.5, Th=15", I=12, J=1, DATAPACKING=POINT
15.9        0.224       0.068
15.1        0.222       0.074
15.5        0.232       0.074
10.4        0.207       0.087
10.1        0.201       0.093
10.1        0.014       0.007
5.2         0.147       0.087
5.3         0.146       0.097
4.9         0.140       0.091
2.1         0.085       0.085
2.0         0.092       0.082
2.1         0.109       0.131
ZONE T="AR=0.5, Th=30", I=10, J=1, DATAPACKING=POINT
14.5        0.178       0.080
13.8        0.201       0.092
13.4        0.180       0.082
9.1         0.176       0.081
8.9         0.182       0.080
8.7         0.181       0.081
4.4         0.143       0.068
4.5         0.142       0.082
4.3         0.140       0.095
1.8         0.084       0.080
ZONE T="AR=0.5, Th=45", I=14, J=1, DATAPACKING=POINT
9.4         0.177       0.071
9.8         0.167       0.061
4.8         0.130       0.076
4.8         0.107       0.062
14.7        0.198       0.086
14.3        0.196       0.061
14.3        0.182       0.075
```

```
9.3         0.172       0.066
9.5         0.152       0.060
4.8         0.100       0.055
4.8         0.116       0.068
4.8         0.090       0.059
1.9         0.076       0.075
1.9         0.074       0.090
ZONE T="AR=0.75, Th=45", I=3, J=1, DATAPACKING=POINT
12.9        0.139       0.122
38.5        0.199       0.101
47.5        0.209       0.106
ZONE T="AR=1.3, Th=-30", I=2, J=1, DATAPACKING=POINT
31.0        0.028       0.026
95.1        0.044       0.022
ZONE T="AR=2, Th=-45", I=3, J=1, DATAPACKING=POINT
40.5        0.233       0.193
121.5       0.392       0.164
150.2       0.408       0.160
ZONE T="AR=1.33, Th=-45", I=3, J=1, DATAPACKING=POINT
32.5        0.210       0.167
97.4        0.306       0.150
121.3       0.318       0.138
ZONE T="Groove, Th=0", I=7, J=1, DATAPACKING=POINT
26.9        0.271       1.130
53.8        0.656       2.005
53.8        0.625       1.956
80.6        0.933       2.407
80.6        0.927       1.852
107.5       1.240       2.186
107.5       1.239       2.140
ZONE T="Groove, Th=15", I=8, J=1, DATAPACKING=POINT
27.4        0.398       1.397
27.4        0.355       1.405
54.8        0.728       2.110
54.8        0.728       1.701
82.2        1.034       2.406
82.2        1.046       2.342
109.6       1.236       2.443
109.6       1.239       2.581
ZONE T="Groove, Th=30", I=15, J=1, DATAPACKING=POINT
27.3        0.383       1.545
54.5        0.676       1.926
54.5        0.714       2.121
81.8        0.966       1.979
81.8        0.842       1.930
109.0       0.784       1.486
109.0       0.786       1.512
27.8        0.463       1.892
27.8        0.416       1.776
55.7        0.759       2.192
55.7        0.749       2.307
83.5        1.076       2.105
```

```
83.5       1.028      2.016
111.4      0.854      1.582
111.4      0.838      1.547
ZONE T="Groove, Th=45", I=16, J=1, DATAPACKING=POINT
27.1       0.373      1.547
54.1       0.612      1.834
54.1       0.624      1.915
81.2       0.931      2.114
81.2       0.946      2.243
108.3      0.633      0.998
108.3      0.647      1.023
28.2       0.392      1.493
28.2       0.376      1.410
28.2       0.364      1.486
56.3       0.707      2.033
56.3       0.666      1.942
84.5       0.976      2.164
84.5       1.011      2.264
112.7      0.672      1.045
112.7      0.676      1.067
```

B.14.2 Scaling with *L**

```
TITLE="Max Velocity/Vorticity Chart for L*"
VARIABLES="ReM","V/Vs","W/Ws"
ZONE T="AR=2, Th=0", I=6, J=1, DATAPACKING=POINT
44.7       0.116      0.059
29.8       0.098      0.055
29.8       0.101      0.057
14.9       0.079      0.054
14.9       0.081      0.056
14.9       0.091      0.061
ZONE T="AR=1.3, Th=0", I=11, J=1, DATAPACKING=POINT
66.9       0.172      0.085
66.9       0.173      0.087
66.9       0.184      0.088
44.6       0.164      0.090
44.6       0.166      0.087
44.6       0.170      0.089
22.3       0.134      0.078
22.3       0.136      0.091
22.3       0.140      0.087
25.6       0.145      0.089
25.6       0.148      0.090
ZONE T="AR=1, Th=0", I=18, J=1, DATAPACKING=POINT
90.0       0.230      0.103
90.0       0.221      0.103
30.0       0.187      0.111
30.0       0.180      0.115
103.4      0.239      0.106
103.4      0.234      0.102
82.7       0.230      0.098
```

```
68.9       0.230      0.111
68.9       0.221      0.104
55.2       0.214      0.117
55.2       0.205      0.111
27.6       0.192      0.139
27.6       0.180      0.133
41.8       0.200      0.117
41.8       0.202      0.116
60.0       0.218      0.120
60.0       0.217      0.103
60.0       0.210      0.122
ZONE T="AR=0.75, Th=0", I=9, J=1, DATAPACKING=POINT
66.4       0.277      0.106
66.4       0.277      0.098
66.4       0.287      0.107
44.3       0.255      0.113
44.3       0.254      0.111
44.3       0.516      0.215
22.1       0.208      0.117
22.1       0.425      0.228
8.9        0.138      0.139
ZONE T="AR=0.5, Th=0", I=12, J=1, DATAPACKING=POINT
29.5       0.283      0.165
5.9        0.133      0.179
44.3       0.364      0.128
44.3       0.381      0.137
44.3       0.391      0.137
29.5       0.333      0.137
29.5       0.330      0.141
29.5       0.328      0.147
14.8       0.239      0.137
14.8       0.246      0.158
14.8       0.243      0.161
5.9        0.142      0.147
ZONE T="AR=0.3, Th=0", I=8, J=1, DATAPACKING=POINT
22.3       0.517      0.164
22.3       0.502      0.177
14.9       0.405      0.169
14.9       0.403      0.162
7.4        0.276      0.159
7.4        0.257      0.154
7.4        0.256      0.157
3.0        0.140      0.134
ZONE T="AR=0.5, Th=15", I=12, J=1, DATAPACKING=POINT
45.8       0.380      0.116
45.0       0.383      0.127
45.2       0.395      0.127
30.1       0.354      0.149
30.0       0.347      0.160
29.8       0.025      0.012
15.1       0.251      0.149
15.3       0.248      0.164
```

```
14.8       0.244      0.159
6.0        0.146      0.144
6.0        0.159      0.142
6.0        0.186      0.224
ZONE T="AR=0.5, Th=30", I=10, J=1, DATAPACKING=POINT
43.9       0.309      0.139
43.0       0.356      0.162
42.8       0.323      0.147
28.8       0.313      0.144
28.7       0.327      0.143
28.2       0.326      0.147
14.3       0.256      0.123
14.3       0.254      0.146
14.1       0.253      0.171
5.7        0.150      0.143
ZONE T="AR=0.5, Th=45", I=14, J=1, DATAPACKING=POINT
29.3       0.311      0.125
29.3       0.288      0.105
14.9       0.228      0.134
14.5       0.186      0.108
44.2       0.342      0.149
44.2       0.346      0.107
44.2       0.320      0.131
29.2       0.304      0.117
29.6       0.269      0.106
14.6       0.175      0.095
14.5       0.201      0.119
14.6       0.157      0.104
5.8        0.132      0.132
5.8        0.129      0.157
ZONE T="AR=0.75, Th=45", I=3, J=1, DATAPACKING=POINT
20.2       0.174      0.153
60.9       0.250      0.128
75.8       0.264      0.134
ZONE T="AR=1.3, Th=-30", I=2, J=1, DATAPACKING=POINT
19.2       0.022      0.020
58.0       0.035      0.017
ZONE T="AR=2, Th=-45", I=3, J=1, DATAPACKING=POINT
13.1       0.133      0.110
39.4       0.223      0.093
49.0       0.233      0.092
ZONE T="AR=1.33, Th=-45", I=3, J=1, DATAPACKING=POINT
20.0       0.165      0.131
60.0       0.240      0.118
75.5       0.251      0.109
ZONE T="Groove, Th=0", I=7, J=1, DATAPACKING=POINT
43.4       0.344      1.436
86.8       0.833      2.548
86.8       0.794      2.485
130.2      1.185      3.059
130.2      1.178      2.353
173.6      1.575      2.777
```

```
173.6      1.575      2.720
ZONE T="Groove, Th=15", I=8, J=1, DATAPACKING=POINT
44.2       0.505      1.774
44.2       0.451      1.785
88.4       0.925      2.681
88.4       0.925      2.162
132.7      1.313      3.058
132.7      1.329      2.976
176.9      1.570      3.105
176.9      1.575      3.280
ZONE T="Groove, Th=30", I=15, J=1, DATAPACKING=POINT
44.0       0.486      1.963
88.0       0.859      2.447
88.0       0.907      2.695
132.0      1.227      2.515
132.0      1.069      2.452
176.0      0.997      1.888
176.0      0.998      1.921
44.9       0.588      2.404
44.9       0.528      2.257
89.9       0.965      2.785
89.9       0.952      2.931
134.8      1.368      2.674
134.8      1.307      2.561
179.8      1.085      2.010
179.8      1.065      1.965
ZONE T="Groove, Th=45", I=16, J=1, DATAPACKING=POINT
43.7       0.474      1.966
87.4       0.777      2.331
87.4       0.793      2.433
131.1      1.183      2.687
131.1      1.201      2.851
174.8      0.805      1.268
174.8      0.822      1.299
45.5       0.498      1.897
45.5       0.478      1.791
45.5       0.463      1.889
91.0       0.898      2.583
91.0       0.847      2.467
136.4      1.240      2.749
136.4      1.284      2.877
181.9      0.854      1.328
181.9      0.859      1.356
```

B.15 Data for Figure 7.9

```
TITLE = "Theta vs A"
VARIABLES = "Theta (deg)", "A (deg)", "err A"
ZONE T="Re=1.7,eps=0.1", I=6, J=1, DATAPACKING=POINT
0          7.11       1.51
15         -4.24      1.60
```

```
30          -18.95      1.60
30          -18.57      1.60
45          -25.77      1.60
45          -29.16      1.54
ZONE T="Re=1.7,eps=0.2", I=6, J=1, DATAPACKING=POINT
0           -1.58       1.50
15          -7.81       1.59
30          -9.36       1.60
30          -11.85      1.61
45          -27.92      1.60
45          -26.16      1.58
ZONE T="Re=1.7,eps=0.36", I=2, J=1, DATAPACKING=POINT
30          -12.29      1.60
45          -26.16      1.57
ZONE T="Re=3.4,eps=0.1", I=6, J=1, DATAPACKING=POINT
0           0.93        1.50
15          8.98        1.58
30          -0.20       1.60
30          4.43        1.60
45          2.74        1.60
45          -2.40       1.60
ZONE T="Re=3.4,eps=0.2", I=6, J=1, DATAPACKING=POINT
0           0.22        1.50
15          5.09        1.59
30          2.19        1.60
30          8.48        1.60
45          -0.66       1.59
45          0.71        1.57
ZONE T="Re=3.4,eps=0.36", I=1, J=1, DATAPACKING=POINT
30          7.42        1.59
ZONE T="Re=5,eps=0.1", I=6, J=1, DATAPACKING=POINT
0           1.08        1.51
15          8.03        1.59
30          15.92       1.60
30          14.53       1.59
45          9.44        1.58
45          17.44       1.55
ZONE T="Re=5,eps=0.2", I=6, J=1, DATAPACKING=POINT
0           -1.98       1.50
15          9.13        1.59
30          17.36       1.60
30          19.79       1.60
45          14.60       1.57
45          20.25       1.56
ZONE T="Re=7,eps=0.1", I=6, J=1, DATAPACKING=POINT
0           1.92        1.50
15          5.12        1.59
30          -3.23       1.61
30          3.74        1.59
45          -8.35       1.58
45          -7.27       1.57
ZONE T="Re=7,eps=0.2", I=6, J=1, DATAPACKING=POINT
```

```
0          0.71       1.50
15         4.53       1.58
30         0.10       1.60
30         1.30       1.60
45         -3.53      1.59
45         -3.36      1.57
```

B.16 Data for Figure 8.7

```
TITLE="ReM vs MaxSpeed"
VARIABLES="ReM","Vmax/Vs"
ZONE T="0A", I =9,  J = 1, DATAPACKING = POINT
30.8       0.326
45.6       0.421
46.6       0.353
60.8       0.502
60.9       0.486
77.0       0.532
77.0       0.561
90.5       0.595
90.7       0.626
ZONE T="0B", I =11,  J = 1, DATAPACKING = POINT
30.6       0.297
30.6       0.305
44.7       0.351
45.0       0.279
45.2       0.342
60.8       0.390
60.9       0.392
75.4       0.388
75.8       0.415
89.5       0.421
90.0       0.422
ZONE T="30A", I =12,  J = 1, DATAPACKING = POINT
32.9       0.284
32.9       0.260
34.1       0.252
49.5       0.363
51.2       0.323
67.2       0.431
67.7       0.394
82.8       0.534
83.3       0.474
101.8      0.476
103.3      0.525
103.3      0.605
ZONE T="30B", I =10,  J = 1, DATAPACKING = POINT
29.0       0.186
29.0       0.183
43.1       0.234
43.1       0.239
```

```
57.5       0.271
57.8       0.274
71.9       0.306
72.1       0.301
85.7       0.334
85.9       0.337
ZONE T="45A", I =10,  J = 1, DATAPACKING = POINT
31.3       0.197
31.3       0.214
47.0       0.232
47.4       0.235
62.6       0.283
62.8       0.275
78.9       0.327
78.9       0.324
92.9       0.387
93.1       0.378
ZONE T="45B", I =10,  J = 1, DATAPACKING = POINT
28.8       0.167
28.8       0.161
42.7       0.188
42.9       0.183
57.2       0.213
57.2       0.210
71.6       0.255
71.6       0.261
85.5       0.309
85.5       0.313
ZONE T="75A", I =10,  J = 1, DATAPACKING = POINT
28.5       0.086
28.5       0.180
42.0       0.137
42.5       0.116
57.0       0.143
57.0       0.146
70.9       0.164
70.9       0.169
82.9       0.192
82.9       0.194
ZONE T="75B", I =10,  J = 1, DATAPACKING = POINT
29.6       0.117
29.8       0.139
43.4       0.163
43.4       0.173
58.6       0.209
59.0       0.096
72.3       0.244
73.1       0.259
86.3       0.272
86.6       0.207
```

B.17 Data for Figure 8.9

```
TITLE="ReM vs MaxVort"
VARIABLES="ReM","Wmax/Ws"
ZONE T="0A", I =8,  J = 1, DATAPACKING = POINT
30.8       0.652
30.8       0.630
45.6       0.665
46.6       0.642
60.9       0.705
60.8       0.672
77.0       0.873
77.0       0.704
90.5       1.134
90.7       0.709
ZONE T="0B", I =10,  J = 1, DATAPACKING = POINT
30.6       0.467
30.6       0.522
44.7       0.483
45.0       0.507
60.8       0.502
60.9       0.528
75.4       0.511
75.8       0.422
89.5       0.480
90.0       0.490
ZONE T="30A", I =12,  J = 1, DATAPACKING = POINT
32.9       0.619
32.9       0.664
34.1       0.638
49.5       0.752
51.2       0.716
67.2       0.973
67.7       0.748
82.8       0.779
83.3       0.753
101.8      1.077
103.3      1.052
103.3      1.039
ZONE T="30B", I =10,  J = 1, DATAPACKING = POINT
29.0       0.494
29.0       0.471
43.1       0.540
43.1       0.572
57.5       0.553
57.8       0.556
71.9       0.576
72.1       0.567
85.7       0.586
85.9       0.595
ZONE T="45A", I =10,  J = 1, DATAPACKING = POINT
```

```
31.3       0.423
31.3       0.474
47.0       0.753
47.4       0.471
62.6       0.841
62.8       0.708
78.9       1.004
78.9       0.823
92.9       1.133
93.1       1.009
ZONE T="45B", I =10,  J = 1, DATAPACKING = POINT
28.8       0.390
28.8       0.419
42.7       0.429
42.9       0.428
57.2       0.461
57.2       0.466
71.6       0.487
71.6       0.475
85.5       0.535
85.5       0.519
ZONE T="75A", I =8,  J = 1, DATAPACKING = POINT
28.5       0.177
28.5       0.132
42.0       0.225
42.5       0.210
57.0       0.241
57.0       0.248
70.9       0.262
70.9       0.275
82.9       0.302
82.9       0.355
ZONE T="75B", I=8,  J = 1, DATAPACKING = POINT
29.6       0.221
29.8       0.207
43.4       0.244
43.4       0.255
58.6       0.388
59.0       0.283
72.3       0.281
73.1       0.320
86.3       0.390
86.6       0.273
```

APPENDIX C

LIST OF EXPERIMENTAL CASES

C.1 Axisymmetric Cases

The first set of test cases consists of axisymmetric spheroidal bodies oscillated at a single frequency. The bodies were constructed of molded polyurethane (the spheroids) or colored acrylic (the sphere). The bodies were illuminated from both sides. The displacement was measured using an LVDT. The kinematic viscosity was determined from the composition of the solution and a typical temperature measurement. With the exception of 3 test cases, the oscillation frequency was equal to the frame rate. The exceptions are october032005/10Hzg (frame rate of 5 Hz), october032005/5Hzc (frame rate of 2.5 Hz), and march302005/15Hza (frame rate of 7.5 Hz).

The bodies tested are described in Table C.1. The test cases are described in Table C.2.

Table C.1 Description of axisymmetric experimental bodies.

Body designation	**Body description**	***AR* = *a*/*b***	***a* [mm]**	***b* [mm]**	**Equivalent radius [mm]**	***L* [mm]**
PS1	1:2 prolate spheroid	2.03	12.75	6.29	7.96	16.14
PS2	3:4 prolate spheroid	1.35	12.70	9.44	10.42	14.02
S1	1" diameter sphere	1.00	12.70	12.70	12.70	12.70
OS1	3:4 oblate spheroid	0.76	9.51	12.52	11.42	8.67
OS2	1:2 oblate spheroid	0.51	6.39	12.43	9.96	5.12
OS3	1:4 oblate spheroid	0.27	3.26	12.29	7.90	2.09

Table C.2 List of experimental test cases for axisymmetric bodies.

Folder	Test files	Body designation	θ (nominal) [deg.]	θ (measured) [deg.]	f [Hz]	s [mm]	$\varepsilon = s/L$	ν [mm^2/s]	$Re = \omega s L/\nu$	$Re_M = \omega L^2/\nu$	$Re_s = \omega s^2/\nu$	px/mm	Number of images
april012005	15Hza	PS1	0	n/a	15.0	2.41	0.15	169	21.72	145.18	3.25	17.8	136
april012005	10Hza	PS1	0	n/a	10.0	2.50	0.16	169	15.00	96.79	2.33	17.8	136
april012005	10Hzb	PS1	0	n/a	10.0	1.23	0.08	169	7.36	96.79	0.56	17.8	136
july252005	5Hzb	PS1	0	n/a	5.0	2.41	0.15	169	7.24	48.40	1.08	18.5	204
july252005	5Hzc	PS1	0	n/a	5.0	1.20	0.07	169	3.59	48.40	0.27	18.5	204
july252005	5Hzd	PS1	0	n/a	5.0	0.59	0.04	169	1.77	48.40	0.07	18.5	204
october062005	15Hza	PS2	0	n/a	15.0	2.62	0.19	169	20.49	109.71	3.83	15.8	195
october062005	15Hzb	PS2	0	n/a	15.0	1.31	0.09	169	10.28	109.71	0.96	15.8	195
october062005	15Hzc	PS2	0	n/a	15.0	0.65	0.05	169	5.11	109.71	0.24	15.8	195
october062005	10Hza	PS2	0	n/a	10.0	2.39	0.17	169	12.47	73.12	2.13	15.8	195
october062005	10Hzb	PS2	0	n/a	10.0	1.28	0.09	169	6.66	73.12	0.61	15.8	195
october062005	10Hzc	PS2	0	n/a	10.0	0.64	0.05	169	3.33	73.13	0.15	15.8	195
october062005	5Hza	PS2	0	n/a	5.0	2.57	0.18	169	6.69	36.57	1.22	15.8	195
october062005	5Hzb	PS2	0	n/a	5.0	1.28	0.09	169	3.33	36.56	0.30	15.8	195
october062006	5Hzc	PS2	0	n/a	5.0	0.63	0.05	169	1.65	36.56	0.07	15.8	195
november152005	6ishHza	PS2	0	n/a	5.7	2.17	0.15	169	6.50	42.04	1.01	16.6	195
november152005	6ishHzb	PS2	0	n/a	5.8	2.16	0.15	169	6.48	42.05	1.00	16.6	195
september212005	15Hzc	S1	0	n/a	15.0	2.45	0.19	169	17.33	89.97	3.34	14.5	195
september212005	15Hzb	S1	0	n/a	15.0	1.21	0.09	169	8.54	89.97	0.81	14.5	195
september212005	5Hzd	S1	0	n/a	5.0	2.50	0.20	169	5.91	29.98	1.17	14.5	195
september212005	5Hze	S1	0	n/a	5.0	1.24	0.10	169	2.93	29.98	0.29	14.5	195
november162005	7ishHza	S1	0	n/a	7.0	1.99	0.16	169	6.54	41.80	1.02	15.6	195
november162005	7ishHzb	S1	0	n/a	7.0	1.98	0.16	169	6.52	41.80	1.02	15.5	195
november162005	10Hza	S1	0	n/a	10.0	2.34	0.18	169	11.05	59.96	2.03	15.5	195

Table C.2 (continued).

november162005	10Hzb	S1	0	n/a	10.0	1.26	0.10	169	5.93	59.96	0.59	15.6	195
november162005	10Hzc	S1	0	n/a	10.0	0.63	0.05	169	2.97	59.96	0.15	15.5	195
january132006	15Hzc	S1	0	n/a	15.0	2.46	0.19	147	20.01	103.44	3.87	16.9	195
january132006	15Hzd	S1	0	n/a	15.0	1.22	0.10	147	9.97	103.44	0.96	17.0	195
january132006	12Hza	S1	0	n/a	12.0	2.21	0.17	147	14.41	82.70	2.51	17.0	195
january132006	12Hzb	S1	0	n/a	12.0	1.08	0.09	147	7.03	82.70	0.60	17.0	195
january132006	10Hza	S1	0	n/a	10.0	2.32	0.18	147	12.61	68.95	2.31	17.0	195
january132006	10Hzb	S1	0	n/a	10.0	1.25	0.10	147	6.77	68.95	0.66	17.0	195
january132006	8Hza	S1	0	n/a	8.0	2.29	0.18	147	9.94	55.16	1.79	17.0	195
january132006	8Hzb	S1	0	n/a	8.0	1.12	0.09	147	4.88	55.16	0.43	17.0	195
january132006	4Hza	S1	0	n/a	4.0	2.53	0.20	147	5.50	27.57	1.10	17.0	195
january132006	4Hzb	S1	0	n/a	4.0	1.25	0.10	147	2.72	27.57	0.27	17.0	195
october032005	15Hzd	OS1	0	n/a	15.0	2.62	0.30	169	12.68	41.97	3.83	14.7	195
october032005	15Hze	OS1	0	n/a	15.0	1.31	0.15	169	6.33	41.97	0.95	14.7	195
october032005	15Hzf	OS1	0	n/a	15.0	0.65	0.07	169	3.13	41.97	0.23	14.7	195
october032005	10Hzb	OS1	0	n/a	10.0	2.32	0.27	169	7.47	27.97	1.99	14.7	195
october032005	10Hzc	OS1	0	n/a	10.0	1.23	0.14	169	3.98	27.97	0.57	14.7	195
october032005	10Hzg	OS1	0	n/a	10.0	0.62	0.07	169	2.00	27.97	0.14	14.7	195
october032005	5Hza	OS1	0	n/a	5.0	2.53	0.29	169	4.08	13.99	1.19	14.7	195
october032005	5Hzc	OS1	0	n/a	5.0	1.26	0.15	169	2.04	13.99	0.30	14.7	195
october032005	2Hza	OS1	0	n/a	2.0	2.56	0.30	169	1.65	5.59	0.49	14.7	195
march302005	15Hza	OS2	0	1.7	15.0	2.38	0.47	169	6.81	14.63	3.17	19.8	136
march302005	10Hza	OS2	0	1.7	10.0	2.44	0.48	169	4.65	9.75	2.22	19.8	136
march302005	2Hza	OS2	0	1.6	2.0	2.42	0.47	169	0.92	1.95	0.43	19.8	136
october312005	15Hza	OS2	0	2.0	15.0	2.40	0.47	169	6.87	14.63	3.22	16.1	195
october312005	15Hzb	OS2	0	1.5	15.0	1.19	0.23	169	3.40	14.63	0.79	16.1	195
october312005	15Hzc	OS2	0	1.7	15.0	0.59	0.12	169	1.70	14.63	0.20	16.1	195

Table C.2 (continued).

october312005	10Hza	OS2	0	1.7	10.0	2.29	0.45	169	4.36	9.75	1.95	16.1	195
october312005	10Hzb	OS2	0	1.6	10.0	1.23	0.24	169	2.33	9.75	0.56	16.1	195
october312005	10Hzc	OS2	0	1.9	10.0	0.61	0.12	169	1.17	9.75	0.14	16.1	195
october312005	5Hza	OS2	0	1.8	5.0	2.52	0.49	169	2.40	4.88	1.18	16.1	195
october312005	5Hzb	OS2	0	1.6	5.0	1.26	0.25	169	1.20	4.88	0.29	16.1	195
october312005	5Hzc	OS2	0	1.8	5.0	0.63	0.12	169	0.60	4.88	0.07	16.1	195
october312005	2Hza	OS2	0	1.5	2.0	2.58	0.50	169	0.98	1.95	0.49	16.1	195
october052005	15Hza	OS3	0	n/a	15.0	2.57	1.23	169	3.00	2.45	3.69	16.0	195
october052005	15Hzb	OS3	0	n/a	15.0	1.28	0.61	169	1.49	2.45	0.91	16.0	195
october052005	15Hzc	OS3	0	n/a	15.0	0.64	0.30	169	0.74	2.45	0.23	16.0	195
october052005	10Hza	OS3	0	n/a	10.0	2.36	1.13	169	1.84	1.63	2.08	16.0	195
october052005	10Hzb	OS3	0	n/a	10.0	1.27	0.61	169	0.99	1.63	0.60	16.0	195
october052005	10Hzc	OS3	0	n/a	10.0	0.64	0.30	169	0.49	1.63	0.15	16.0	195
october052005	5Hza	OS3	0	n/a	5.0	2.54	1.21	169	0.99	0.82	1.20	16.0	195
october052005	5Hzb	OS3	0	n/a	5.0	1.27	0.61	169	0.49	0.82	0.30	16.0	195
october052005	5Hzc	OS3	0	n/a	5.0	0.63	0.30	169	0.25	0.82	0.07	16.0	195
october052005	2Hza	OS3	0	n/a	2.0	2.58	1.23	169	0.40	0.33	0.49	16.0	195
may212008	OS1_4Hza	OS1	0	n/a	4.00	0.88	0.10	161	1.19	11.73	0.12	25.8	300
may212008	OS1_12Hza	OS1	0	n/a	12.00	0.87	0.10	161	3.54	35.21	0.36	25.8	300
may212008	OS2_4Hza	OS2	0	n/a	4.00	0.56	0.11	160	0.45	4.12	0.05	28.6	300
may212008	OS2_12Hza	OS2	0	n/a	12.00	0.51	0.10	160	1.24	12.35	0.12	28.6	300
may212008	OS2_12Hzb	OS2	0	n/a	12.00	0.26	0.05	160	0.62	12.36	0.03	28.6	300
may212008	OS3_12Hze	OS3	0	n/a	12.00	0.42	0.20	161	0.42	2.05	0.08	30.8	300

C.2 Angled Cases

The second set of test cases consists of angled spheroidal bodies oscillated at a single frequency. The bodies were constructed of molded polyurethane and illuminated from both sides. The displacement was measured using an LVDT. The kinematic viscosity was determined from the composition of the solution and a typical temperature measurement. The frame rate was equal to the oscillation frequency for these test cases.

A description of the test bodies may be found in Table C.3. A description of the experimental test cases may be found in Table C.4.

Table C.3 Description of angled experimental bodies.

Body designation	**Body description**	***AR* = *a*/*b***	***a* [mm]**	***b* [mm]**	**Equivalent radius [mm]**	***L* [mm]**	***L**** **[mm]**
OS2_15	15° tilt, 1:2 oblate	0.52	6.52	12.43	10.03	5.26	9.00
OS2_30	30° tilt, 1:2 oblate	0.50	6.20	12.42	9.85	4.92	8.78
OS2_45	45° tilt, 1:2 oblate	0.51	6.35	12.42	9.93	5.08	8.88
PS1_45	45° tilt, 1:2 prolate	1.96	12.30	6.27	7.85	15.40	8.78
OS1_45	45° tilt, 3:4 oblate	0.76	9.51	12.51	11.42	8.68	10.91
OS1_30	30° tilt, 3:4 prolate	1.34	12.62	9.41	10.38	13.92	10.90
PS2_45	45° tilt, 3:4 prolate	1.33	12.55	9.41	10.36	13.81	10.87

Table C.4 List of experimental test cases for angled bodies.

Folder	Test files	Body designation	θ (nominal) [deg.]	θ (measured) [deg.]	f [Hz]	s [mm]	$\varepsilon^* = s/L^*$	ν [mm^2/s]	$Re_M^* = \omega L^{*2}/\nu$	$Re_M = \omega L^2/\nu$	$Re_s = \omega s^2/\nu$	px/mm	Number of images
november032005	15Hza	OS2_15	15	15	15.00	2.47	0.27	169	45.2	15.43	3.41	16.4	195
november032005	15Hzb	OS2_15	15	15	15.00	1.21	0.13	169	45.2	15.43	0.82	16.4	195
november032005	15Hzc	OS2_15	15	15	15.00	0.60	0.07	169	45.2	15.43	0.20	16.4	195
november032005	10Hza	OS2_15	15	15	10.00	2.35	0.26	169	30.1	10.28	2.05	16.4	195
november032005	10Hzb	OS2_15	15	15	10.00	1.25	0.14	169	30.1	10.28	0.58	16.4	195
november032005	10Hzc	OS2_15	15	15	10.00	2.35	0.26	169	30.1	10.28	2.05	16.4	195
november032005	5Hza	OS2_15	15	15	5.00	2.51	0.28	169	15.1	5.14	1.17	16.4	195
november032005	5Hzb	OS2_15	15	15	5.00	1.26	0.14	169	15.1	5.14	0.30	16.4	195
november032005	5Hzc	OS2_15	15	15	5.00	0.63	0.07	169	15.1	5.14	0.07	16.4	195
november032005	2Hza	OS2_15	15	15	2.00	2.58	0.29	169	6.0	2.06	0.49	16.4	195
november032005	2Hzb	OS2_15	15	15	2.00	1.30	0.14	169	6.0	2.06	0.12	16.4	195
november032005	2Hzc	OS2_15	15	15	2.00	0.64	0.07	169	6.0	2.06	0.03	16.4	195
november012005	15Hza	OS2_30	30	31	15.00	2.54	0.29	169	43.0	13.51	3.59	16.3	195
november012005	15Hzb	OS2_30	30	31	15.00	1.26	0.14	169	43.0	13.51	0.88	16.3	195
november012005	15Hzc	OS2_30	30	31	15.00	0.62	0.07	169	43.0	13.51	0.22	16.3	195
november012005	10Hza	OS2_30	30	31	10.00	2.34	0.27	169	28.6	9.00	2.03	16.3	195
november012005	10Hzb	OS2_30	30	31	10.00	1.25	0.14	169	28.6	9.00	0.58	16.3	195
november012005	10Hzc	OS2_30	30	31	10.00	0.63	0.07	169	28.6	9.00	0.15	16.3	195
november012005	5Hza	OS2_30	30	31	5.00	2.56	0.29	169	14.3	4.50	1.21	16.3	195
november012005	5Hzb	OS2_30	30	31	5.00	1.28	0.15	169	14.3	4.50	0.30	16.3	195
november012005	5Hzc	OS2_30	30	31	5.00	0.64	0.07	169	14.3	4.50	0.08	16.3	195
november012005	2Hza	OS2_30	30	31	2.00	2.59	0.30	169	5.7	1.80	0.50	16.3	195
november052005	10Hzd	OS2_45	45	47	10.00	2.37	0.27	169	29.3	9.58	2.09	16.3	195
november052005	10Hze	OS2_46	45	47	10.00	1.27	0.14	169	29.3	9.58	0.60	16.3	195

Table C.4 (continued).

november052005	5Hzd	OS2_47	45	47	5.00	2.56	0.29	169	14.7	4.79	1.22	16.3	195
november052005	5Hze	OS2_48	45	47	5.00	1.28	0.14	169	14.7	4.79	0.30	16.3	195
october282005	15Hza	OS2_49	45	47	15.00	2.49	0.28	169	44.0	14.38	3.46	16.2	195
october282005	15Hzb	OS2_50	45	47	15.00	1.23	0.14	169	44.0	14.38	0.84	16.2	195
october282005	15Hzc	OS2_51	45	47	15.00	0.61	0.07	169	44.0	14.38	0.21	16.2	195
october282005	10Hza	OS2_52	45	47	10.00	2.32	0.26	169	29.3	9.58	1.99	16.2	195
october282005	10Hzb	OS2_53	45	47	10.00	1.24	0.14	169	29.3	9.58	0.57	16.2	195
october282005	10Hzc	OS2_54	45	47	10.00	0.62	0.07	169	29.3	9.58	0.14	16.2	195
october282005	5Hza	OS2_55	45	47	5.00	2.53	0.28	169	14.7	4.79	1.19	16.2	195
october282005	5Hzb	OS2_56	45	47	5.00	1.26	0.14	169	14.7	4.79	0.30	16.2	195
october282005	5Hzc	OS2_57	45	47	5.00	0.63	0.07	169	14.7	4.79	0.07	16.2	195
october282005	2Hza	OS2_58	45	47	2.00	2.58	0.29	169	5.9	1.92	0.50	16.2	195
october282005	2Hzb	OS2_59	45	47	2.00	1.30	0.15	169	5.9	1.92	0.13	16.2	195
october282005	2Hzc	OS2_60	45	47	2.00	0.65	0.07	169	5.9	1.92	0.03	16.2	195
january282006	4Hzb	PS1_45	45	46	4.00	1.25	0.14	148	13.1	40.25	0.26	18.5	195
january282006	12Hzb	PS1_45	45	46	12.00	1.27	0.14	148	39.3	120.72	0.82	18.5	195
january282006	15Hzb	PS1_45	45	46	15.00	1.19	0.14	148	49.2	150.97	0.90	18.5	195
january282006	4Hzc	PS2_45	45	43	4.00	1.26	0.12	148	20.2	32.38	0.27	19.3	195
january282006	12Hzc	PS2_45	45	43	12.00	1.28	0.12	148	60.6	97.12	0.84	19.3	195
january282006	15Hzc	PS2_45	45	43	15.00	1.22	0.11	148	75.8	121.46	0.94	19.3	195
january282006	4Hzd	OS1_45	45	45	4.00	1.26	0.12	148	20.2	12.81	0.27	19.2	195
january282006	12Hzd	OS1_45	45	45	12.00	1.28	0.12	148	60.5	38.41	0.84	19.2	195
january282006	15Hzd	OS1_45	45	45	15.00	1.23	0.11	148	75.7	48.05	0.97	19.2	195
february202006	4Hza	OS1_30	30	31	4.00	3.24	0.30	155	19.1	31.41	1.70	20.0	195
february202006	12Hza	OS1_30	30	31	12.00	3.65	0.34	155	57.4	94.22	6.48	20.0	195

C.3 Variation in Phase Cases

The variation in phase data comes from imaging the oscillating clear acrylic sphere (similar to S1 in Table C.1) at the top middle and bottom of its oscillation. The sphere was illuminated from the right. The kinematic viscosity was determined from the fluid composition and the average measured temperature. The frame rate was equal to the oscillation frequency for these test cases.

The test description is found in Table C.5.

Table C.5 List of experimental cases for variation in phase.

Folder	Test files	Body designation	θ (nominal) [deg.]	θ (measured) [deg.]	f [Hz]	s [mm]	$\varepsilon = s/L$	ν [mm2/s]	$Re = \omega s L/\nu$	$Re_M = \omega L^2/\nu$	$Re_s = \omega s^2/\nu$	px/mm	Number of images
february202007	8Hzbotsubavg	S1	0	n/a	8	1.35	0.11	141.97	6.05	57.11	0.64	25.1	300
february202007	8Hztopsubavg	S1	0	n/a	8	1.35	0.11	141.97	6.05	57.11	0.64	25.1	300
february202007	8Hzsub	S1	0	n/a	8	1.35	0.11	141.97	6.05	57.11	0.64	25.1	300

C.4 Multiple Frequency Cases

Three clear acrylic bodies were oscillated (vertically relative to the images) in a pattern formed from either a sinusoid or the sum of two sinusoids. The bodies were illuminated from one side, shown as the right side of the images, and imaged at the center of the oscillation.

The oscillation is described by:

$$y(t) = s_1 \sin(2\pi f_1 t) + s_2 \sin(2\pi f_2 t) = L\left[\varepsilon_1 \sin(2\pi f_1 t) + \varepsilon_2 \sin(2\pi f_2 t)\right] \qquad \text{C.1}$$

Recall from Chapter 2 that for multiple frequency flows, some dimensionless parameters maybe defined in terms of the maximum oscillation velocity U_∞ and a base frequency f_0.

$$Re_1 = \frac{U_\infty L}{\nu} = \frac{2\pi L^2 (f_1\varepsilon_1 + f_2\varepsilon_2)}{\nu} \qquad \text{C.2}$$

$$\varepsilon^* \equiv \frac{U_\infty}{2\pi f_0 L} = \frac{f_1\varepsilon_1 + f_2\varepsilon_2}{f_0} \qquad \text{C.3}$$

$$V_s = \varepsilon^* U_\infty = \frac{U_\infty^2}{2\pi f_0 L} = \frac{2\pi L (f_1\varepsilon_1 + f_2\varepsilon_2)^2}{f_0} \qquad \text{C.4}$$

A description of the spheroids may be found in Table C.6. A description of the experimental test cases may be found in Table C.7. A description of the dimensionless parameters for these cases may be found in Table C.8.

Table C.6 Description of experimental bodies used for multiple frequency cases.

Body designation	**Body description**	***AR* = *a*/*b***	***a* [mm]**	***b* [mm]**	**Equivalent radius [mm]**	***L* [mm]**
S1	Sphere	1.00	12.70	12.70	12.70	12.70
PS3	Prolate Spheroid	1.31	11.33	8.66	9.47	12.39
OS4	Oblate Spheroid	0.74	13.81	18.60	16.84	12.51

Table C.7 List of experimental test descriptions for multiple frequency cases.

Folder	Test files	Body designation	f_1	s_1 [mm]	ε_1	f_2	s_2 [mm]	ε_2	Trigger Frequency [Hz]	ν [mm^2/s]	px/mm	Number of images
march212007	4Hza	OS4	4	0.66	0.05				4.00	151.35	33.4	300
march212007	8Hza	OS4	8	0.67	0.05				8.00	151.35	33.4	300
march212007	12Hza	OS4	12	0.67	0.05				12.00	151.35	33.4	300
march212007	4and8Hza	OS4	4	0.66	0.05	8	0.67	0.05	4.00	151.35	33.4	300
march212007	4and12Hza	OS4	4	0.65	0.05	12	0.67	0.05	4.00	151.35	33.4	300
march212007	8and12Hza	OS4	8	0.67	0.05	12	0.68	0.05	4.00	151.35	33.4	300
march052007	4Hzb	S1	4	0.66	0.05				4.00	141.97	32.0	300
march052007	8Hza	S1	8	0.68	0.05				8.00	141.97	32.0	300
march052007	4and8Hza	S1	4	0.65	0.05	8	0.66	0.05	4.00	141.97	32.0	300
march082007	4Hza	S1	4	1.29	0.10				4.00	133.27	34.0	300
march082007	4Hzb	S1	4	0.65	0.05				4.00	133.27	34.0	300
march082007	8Hza	S1	8	1.25	0.10				8.00	133.27	34.0	300
march082007	8Hzb	S1	8	0.64	0.05				8.00	133.27	34.0	300
march082007	4and8Hza	S1	4	1.34	0.11	8	1.31	0.10	4.00	133.27	34.0	300
march082007	4and8Hzb	S1	4	0.66	0.05	8	0.65	0.05	4.00	133.27	34.0	300
february222007	4Hza	S1	4	1.30	0.10				4.00	136.66	24.7	300
february222007	4Hzb	S1	4	1.94	0.15				4.00	136.66	24.7	300
february222007	8Hza	S1	8	0.67	0.05				8.00	136.66	24.7	300
february222007	12Hza	S1	12	0.68	0.05				12.00	136.66	24.7	300
february222007	4and8Hza	S1	4	1.28	0.10	8	0.64	0.05	4.00	136.66	24.7	300
february222007	4and12Hza	S1	4	1.93	0.15	12	0.64	0.05	4.00	136.66	24.7	300
march012007	4Hz1	S1	4	1.32	0.10				4.00	150.82	26.5	300
march012007	4Hz2	S1	4	1.32	0.10				4.00	150.82	26.5	300
march012007	4Hz3	S1	4	1.32	0.10				4.00	150.82	26.5	300

Table C.7 (continued).

march012007	8Hz1	S1	8	1.35	0.11				8.00	150.82	26.5	300
march012007	8Hz2	S1	8	1.34	0.11				8.00	150.82	26.5	300
march012007	8Hz3	S1	8	1.34	0.11				8.00	150.82	26.5	300
march012007	4and8Hz1	S1	4	1.31	0.10	8	1.33	0.10	4.00	150.82	26.5	300
march012007	4and8Hz2	S1	4	1.32	0.10	8	1.34	0.11	4.00	150.82	26.5	300
march012007	4and8Hz3	S1	4	1.32	0.10	8	1.33	0.11	4.00	150.82	26.5	300
march062007	4Hza	S1	4	1.32	0.10				4.00	141.97	32.4	300
march062007	8Hza	S1	8	1.33	0.10				8.00	141.97	32.4	300
march062007	4and8Hza	S1	4	1.32	0.10	8	1.34	0.11	4.00	141.97	32.4	300
march062007	4and8Hzb	S1	4	1.33	0.10	8	1.35	0.11	4.00	141.97	32.4	300
march142007	4Hza	S1	4	0.65	0.05				4.00	153.03	37.9	300
march142007	6Hza	S1	6	0.64	0.05				6.00	153.03	37.9	300
march142007	6Hzb	S1	6	0.32	0.03				6.00	153.03	37.9	300
march142007	12Hzb	S1	12	0.63	0.05				12.00	153.03	37.9	300
march142007	12Hzc	S1	12	0.31	0.02				12.00	153.03	37.9	300
march142007	4and12Hza	S1	4	0.63	0.05	12	0.62	0.05	4.00	153.03	37.9	300
march142007	6and12Hza	S1	6	0.64	0.05	12	0.62	0.05	6.00	153.03	37.9	300
march142007	6and12Hzb	S1	6	0.33	0.03	12	0.32	0.03	6.00	153.03	37.9	300
march142007	6and12Hzc	S1	6	0.66	0.05	12	0.33	0.03	6.00	153.03	37.9	300
march192007	4Hzc	PS3	4	0.67	0.05				4.00	151.27	43.0	300
march192007	8Hza	PS3	8	0.68	0.06				8.00	151.27	43.0	300
march192007	12Hza	PS3	12	0.69	0.06				12.00	151.27	43.0	300
march192007	4and8Hza	PS3	4	0.68	0.05	8	0.69	0.06	4.00	151.27	43.0	300
march192007	4and12Hza	PS3	4	0.67	0.05	12	0.68	0.06	4.00	151.27	43.0	300
march192007	8and12Hza	PS3	8	0.69	0.06	12	0.70	0.06	4.00	151.27	43.0	300

Table C.8 List of dimensionless parameters for multiple frequency test cases.

Folder	Test files	Body designation	ε*	V_s [mm/s]	$Re = \omega_1 s_1 L/\nu$	$Re_M = \omega_1 L^2/\nu$	$Re_s = \omega_1 s_1^2/\nu$	$Re = \omega_2 s_2 L/\nu$	$Re_M = \omega_2 L^2/\nu$	$Re_s = \omega_2 s_2^2/\nu$	$Re_1 = V_s L/\nu$	$Re_2 = Re_1 \varepsilon^*$	$Re_3 = Re_1/\varepsilon^*$
march212007	4Hza	OS4		0.86	1.36	25.98	0.07						
march212007	8Hza	OS4		1.81	2.79	51.95	0.15						
march212007	12Hza	OS4		2.73	4.20	77.93	0.23						
march212007	4and8Hza	OS4	0.16	8.05	1.37	25.98	0.07	0.01	51.95	0.15	0.67	0.11	50.31
march212007	4and12Hza	OS4	0.21	14.40	1.36	25.98	0.07	0.02	77.93	0.23	1.19	0.25	67.27
march212007	8and12Hza	OS4	0.27	22.85	2.77	51.95	0.15	0.02	77.93	0.23	1.89	0.51	84.76
march052007	4Hzb	S1		0.87	1.49	28.55	0.08						
march052007	8Hza	S1		1.83	3.06	57.11	0.16						
march052007	4and8Hza	S1	0.16	7.78	1.47	28.55	0.08	0.01	57.11	0.16	0.70	0.11	49.84
march082007	4Hza	S1		3.28	3.09	30.42	0.31						
march082007	4Hzb	S1		0.84	1.56	30.42	0.08						
march082007	8Hza	S1		6.16	5.97	60.84	0.59						
march082007	8Hzb	S1		1.65	3.09	60.84	0.16						
march082007	4and8Hza	S1	0.31	31.10	3.21	30.42	0.34	0.05	60.84	0.65	2.96	0.93	99.63
march082007	4and8Hzb	S1	0.15	7.58	1.58	30.42	0.08	0.01	60.84	0.16	0.72	0.11	49.19
february222007	4Hza	S1		3.35	3.04	29.66	0.31						
february222007	4Hzb	S1		7.48	4.54	29.66	0.70						
february222007	8Hza	S1		1.76	3.11	59.32	0.16						
february222007	12Hza	S1		2.72	4.74	88.99	0.25						
february222007	4and8Hza	S1	0.20	12.98	2.98	29.66	0.30	0.01	59.32	0.15	1.21	0.24	64.35
february222007	4and12Hza	S1	0.30	29.31	4.51	29.66	0.69	0.02	88.99	0.23	2.72	0.83	96.72
march012007	4Hz1	S1		3.46	2.80	26.88	0.29						
march012007	4Hz2	S1		3.45	2.80	26.88	0.29						

march012007	4Hz3	S1		3.45	2.79	26.88	0.29						

Table C.8 (continued).

march012007	8Hz1	S1		7.17	5.70	53.75	0.60						
march012007	8Hz2	S1		7.14	5.69	53.75	0.60						
march012007	8Hz3	S1		7.13	5.68	53.75	0.60						
march012007	4and8Hz1	S1	0.31	31.19	2.77	26.88	0.29	0.05	53.75	0.59	2.63	0.82	99.77
march012007	4and8Hz2	S1	0.31	31.55	2.79	26.88	0.29	0.05	53.75	0.60	2.66	0.84	100.35
march012007	4and8Hz3	S1	0.31	31.41	2.78	26.88	0.29	0.05	53.75	0.59	2.64	0.83	100.12
march062007	4Hza	S1		3.46	2.97	28.55	0.31						
march062007	8Hza	S1		6.97	5.97	57.11	0.62						
march062007	4and8Hza	S1	0.32	31.83	2.98	28.55	0.31	0.05	57.11	0.64	2.85	0.90	100.80
march062007	4and8Hzb	S1	0.32	32.03	2.99	28.55	0.31	0.05	57.11	0.64	2.87	0.91	101.11
march142007	4Hza	S1		0.83	1.35	26.49	0.07						
march142007	6Hza	S1		1.21	2.00	39.73	0.10						
march142007	6Hzb	S1		0.31	1.00	39.73	0.03						
march142007	12Hzb	S1		2.36	3.95	79.47	0.20						
march142007	12Hzc	S1		0.58	1.95	79.47	0.05						
march142007	4and12Hza	S1	0.20	12.20	1.32	26.49	0.07	0.01	79.47	0.19	1.01	0.20	62.40
march142007	6and12Hza	S1	0.15	10.63	2.01	39.73	0.10	0.02	79.47	0.19	0.88	0.13	71.33
march142007	6and12Hzb	S1	0.08	2.77	1.03	39.73	0.03	0.00	79.47	0.05	0.23	0.02	36.42
march142007	6and12Hzc	S1	0.10	5.14	2.07	39.73	0.11	0.00	79.47	0.05	0.43	0.04	49.59
march192007	4Hzc	PS3		0.92	1.38	25.52	0.08						
march192007	8Hza	PS3		1.90	2.82	51.03	0.16						
march192007	12Hza	PS3		2.86	4.23	76.55	0.23						
march192007	4and8Hza	PS3	0.17	8.50	1.39	25.52	0.08	0.01	51.03	0.16	0.70	0.11	51.44
march192007	4and12Hza	PS3	0.22	14.99	1.37	25.52	0.07	0.02	76.55	0.23	1.23	0.27	68.33
march192007	8and12Hza	PS3	0.28	24.47	2.83	51.03	0.16	0.02	76.55	0.24	2.00	0.56	87.30

C.5 Angled Grooved Spheroid Cases

A clear acrylic oblate spheroid with a groove of radius *c* cut along one side was oscillated in a sinusoidal pattern at a single frequency and imaged at the middle of its oscillation. The body was illuminated along one direction (from the right side of the image). The kinematic viscosity was determined from the fluid composition and the average measured temperature. The frame rate was equal to the oscillation frequency for these test cases, and 1000 images were taken for each case.

A description of the body can be found in Table C.9. A list of experimental test cases can be found in Table C.10.

Table C.9 Description of experimental bodies used for angled grooved spheroid cases.

Body description	***AR* = *a*/*b***	***a* [mm]**	***b* [mm]**	***c* [mm]**	**Equivalent radius [mm]**	***L* [mm]**
Oblate spheroid	0.75	13.97	18.64	3.18	16.93	12.70

Table C.10 List of experimental cases for angled grooved spheroidal bodies.

Folder	Test files	θ (nominal) [deg.]	f [Hz]	s [mm]	$\varepsilon = s/L$	$\varepsilon = s/c$	ν [mm^2/s]	$Re = \omega s c/\nu$	$Re = \omega s L/\nu$	$Re_M = \omega c^2/\nu$	$Re_M{}^* = \omega L^{*2}/\nu$	$Re_s = \omega s^2/\nu$	px/mm
september272007	4Hza	0	4	0.32	0.02	0.10	150.82	0.17	0.17	1.68	43.4	0.02	102
september272007	4Hzb	0	4	0.63	0.05	0.20	150.82	0.33	0.33	1.68	43.4	0.07	102
september272007	8Hza	0	8	0.29	0.02	0.09	150.82	0.31	0.16	3.36	86.8	0.03	102
september272007	8Hzb	0	8	0.59	0.05	0.19	150.82	0.63	0.31	3.36	86.8	0.12	102
september272007	12Hza	0	12	0.30	0.02	0.09	150.82	0.48	0.16	5.04	130.2	0.05	102
september272007	12Hzb	0	12	0.61	0.05	0.19	150.82	0.97	0.32	5.04	130.2	0.19	102
september272007	16Hza	0	16	0.29	0.02	0.09	150.82	0.62	0.16	6.72	173.6	0.06	102
september272007	16Hzb	0	16	0.58	0.05	0.18	150.82	1.24	0.31	6.72	173.6	0.23	102
september282007	4Hza	15	4	0.30	0.02	0.09	147.99	0.16	0.16	1.71	44.2	0.02	96.5
september282007	4Hzb	15	4	0.58	0.05	0.18	147.99	0.31	0.31	1.71	44.2	0.06	96.5
september282007	8Hzc	15	8	0.30	0.02	0.09	147.99	0.32	0.16	3.42	88.4	0.03	95
september282007	8Hzb	15	8	0.58	0.05	0.18	147.99	0.63	0.32	3.42	88.4	0.12	95
september282007	12Hza	15	12	0.30	0.02	0.10	147.99	0.49	0.16	5.14	132.7	0.05	95
september282007	12Hzc	15	12	0.58	0.05	0.18	147.99	0.94	0.31	5.14	132.7	0.17	95
september282007	16Hza	15	16	0.30	0.02	0.10	147.99	0.65	0.16	6.85	176.9	0.06	95
september282007	16Hzb	15	16	0.58	0.05	0.18	147.99	1.25	0.31	6.85	176.9	0.23	95
october012007	4Hza	30	4	0.29	0.02	0.09	148.72	0.16	0.16	1.70	44.0	0.01	95.4
october012007	4Hzb	30	4	0.58	0.05	0.18	148.72	0.31	0.31	1.70	44.0	0.06	95.4
october012007	8Hza	30	8	0.30	0.02	0.09	148.72	0.32	0.16	3.41	88.0	0.03	95.4
october012007	8Hzb	30	8	0.58	0.05	0.18	148.72	0.62	0.31	3.41	88.0	0.11	95.4
october012007	12Hza	30	12	0.31	0.02	0.10	148.72	0.50	0.17	5.11	132.0	0.05	95.4
october012007	12Hzb	30	12	0.60	0.05	0.19	148.72	0.96	0.32	5.11	132.0	0.18	95.4
october012007	16Hza	30	16	0.31	0.02	0.10	148.72	0.66	0.16	6.81	176.0	0.06	95.4

Table C.10 (continued).

october012007	16Hzb	30	16	0.61	0.05	0.19	148.72	1.31	0.33	6.81	176.0	0.25	95.4
october242007	4Hza	30	4	0.29	0.02	0.09	145.60	0.16	0.16	1.74	44.9	0.01	95.5
october242007	4Hzb	30	4	0.58	0.05	0.18	145.60	0.32	0.32	1.74	44.9	0.06	95.5
october242007	4Hzc	30	4	1.14	0.09	0.36	145.60	0.63	0.63	1.74	44.9	0.23	95.5
october242007	8Hza	30	8	0.30	0.02	0.09	145.60	0.33	0.16	3.48	89.9	0.03	95.5
october242007	8Hzb	30	8	0.59	0.05	0.18	145.60	0.64	0.32	3.48	89.9	0.12	95.5
october242007	8Hzc	30	8	1.16	0.09	0.37	145.60	1.27	0.64	3.48	89.9	0.47	95.5
october242007	12Hza	30	12	0.30	0.02	0.10	145.60	0.50	0.17	5.22	134.8	0.05	95.5
october242007	12Hzb	30	12	0.60	0.05	0.19	145.60	0.99	0.33	5.22	134.8	0.19	95.5
october242007	16Hza	30	16	0.31	0.02	0.10	145.60	0.68	0.17	6.96	179.8	0.07	95.5
october242007	16Hzb	30	16	0.61	0.05	0.19	145.60	1.34	0.33	6.96	179.8	0.26	95.5
october032007	4Hza	45	4	0.29	0.02	0.09	149.74	0.16	0.16	1.69	43.7	0.01	96.1
october032007	4Hzb	45	4	0.57	0.05	0.18	149.74	0.30	0.30	1.69	43.7	0.05	96.1
october032007	8Hza	45	8	0.30	0.02	0.09	149.74	0.32	0.16	3.38	87.4	0.03	96.1
october032007	8Hzb	45	8	0.59	0.05	0.18	149.74	0.63	0.31	3.38	87.4	0.12	96.1
october032007	12Hza	45	12	0.30	0.02	0.09	149.74	0.48	0.16	5.08	131.1	0.05	96.1
october032007	12Hzb	45	12	0.59	0.05	0.19	149.74	0.94	0.31	5.08	131.1	0.17	96.1
october032007	16Hza	45	16	0.31	0.02	0.10	149.74	0.66	0.17	6.77	174.8	0.07	96.1
october032007	16Hzc	45	16	0.61	0.05	0.19	149.74	1.31	0.33	6.77	174.8	0.25	96.1
october252007	4Hza	45	4	0.29	0.02	0.09	143.90	0.16	0.16	1.76	45.5	0.01	95.4
october252007	4Hzb	45	4	0.57	0.04	0.18	143.90	0.32	0.32	1.76	45.5	0.06	95.4
october252007	4Hzc	45	4	1.13	0.09	0.36	143.90	0.63	0.63	1.76	45.5	0.22	95.4
october252007	8Hza2	45	8	0.29	0.02	0.09	143.90	0.33	0.16	3.52	91.0	0.03	95.4
october252007	8Hzb	45	8	0.58	0.05	0.18	143.90	0.64	0.32	3.52	91.0	0.12	95.4
october252007	12Hza	45	12	0.30	0.02	0.09	143.90	0.49	0.16	5.28	136.4	0.05	95.4

Table C.10 (continued).

october252007	12Hzb	45	12	0.59	0.05	0.19	143.90	0.99	0.33	5.28	136.4	0.19	95.4
october252007	16Hza	45	16	0.32	0.03	0.10	143.90	0.70	0.18	7.04	181.9	0.07	95.4
october252007	16Hzb2	45	16	0.60	0.05	0.19	143.90	1.34	0.33	7.04	181.9	0.25	95.4

C.6 Scale Model Otolith Cases

A 350% scale model of a cod otolith was used to study the fluid flows near a biologically relevant body. This scaling produced a critical length, L, based on the sulcus width of approximately 10 mm. The frame rate was equal to the oscillation frequency for these test cases. The body was illuminated and 500 image sequences taken in three locations, as shown by the lines A, B, and C in Figure C.1. The lightsheet and oscillation direction were always in the vertical plane, necessitating the rotation of the model otolith for some measurements. A listing of the test cases for the "horizontal" orientation A and B is given in Table C.11, while the "vertical' test cases (C) are given in Table C.12. The orientation angles given are relative.

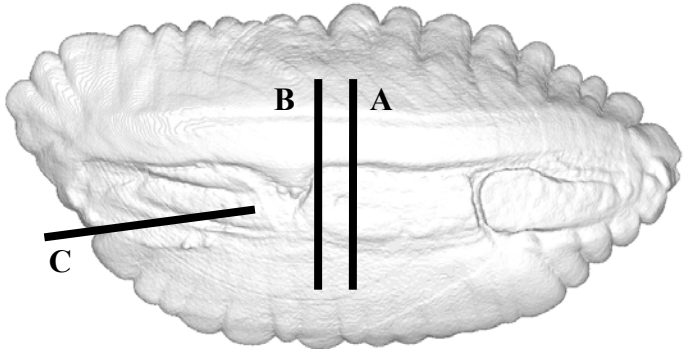

Figure C.1 Test locations for data near otolith scale models.

Table C.11 List of experimental test cases for the scale model otolith, with otolith oriented with the longer dimension horizontal.

Folder	Test files	Orient-ation (degrees)	Test location	f [Hz]	s [mm]	ε	ν [mm^2/s]	Re_s	Re	Re_M	px/mm
march062008	8Hza	0	A	8	0.494	0.049	163.2	0.075	1.520	30.80	72.3
march062008	8Hzb	0	A	8	0.242	0.024	163.2	0.018	0.747	30.80	72.3
march062008	12Hza	0	A	12	0.500	0.050	165.4	0.114	2.281	45.59	72.3
march062008	12Hzb	0	A	12	0.248	0.025	161.9	0.029	1.157	246.58	72.3
march062008	16Hza	0	A	16	0.473	0.047	165.0	0.136	2.884	60.94	72.3
march062008	16Hzb	0	A	16	0.234	0.023	165.4	0.033	1.420	60.78	72.3
march062008	20Hza	0	A	20	0.473	0.047	163.2	0.172	3.639	77.00	72.3
march062008	20Hzb	0	A	20	0.235	0.024	163.2	0.043	1.812	77.00	72.3
march062008	24Hza	0	A	24	0.457	0.046	166.7	0.189	4.135	90.44	72.3
march062008	24Hzb	0	A	24	0.225	0.023	166.3	0.046	2.041	90.68	72.3
march042008	8Hza	0	B	8	0.506	0.051	164.5	0.078	1.545	30.55	73.4
march042008	8Hzb	0	B	8	0.251	0.025	164.5	0.019	0.767	30.55	73.4
march042008	12Hza	0	B	12	0.507	0.051	168.5	0.115	2.269	44.75	73.4
march042008	12Hzb	0	B	12	0.258	0.026	167.6	0.030	1.159	44.98	73.4
march042008	12Hzc	0	B	12	0.256	0.026	166.7	0.030	1.159	45.22	73.4
march042008	16Hza	0	B	16	0.518	0.052	165.4	0.163	3.150	60.78	73.4
march042008	16Hzb	0	B	16	0.251	0.025	165.0	0.039	1.532	60.94	73.4
march042008	20Hza	0	B	20	0.541	0.054	166.7	0.220	4.074	75.37	73.4
march042008	20Hzb	0	B	20	0.262	0.026	165.8	0.052	1.988	75.77	73.4
march042008	24Hza	0	B	24	0.507	0.051	168.5	0.230	4.537	89.50	73.4
march042008	24Hzb	0	B	24	0.253	0.025	167.6	0.057	2.273	89.97	73.4
february272008	8Hza	30	A	8	0.479	0.048	147.3	0.078	1.633	34.13	71.5
february272008	8Hzb	30	A	8	0.228	0.023	152.6	0.017	0.752	32.94	71.5
february272008	8Hzc	30	A	8	0.460	0.046	152.6	0.070	1.515	32.94	71.5
february272008	12Hza	30	A	12	0.456	0.046	147.3	0.107	2.337	51.19	71.5
february272008	12Hzb	30	A	12	0.225	0.022	152.2	0.025	1.114	49.56	71.5

Table C.11 (continued).

February272008	16Hza	30	A	16	0.476	0.048	148.6	0.153	3.217	67.65	71.5
february272008	16Hzb	30	A	16	0.222	0.022	149.5	0.033	1.495	67.24	71.5
february272008	20Hza	30	A	20	0.408	0.041	150.8	0.139	3.399	83.32	71.5
february272008	20Hzb	30	A	20	0.207	0.021	151.7	0.035	1.712	82.83	71.5
february272008	24Hza	30	A	24	0.509	0.051	148.2	0.263	5.176	101.77	71.5
february272008	24Hzb	30	A	24	0.527	0.053	146.0	0.287	5.445	103.31	71.5
february272008	24Hzc	30	A	24	0.228	0.023	146.0	0.054	2.360	103.31	71.5
march212008	8Hza	30	B	8	0.499	0.050	173.3	0.072	1.448	29.00	74.3
march212008	8Hzb	30	B	8	0.250	0.025	173.3	0.018	0.725	29.00	74.3
march212008	12Hza	30	B	12	0.495	0.049	175.1	0.105	2.130	43.06	74.3
march212008	12Hzb	30	B	12	0.247	0.025	175.1	0.026	1.063	43.06	74.3
march212008	16Hza	30	B	16	0.489	0.049	174.7	0.138	2.815	57.55	74.3
march212008	16Hzb	30	B	16	0.246	0.025	173.8	0.035	1.422	57.85	74.3
march212008	20Hza	30	B	20	0.460	0.046	174.7	0.152	3.311	71.94	74.3
march212008	20Hzb	30	B	20	0.234	0.023	174.2	0.039	1.687	72.13	74.3
march212008	24Hza	30	B	24	0.455	0.045	176.0	0.177	3.896	85.68	74.3
march212008	24Hzb	30	B	24	0.225	0.022	175.6	0.043	1.931	85.90	74.3
march092008	8Hza	45	A	8	0.479	0.048	160.5	0.072	1.498	31.31	71.6
march092008	8Hzb	45	A	8	0.239	0.024	160.5	0.018	0.747	31.31	71.6
march092008	12Hza	45	A	12	0.494	0.049	160.5	0.115	2.319	46.97	71.6
march092008	12Hzb	45	A	12	0.244	0.024	159.2	0.028	1.154	47.35	71.6
march092008	16Hza	45	A	16	0.475	0.048	160.1	0.142	2.985	62.79	71.6
march092008	16Hzb	45	A	16	0.238	0.024	160.5	0.036	1.493	62.62	71.6
march092008	20Hza	45	A	20	0.477	0.048	159.2	0.179	3.762	78.92	71.6
march092008	20Hzb	45	A	20	0.237	0.024	159.2	0.044	1.870	78.92	71.6
march092008	24Hzb	45	A	24	0.244	0.024	162.3	0.055	2.263	92.91	71.6
march092008	24Hzc	45	A	24	0.460	0.046	161.9	0.197	4.283	93.16	71.6
march102008	8Hza	45	B	8	0.472	0.047	174.7	0.064	1.358	28.78	71.8
march102008	8Hzb	45	B	8	0.237	0.024	174.7	0.016	0.682	28.78	71.8

Table C.11 (continued).

march102008	12Hza	45	B	12	0.465	0.047	176.4	0.092	1.988	42.74	71.8
march102008	12Hzb	45	B	12	0.232	0.023	175.6	0.023	0.998	42.95	71.8
march102008	16Hza	45	B	16	0.461	0.046	175.6	0.122	2.640	57.27	71.8
march102008	16Hzb	45	B	16	0.231	0.023	175.6	0.031	1.325	57.27	71.8
march102008	20Hza	45	B	20	0.432	0.043	175.6	0.133	3.089	71.58	71.8
march102008	20Hzb	45	B	20	0.218	0.022	175.6	0.034	1.558	71.58	71.8
march102008	24Hzb	45	B	24	0.210	0.021	176.4	0.038	1.791	85.47	71.8
march102008	24Hzc	45	B	24	0.428	0.043	176.4	0.157	3.660	85.47	71.8
march132008	8Hza	75	A	8	0.508	0.051	176.4	0.073	1.447	28.49	72.9
march132008	8Hzb	75	A	8	0.253	0.025	176.4	0.018	0.719	28.49	72.9
march132008	12Hzb	75	A	12	0.253	0.025	179.6	0.027	1.061	41.99	72.9
march132008	12Hzc	75	A	12	0.515	0.052	177.3	0.113	2.191	42.52	72.9
march132008	16Hza	75	A	16	0.519	0.052	176.4	0.153	2.957	56.98	72.9
march132008	16Hzb	75	A	16	0.260	0.026	176.4	0.038	1.480	56.98	72.9
march132008	20Hza	75	A	20	0.526	0.053	177.3	0.196	3.728	70.87	72.9
march132008	20Hzb	75	A	20	0.260	0.026	177.3	0.048	1.841	70.87	72.9
march132008	24Hza	75	A	24	0.522	0.052	181.8	0.226	4.328	82.94	72.9
march132008	24Hzb	75	A	24	0.259	0.026	181.8	0.056	2.146	82.94	72.9
march202008	8Hza	75	B	8	0.520	0.052	169.8	0.080	1.541	29.60	71.3
march202008	8Hzb	75	B	8	0.257	0.026	168.9	0.020	0.766	29.76	71.3
march202008	12Hza	75	B	12	0.529	0.053	173.8	0.121	2.296	43.38	71.3
march202008	12Hzb	75	B	12	0.260	0.026	173.8	0.029	1.127	43.38	71.3
march202008	16Hza	75	B	16	0.562	0.056	171.6	0.185	3.292	58.59	71.3
march202008	16Hzb	75	B	16	0.281	0.028	170.3	0.047	1.658	59.05	71.3
march202008	20Hza	75	B	20	0.567	0.057	173.8	0.233	4.101	72.31	71.3
march202008	20Hzb	75	B	20	0.297	0.030	172.0	0.065	2.173	73.05	71.3
march202008	24Hza	75	B	24	0.571	0.057	174.7	0.281	4.928	86.33	71.3
march202008	24Hzb	75	B	24	0.287	0.029	174.2	0.071	2.481	86.55	71.3

Table C.12 List of experimental test cases for the scale model otolith, with otolith oriented with the longer dimension vertical.

Folder	Test files	Orient-ation (degrees)	Test location	f [Hz]	s [mm]	ε	ν [mm^2/s]	Re_s	Re	Re_M	px/mm
march272008	8Hza	0	C	8	0.499	0.050	174.7	0.072	1.437	28.78	69.3
march272008	8Hzb	0	C	8	0.247	0.025	174.2	0.018	0.712	28.85	69.3
march272008	12Hza	0	C	12	0.508	0.051	173.3	0.112	2.208	43.50	69.3
march272008	12Hzb	0	C	12	0.252	0.025	173.3	0.028	1.098	43.50	69.3
march272008	16Hza	0	C	16	0.519	0.052	172.0	0.157	3.033	58.44	69.3
march272008	16Hzb	0	C	16	0.253	0.025	172.0	0.038	1.481	58.44	69.3
march272008	20Hza	0	C	20	0.512	0.051	172.9	0.191	3.724	72.68	69.3
march272008	20Hzb	0	C	20	0.261	0.026	172.9	0.050	1.899	72.68	69.3
march272008	24Hza	0	C	24	0.509	0.051	174.2	0.225	4.410	86.55	69.3
march272008	24Hzb	0	C	24	0.252	0.025	173.8	0.055	2.188	86.77	69.3
june132008	8Hza	0	C	8	0.501	0.050	168.1	0.075	1.498	29.91	39.5
june132008	8Hzb	0	C	8	0.248	0.025	168.1	0.018	0.741	29.91	39.5
june132008	12Hza	0	C	12	0.496	0.050	168.5	0.110	2.221	44.75	39.5
june132008	12Hzb	0	C	12	0.245	0.025	168.9	0.027	1.095	44.63	39.5
june132008	16Hza	0	C	16	0.533	0.053	168.1	0.170	3.190	59.82	39.5
june132008	16Hzb	0	C	16	0.262	0.026	168.1	0.041	1.569	59.82	39.5
june132008	20Hza	0	C	20	0.619	0.062	168.5	0.286	4.615	74.58	39.5
june132008	20Hzb	0	C	20	0.305	0.031	168.1	0.070	2.284	74.78	39.5
june132008	24Hza	0	C	24	0.487	0.049	168.5	0.212	4.356	89.50	39.5
june132008	24Hzb	0	C	24	0.244	0.024	168.5	0.053	2.186	89.50	39.5
june162008	8Hza	15	C	8	0.499	0.050	162.3	0.077	1.545	30.97	40.6
june162008	8Hzb	15	C	8	0.248	0.025	163.2	0.019	0.763	30.80	40.6
june162008	8Hzc	15	C	8	0.501	0.050	163.2	0.077	1.542	30.80	40.6
june162008	12Hza	15	C	12	0.494	0.049	162.3	0.114	2.297	46.45	40.6
june162008	12Hzb	15	C	12	0.244	0.024	163.2	0.028	1.129	46.20	40.6
june162008	16Hza	15	C	16	0.151	0.015	163.2	0.014	0.931	61.60	40.6

Table C.12 (continued).

june162008	20Hza	15	C	20	0.483	0.048	163.2	0.179	3.716	77.00	40.6
june162008	20Hzb	15	C	20	0.242	0.024	162.3	0.045	1.874	77.42	40.6
june162008	20Hzc	15	C	20	0.488	0.049	163.2	0.183	3.758	77.00	40.6
june162008	24Hza	15	C	24	0.518	0.052	161.4	0.250	4.835	93.41	40.6
june162008	24Hzb	15	C	24	0.255	0.026	162.3	0.061	2.371	92.91	40.6

APPENDIX D

LABVIEW™ CODE

Most of the experimental controls were implemented using simple LABVIEW™ codes. The control panel is found in

Figure D.1. The code diagrams are given in Figures B.2-B.12 as follows:

- Figure D.2 shows the initialization of the variables.
- Figure D.3 shows the definition of the sinusoidal motion.
- Figure D.4 shows the definition the camera trigger pulse.
- Figure D.5 shows the population of the output buffers.
- Figure D.6 shows the initialization of the analog output which controls the shaker motion and the camera trigger.
- Figure D.7 shows the initialization of the analog input which monitors the shaker motion.
- Figure D.8 shows the code for beginning the analog output.
- Figure D.9 shows the code for beginning the analog input.
- Figure D.10 shows the code for pausing the program until the output is completed.
- Figure D.11 shows the code for saving the input data.
- Figure D.12 shows the code for clearing the buffers and stopping execution.

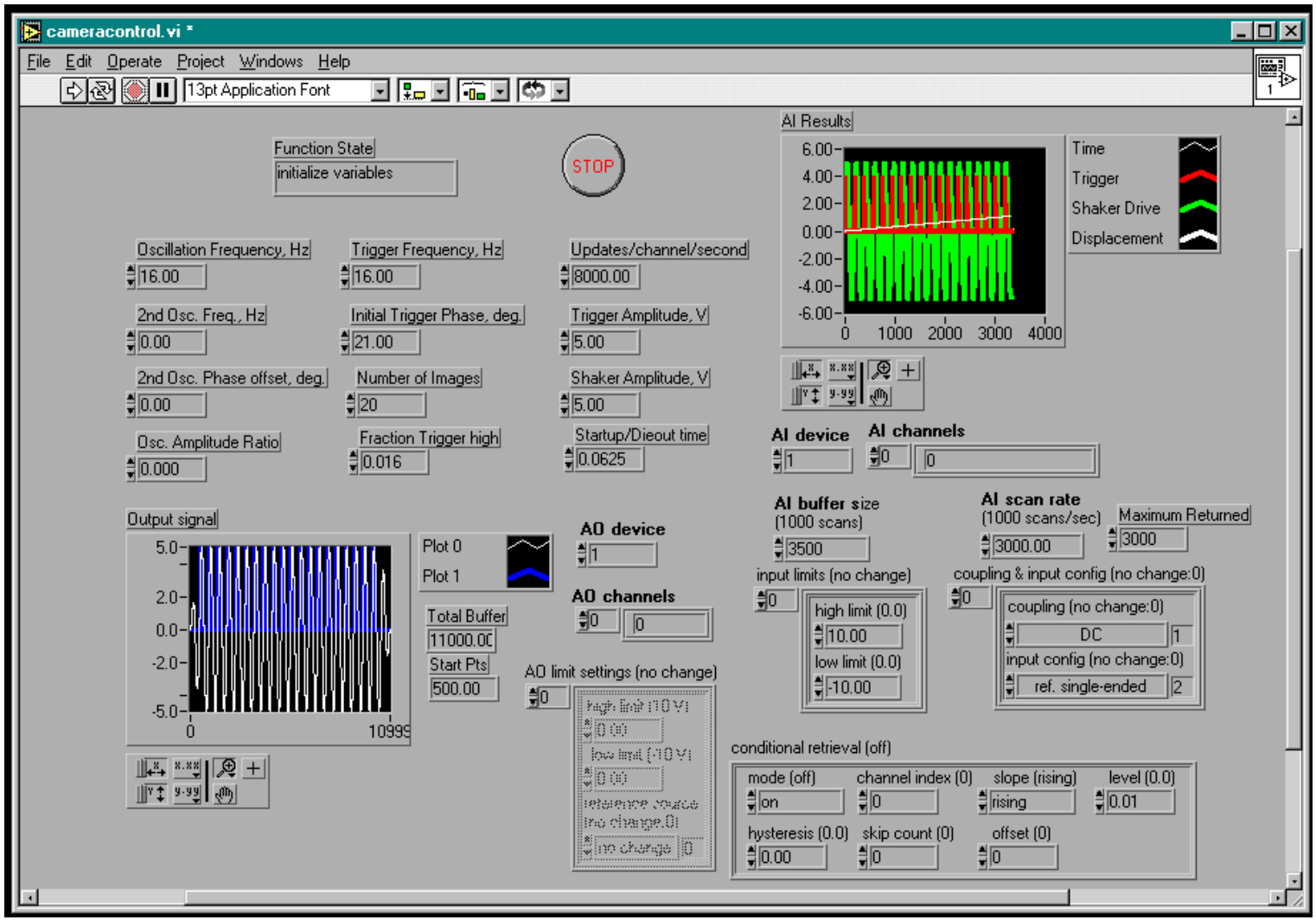

Figure D.1 Control panel for LabVIEW™ code used to run experiments.

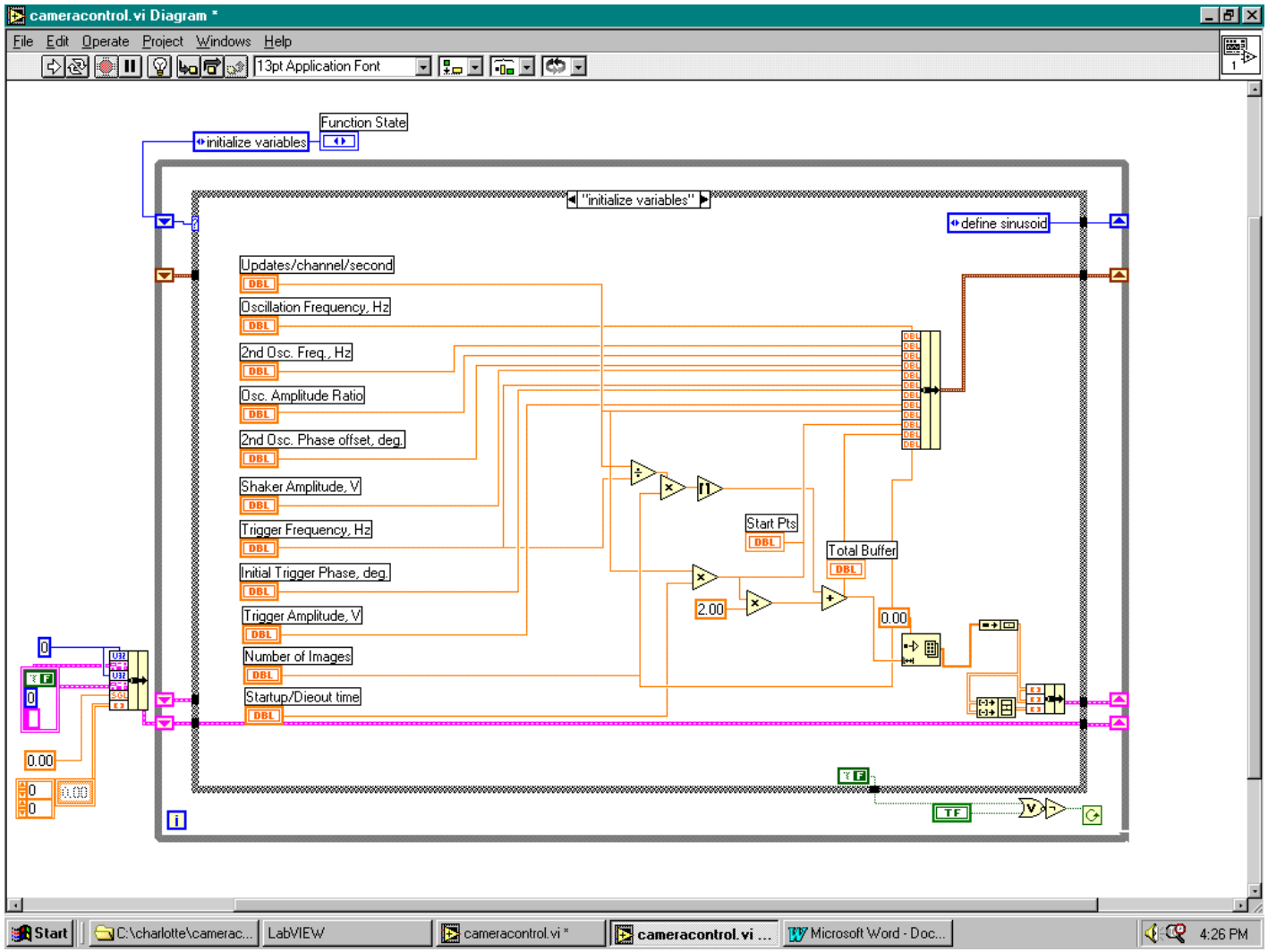

Figure D.2 LabVIEW™ diagram initializing variables.

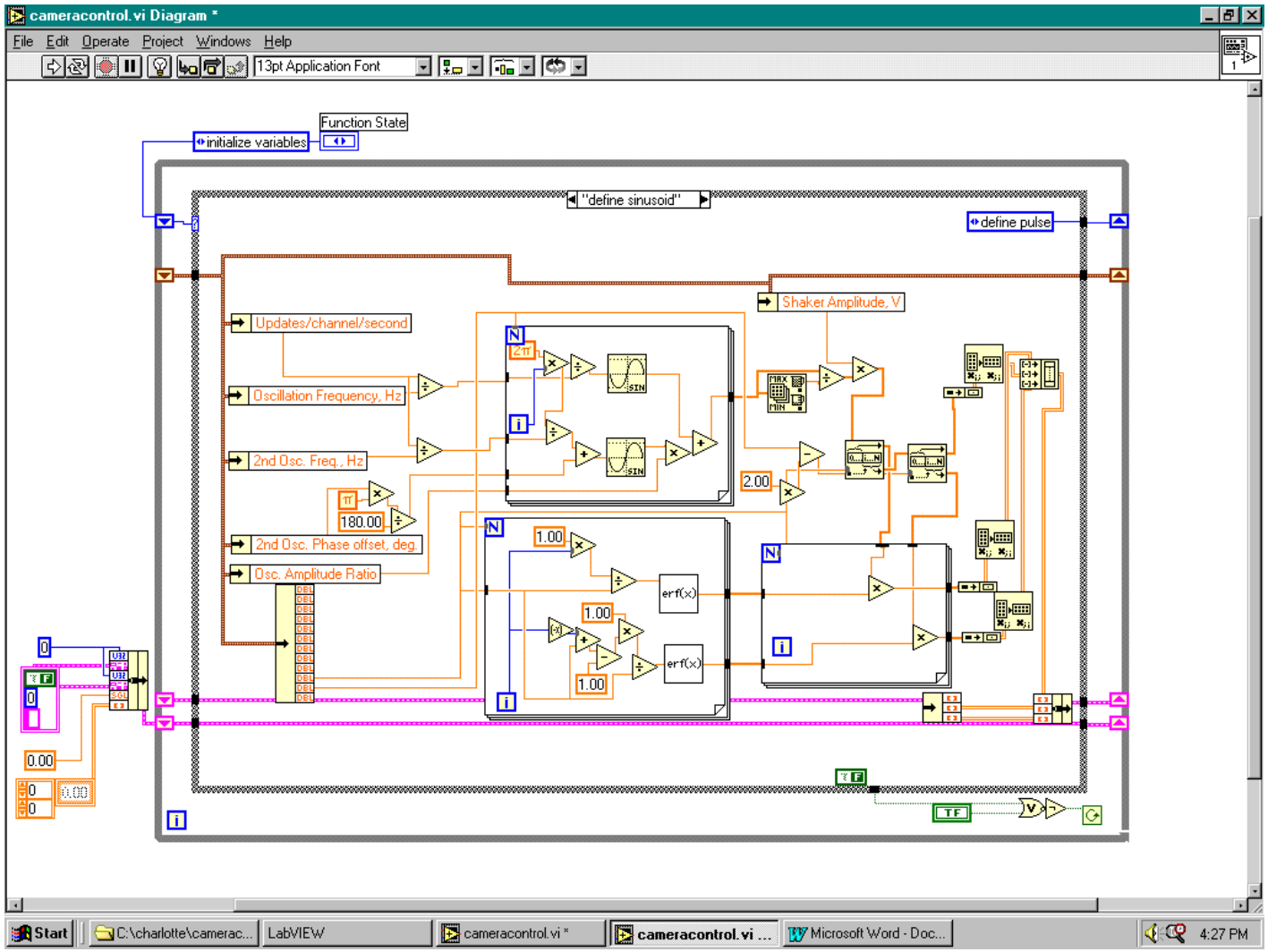

Figure D.3 LabVIEW™ diagram generating sinusoid.

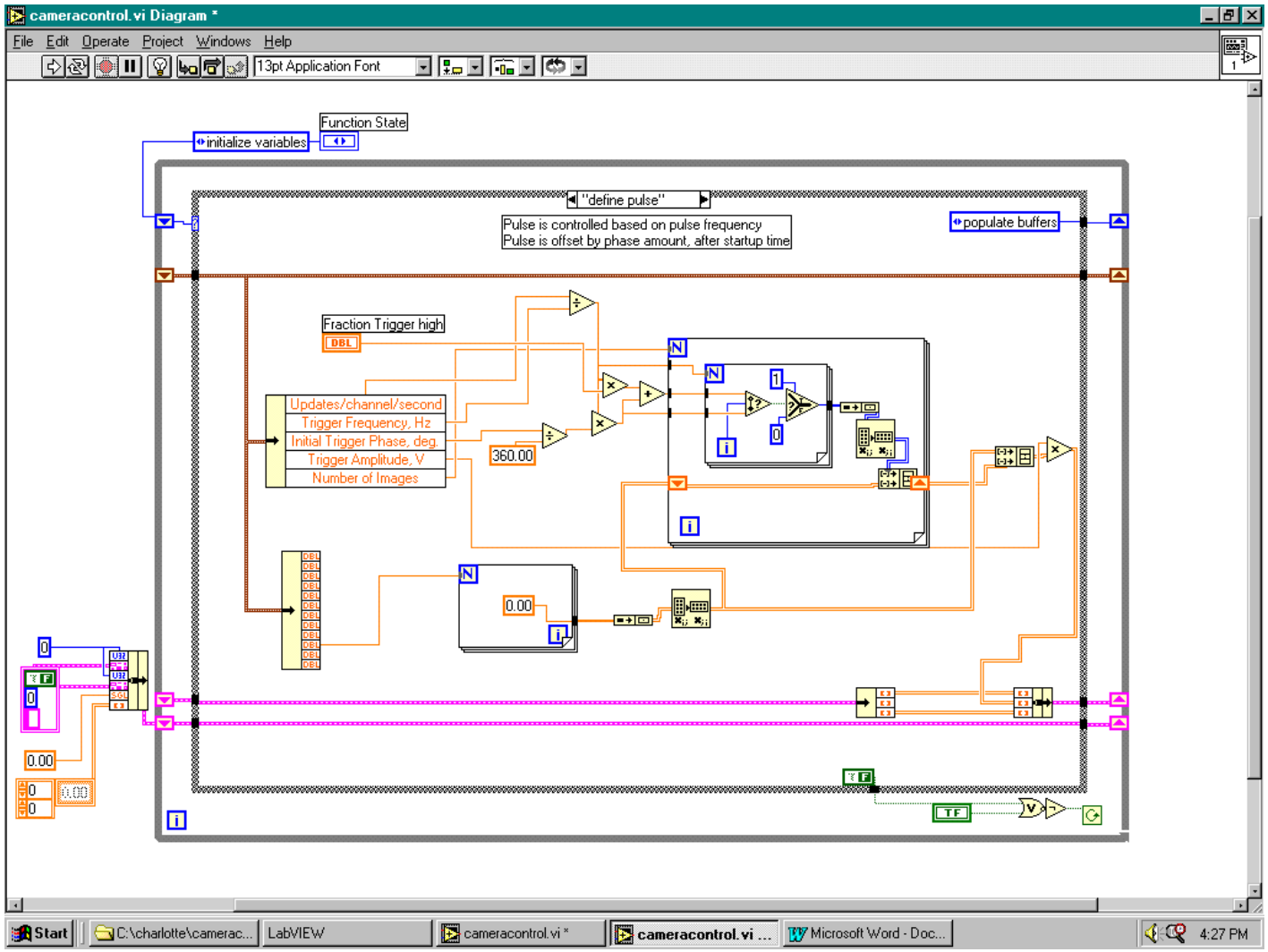

Figure D.4 LabVIEW™ diagram generating trigger pulse.

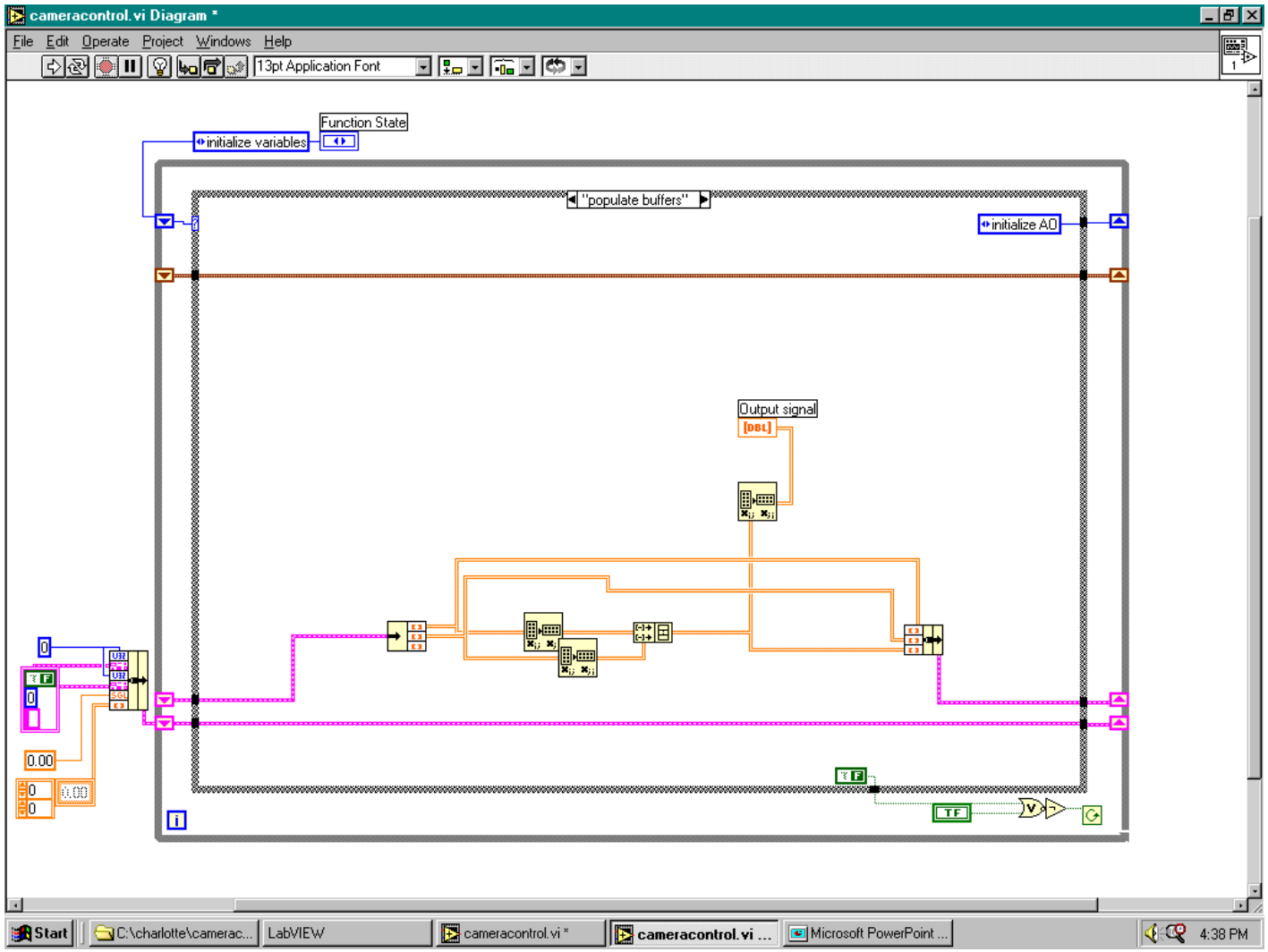

Figure D.5 LabVIEW™ diagram populating output buffers with sinusoid and trigger pulse signals.

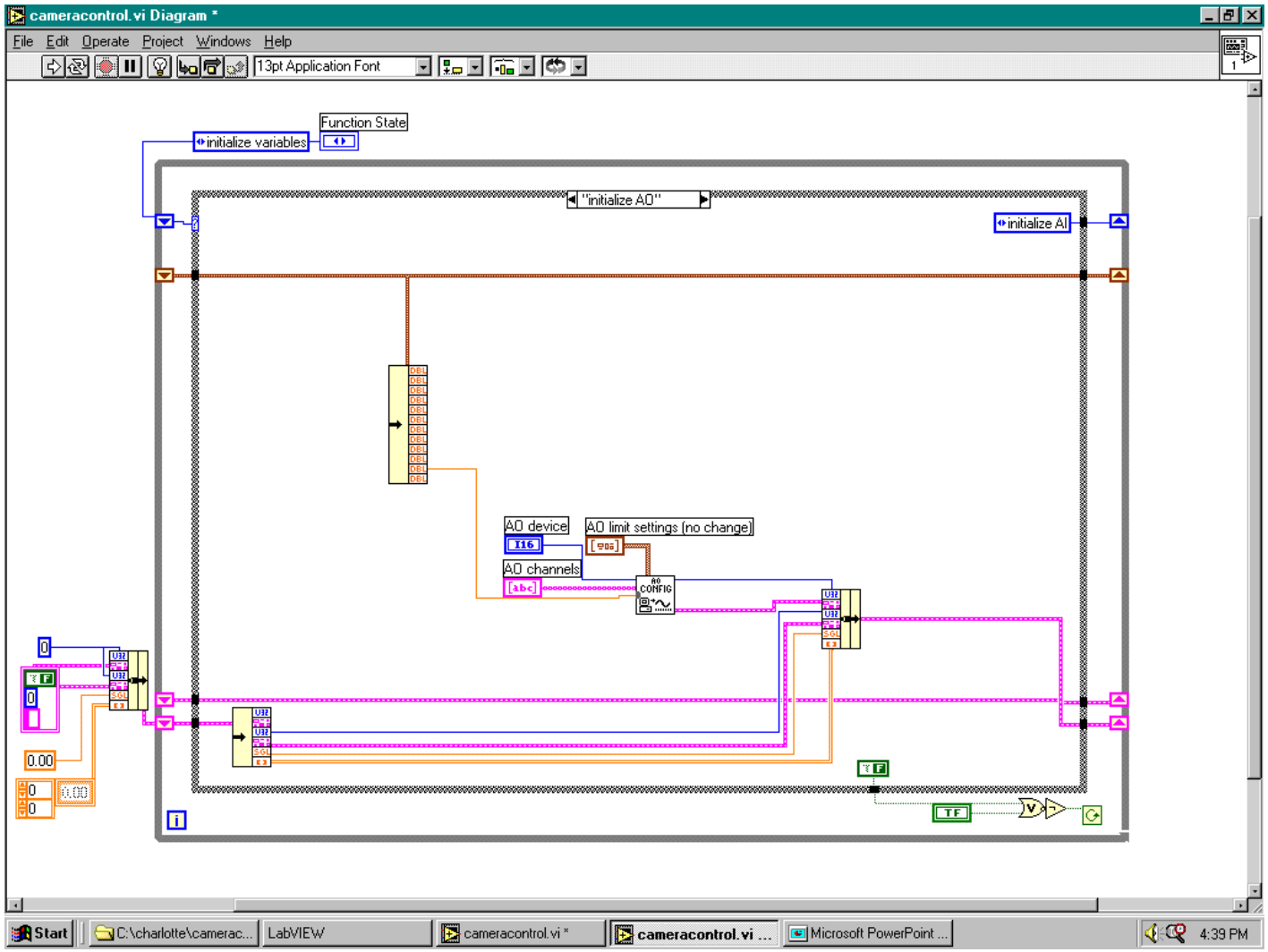

Figure D.6 LabVIEW™ diagram initializing the analog output channels.

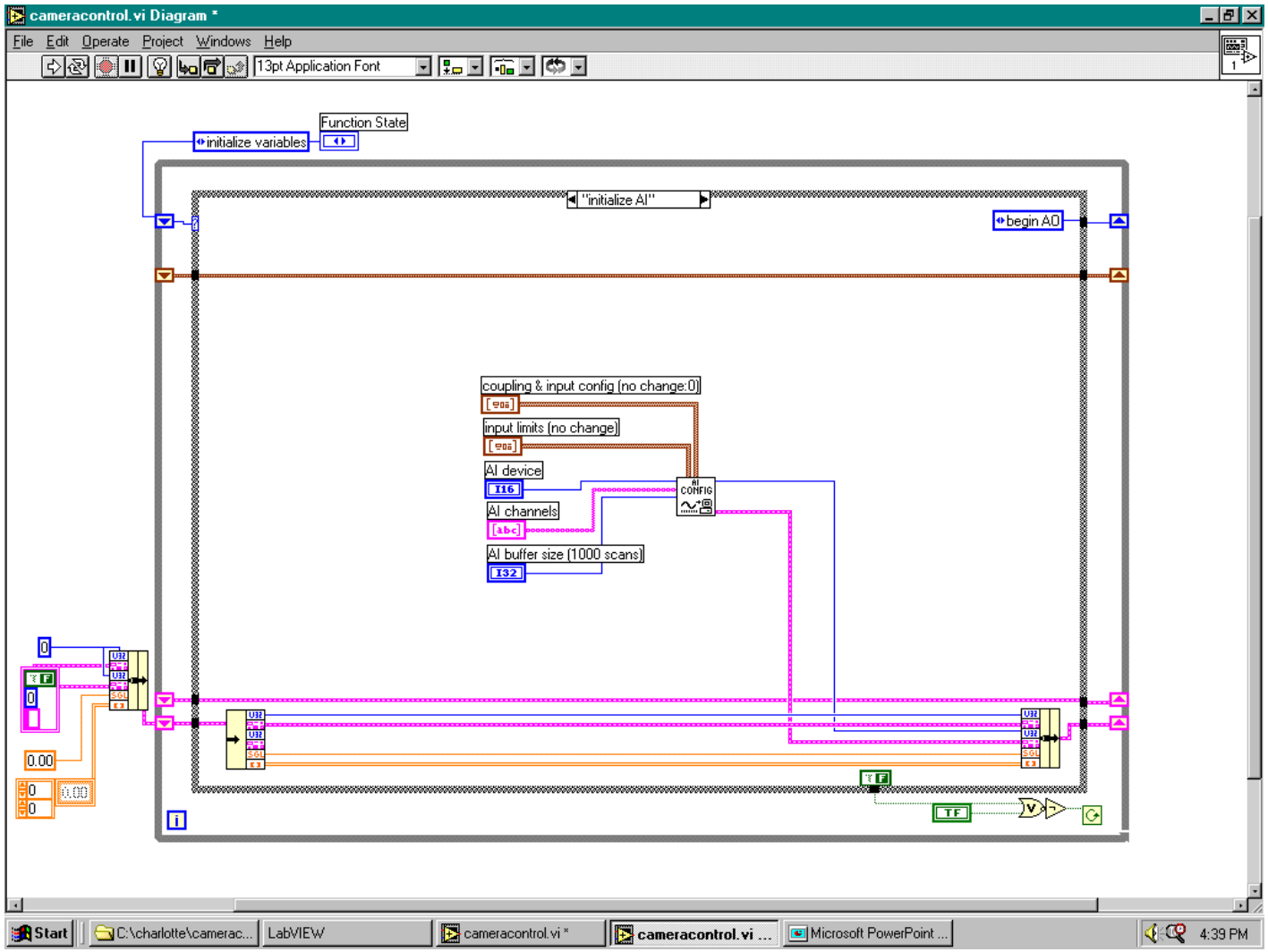

Figure D.7 LabVIEW™ diagram initializing the analog input channels.

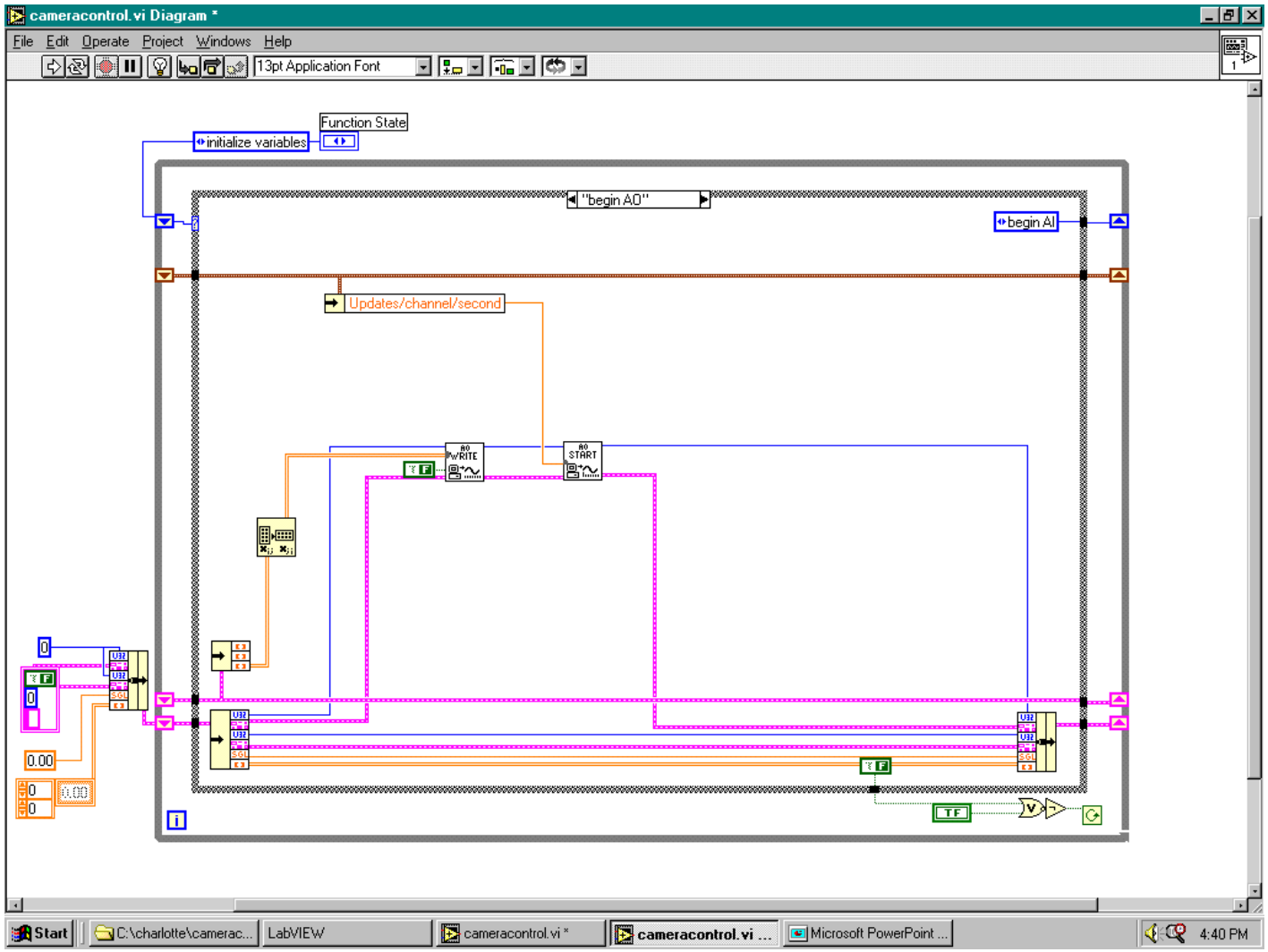

Figure D.8 LabVIEW™ diagram to start analog output of sinusoid and trigger pulse.

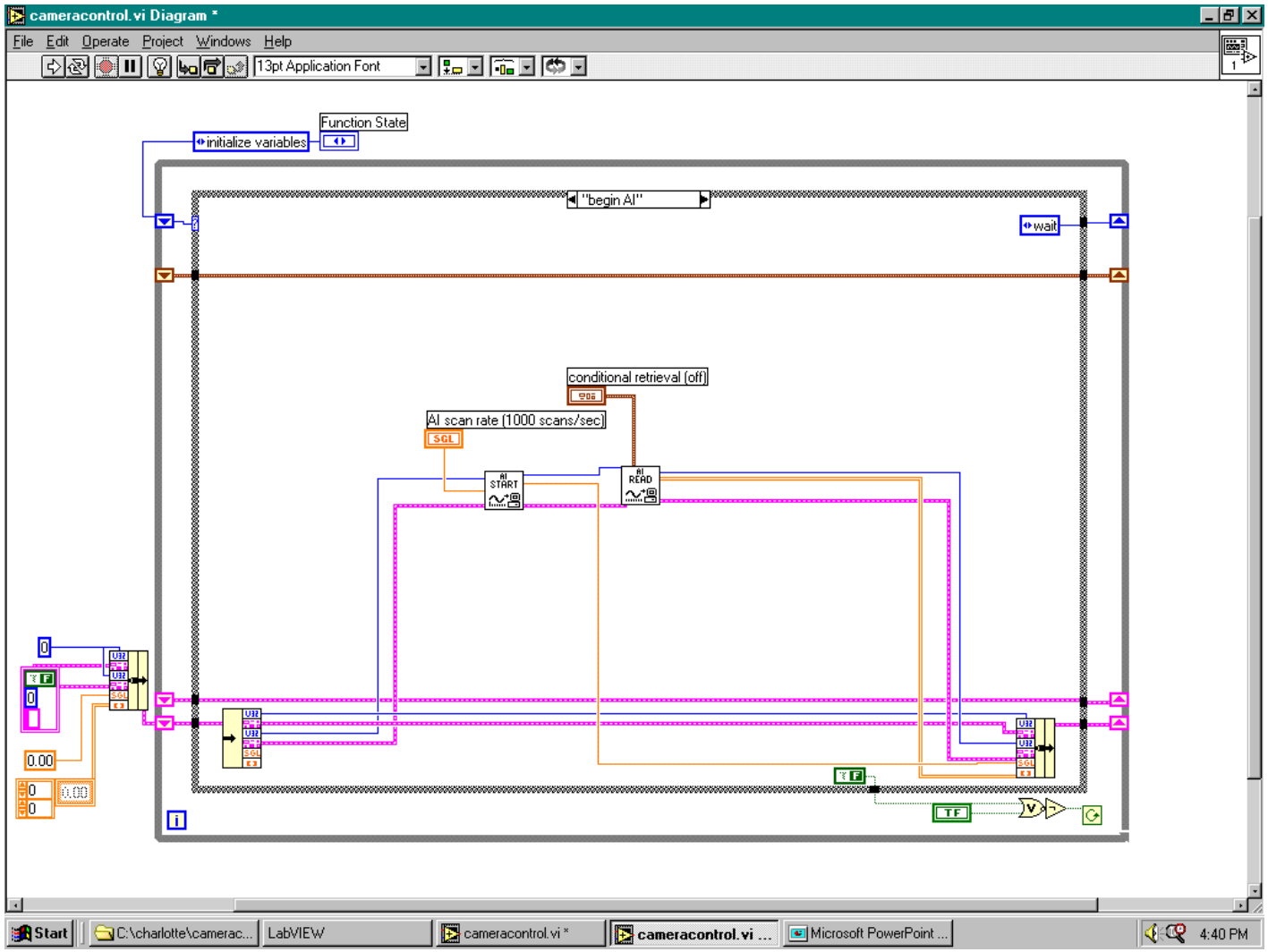

Figure D.9 LabVIEW™ diagram to acquire analog input.

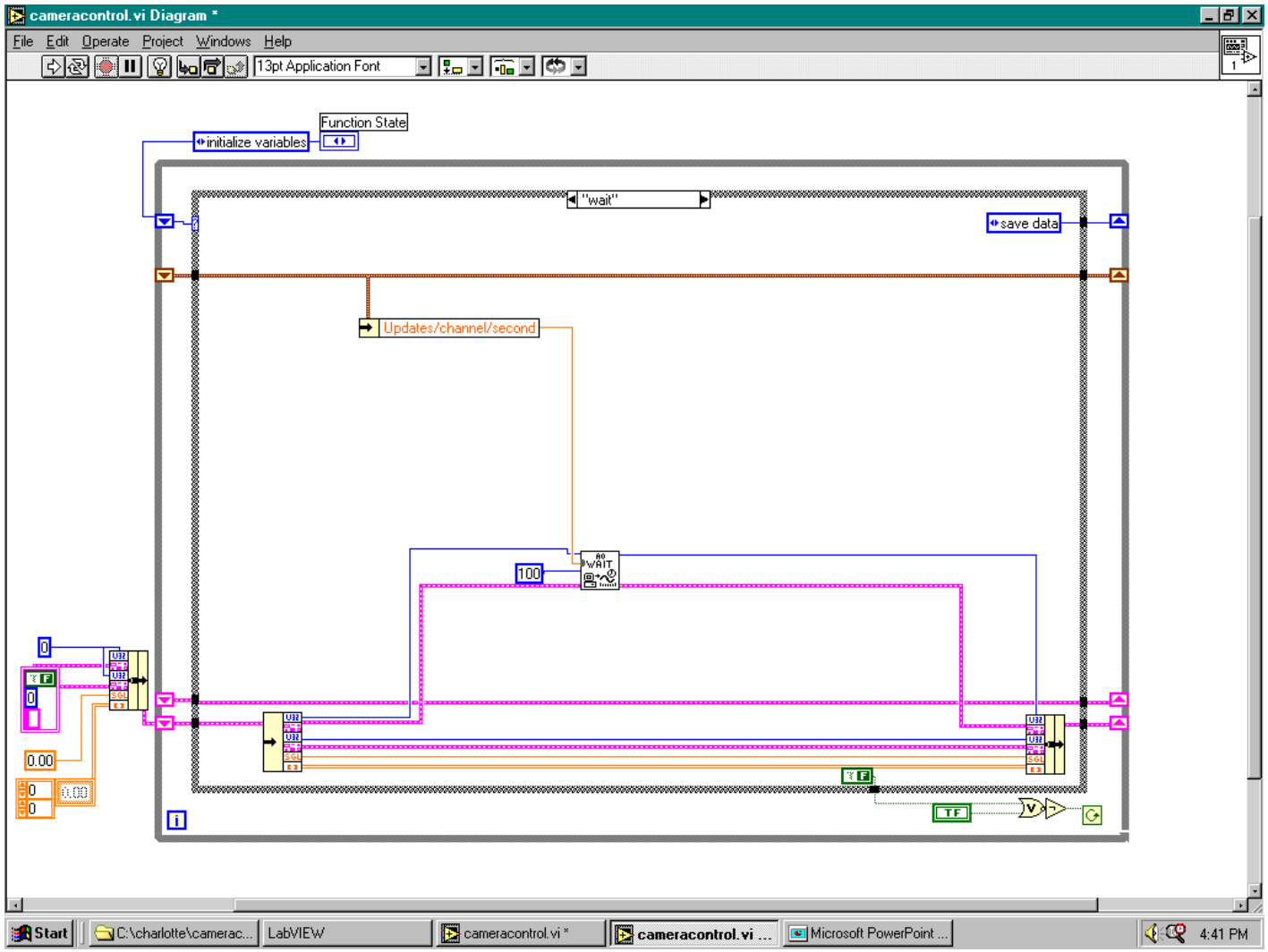

Figure D.10 LabVIEW™ diagram to make wait to save the acquired data until output completed.

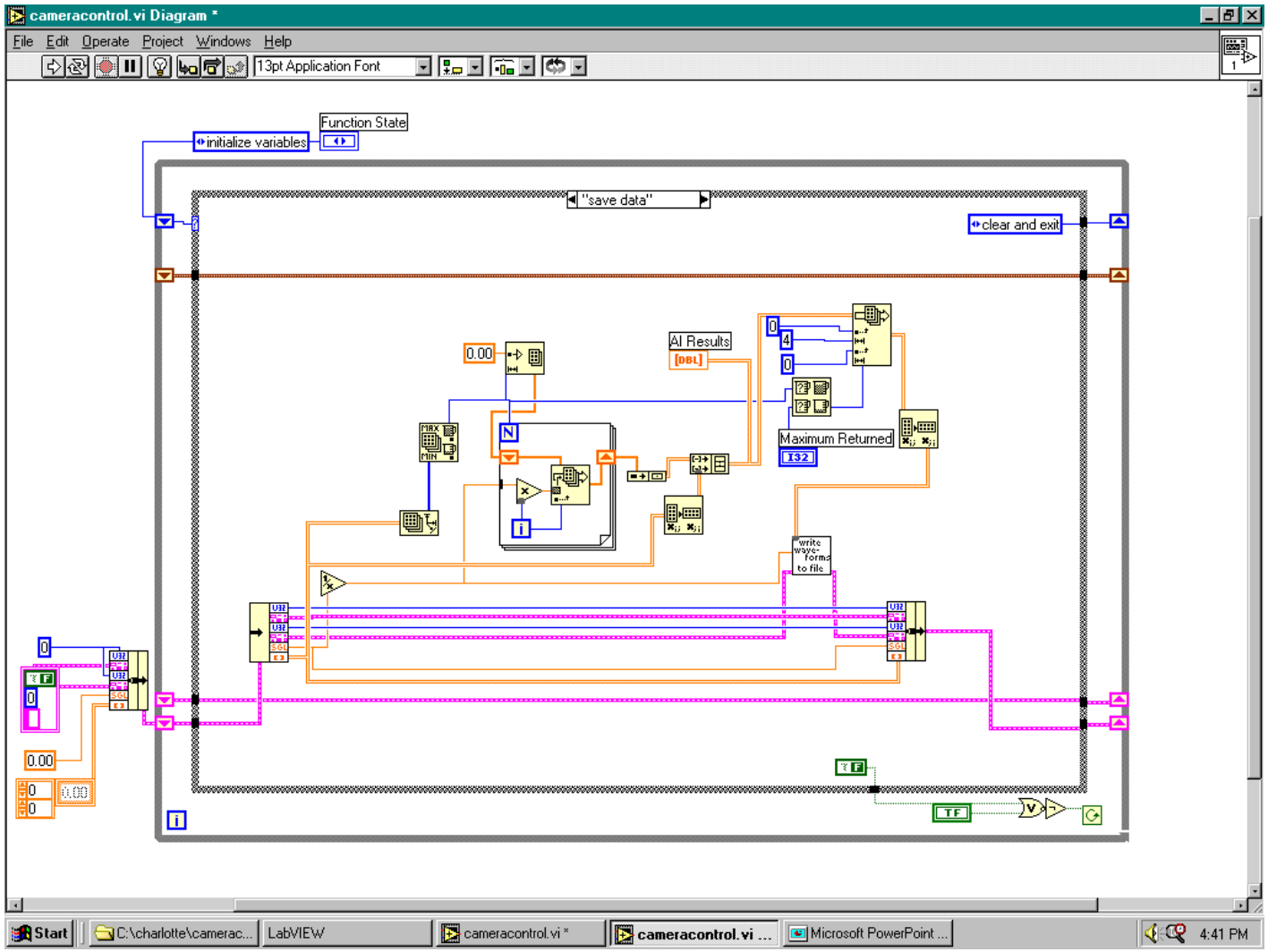

Figure D.11 LabVIEW™ diagram to save the acquired data.

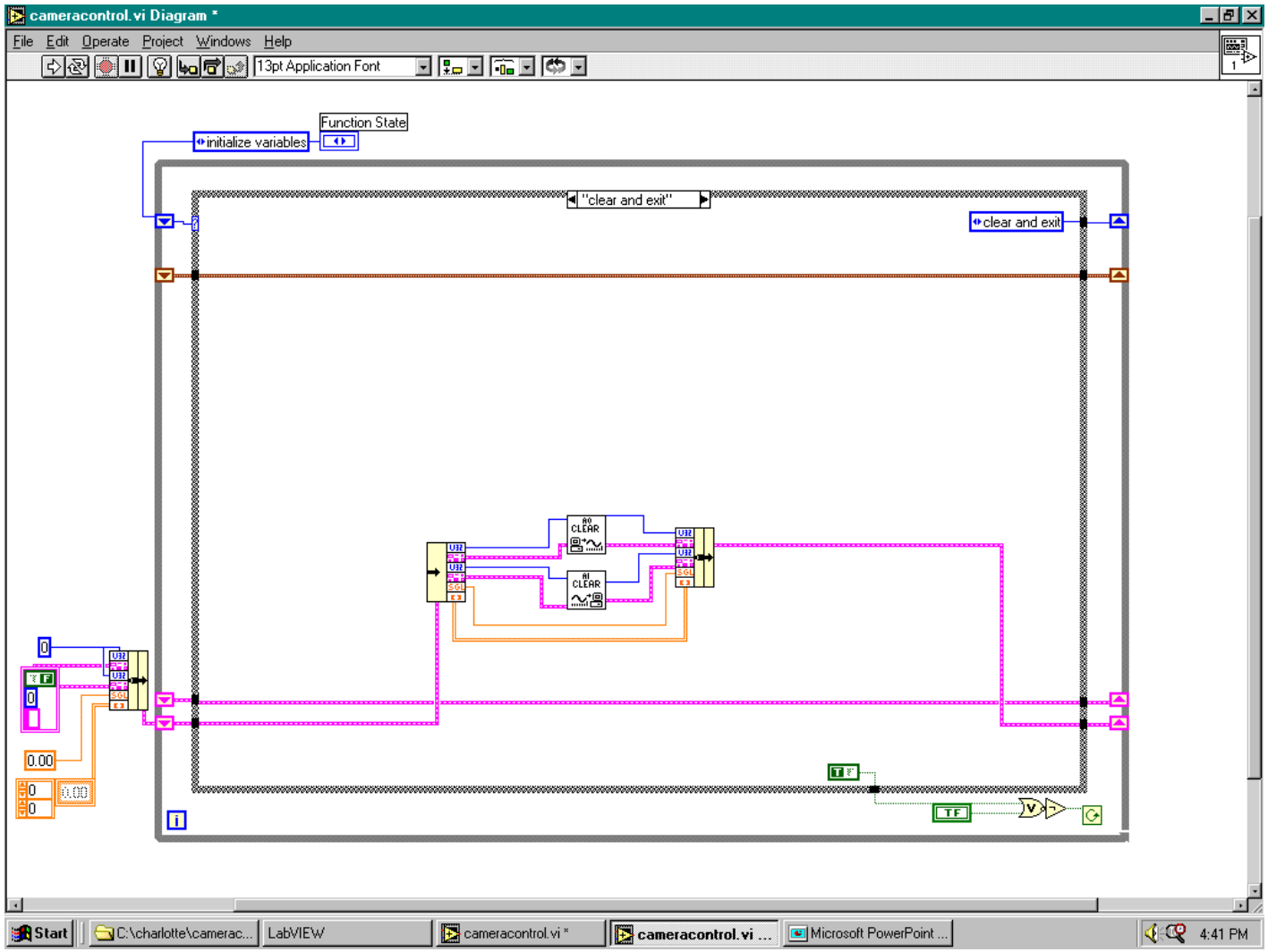

Figure D.12 LabVIEW™ diagram to clear analog buffers and stop program execution.

APPENDIX E

MATLAB® CODES

E.1 MATLAB® Nonlinear Least Squares Curve Fitting Subroutines

These subroutines follow a general pattern given by:

1. Establish initial guess of the arguments (position, size, orientation) of the function describing the body
2. Calculate the derivative of the function with respect to the arguments for each location along the edge
3. Verify that at least as many points as unknown arguments had valid derivatives
4. Calculate the change in the arguments to minimize the "error"
5. Establish a new initial guess, and repeat steps 2 and 3 until either the maximum number of iterations has been achieved or the error is "low enough"

E.1.1 Circle

```
function [xg,yg,rg,err]=nllsq(x0,y0,r0,xx,yy,npts)
%   Non-linear least squares curve fit for a circle.
%   Input:
%      x0    Initial guess for x-location of circle center
%      y0    Initial guess for y-location of circle center
%      r0    Initial guess for circle radius
%      xx    Vector of x-locations along circle boundary
%             (corresponding to yy)
%      yy    Vector of y-locations along circle boundary
%             (corresponding to xx)
%      npts  Number of points in xx and yy
%   Output:
%      xg    Fitted x-location of circle center
%      yg    Fitted y-location of circle center
%      rg    Fitted circle radius
%      err   Error code
%              0 for none
%              1 for maximum number of iteration exceeded
```

```
%
rg = r0;
xg = x0;
yg = y0;

done = 0;
itn = 0;
while ~done
    itn = itn+1;
    count = 0;
    clear mat dB
    for num = 1:npts
        xi = xx(num);
        if (rg^2-(xi-xg)^2)>0
            count = count+1;
            temp = sqrt(rg^2-(xi-xg)^2);
            posroot = temp+yg;
            negroot = -temp+yg;
            if abs(posroot-yy(num)) < abs(negroot-yy(num))
                dB(count) = yy(num)-posroot;
                dfdxo = (xi-xg)/temp;
                dfdyo = 1;
                dfdro = rg/temp;
            else
                dB(count) = yy(num)-negroot;
                dfdxo = -(xi-xg)/temp;
                dfdyo = 1;
                dfdro = -rg/temp;
            end
            mat(count,:) = [dfdro dfdxo dfdyo];
        end
    end
    if count < 3
        disp('crap')
        err = 1;
        return;
    end
    delta = (mat'*mat)\(mat'*dB');
    rg = rg+delta(1);
    xg = xg+delta(2);
    yg = yg+delta(3);

    if max(max(abs(delta./[rg xg yg]'))) < 1e-3
        done = 1;
        err = 0;
    end
    if itn > 1000
        disp(['error: itn= ' num2str(itn) ])
        delta'
        err = 1;
        keyboard;
    end
```

```
end
```

E.1.2 Ellipse (Known Orientation)

```
function
[x0,y0,rx,ry,theta,err]=nllsq(x0,y0,rx,ry,theta,xx,yy,npts)
%   Non-linear least squares curve fit for an ellipse.
%   Input:
%      x0    Initial guess for x-location of ellipse center
%      y0    Initial guess for y-location of ellipse center
%      rx    Initial guess for ellipse axis dimension ...
%            along x-direction
%      ry    Initial guess for ellipse axis dimension ...
%            along y-direction
%      theta Orientation angle of ellipse, radians
%      xx    Vector of x-locations along ellipse boundary
%             (corresponding to yy)
%      yy    Vector of y-locations along ellipse boundary
%             (corresponding to xx)
%      npts  Number of points in xx and yy
%   Output:
%      x0    Fitted x-location of ellipse center
%      y0    Fitted y-location of ellipse center
%      rx    Fitted ellipse x-direction dimension
%      ry    Fitted ellipse y-direction dimension
%      theta Orientation angle of ellipse, radians (unchanged)
%      err   Error code
%              0 for none
%              1 for maximum number of iteration exceeded
%
myy1 = inline(['(rx*ry/'...
    '(rx*rx*cos(theta)*cos(theta)+'...
    'ry*ry*sin(theta)*sin(theta)))*' ...
    'sqrt(rx*rx*cos(theta)*cos(theta)+'...
    'ry*ry*sin(theta)*sin(theta) –'...
    '(x-x0).^2) + y0 +'...
    '(x-x0)*(cos(theta)*sin(theta)*(rx*rx-ry*ry)/'...
    '(rx*rx*cos(theta)*cos(theta)+ '...
    'ry*ry*sin(theta)*sin(theta)))'],...
    'rx','ry','x0','y0','theta','x');
myy2 = inline(['-(rx*ry/'...
    '(rx*rx*cos(theta)*cos(theta)+ '...
    'ry*ry*sin(theta)*sin(theta)))*'...
    'sqrt(rx*rx*cos(theta)*cos(theta)+ '...
    'ry*ry*sin(theta)*sin(theta)'...
    '- (x-x0).^2) + y0 +'...
    '(x-x0)*(cos(theta)*sin(theta)*(rx*rx-ry*ry)/'...
    '(rx*rx*cos(theta)*cos(theta)+ '...
    'ry*ry*sin(theta)*sin(theta)))'],...
    'rx','ry','x0','y0','theta','x');
```

```
done = 0;
itn = 0;
while ~done
    itn = itn+1;
    count = 0;
    clear mat dB
    PP = rx*rx*cos(theta)*cos(theta)+...
        ry*ry*sin(theta)*sin(theta);
    for num = 1:npts
        xi = xx(num);
        if (PP - (xi-x0).^2)>0
            count = count+1;
            BB = sqrt(PP - (xi-x0).^2);
            posroot = myy1(rx,ry,x0,y0,theta,xi);
            negroot = myy2(rx,ry,x0,y0,theta,xi);
            if abs(posroot-yy(num)) < abs(negroot-yy(num))
                dB(count) = yy(num)-posroot;
                dydrx = rx^2*ry*cos(theta)^2/(BB*PP) + ...
                    ry^3*sin(theta)^2*BB/PP^2 + ...
                    (xi-x0)*...
                    cos(theta)*sin(theta)*2*rx*ry^2/PP^2;
                dydry = rx*ry^2*sin(theta)^2/(BB*PP) ...
                    + rx^3*cos(theta)^2*BB/PP^2 + ...
                    (xi-x0)*cos(theta)*sin(theta)*...
                    (-2)*ry*rx^2/PP^2;
                dydx0 = rx*ry*(xi-x0)/(BB*PP) - ...
                    cos(theta)*sin(theta)*(rx^2-ry^2)/PP;
                dydy0 = 1;
            else
                dB(count) = yy(num)-negroot;
                BB = -BB;
                dydrx = rx^2*ry*cos(theta)^2/(BB*PP) + ...
                    ry^3*sin(theta)^2*BB/PP^2 + ...
                    (xi-x0)* ...
                    cos(theta)*sin(theta)*2*rx*ry^2/PP^2;
                dydry = rx*ry^2*sin(theta)^2/(BB*PP) + ...
                    rx^3*cos(theta)^2*BB/PP^2 + ...
                    (xi-x0)*cos(theta)*sin(theta)* ...
                    (-2)*ry*rx^2/PP^2;
                dydx0 = rx*ry*(xi-x0)/(BB*PP) - ...
                    cos(theta)*sin(theta)*(rx^2-ry^2)/PP;
                dydy0 = 1;
            end
            mat(count,:) = [dydrx dydry dydx0 dydy0];
        end
    end
    if count < 4
        disp(['error: itn= ' num2str(itn) ', too few points'])
        err = 1;
        return;
    end
    delta = (mat'*mat)\(mat'*dB');
```

```
    rx = rx+delta(1);
    ry = ry+delta(2);
    x0 = x0+delta(3);
    y0 = y0+delta(4);
    [rx ry x0 y0];
    if max(max(abs(delta./[rx ry x0 y0]'))) < 1e-3
        done = 1;
        err = 0;
    end
    if itn > 100
        disp(['error: itn= ' num2str(itn) ...
            ', too many iterations'])
        delta'
        err = 1;
        keyboard;
    end
end
```

E.1.3 Ellipse (Unknown Orientation)

```
function [x0,y0,rx,ry,theta,err] =
nllsq(x0,y0,a0,c0,theta0,xx,yy,npts)
%   Non-linear least squares curve fit for an ellipse.
%   Input:
%      x0     Initial guess for x-location of ellipse center
%      y0     Initial guess for y-location of ellipse center
%      rx     Initial guess for ellipse axis dimension along
%               x-direction
%      ry     Initial guess for ellipse axis dimension along
%               y-direction
%      theta0 Initial guess of orientation angle of ...
%               ellipse, radians
%      xx     Vector of x-locations along ellipse boundary
%               (corresponding to yy)
%      yy     Vector of y-locations along ellipse boundary
%               (corresponding to xx)
%      npts   Number of points in xx and yy
%   Output:
%      x0     Fitted x-location of ellipse center
%      y0     Fitted y-location of ellipse center
%      rx     Fitted ellipse x-direction dimension
%      ry     Fitted ellipse y-direction dimension
%      theta  Orientation angle of ellipse, radians
%      err    Error code
%               0 for none
%               1 for maximum number of iteration exceeded
%
asq = a0^2;
csq = c0^2;
if abs(asq-csq)/abs(asq+csq) < 1e-5
    theta0 = 0;
```

```
end
aa = cos(theta0)^2/asq+sin(theta0)^2/csq;
cc = sin(theta0)^2/asq+cos(theta0)^2/csq;
if theta0 == 45*pi/180
    bb = 0.5*(1/asq-1/csq);
elseif theta0 == -45*pi/180
    bb = -0.5*(1/asq-1/csq);
else
    bb = -0.5*tan(2*theta0)*(cc-aa);
end
dd = (-x0*cos(theta0)^2-y0*cos(theta0)*sin(theta0))/asq+...
    (-x0*sin(theta0)^2+y0*cos(theta0)*sin(theta0))/csq;
ff = (-y0*sin(theta0)^2-x0*cos(theta0)*sin(theta0))/asq+...
    (-y0*cos(theta0)^2+x0*cos(theta0)*sin(theta0))/csq;
gg = (x0*cos(theta0)+y0*sin(theta0))^2/asq+...
    (-x0*sin(theta0)+y0*cos(theta0))^2/csq-1;

myy1 = inline(['sqrt((bb.^2-aa.*cc)*xi.^2+'...
    '2.*(bb.*ff-dd.*cc).*xi+ff.^2-gg.*cc)./ '...
    'cc-(bb.*xi+ff)./cc'],...
    'aa','bb','cc','dd','ff','gg','xi');

myy2 = inline(['-sqrt((bb.^2-aa.*cc)*xi.^2+'
    '2.*(bb.*ff-dd.*cc).*xi+ff.^2-gg.*cc)./cc-...
    (bb.*xi+ff)./cc'],...
    'aa','bb','cc','dd','ff','gg','xi');

done = 0;
itn = 0;
while ~done
    itn = itn+1;
    count = 0;
    clear mat dB
    for num = 1:npts
        xi = xx(num);
        if ((bb^2-aa*cc)*xi^2+2*(bb*ff-dd*cc)*xi+ff^2-gg*cc)>0
            count = count+1;
            temp = sqrt((bb^2-aa*cc)*xi^2+...
                2*(bb*ff-dd*cc)*xi+ff^2-gg*cc);
            posroot = (1/cc)*temp-(bb*xi+ff)/cc;
            negroot = -(1/cc)*temp-(bb*xi+ff)/cc;
            if abs(posroot-yy(num)) < abs(negroot-yy(num))
                dB(count) = yy(num)-posroot;
                dfdaa = -0.5*xi^2/temp;
                dfdbb = (bb*xi^2+ff*xi)/(cc*temp)-xi/cc;
                dfdcc = -temp/cc^2 - ...
                    0.5*(aa*xi^2+2*dd*xi+gg)/(cc*temp) +...
                    (bb*xi+ff)/cc^2;
                dfddd = -xi/temp;;
                dfdff = (bb+ff)/(cc*temp)-1/cc;
                dfdgg = -0.5/temp;
            else
```

```
                dB(count) = yy(num)-negroot;
                dfdaa = 0.5*xi^2/temp;
                dfdbb = -(bb*xi^2+ff*xi)/(cc*temp)-xi/cc;
                dfdcc = temp/cc^2 + ...
                    0.5*(aa*xi^2+2*dd*xi+gg)/(cc*temp) +...
                    (bb*xi+ff)/cc^2;
                dfddd = xi/temp;
                dfdff = -(bb+ff)/(cc*temp)-1/cc;
                dfdgg = 0.5/temp;
            end
            mat(count,:) = [dfdaa dfdbb dfdcc dfddd dfdff];
        end
    end
    if count < 5
        disp(['error: itn= ' num2str(itn) ...
            ', aa = ' num2str(aa) ...
            ', bb = ' num2str(bb) ', cc = ' num2str(dd) ...
            ', dd = ' num2str(dd) ', ff = ' num2str(ff) ...
            ', gg = ' num2str(gg)])
        err = 1;
        return;
    end
    delta = (mat'*mat)\(mat'*dB');
    aa = aa+delta(1);
    bb = bb+delta(2);
    cc = cc+delta(3);
    dd = dd+delta(4);
    ff = ff+delta(5);
    if max(max(abs(delta./[aa bb cc dd ff]'))) < 1e-3
        done = 1;
        err = 0;
    end
    if itn > 1000
        disp(['error: itn= ' num2str(itn) ...
            ', aa = ' num2str(aa) ...
            ', bb = ' num2str(bb) ', cc = ' num2str(cc) ...
            ', dd = ' num2str(dd) ', ff = ' num2str(ff) ...
            ', gg = ' num2str(gg)])
        delta'
        err = 1;
        keyboard;
    end
end
if abs(bb) < 1e-10
    theta = 0;
elseif abs(cc-aa)/abs(cc+aa) < 1e-5
    theta = pi/4;
else
    theta = 0.5*atan2((-2*bb),(cc-aa));
end
x0 = (cc*dd-bb*ff)/(bb^2-aa*cc);
y0 = (-bb*dd+aa*ff)/(bb^2-aa*cc);
```

```
rx=sqrt(-(aa*xo^2+2*bb*xo*yo+cc*yo^2+2*dd*xo+2*ff*yo+gg)/...
    (aa*cos(theta)^2+...
    2*bb*cos(theta)*sin(theta)+cc*sin(theta)^2));
ry=sqrt(-(aa*xo^2+2*bb*xo*yo+cc*yo^2+2*dd*xo+2*ff*yo+gg)/...
    (aa*sin(theta)^2-...
    2*bb*cos(theta)*sin(theta)+cc*cos(theta)^2));
```

E.2 MATLAB® Spurious Vector Identification Subroutine

```
function [ufilt,vfilt,badspurpts] =
spurfilt(uraw,vraw,insidebody)
%   A modified median filter algorithm (based on Westerweel's
%   1994 Exp. in Fluids paper and 2005 Exp. in Fluids letter
%    (with Scarano)).
%   Input:
%       uraw:   matrix containing the horizontal displacements
%       vraw:   matrix containing the vertical displacements
%       insidebody:    matrix containing points inside body
%   Output:
%       ufilt:  filtered horizontal displacements (bad
%               points replaced with NaN's)
%       vfilt:  filtered vertical displacements
%       badspurpts: matrix containing bad point locations
%
eps = 0.1;
crit = 2.25;
%   Find the residual
[nr,nc]=size(uraw);
uorig = uraw;
vorig = vraw;
ind = find(insidebody==1);
uraw(ind) = NaN; vraw(ind) = NaN;
umat = zeros(nr+2,nc+2);
umat(:,:) = NaN;
umat(2:nr+1,2:nc+1) = uraw;
vmat = zeros(nr+2,nc+2);
vmat(:,:) = NaN;
vmat(2:nr+1,2:nc+1) = vraw;
umed = nlfilter(umat,...
    [3 3],...
    inline('nanmedian([x(1,:),x(2,1),x(2,3),x(3,:)])','x'));
r_u = sqrt((uraw-umed(2:nr+1,2:nc+1)).^2);
rm_u = nlfilter(r_u,[3 3],...
    inline('nanmedian([x(1,:),x(2,1),x(2,3),x(3,:)])','x'));
rprime_u = r_u./(rm_u+eps);
vmed = nlfilter(vmat,[3 3],...
    inline('nanmedian([x(1,:),x(2,1),x(2,3),x(3,:)])','x'));
r_v = sqrt((vraw-vmed(2:nr+1,2:nc+1)).^2);
rm_v = nlfilter(r_v,[3 3],...
    inline('nanmedian([x(1,:),x(2,1),x(2,3),x(3,:)])','x'));
rprime_v = (r_v)./(rm_v+eps);
```

```
ufilt = uorig;
vfilt = vorig;
badspurpts = zeros(nr,nc);
ind = find(rprime_u > crit);
ufilt(ind) = NaN;
vfilt(ind) = NaN;
clear ind
ind=find(rprime_v > crit);
ufilt(ind) = NaN;
vfilt(ind) = NaN;
ind = find(insidebody==1);
ufilt(ind) = 0;
vfilt(ind) = 0;
badspurpts(isnan(ufilt)) = 1;
badspurpts(isnan(vfilt)) = 1;
```

E.3 MATLAB® Stagnation Point Locator Subroutines

The following subroutines locate stagnation points based on a known velocity field and body location. To locate stagnation points within the flow field, possible stagnation point locations are determined based upon the flow changing direction in both the vertical and horizontal within a grid square. The stagnation point is then assigned to the location of the change (where the velocity equals zero) based upon a linear interpolation of the velocity at the four corners of the grid square. Locating a stagnation point near the edge of the body is a little trickier, and requires some information about the location of the edge. The stagnation point can then be approximated by finding an intersection of the body and a line drawn through a series of points where the velocity is equal to zero in the direction tangential to the surface of the body.

E.3.1 Stagnation Points within the Flow Field

```
function [x0,y0] = stagloc(center_x,center_y,udisp,vdisp,insbdy)
%   Locate stagnation points in velocity field using a
%   linear interpolation of velocity values
%   Input:
%       center_x:   X grid locations, pixels (as from meshgrid)
%       center_y:   Y grid locations
%       udisp:      Horizontal displacment component (matrix)
%       vdisp:      Vertical displacement component (matrix)
%       insbdy:     Matrix of grid points inside body
%   Output:
```

```
%       x0,y0:      Stagnation points, pixels
%
[gnumy,gnumx]=size(center_x);
usign = round(sign(udisp));
vsign = round(sign(vdisp));
x0 = 0; y0 = 0; kk = 0;

for ii = 1:(gnumy-1)
    for jj = 1:(gnumx-1)
        if (insbdy(ii,jj) ~= 1 && insbdy(ii+1,jj) ~= 1 && ...
                insbdy(ii,jj+1) ~= 1 && ...
                insbdy(ii+1,jj+1) ~= 1)
            if ((usign(ii,jj) ~= usign(ii+1,jj)) || ...
                    (usign(ii,jj) ~= usign(ii,jj+1)) || ...
                    (usign(ii+1,jj) ~= usign(ii+1,jj+1)) || ...
                    (usign(ii,jj+1) ~= usign(ii+1,jj+1))) && ...
                    ((vsign(ii,jj) ~= vsign(ii+1,jj)) || ...
                    (vsign(ii,jj) ~= vsign(ii,jj+1)) || ...
                    (vsign(ii+1,jj) ~= vsign(ii+1,jj+1)) || ...
                    (vsign(ii,jj+1) ~= vsign(ii+1, jj+1)))
                u(1) = udisp(ii,jj);
                v(1) = vdisp(ii,jj);
                x(1) = center_x(ii,jj);
                y(1) = center_y(ii,jj);
                u(2) = udisp(ii+1,jj);
                v(2) = vdisp(ii+1,jj);
                x(2) = center_x(ii+1,jj);
                y(2) = center_y(ii+1,jj);
                u(3) = udisp(ii,jj+1);
                v(3) = vdisp(ii,jj+1);
                x(3) = center_x(ii,jj+1);
                y(3) = center_y(ii,jj+1);
                u(4) = udisp(ii+1,jj+1);
                v(4) = vdisp(ii+1,jj+1);
                x(4) = center_x(ii+1,jj+1);
                y(4) = center_y(ii+1,jj+1);
                if all(u) && all(v)
                    f1 = u(1)*x(4)*y(4)-u(2)*x(4)*y(1)-...
                        u(3)*x(1)*y(4)+u(4)*x(1)*y(1);
                    f2 = -u(1)*x(4)+u(2)*x(4)+...
                        u(3)*x(1)-u(4)*x(1);
                    f3 = -u(1)*y(4)+u(2)*y(1)+...
                        u(3)*y(4)-u(4)*y(1);
                    f4 = u(1)-u(2)-u(3)+u(4);
                    g1 = v(1)*x(4)*y(4)-v(2)*x(4)*y(1)-...
                        v(3)*x(1)*y(4)+v(4)*x(1)*y(1);
                    g2 = -v(1)*x(4)+v(2)*x(4)+...
                        v(3)*x(1)-v(4)*x(1);
                    g3 = -v(1)*y(4)+v(2)*y(1)+...
                        v(3)*y(4)-v(4)*y(1);
                    g4 = v(1)-v(2)-v(3)+v(4);
                    A = g3*f4-g4*f3;
```

```
                    B = g3*f2+g1*f4-g2*f3-g4*f1;
                    C = g1*f2-g2*f1;
                    tempx = [(-B+sqrt(B^2-4*A*C))/(2*A),...
                        (-B-sqrt(B^2-4*A*C))/(2*A)];
                    % D = g2*f4-g4*f2;
                    % E = g2*f3+g1*f4-g3*f2-g4*f1;
                    % F = g1*f3-g3*f1;
                    % tempy = [(-E+...
                        % sqrt(E^2-4*D*F))/(2*D),...
                        % (-E-sqrt(E^2-4*D*F))/(2*D)];
                    if imag(tempx(1))==0 && ...
                            tempx(1) >= x(1) ...
                            && tempx(1) <= x(3)
                        tempy = -(g3.*tempx(1)+g1)./...
                            (g4.*tempx(1)+g2);
                        % tempx = -(g2.*tempy(1)+g1)./...
                            (g4.*tempy(1)+g3);
                        if tempy > y(1) && tempy < y(2)
                            kk = kk+1;
                            x0(kk) = tempx(1);
                            y0(kk) = tempy;
                        end
                    end
                    if imag(tempx(2))==0 && ...
                            tempx(2) >= x(1) ...
                            && tempx(2) <= x(3)
                        tempy = -(g3.*tempx(2)+g1)./...
                            (g4.*tempx(2)+g2);
                        % tempx = -(f2.*tempy(2)+f1)./...
                            (f4.*tempy(2)+f3);
                        if tempy > y(1) && tempy < y(2)
                            kk = kk+1;
                            x0(kk) = tempx(2);
                            y0(kk) = tempy;
                        end
                    end
                end
                clear u v x y
            end
        end
    end
end
```

E.3.2 Stagnation Points near a Spheroidal Body

```
function
stgpt=surfstagpt(X,Y,U,V,rx,ry,th,x0,y0,insidebody,imgdir,fname,s
ep)
%   Estimate stagnation point near the body by:
%      1. Use existing PIV data to estimate points near the body
%         where the velocity changes sign.
```

```
%      2. Refine PIV data near estimated location
%      3. Use refined data to estimate stagnation point
%   Input:
%      X    Matrix defining grid x-locations
%      Y    Matrix defining grid y-locations
%      U    Matrix defining x-velocities
%      V    Matrix defining y-velocities
%      rx   x-axis dimension of ellipse
%      ry   y-axis dimension of ellipse
%      th   Orientation angle of ellipse, radians
%      x0   x-location of center of ellipse
%      y0   y-location of center of ellipse
%      insidebody
%           Matrix denoting grid locations that are inside
%               the elliptical body
%      imgdir
%           String containing the image directory path
%      fname
%           Image file name
%      sep
%           Separation between images to use for PIV
%   Output:
%      stgpt
%           Matrix containing the stagnation point locations
%           Each line is a different stagnation point
%           and is in the form [x-location, y-location]
%
nlg = 48;    % 32 usually works.  Check flow field
U(insidebody) = NaN;
V(insidebody) = NaN;
outln = findoutln(X,Y,insidebody);
totgoodimg=countimg(imgdir);
subavgdone = 0;
sep = sep;    % 2*sep used if flow near stagnation point
              %unusually slow

border = zeros(1,length(outln));
for ii = 1:length(outln)
    [stgpt,direc] = closetocurve(X(outln(ii,1),outln(ii,2)),...
        Y(outln(ii,1),outln(ii,2)),rx,ry,x0,y0,th);
    w1 = direc;
    w2 = [U(outln(ii,1),outln(ii,2)),V(outln(ii,1),outln(ii,2))];
    border(ii) = (sum(w1.*w2));
    clear stgpt
end
ind = find(abs(diff(sign(border))) >= 1);
jj = 1;
for ii = 1:length(ind)
    vel1 = sqrt(U(outln(ind(ii),1),outln(ind(ii),2)).^2+...
        V(outln(ind(ii),1),outln(ind(ii),2)).^2);
    vel2 = sqrt(U(outln(ind(ii)+1,1),outln(ind(ii)+1,2)).^2+...
        V(outln(ind(ii)+1,1),outln(ind(ii)+1,2)).^2);
```

```
    if ind(ii) > 2 && ind(ii) < (length(border)-3) && ...
            median(sign(border(ind(ii)-2:ind(ii)))) ~= ...
            median(sign(border(ind(ii)+1:ind(ii)+3)))
        if border(ind(ii)) < border(ind(ii)+1)
            strtloc(jj,:) = ...
                [X(outln(ind(ii),1),outln(ind(ii),2)),...
                Y(outln(ind(ii),1),outln(ind(ii),2))];
        else
            strtloc(jj,:) = ...
                [X(outln(ind(ii)+1,1),outln(ind(ii)+1,2)),...
                Y(outln(ind(ii)+1,1),outln(ind(ii)+1,2))];
        end
            jj = jj+1;
    elseif ind(ii) <= 2 || ind(ii) >= (length(border)-3)
        if border(ind(ii)) < border(ind(ii)+1)
            strtloc(jj,:) = ...
                [X(outln(ind(ii),1),outln(ind(ii),2)),...
                Y(outln(ind(ii),1),outln(ind(ii),2))];
        else
            strtloc(jj,:) = ...
                [X(outln(ind(ii)+1,1),outln(ind(ii)+1,2)),...
                Y(outln(ind(ii)+1,1),outln(ind(ii)+1,2))];
        end
        jj = jj+1;
    end
end
clear ind

if exist('strtloc')~=0
    [nump,temp] = size(strtloc);
    for ii = 1:nump
        gx0 = strtloc(ii,1)-nlg;
        gxf = strtloc(ii,1)+nlg;
        gy0 = strtloc(ii,2)-nlg;
        gyf = strtloc(ii,2)+nlg;
        sp = 8;
        if gx0 < 50
            gx0 = 50;
        end
        if gy0 < 50
            gy0 = 50;
        end
        if gxf > 950
            gxf = 950;
        end
        if gyf > 950
            gyf = 950;
        end
        [tx,ty] = meshgrid(gx0:sp:gxf,gy0:sp:gyf);
        insbdy =  findbody(tx,ty,x0,y0,rx,ry,th);
        if exist([imgdir '\NewAfpiv\' fname '__DCC_25_' ...
            num2str(300) ...
```

```
            '_' num2str(sep) '_16_24_' num2str(gx0) ...
            '_' num2str(gy0) ...
            '.dat'],'file') == 2
            vec = load([imgdir '\NewAfpiv\' fname '__DCC_25_' ...
                num2str(300) '_' ...
                num2str(sep) '_16_24_'...
                num2str(gx0) '_' num2str(gy0) '.dat']);
            nx = length(find(vec(:,1) == vec(1,1)));
            xx = reshape(vec(:,1),[],nx)';
            yy = reshape(vec(:,2),[],nx)';
            uu = reshape(vec(:,3),[],nx)';
            vv = reshape(vec(:,4),[],nx)';
            insbdy =  findbody(xx,yy,x0,y0,rx,ry,th);
            uu(insbdy) = NaN;
            vv(insbdy) = NaN;
            %[uu,vv,badspurpts] = mypiv_filt3(uu,vv,insbdy);
        elseif exist([imgdir '\NewAfpiv\' fname '__DCC_25_' ...
                    num2str(min([totgoodimg-25-sep])) ...
                    '_' num2str(sep) '_16_24_' num2str(gx0) ...
                    '_' num2str(gy0) '.dat'],'file') == 2
            vec = load([imgdir '\NewAfpiv\' fname '__DCC_25_' ...
                num2str(min([totgoodimg-25-sep])) '_' ...
                num2str(sep) '_16_24_'...
                num2str(gx0) '_' num2str(gy0) '.dat']);
            nx = length(find(vec(:,1) == vec(1,1)));
            xx = reshape(vec(:,1),[],nx)';
            yy = reshape(vec(:,2),[],nx)';
            uu = reshape(vec(:,3),[],nx)';
            vv = reshape(vec(:,4),[],nx)';
            insbdy = ...

    findbody(tx,ty,x0,y0,rx,ry,th,x01,y01,rx1,ry1,th1);
            uu(insbdy) = NaN;
            vv(insbdy) = NaN;
            % Filter below optional
            [uu,vv,badspurpts] = mypiv_filt3(uu,vv,insbdy);
        else
            if subavgdone == 0
                if strcmp(imgdir(1:23),'F:\MultFreq\march142007')
                    dirin = ...
                        ['F:\MultFreq\march142007\Tempfiles\'...
                        fname 'temp'];
                    copyfile([dirin '\*.bmp'],...
                        'C:\Charlotte\Temp')
                    totgoodimg = 300;
                    subavgdone = 1;
                else
                    totgoodimg = ...
                        createPIVinput(imgdir,...
                        'C:\Charlotte\Temp');
                    subavgdone = 1;
                end
```

```
    end
    [xx,yy,uu,vv] =...
        shortPIV('C:\Charlotte\Temp',...
        fname,sep,gx0,gy0,gxf,gyf,sp,insbdy,...
        totgoodimg);
    %[uu,vv,badspurpts] = mypiv_filt3(uu,vv,insbdy);
end

[nr,nc] = size(uu);
u_mu = zeros(nr,nc);
u_nu = zeros(nr,nc);

if sqrt(max([rx,ry])^2-min([rx,ry])^2)/...
        max([rx,ry]) < 0.25
    for iii = 1:nr
        for jjj = 1:nc
            th = atan2(yy(iii,jjj)-y0,xx(iii,jjj)-x0);
            rr = ((yy(iii,jjj)-y0).^2+...
                (xx(iii,jjj)-x0).^2).^0.5;
            dxdnu = -rr*sin(th);
            dydnu = rr*cos(th);
            dxdmu = cos(th);
            dydmu = sin(th);
            V1V2 = inv([dxdmu^2+dydmu^2,...
                dxdmu*dxdnu+dydmu*dydnu;...
                dxdmu*dxdnu+dydmu*dydnu,...
                dxdnu^2+dydnu^2])*...
                [uu(iii,jjj)*dxdmu+vv(iii,jjj)*dydmu;...
                uu(iii,jjj)*dxdnu+vv(iii,jjj)*dydnu];
            u_mu(iii,jjj) =...
                V1V2(1)*sqrt(dxdmu.^2+dydmu.^2);
            u_nu(iii,jjj) =...
                V1V2(2)*sqrt(dxdnu.^2+dydnu.^2);
        end
    end
else
    if rx>ry
        a = sqrt(rx^2-ry^2);
        JJ = [cos(th),sin(th);-sin(th),cos(th)];
        xrot = (xx-x0)*JJ(1,1) + (yy-y0)*JJ(1,2);
        yrot = (xx-x0)*JJ(2,1) + (yy-y0)*JJ(2,2);
        uur = uu*JJ(1,1) + vv*JJ(1,2);
        vvr = uu*JJ(2,1) + vv*JJ(2,2);
        clear JJ
    else
        a = sqrt(ry^2-rx^2);
        JJ = [cos(th+pi/2),sin(th+pi/2);...
            -sin(th+pi/2),cos(th+pi/2)];
        xrot = (xx-x0)*JJ(1,1) + (yy-y0)*JJ(1,2);
        yrot = (xx-x0)*JJ(2,1) + (yy-y0)*JJ(2,2);
        uur = uu*JJ(1,1) + vv*JJ(1,2);
        vvr = uu*JJ(2,1) + vv*JJ(2,2);
```

```
    clear JJ
end
for iii = 1:nr
    for jjj = 1:nc
        S = (roots([1,...
            1-xrot(iii,jjj)^2/a^2-...
            yrot(iii,jjj)^2/a^2,...
            -yrot(iii,jjj)^2/a^2])).^0.5;
        S(S==0) = [];
        if length(find(imag(S)==0)) ~= 1
            C = (roots([1,...
                -1-xrot(iii,jjj)^2/a^2-...
                yrot(iii,jjj)^2/a^2,...
                xrot(iii,jjj)^2/a^2])).^0.5;
            C(imag(C)~=0)=[];
            C(abs(C-1)<1e-6)=[];
            C(abs(C-0)<1e-6)=[];
            mu = acosh(C);
            if isempty(mu)
                disp('hmmm. trouble in mu.')
            end
        else
            S(imag(S)~=0)=[];
            mu = asinh(S);
            if mu < 0
                mu = asinh(-S);
            end
        end
        nu =...
            atan2(yrot(iii,jjj)*cosh(mu),...
            xrot(iii,jjj)*sinh(mu));
        if length(mu)~=1 || length(nu)~=1
            disp('Error in mu/nu')
        end
        if abs(a*cosh(mu)*cos(nu)-xrot(iii,jjj))>...
                1e-3
            [a*cosh(mu)*cos(nu),xrot(iii,jjj)]
            disp('x wrong')
        end
        if abs(a*sinh(mu)*sin(nu)-yrot(iii,jjj))>...
                1e-3
            [a*sinh(mu)*sin(nu),yrot(iii,jjj)]
            disp('y wrong')
        end
        dxdmu = a*sinh(mu)*cos(nu);
        dxdnu = -a*cosh(mu)*sin(nu);
        dydmu = a*cosh(mu)*sin(nu);
        dydnu = a*sinh(mu)*cos(nu);
        V1V2 = inv([dxdmu^2+dydmu^2,...
            dxdmu*dxdnu+dydmu*dydnu;...
            dxdmu*dxdnu+dydmu*dydnu,...
            dxdnu^2+dydnu^2])*...
```

```
                        [uur(iii,jjj)*dxdmu+vvr(iii,jjj)*...
                        dydmu;...
                        uur(iii,jjj)*dxdnu+vvr(iii,jjj)*dydnu];
                    u_mu(iii,jjj) =...
                        V1V2(1)*sqrt(dxdmu.^2+dydmu.^2);
                    u_nu(iii,jjj) =...
                        V1V2(2)*sqrt(dxdnu.^2+dydnu.^2);
                    clear S nu mu
                    clear dxdmu dxdnu dydmu dydnu V1V2
                end
            end
        end
        % stgptU(ii,:)=...
        % findit(xx,yy,u_mu,rx,ry,th,x0,y0,strtloc(ii,:),8);
        stgptV(ii,:) = ...
            findit(xx,yy,u_nu,rx,ry,th,x0,y0,strtloc(ii,:),8);
    end
    stgpt=[stgptV];
else
    stgpt = [NaN,NaN];
end
%   Delete temporary files
if subavgdone==1
    movefile('C:\Charlotte\Temp\NewAfpiv',imgdir);
    delete('C:\Charlotte\Temp\*.bmp');
end

function outln = findoutln(cenx,ceny,insidebody)
%   Determine the grid locations forming a continuous outline of
%   the body
%   Input:
%      cenx    Matrix defining grid x-locations
%      ceny    Matrix defining grid y-locations
%      insidebody   Logical atrix defining body
%                      (0 if outside body, 1 if inside)
%   Output:
%      outln   Continuous outline of body in terms of matrix
locations
%
[nr,nc] = size(cenx);
byndbdy = zeros(size(insidebody));
for ii = 1:nr
    ind = find(diff(insidebody(ii,:)) == 1);
    byndbdy(ii,ind) = 1;
    ind = find(diff(insidebody(ii,:)) == -1);
    byndbdy(ii,ind+1) = 1;
end
for ii = 1:nc
    ind = find(diff(insidebody(:,ii)) == 1);
    byndbdy(ind,ii) = 1;
    ind = find(diff(insidebody(:,ii)) == -1);
    byndbdy(ind+1,ii) = 1;
```

```
end
clear ind
[rr,cc] = find(byndbdy);
temp = sortrows([rr,cc],1);
rr = temp(:,1);
cc = temp(:,2);
clear temp
% Order byndbody into outline as a continuous edge
attachments = zeros(size(rr));
for ii = 1:length(rr)
    if rr(ii) == 1
        rrange = 1:2;
    elseif rr(ii) == nr
        rrange = (nr-1):nr;
    else
        rrange = (rr(ii)-1):(rr(ii)+1);
    end
    if cc(ii) == 1
        crange = 1:2;
    elseif cc(ii) == nc
        crange = (nc-1):nc;
    else
        crange = (cc(ii)-1):(cc(ii)+1);
    end
    attachments(ii) = sum(reshape(byndbdy(rrange,crange),[],1))-
1;
end
ind = find(attachments==0);
attachments(ind) = [];
rr(ind) = [];
cc(ind) = [];
[val,ind] = min(attachments);
outln(1,:) = [rr(ind),cc(ind)];
rr(ind) = [];
cc(ind) = [];
attachments(ind) = [];
clear ind
done = 0;
len = 1;
outln_orig = [];
while ~done
    for ii = 1:length(rr)
        dist(ii) = sqrt((outln(len,1)-rr(ii)).^2+...
            (outln(len,2)-cc(ii)).^2);
    end
    [mindist,ind] = min(dist);
    if mindist > 2
        if length(outln) > length(rr)
            done = 1;
        else
            outln_orig = outln;
            outln = [];
```

```
            [val,ind] = min(attachments);
            outln(1,:) = [rr(ind),cc(ind)];
            rr(ind) = [];
            cc(ind) = [];
            attachments(ind) = [];
            len = 1;
        end
    else
        len = len+1;
        outln(len,:) = [rr(ind),cc(ind)];
        rr(ind) = [];
        cc(ind) = [];
        attachments(ind) = [];
    end
    if isempty(rr)
        done = 1;
    end
    clear dist
end
if ~isempty(outln_orig)
    if length(outln_orig)>length(outln)
        outln = outln_orig;
    end
end
clear ind done mindist dist rr cc

function totalgoodimg=countimg(fdirin)
%   Count the number of images in the directory for use in PIV
%   Input:
%      fdirin   String containing directory path
%   Output:
%      totalgoodimg   Number of images
%
done = 0;
while ~done
    if fdirin(end) == '\'
        fdirin = fdirin(1:(end-1));
    else
        done = 1;
    end
end
fname = fdirin((find(fdirin=='\',1,'last')+1):end);
cd(fdirin);
%   Look for images and create average image
FN = dir('*.bmp');
namelen = length(fname);
kk = 0;
for jj = 1:length(FN)
    if strcmp(FN(jj).name(1:namelen),fname) && ...
            ~isnan(str2double(FN(jj).name(end-5)))
        kk = kk+1;
        FNgood(kk).name = FN(jj).name;
```

```
    end
end
totalgoodimg = kk;

function insidebody = findbody(cenx,ceny,x0,y0,rx,ry,th)
%   Determine if the grid squares are inside or outside of the
%   elliptical body
%   Input:
%      cenx    Matrix defining grid x-locations
%      ceny    Matrix defining grid y-locations
%      rx      x-axis dimension of ellipse
%      ry      y-axis dimension of ellipse
%      th      Orientation angle of ellipse, radians
%      x0      x-location of center of ellipse
%      y0      y-location of center of ellipse
%   Output
%      insidebody   Logical matrix corresponding to grid in
%                   cenx and ceny, 0 if outside body, 1 if inside
%
myy1 = inline(['(rx*ry/'...
    '(rx*rx*cos(theta)*cos(theta)+'...
    'ry*ry*sin(theta)*sin(theta)))*' ...
    'sqrt(rx*rx*cos(theta)*cos(theta)+'...
    'ry*ry*sin(theta)*sin(theta) –'...
    '(x-x0).^2) + y0 +'...
    '(x-x0)*(cos(theta)*sin(theta)*(rx*rx-ry*ry)/'...
    '(rx*rx*cos(theta)*cos(theta)+ '...
    'ry*ry*sin(theta)*sin(theta)))'],...
    'rx','ry','x0','y0','theta','x');
myy2 = inline(['-(rx*ry/'...
    '(rx*rx*cos(theta)*cos(theta)+ '...
    'ry*ry*sin(theta)*sin(theta)))*'...
    'sqrt(rx*rx*cos(theta)*cos(theta)+ '...
    'ry*ry*sin(theta)*sin(theta)'...
    '- (x-x0).^2) + y0 +'...
    '(x-x0)*(cos(theta)*sin(theta)*(rx*rx-ry*ry)/'...
    '(rx*rx*cos(theta)*cos(theta)+ '...
    'ry*ry*sin(theta)*sin(theta)))'],...
    'rx','ry','x0','y0','theta','x');

sp = cenx(2,2)-cenx(1,1);
rx = rx+round(0.5*sp);
ry = ry+round(0.5*sp);
[nr,nc] = size(cenx);
insidebody = zeros(nr,nc);
for jj = 1:nc
    ymax = myy1(rx,ry,x0,y0,th,cenx(1,jj));
    ymin = myy2(rx,ry,x0,y0,th,cenx(1,jj));
    if isreal(ymax)
        for ii = 1:nr
            if ceny(ii,jj) <= ymax && ceny(ii,jj) >= ymin
                insidebody(ii,jj) = 1;
```

```
            end
        end
    end
end
insidebody = logical(insidebody);


function stgpt =
findit(cenx,ceny,psi,rx,ry,th,x0,y0,strtloc,lnlen)
%   Locate the intersection of the ellipse and a line through the
%   zeros of variable psi. If the line does not connect with the
%   ellipse, return the closest point on the ellipse to the
%   closest point of zero psi.
%   Input:
%      cenx    Matrix defining x-locations of variable psi
%      ceny    Matrix defining y-locations of variable psi
%      psi     Matrix defining a variable which has a zero
%                 near the body (streamfunction, velocity, etc)
%      rx      x-axis dimension of ellipse
%      ry      y-axis dimension of ellipse
%      th      Orientation angle of ellipse, radians
%      x0      x-location of center of ellipse
%      y0      y-location of center of ellipse
%      strtloc Starting location, should be near a zero of
%                variable psi
%      lnlen   Number of points to use to use in the curve fit
%                 which defines the line
%   Output:
%      stgpt   Intersection (presumed stagnation point)
%
myy1 = inline(['(rx*ry/'...
    '(rx*rx*cos(theta)*cos(theta)+'...
    'ry*ry*sin(theta)*sin(theta)))*' ...
    'sqrt(rx*rx*cos(theta)*cos(theta)+'...
    'ry*ry*sin(theta)*sin(theta) –'...
    '(x-x0).^2) + y0 +'...
    '(x-x0)*(cos(theta)*sin(theta)*(rx*rx-ry*ry)/'...
    '(rx*rx*cos(theta)*cos(theta)+ '...
    'ry*ry*sin(theta)*sin(theta)))'],...
    'rx','ry','x0','y0','theta','x');
myy2 = inline(['-(rx*ry/'...
    '(rx*rx*cos(theta)*cos(theta)+ '...
    'ry*ry*sin(theta)*sin(theta)))*'...
    'sqrt(rx*rx*cos(theta)*cos(theta)+ '...
    'ry*ry*sin(theta)*sin(theta)'...
    '- (x-x0).^2) + y0 +'...
    '(x-x0)*(cos(theta)*sin(theta)*(rx*rx-ry*ry)/'...
    '(rx*rx*cos(theta)*cos(theta)+ '...
    'ry*ry*sin(theta)*sin(theta)))'],...
    'rx','ry','x0','y0','theta','x');
poss = findzero(cenx,ceny,psi);
[nump,temp] = size(poss);
```

```
[nums,temp] = size(strtloc);
stgpt = [NaN,NaN];
if nums > 1
    disp('Error. Only first location checked')
    strtloc(2:end,:) = [];
end
iii = 1;
done = 0;
repeat = 0;
if nump > 3
    minx = x0-max([rx,ry]);
    maxx = x0+max([rx,ry]);
    mycurvex = [maxx:-1:minx,minx:maxx];
    mycurvey = [myy1(rx,ry,x0,y0,th,...
        maxx:-1:minx),myy2(rx,ry,x0,y0,th,minx:maxx)];
        [p,stat] = robustfit(poss(:,1),poss(:,2));
        m = p(2);  b = p(1);
        if stat.robust_s>5 || repeat == 1
            ind = find(imag(mycurvey)~=0);
            mycurvex(ind) = [];
            mycurvey(ind) = [];
            numcp = length(mycurvex);
            for jjj = 1:nump
                for jj = 1:numcp
                    dis(jj) = sqrt((poss(jjj,1)-...
                        mycurvex(jj))^2+...
                        (poss(jjj,2)-mycurvey(jj))^2);
                end
                [val(jjj),indn(jjj)] = min(dis);
            end
            [temp,indnn]=min(val);
            loc(1,:) = [poss(indnn,1),poss(indnn,2)];
            poss(indnn,:) = [];
            nump=nump-1;
            clear dis val indn indnn
            for jjj = 1:nump
                dis(jjj) = sqrt((poss(jjj,1)-loc(1,1))^2+...
                    (poss(jjj,2)-loc(1,2))^2);
            end
            [temp,indnn]=min(dis);
            loc(2,:) = [poss(indnn,1),poss(indnn,2)];
            poss(indnn,:) = [];
            nump = nump-1;
            clear dis indnn
            for jjj = 1:nump
                dis(jjj) = sqrt((poss(jjj,1)-loc(2,1))^2+...
                    (poss(jjj,2)-loc(2,2))^2);
            end
            [temp,indnn]=min(dis);
            loc(3,:) = [poss(indnn,1),poss(indnn,2)];
            poss(indnn,:) = [];
            nump = nump-1;
```

```
            clear dis indnn
            p = polyfit(loc(:,1),loc(:,2),1);
            m = p(1);  b = p(2);
        end
        %   Intersect curve
        A = (rx*cos(th))^2+(ry*sin(th))^2;
        B = cos(th)*sin(th)*(rx^2-ry^2);
        t1 = (m-B/A)^2+rx^2*ry^2/A^2;
        t2 = 2*(m-B/A)*(b+x0*B/A-y0)-2*x0*rx^2*ry^2/A^2;
        t3 = (b+x0*B/A-y0)^2-rx^2*ry^2/A^2*(A-x0^2);
        xi1 = (-t2+sqrt(t2^2-4*t1*t3))/(2*t1);
        xi2 = (-t2-sqrt(t2^2-4*t1*t3))/(2*t1);
        yi1 = m*xi1+b;
        yi2 = m*xi2+b;
        if sqrt((strtloc(iii,1)-xi1)^2+...
                (strtloc(iii,2)-yi1)^2) < ...
                sqrt((strtloc(iii,1)-xi2)^2+...
                (strtloc(iii,2)-yi2)^2)
            if isreal(xi1)
                stgpt(iii,:) = [xi1,yi1];
            else
                stgpt(iii,:) = [NaN,NaN];
            end
        else
            if isreal(xi2)
                stgpt(iii,:) = [xi2,yi2];
            else
                stgpt(iii,:) = [NaN,NaN];
            end
        end
        if isnan(stgpt(iii,1)) && isnan(loc(1,1)) && repeat == 0
            done = 0;
            repeat = 1;
        else
            done = 1;
        end
    end
end
if isnan(stgpt(iii,1)) && nump > 0
    minx = x0-max([rx,ry]);
    maxx = x0+max([rx,ry]);
    mycurvex = [maxx:-1:minx,minx:maxx];
    mycurvey = [myy1(rx,ry,x0,y0,th,maxx:-
1:minx),myy2(rx,ry,x0,y0,th,minx:maxx)];
    ind = find(imag(mycurvey)~=0);
    mycurvex(ind) = [];
    mycurvey(ind) = [];
    numcp = length(mycurvex);
    for jjj = 1:nump
        for jj = 1:numcp
            dis(jj) = sqrt((poss(jjj,1)-
mycurvex(jj))^2+(poss(jjj,2)-mycurvey(jj))^2);
```

```
        end
        [val(jjj),indn(jjj)] = min(dis);
    end
    [temp,indnn]=min(val);
    stgpt(iii,:) = [mycurvex(indn(indnn)),mycurvey(indn(indnn))];
end
clear poss nump

function [stgpt,direc] = closetocurve(xp,yp,rx,ry,x0,y0,th)
%   Locate the point on the body that is closest to the point
%   given by (xp, yp)
%   Input:
%      xp    x-location to find point on body closest to
%      yp    y-location to find point on body closest to
%      rx    x-axis dimension of ellipse
%      ry    y-axis dimension of ellipse
%      th    Orientation angle of ellipse, radians
%      x0    x-location of center of ellipse
%      y0    y-location of center of ellipse
%   Output:
%      stgpt   Intersection (presumed stagnation point)
%      direc   Unit vector of line tangent to ellipse at stgpt
%              location
%
myy1 = inline(['(rx*ry/'...
    '(rx*rx*cos(theta)*cos(theta)+'...
    'ry*ry*sin(theta)*sin(theta)))*' ...
    'sqrt(rx*rx*cos(theta)*cos(theta)+'...
    'ry*ry*sin(theta)*sin(theta) –'...
    '(x-x0).^2) + y0 +'...
    '(x-x0)*(cos(theta)*sin(theta)*(rx*rx-ry*ry)/'...
    '(rx*rx*cos(theta)*cos(theta)+ '...
    'ry*ry*sin(theta)*sin(theta)))'],...
    'rx','ry','x0','y0','theta','x');
myy2 = inline(['-(rx*ry/'...
    '(rx*rx*cos(theta)*cos(theta)+ '...
    'ry*ry*sin(theta)*sin(theta)))*'...
    'sqrt(rx*rx*cos(theta)*cos(theta)+ '...
    'ry*ry*sin(theta)*sin(theta)'...
    '- (x-x0).^2) + y0 +'...
    '(x-x0)*(cos(theta)*sin(theta)*(rx*rx-ry*ry)/'...
    '(rx*rx*cos(theta)*cos(theta)+ '...
    'ry*ry*sin(theta)*sin(theta)))'],...
    'rx','ry','x0','y0','theta','x');
minx = x0-max([rx,ry]);
maxx = x0+max([rx,ry]);
mycurvex = [maxx:-1:minx,minx:maxx];
mycurvey = [myy1(rx,ry,x0,y0,th,...
    maxx:-1:minx),myy2(rx,ry,x0,y0,th,minx:maxx)];
ind = find(imag(mycurvey)~=0);
mycurvex(ind) = [];
mycurvey(ind) = [];
```

```
mycurvex = [mycurvex(end),mycurvex,mycurvex(1)];
mycurvey = [mycurvey(end),mycurvey,mycurvey(1)];
nump = length(mycurvex);
dis1 = NaN*zeros(1,nump);
for ii = 2:(nump-1)
    dis1(ii) = sqrt((xp-mycurvex(ii))^2+(yp-mycurvey(ii))^2);
end
[val1,ind1] = nanmin(dis1);
if val1 < 64 % Was 32, changed to grid changes 7/21/2008
    stgpt = [mycurvex(ind1),mycurvey(ind1)];
    w1 = [(mycurvex(ind1+1)-mycurvex(ind1-1)),...
        (mycurvey(ind1+1)-mycurvey(ind1-1))];
    direc = w1./sqrt(sum(w1.*w1));
else
    stgpt = [NaN,NaN];
    direc= [NaN,NaN];
end
```

E.4 MATLAB® Vorticity Subroutine

```
function om=vortdiff(xx,yy,u,v)
%   vortdiff(xx,yy,u,v)
%   Vorticity calculation using circulation method.  Will
%   recalculate bad points using finite difference derivatives.
%   Input:
%      xx   Vector or grid of x-locations (as from meshgrid)
%      yy   Vector or grid of y-locations (as from meshgrid)
%      u    Matrix of velocities in the x-direction
%      v    Matrix of velocities in the y-direction
%   Output:
%      om   Matrix of vorticity values
%
[nr,nc] = size(xx);
if nr == 1 || nc == 1
    [xx,yy] = meshgrid(xx,yy);
end
dx = xx(2,2)-xx(1,1);
dy = yy(2,2)-yy(1,1);

%   Estimate vorticity using circulation method
[nr,nc] = size(u);
G = zeros(nr,nc)*NaN;
for ii = 2:nr-1
    for jj = 2:nc-1
        G(ii,jj) = dy*(v(ii-1,jj-1)+4*v(ii,jj-1)+...
            v(ii+1,jj-1)) - ...
            dy*(v(ii-1,jj+1)+4*v(ii,jj+1)+v(ii+1,jj+1)) - ...
            dx*(u(ii-1,jj-1)+4*u(ii-1,jj)+u(ii-1,jj+1)) + ...
            dx*(u(ii+1,jj-1)+4*u(ii+1,jj)+u(ii+1,jj+1));
    end
end
```

```
G = G./3;
om = -G./(4*dx*dy);

%   Estimate vorticity from definition using highest order
%   derivatives available
[badr,badc] = find(isnan(om));
nn = length(badr);
for ii = 1:nn
    %   Estimate dv/dx
    if badc(ii) == 1
        vel(1) = NaN;
    else
        vel(1) = v(badr(ii),badc(ii)-1);
    end
    vel(2) = v(badr(ii),badc(ii));
    if badc(ii) == nc
        vel(3) = NaN;
    else
        vel(3) = v(badr(ii),badc(ii)+1);
    end
    deriv = [(vel(2)-vel(1))/dx (vel(3)-vel(2))/dx ...
        (vel(3)-vel(1))/(2*dx)];
    if ~isnan(deriv(3))
        dvdx = deriv(3);
    elseif ~isnan(deriv(2))
        dvdx = deriv(2);
    elseif ~isnan(deriv(1))
        dvdx = deriv(1);
    else
        dvdx = NaN;
    end
    clear deriv vel
       Estimate du/dy
    if badr(ii) == 1
        vel(1) = NaN;
    else
        vel(1) = u(badr(ii)-1,badc(ii));
    end
    vel(2) = u(badr(ii),badc(ii));
    if badr(ii) == nr
        vel(3) = NaN;
    else
        vel(3) = u(badr(ii)+1,badc(ii));
    end
    deriv = [(vel(2)-vel(1))/dy (vel(3)-vel(2))/dy ...
        (vel(3)-vel(1))/(2*dy)];
    if ~isnan(deriv(3))
        dudy = deriv(3);
    elseif ~isnan(deriv(2))
    dudy = deriv(2);
    elseif ~isnan(deriv(1))
        dudy = deriv(1);
```

```
    else
        dudy = NaN;
    end
    clear deriv vel
    %   Replace bad values with new vorticity estimate
    om(badr(ii),badc(ii)) = (dvdx-dudy);
end
```

APPENDIX F

ACCELEROMETER MODEL OF THE OTOLITH

In order to determine the sensitivity of the hair cells, a model of the otolith system, including the otolith, hair cells, and surrounding tissues, is needed which will explain how much of the acoustic particle motion is sensed by the cilia. Most models of the otolith assume that it can be modeled as an accelerometer. Essentially, an accelerometer is a mass connected to an oscillating body by a spring. The sensor part of the accelerometer determines the relative distance between the mass and the oscillating body, which is proportional to the acceleration for frequencies much less than the resonant frequency of the accelerometer.

For the otolithic organ, the acoustically generated motion of the otolith with respect to the surrounding tissue can be determined by considering the effect of the finite density of the otolith. When excited by an acoustic wave, the otolith will oscillate with respect to the surrounding fluid, although the oscillation amplitude of the otolith will be smaller than the wave amplitude, and the otolith oscillation will be out of phase with the wave. For a particle of overall dimension less than the wavelength of the incident sound, the particle will scatter the incident sound. If the particle (*i.e.*, otolith) is in a fluid (without the surrounding fluid providing any damping or restoring forces), the relative motion will be reduced by a factor of (Pierce 1994)

$$\frac{S.G.-1}{S.G.+0.5} \qquad \text{F.1}$$

where *S.G.* is the ratio of the otolith and fluid densities, or in this case the specific gravity of the otolith (*S.G.* ≈ 3). The motion of the otolith relative to the surrounding fluid will therefore be about 60% of the acoustic particle motion.

When modeling the otolithic system as an accelerometer, the otolith is considered to be the proof mass and the surrounding fluid and tissue provide the elasticity and damping (de Vries 1951). Schematically, this looks like the diagram shown in Figure F.1, with m representing the otolith mass, x representing the motion of the otolith, and y representing the motion of the surroundings. The spring constant, k, represents a restoring force that is proportional to the displacement, while the damping constant, c, represents a force that is proportional to the velocity. As can be found in any vibrations textbook (for example, Dimarogonas 1996), a force balance on the body gives a 2nd order ordinary differential equation for the relative motion of the otolith with respect to its surroundings $z = x\text{-}y$ as follows:

$$m\ddot{z} + c\dot{z} + kz = 0. \qquad \text{F.2}$$

where the dots represent temporal derivatives. For the case where the surroundings move sinusoidally with an angular frequency ω

$$y(t) = Y\sin(\omega t) \qquad \text{F.3}$$

Equation F.2 becomes the equation of motion for a damped system undergoing forced harmonic excitation, or

$$m\ddot{z} + c\dot{z} + kz = m\omega^2 Y\sin(\omega t). \qquad \text{F.4}$$

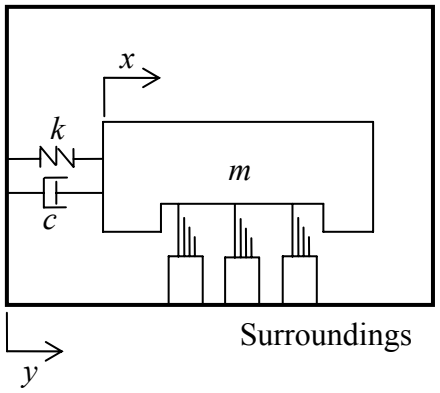

Figure F.1 Schematic of the otolith as an accelerometer.

The solution for the relative motion, z, is then

$$z = \frac{\left(\frac{\omega}{\omega_n}\right)^2}{\left\{\left[1-\left(\frac{\omega}{\omega_n}\right)^2\right]^2 + \left[2\varsigma\left(\frac{\omega}{\omega_n}\right)\right]^2\right\}^{\frac{1}{2}}} Y\sin\left(\omega t - \phi\right) \qquad \text{F.5}$$

where $\omega_n = \sqrt{k/m}$ is the natural (resonant) frequency of the system, $\varsigma = c/(2m\omega_n)$ is the damping coefficient, and

$$\phi = \arctan\left(\frac{2\varsigma\left(\frac{\omega}{\omega_n}\right)}{1-\left(\frac{\omega}{\omega_n}\right)^2}\right) \qquad \text{F.6}$$

is the relative phase in the response. The otolith is believed to be nearly critically damped, corresponding to $\varsigma \approx 1$ (Sand and Karlsen 2000). The magnitude of the relative displacement as a function of input displacement (a) and input acceleration (b) is shown in Figure F.2 for an undamped (solid line) and critically damped (dashed line) system.

At low frequencies, the relative motion can be simplified to:

$$z = \left(\frac{\omega}{\omega_n}\right)^2 Y\sin\left(\omega t\right) \qquad \text{F.7}$$

In other words, the amplitude of the relative motion of the otolith to its surroundings (z) is less than the driving motion's amplitude by a factor of $\left(\frac{\omega}{\omega_n}\right)^2$. At high frequencies, the relative motion between the mass and the surroundings is approximately equal to the motion of the base, or

$$z \approx Y\sin\left(\omega t - \pi\right). \qquad \text{F.8}$$

Therefore, in the limit of very high frequencies, the mass remains stationary while the surroundings oscillate about this mass.

The shapes of these resonance curves remain the same if the equations of motion are formulated in terms of the angular momentum, *vs.* the relative motion. In this case, the governing equation takes the form

$$J\ddot{\phi} + c_T\dot{\phi} + k_T\phi = J\omega^2\Theta\sin(\omega t) \qquad \text{F.9}$$

where ϕ is the angular displacement, J is the mass moment of inertia, c_T and k_T are the torsional damping and stiffness constants, respectively, and Θ is a constant describing the amplitude of the angular forcing function. The solution is then given in terms of the relative angular (*vs.* linear) displacement of the body.

The usual model of the otolithic system suggests that the hair cells essentially measure the relative displacement between the otolith and its surroundings. If the otolithic system operates above its resonant frequency, the response of the hair cells should be proportional to the acoustic particle motion. If the otolith is operating below its resonant frequency, the response of the hair cells should be proportional to the

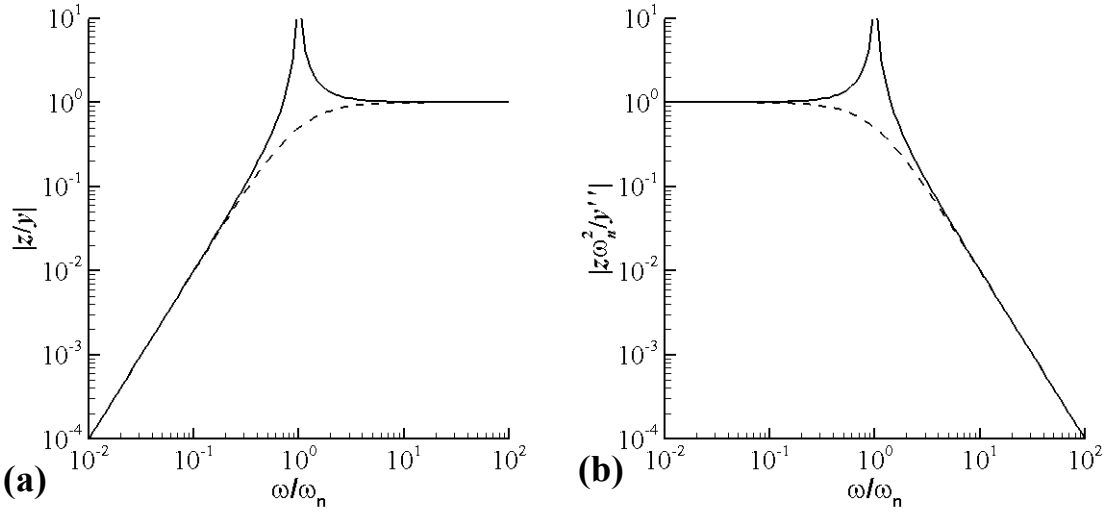

Figure F.2 Response of a spring-mass system as a function of frequency, normalized by the resonant frequency of the system for an undamped (solid line) and critically damped system (dashed line). The response is shown in terms of the magnitude of the relative

acceleration of the otolith.

When plotted in terms of the velocity of the surroundings ($\dot{y}$), the sensitivity of an accelerometer would be seen to decrease at low frequencies, since increasingly large amplitudes ($Y\omega$) would be required to generate the same acceleration. This is exactly the behavior that is seen in fish audiograms, which are plotted in terms of the acoustic pressure, which is proportional to the particle velocity, as shown in Figure 2.8. When plotted in terms of the acoustic particle acceleration, the response at low frequencies is observed to be essentially constant (Sand and Karlsen 2000). Several typical fish audiograms are shown in terms of the acceleration, velocity and displacement in Figure F.3. The decrease in sensitivity corresponds to the decrease in the relative acceleration between the relative motion and the surroundings above resonance shown in Figure F.2(b). These audiograms suggest that the otolith organ is operating as an accelerometer over most of its typical frequency range, with a minimum natural frequency that, while likely to be species-dependent, is at least of $O(10^2$ Hz).

De Vries (1951) attempted to measure the natural frequency of the otolithic system by subjecting fish heads to constant accelerations and measuring the displacement of the otolith. From the resulting spring constant, he found that the natural frequency of the otolith to be about 40 Hz. However, a resonant frequency of 40 Hz would be too small to explain the accelerometer-like behavior observed for fish ears since the fish ear would not be operating below its resonant frequency over most of its hearing range. This result then gives rise to the question: *What other structures inside the fish ear could have a high enough resonant frequency (at least a few hundred Hertz or higher) to explain the observed behavior?*

One possible structure is the otolithic membrane which surrounds the hair cells. Its lowest resonant frequency corresponds to a quarter wavelength across its thickness. Examination of a transmission electron microscopy (TEM) image (Dunkelberger *et al.* 1980) of an oblique cross-section reveals that the otolithic membrane of a juvenile mummichog is no thicker than four cilia lengths, or, conservatively, about 40 μm. Given

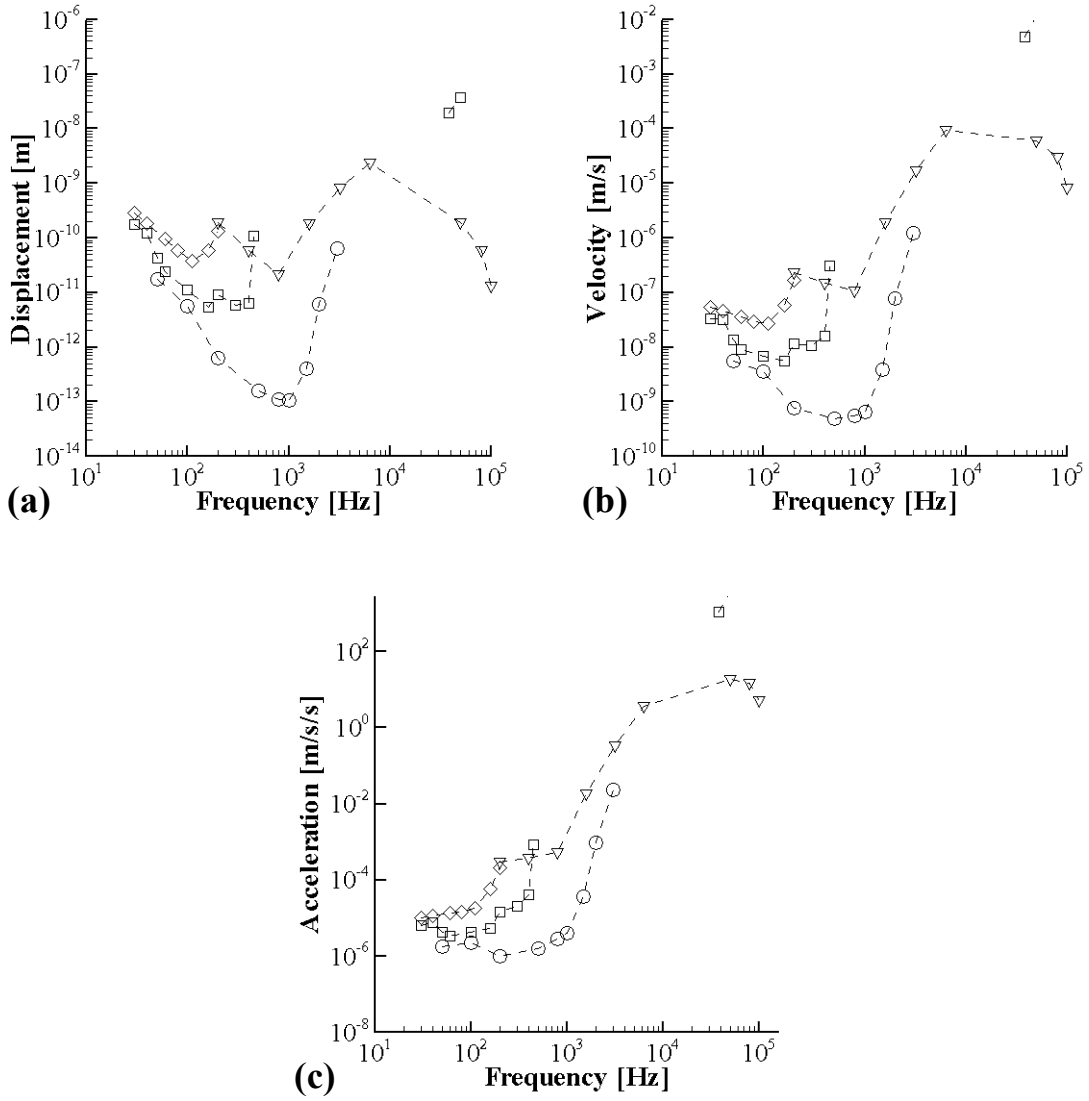

Figure F.3 Fish audiograms in terms of the (peak-to-peak) acoustic particle displacement (a), velocity (b), and acceleration (c) for the dab (diamond) (Chapman and Sand 1974), the cod (square) (Chapman and Hawkins 1973; Astrup and Møhl 1993, 1998), the goldfish (circle) (Jacobs and Tavolga 1967), and the American shad (triangle)

that the shear wave speeds in soft tissue are on the order of a few m/s (Gennisson *et al.* 2003), the resonant frequency is on the order of

$$\omega = 2\pi f = 2\pi \frac{c}{\lambda} = 2\pi \frac{3 \text{ m/s}}{(0.25)(40\times10^{-6} \text{ m})} = 2\times10^{6} \text{ rad/s} \qquad \text{F.10}$$

This frequency of 300 kHz is likely too high to provide the observed accelerometer like behavior, since the displacement between the otolith and the membrane would be reduced by a factor of 10^{-6} near 100 Hz. With this resonant frequency, if the otolithic membrane is pinned to the otolith, it should appear to move rigidly with the otolith itself within the fish's hearing bandwidth.

Another possibility is that the hair cell cilia themselves provide the resonance our model requires to explain the fish audiograms. Hair cell cilia are generally considered to be a stiff rod on a hinge. The stiffness associated with this hinge has been measured by statically displacing the cilia of various sensory hair cells. Benser *et al.* (1993), for example, estimated that the stiffness of a hair bundle of a bullfrog is about 1.35 mN/m. The bullfrog hair cell ciliary bundle is about 7 μm in length and 5 μm in diameter. In general, the response of the hair cell is constant based on the angular displacement of the cilia (Howard *et al.* 1988), so it may be more useful to consider the stiffness in terms of the angular displacement. If it is assumed that the force was applied at the tip of the hair cell, then the torsional stiffness of the hinge is 6.6×10^{-14} N·m/rad [based on the stiffness times the bundle length squared (Howard and Ashmore 1986)]. If it is possible to assume that hair cell cilia can be modeled as a cylinder rotating about the axis normal to its axis of symmetry, then the natural frequency is

$$\omega_n = 2\pi f_n = \sqrt{\frac{k_T}{J_O}} = \sqrt{\frac{k_T}{\rho\pi R^2 l\left(\frac{R^2}{4}+\frac{l^2}{3}\right)}} \qquad \text{F.11}$$

where k_T is the torsional stiffness, J_O is the polar mass moment of inertia, ρ is the density of the hair cell, and R and l are the radius and height of the cylinder, respectively. The

cylinder radius will be approximated by the hair cell's diameter, even though the bundle is not a perfectly cylindrical. Note that in general hair cells range in diameter from 1–10 μm (Shatz 1998). If the hair cell has the density of water, the natural frequency is 1.6×10^5 rad/s, or 26 kHz. A few additional estimates based on stiffness values found in the literature are given in Table F.1. These estimates do not take into account the added mass associated with the surrounding fluid, which would tend to lower the estimated natural frequency. It should, however, be adequate for estimating the natural frequency's order of magnitude. The upswing in the fish audiogram only gives a minimum resonant frequency. Although the loss of sensitivity occurs below 10 kHz, it is possible that the appropriate resonance is $O(10^4$ Hz) as suggested by in Table F.1. The otolithic system is complex, and there could be another mechanism causing the loss of sensitivity.

Table F.1 Hair cell natural frequency calculations.

Species	**Stiffness, k [mN/m]**	**Hair Cell Cilia Length, l [μm]**	**Torsional Stiffness ($\approx kl^2$) [N·m/rad]**	**f_n (assuming R =5 μm) [kHz]**	**f_n (assuming R =2.5 μm) [kHz]**
Bullfrog (Benser *et al.* 1993)	1.35	7	6.6×10^{-14}	12	26
Turtle (Crawford and Fettiplace 1985)	0.6	6–7	$2–3\times10^{-14}$	6–8	14–18
Various (Howard *et al.* 1988)	≈1	6–10	4×10^{-14}–1×10^{-13}	9–10	20–25

The idea that the hair cell cilia themselves could serve as the "accelerometer" in the otolithic system is supported by the work of Freeman and Weiss (1988). Their analysis of the fluid forces on a hair-cell like body between two membranes suggests that

at low frequencies the hair cells respond like an accelerometer if (1) the hair cell is unattached to the upper plate and (2) both membranes are moving together. This is contrasted with their analysis of a hair cell on a moving lower membrane beneath (but unattached to) a still upper membrane which (at low frequencies) responds proportionally to the velocity. If the hair cell is connected to the upper membrane, it would respond proportionally to the displacement between the two membranes. Their model predicts a natural frequency of ≈2 kHz for a hair cell modeled as an uncovered two-dimensional flap, 30 μm tall (Freeman and Weiss 1988). This is similar to the values found using the estimates above, particularly since the natural frequency should increase as the height of the flap is reduced. A similar model incorporating data from an alligator lizard cochlea suggests that the hair cell response natural frequency is ≈1 kHz (Weiss and Leong 1985).

The astute reader might suggest that the swimbladder could play a role, at least for hearing specialists. However, the displacements generated by the swimbladder are proportional to the particle velocity and not the acceleration, which is not the behavior seen in the audiogram. In addition, the swimbladder response, which contains no directional information, is believed to be separate from the particle motion response (which results in direct *vs.* indirect pathways in the ear). Although the resonance is within a plausible frequency range [on the order of 1–2 kHz for goldfish swimbladders (Cox 1987)], it does not appear to be the mechanism responsible for the observed accelerometer-like behavior of the ear at low frequencies.

A sketch of the modified fish ear appears in Figure F.4, which illustrates a few key components of this model. First, the otolithic membrane is not explicitly connected to the surroundings, and second, that the hair cell cilia are not attached to the otolith. The estimate of the sensitivity of the hair cells will be made using the audiogram of a hearing generalist.

Using the maximum particle displacement for audible sounds and the above information about how this particle motion translates into the hair cell deflections, it

should be possible to estimate the minimum sensible hair cell deflection. The acoustic particle motion associated with sounds that hearing generalist fish are able to hear is small, on the order of 10^{-11} m for the dab and the cod at 100 Hz. The motion at the base of the hair cell motion is equal to 60% of the acoustic particle motion, and the tip of the hair cell is moving at most $\left(\frac{\omega}{\omega_n}\right)^2$ times the acoustic particle motion. If the natural frequency of the hair cell is 1 kHz (as predicted by Weiss and Leong), then at 100 Hz the tip deflection is a factor of

$$\left(\frac{S.G.-1}{S.G.+0.5}\right)\left(\frac{\omega}{\omega_n}\right)^2 = 0.6\left(\frac{10^2}{10^3}\right)^2 = 0.006 \qquad \text{F.12}$$

less than the acoustic particle motion, or $O(10^{-13}$ m). This does not mean that the individual hair cells are responding to tip movements of $O(10^{-13}$ m = 1 mÅ), but that the array of hair cells acting together is able to sense these motions. If the natural frequency of the hair cells is closer to 10 kHz (as predicted by the measured stiffness of the hair cells), then the tip deflection would be reduced by a factor of

$$\left(\frac{S.G.-1}{S.G.+0.5}\right)\left(\frac{\omega}{\omega_n}\right)^2 = 0.6\left(\frac{10^2}{10^4}\right)^2 = 6\times10^{-5} \qquad \text{F.13}$$

Which corresponds to tip deflections of $O(10^{-15}$ m = 10 μÅ), which would make the hair cells' sensitivity very impressive indeed.

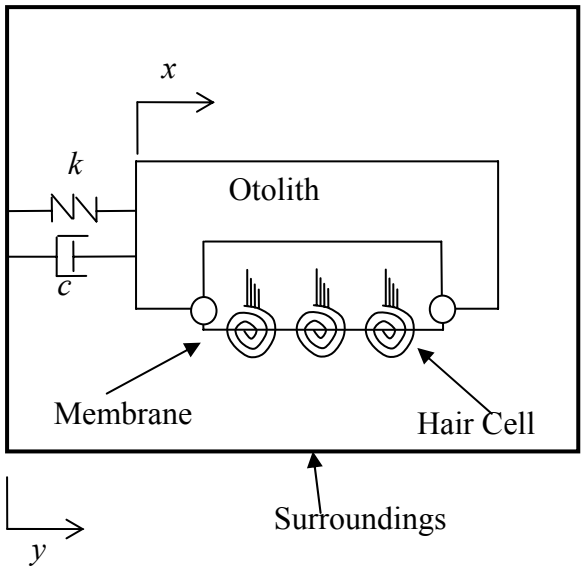

Figure F.4 Modified model fish ear.

REFERENCES

Abrahamson, S. and S. Lonnes (1995). "Uncertainty in Calculating Vorticity from 2D Velocity Fields Using Circulation and Least-Squares Approaches." Experiments in Fluids **20**: 10-20.

Akamatsu, T., D. Wang, K. Nakamura and K. Wang (1998). "Echolocation Range of Captive and Free-Ranging Baiji (*Lipotes vexillifer*), Finless Porpoise (*Neophocaena phocaenoides*), and Bottlenose Dolphin (*Tursiops truncatus*)." Journal of the Acoustical Society of America **104**(4): 2511-2516.

Alassar, R. S. and H. M. Badr (1997). "Oscillating Viscous Flow over a Sphere." Computers and Fluids **26**(7): 661-682.

Alassar, R. S. and H. M. Badr (1999a). "Oscillating Flow over Oblate Spheroids." Acta Mechanica **137**: 237-254.

Alassar, R. S. and H. M. Badr (1999b). "Oscillating Viscous Flow over Prolate Spheroids." Transactions of the Canadian Society for Mechanical Engineering **23**(1A): 83-93.

Amin, N. and N. Riley (1990). "Streaming from a Sphere Due to a Pulsating Source." Journal of Fluid Mechanics **210**: 459-473.

Andres, J. M. and U. Ingard (1953). "Acoustic Streaming at High Reynolds Numbers." Journal of the Acoustical Society of America **25**(5): 928-932.

Astrup, J. and B. Møhl (1993). "Detection of Intense Ultrasound by the Cod *Gadus morhua*." Journal of Experimental Biology **182**(1): 71-80.

Astrup, J. and B. Møhl (1998). "Discrimination between High and Low Repetition Rates of Ultrasonic Pulses by the Cod." Journal of Fish Biology **52**: 205-208.

Batchelor, G. K. (1967). An Introduction to Fluid Dynamics. Cambridge, University Press.

Benser, M. E., N. P. Issa and A. J. Hudspeth (1993). "Hair-Bundle Stiffness Dominates the Elastic Reactance to Otolithic-Membrane Shear." Hearing Research **68**: 243-252.

Bertelsen, A., A. Svardal and S. Tjötta (1973). "Nonlinear Streaming Effects Associated with Oscillating Cylinders." Journal of Fluid Mechanics **59**(3): 493-511.

Bertelsen, A. F. (1974). "An Experimental Investigation of High Reynolds Number Steady Streaming Generated by Oscillating Cylinders." Journal of Fluid Mechanics **64**(3): 589-597.

Bertelsen, A. F. (1980). "A Note on the Steady Streaming Induced around a Circular Cylinder in an Oscillatory Flow Field." Journal of Sound and Vibration **73**(2): 316-320.

Bohme, G. (1992). "On Steady Streaming in Viscoelastic Liquids." Journal of Non-Newtonian Fluid Mechanics **44**: 149-170.

Braun, C. B. and S. Coombs (2000). "The Overlapping Roles of the Inner Ear and Lateral Line: The Active Space of Dipole Source Detection " Philosophical Transactions of the Royal Society of London B: Biological Sciences **355**(1401): 1115-1119.

Brekhovskikh, L. M. and Y. P. Lysanov (2003). Fundamentals of Ocean Acoustics, Third Edition. New York, Springer-Verlag.

Buwalda, R. J. (1981). "A. Segregation of Directional and Nondirectional Acoustic Information in the Cod." Hearing and Sound Communication in Fishes. W. N. Tavolga, A. N. Popper and R. R. Fay, Eds. New York, Springer-Verlag pp. 139-172.

Buwalda, R. J. A., A. Schuijf and A. D. Hawkins (1983). "Discrimination by the Cod of Sounds from Opposing Directions." Journal of Comparative Physiology A **150**(2): 175-184.

Cancelli, C., S. D'Angelo, M. Masili and R. Malvano (1985). "Experimental Results in a Physical Model of the Cochlea." Journal of Fluid Mechanics **153**: 361-388.

Chang, E. J. and M. R. Maxey (1994). "Unsteady Flow about a Sphere at Low to Moderate Reynolds Number. Part 1. Oscillatory Motion." Journal of Fluid Mechanics **277**: 347-379.

Chapman, C. J. and A. D. Hawkins (1973). "A Field Study of Hearing in the Cod, *Gadus morhua* L." Journal of Comparative Physiology **85**(2): 147-167.

Chapman, C. J. and A. D. F. Johnstone (1974). "Some Auditory Discrimination Experiments on Marine Fish." Journal of Experimental Biology **61**: 521-528.

Chapman, C. J. and O. Sand (1974). "Field Studies of Hearing in Two Species of Flatfish, *Pleuronectes platessa* and *Limanda limanda*." Comparative Biochemistry and Physiology - Part A **47**: 371-385.

Chen, S., M. Fatemi and J. F. Greenleaf (2004). "Quantifying Elasticity and Viscosity from Measurement of Shear Wave Speed Dispersion." Journal of the Acoustical Society of America **115**(6): 2781-2785.

Cox, M. (1987). "An Experimental Investigation of the Mechanics of the Periperal Auditory System in Goldfish." Ph.D. dissertation, George W. Woodruff School of Mechanical Engineering, Georgia Institute of Technology, Atlanta, Georgia.

Crawford, A. C. and R. Fettiplace (1985). "The Mechanical Properties of Ciliary Bundles of Turtle Cochlear Hair Cells." The Journal of Physiology **364**(1): 359-379.

Dale, T. (1976). "The Labyrinthine Mechanoreceptor Organs of the Cod *Gadus morhua* L. (Teleostei: Gadidae)." Norwegian Journal of Zoology **24**(2): 85-128.

Danilov, S. D. (1984). "Acoustic Streaming around a Small Sphere." Soviet Physics. Acoustics **30**(6): 452-455.

Danilov, S. D. (1985). "Acoustic Streaming around a Sphere." Soviet Physics. Acoustics **31**(3): 194-196.

Davidson, B. J. and N. Riley (1972). "Jets Induced by Oscillatory Motion." Journal of Fluid Mechanics **53**(2): 287-303.

de Vries, H. L. (1951). "The Mechanics of Labyrinth Otoliths." Acta oto-laryngologica **38**(3): 262-273.

Dimarogonas, A. (1996). Vibrations for Engineers. Upper Saddle River, New Jersey, Prentice-Hall.

Dōhara, N. (1982). "The Unsteady Flow around an Oscillating Sphere in a Viscous Fluid." Journal of the Physical Society of Japan **51**(12): 4095-4103.

Dunkelberger, D. G., J. M. Dean and N. Watabe (1980). "The Ultrastructure of the Otolithic Membrane and Otolith in the Juvenile Mummichog, *Fundulus Heteroclitus*." Journal of Morphology **163**: 367-377.

Enger, P. S. (1981). "Frequency Discrimination in Teleosts -- Central or Peripheral?" Hearing and Sound Communication in Fishes. W. N. Tavolga, A. N. Popper and R. R. Fay, Eds. New York, Springer-Verlag pp. 243-256.

Faraday, M. (1859). Experimental Researches in Chemistry and Physics. London, R. Taylor and W. Francis.

Fay, R. R. (1984). "The Goldfish Ear Codes the Axis of Acoustic Particle Motion in Three Dimensions." Science **225**: 951-954.

Fay, R. R. (1988). "Peripheral Adaptations for Spatial Hearing in Fish." Sensory Biology of Aquatic Animals. J. Atema, R. R. Fay, A. N. Popper and W. N. Tavolga, Eds. New York, Springer-Verlag pp. 711-731.

Fay, R. R. (2005). "Sound Source Localization by Fishes." Sound Source Localization. A. N. Popper and R. R. Fay, Eds. USA, Springer pp. 36-66.

Fay, R. R. and P. L. Edds-Walton (1997). "Directional Response Properties of Saccular Afferents of the Toadfish, *Opsanus tau*." Hearing Research **111**: 1-21.

Flock, Å. (1971). "Sensory Transduction in Hair Cells." Handbook of Sensory Physiology. W. R. Loewenstein, Ed. Berlin, Springer-Verlag pp. 396-441.

Freeman, D. M. and T. F. Weiss (1988). "The Role of Fluid Inertia in Mechanical Stimulation of Hair Cells." Hearing Research **35**: 201-208.

Gennisson, J.-L., S. Catheline, S. Chaffaï and M. Fink (2003). "Transient Elastography in Anisotropic Medium: Application to the Measurement of Slow and Fast Shear Wave Speeds in Muscles." Journal of the Acoustical Society of America **114**(1): 536-541.

Gopal, V. and M. J. Z. Hartmann (2007). "Using hardware models to quantify sensory data acquisition across the rat vibrissal array." Bioinspiration and Biomimetics **2**: S135-S145.

Gopinath, A. (1994). "Steady Streaming Due to Small-Amplitude Superposed Oscillations of a Sphere in a Viscous Fluid." Quarterly Journal of Mechanics and Applied Mathematics **47**(3): 461-480.

Gray, B. (2006). "Artificial Arrays Could Help Submarines Make Like a Fish." Science **313**(5792): 1382-1383.

Haddon, E. W. and N. Riley (1979). "The Steady Streaming Induced between Oscillating Circular Cylinders." Quarterly Journal of Mechanics and Applied Mathematics **32**: 265-282.

Happel, J. and H. Brenner (1965). Low Reynolds Number Hydrodynamics with Special Applications to Particulate Media. Englewood Cliffs, N. J., Prentice-Hall, Inc.

Hartmann, W. (1999). "How We Localize Sound." Physics Today **52**(11): 24-29.

Hassan, E. S. (1985). "A Suggested Role for Secondary Flow in the Stimulation of the Cochlear Hair Cell." Biological Cybernetics **53**: 109-119.

Hawkins, A. D. (1981). "The Hearing Abilities of Fish." Hearing and Sound Communication in Fishes. W. N. Tavolga, A. N. Popper and R. R. Fay, Eds. New York, Springer-Verlag pp. 109-138.

Helfman, G. S., B. B. Collette and D. E. Facey (1997). The Diversity of Fishes. Malden, Massachusetts, Blackwell Science, Inc.

Helle, R. (1974). "Enlarged Hydromechanical Cochlea Model with Basilar Membrane and Tectorial Membrane." Facts and Models in Hearing. E. Zwicker and E. Terhardt, Eds. New York, Springer-Verlag pp. 77-85.

Higa, M. and T. Takahashi (1987). "Stationary Flow Induced by an Unharmonically Oscillating Sphere." Journal of the Physical Society of Japan **56**(5): 1703-1712.

Higgs, D. M., D. T. T. Plachta, A. K. Rollo, M. Singheiser, M. C. Hastings and A. N. Popper (2004). "Development of Ultrasound Detection in American Shad (*Alosa sapidissima*)." The Journal of Experimental Biology **207**: 155-163.

Hofman, P. M. and A. J. Van Opstal (1998). "Spectro-Temporal Factors in Two-Dimensional Human Sound Localization." Journal of the Acoustical Society of America **103**(5): 2634-2648.

Holmes, M. H. (1982). "A Mathematical Model of the Dynamics of the Innner Ear." Journal of Fluid Mechanics **116**: 59-75.

Holtsmark, J., I. Johnsen, T. Sikkeland and S. Skavlem (1954). "Boundary Layer Flow near a Cylindrical Obstacle in an Oscillating Incompressible Fluid." Journal of the Acoustical Society of America **26**(1): 26-39.

Howard, J. and J. F. Ashmore (1986). "Stiffness of Sensory Hair Bundles in the Sacculus of the Frog." Hearing Research **23**: 93-104.

Howard, J., W. M. Roberts and A. J. Hudspeth (1988). "Mechanoelectrical Transduction by Hair Cells." Annual Review of Biophysics and Biophysical Chemistry **17**: 99-124.

Hudspeth, A. J. (2005). "How the Ear's Works Work: Mechanoelectrical Transduction and Amplification by Hair Cells." Comptes Rendus Biologies **328**: 155-162.

Iida, K., T. Mukai, D. Kang and M. Sato (2004). "Morphological Observation of Marine Organisms by Underwater Ultrasonography." OCEANS '04. MTTS/IEEE TECHNO-OCEAN '04 **1**: 357- 363

Jacobs, D. W. and W. N. Tavolga (1967). "Acoustic Intensity Limens in the Goldfish." Animal Behaviour **15**: 324-335.

James, P. W. (1977). "Elastico-Viscous Flow around a Circular Cylinder Executing Small Amplitude, High Frequency Oscillations." Journal of Non-Newtonian Fluid Mechanics **2**: 99-107.

Kalmijn, A. J. (1997). "Electric and Near-Field Acoustic Detection, a Comparative Study." Acta Physiologica Scandinavica **161**(Suppl 638): 25-38.

Kalmijn, A. J. (2003). "Physical Principles of Electric, Magnetic, and Near-Field Acoustic Orientation." Sensory Processing in Aquatic Environments. S. P. Collin and N. J. Marshall, Eds. New York, Springer-Verlag pp. 77-91.

Kaneko, A. and H. Honji (1979). "Double Structures of Steady Streaming in the Oscillatory Viscous Flow over a Wavy Wall." Journal of Fluid Mechanics **93**: 727-736.

Kanwal, R. P. (1955). "Rotatory and Longitudinal Oscillations of Axi-Symmetric Bodies in a Viscous Fluid." Quarterly Journal of Mechanics and Applied Mathematics **8**: 146-163.

Karahalios, G. T. and C. Sfetsos (1988). "On a Sphere Performing Linear and Torsional Oscillations in a Viscous Fluid." Canadian Journal of Physics **66**: 576-579.

Kim, S. K. and A. W. Troesch (1989). "Streaming Flows Generated by High-Frequency Small-Amplitude Oscillations of Arbitrarily Shaped Cylinders." Physics of Fluids A -- Fluid Dynamics **1**(6): 975-985.

Kotas, C. W., M. Yoda and P. H. Rogers (2007). "Visualization of Steady Streaming near Oscillating Spheroids." Experiments in Fluids **42**(1): 111-121.

Kotas, C. W., M. Yoda and P. H. Rogers (2008). "Steady Streaming Flows near Spheroids Oscillated at Multiple Frequencies " Experiments in Fluids.

Kubo, S. and Y. Kitano (1980). "Secondary Flow Induced by a Circular Cylinder Oscillating in Two Directions." Journal of the Physical Society of Japan **49**(5): 2026-2037.

Lai, R. Y. S. and L. F. Mockros (1972). "The Stokes-Flow Drag on Prolate and Oblate Spheroids During Axial Translatory Accelerations." Journal of Fluid Mechanics **52**(1): 1-15.

Lane, C. A. (1955). "Acoustical Streaming in the Vicinity of a Sphere." Journal of the Acoustical Society of America **27**(6): 1082-1086.

Lee, C. P. and T. G. Wang (1989). "Near-Boundary Streaming around a Small Sphere Due to Two Orthogonal Standing Waves." Journal of the Acoustical Society of America **85**(3): 1081-1088.

Lee, C. P. and T. G. Wang (1990). "Outer Acoustic Streaming." Journal of the Acoustical Society of America **88**(5): 2367-2375.

Leong, C. W. and J. M. Ottino (1989). "Experiments on Mixing Due to Chaotic Advection in a Cavity." Journal of Fluid Mechanics **209**: 463-499.

Lesser, M. B. and D. A. Berkley (1972). "Fluid Mechanics of the Cochlea. Part 1." Journal of Fluid Mechanics **51**(3): 497-512.

Lighthill, J. (1978a). "Acoustic Streaming." Journal of Sound and Vibration **61**(3): 391-418.

Lighthill, J. (1978b). Waves in Fluids. Cambridge, Cambridge University Press.

Lighthill, J. (1992). "Acoustic Streaming in the Ear Itself." Journal of Fluid Mechanics **239**: 551-606.

Liu, P. L. F., M. H. Davis and S. Downing (1996). "Wave-Induced Boundary Layer Flows above and in a Permeable Bed." Journal of Fluid Mechanics **325**: 195-218.

Lombarte, A. and A. N. Popper (1994). "Quantitative Analyses of Postembryonic Hair Cell Addition in the Otolithic Endorgans of the Inner Ear of the European Hake, M*erluccius merluccius* (Gadiformes, Teleostei)." Journal of Comparative Neurology **345**(3): 419-428.

Lombarte, A., H. Y. Yan, A. N. Popper, J. S. Chang and C. Platt (1993). "Damage and Regeneration of Hair Cell Ciliary Bundles in a Fish Ear Following Treatment with Gentamicin." Hearing Research **64**(2): 166-174.

Lyne, W. H. (1971). "Unsteady Viscous Flow over a Wavy Wall." Journal of Fluid Mechanics **50**: 33-48.

Mann, D. A., Z. Lu, M. C. Hastings and A. N. Popper (1998). "Detection of Ultrasonic Tones and Simulated Dolphin Echolocation Clicks by a Teleost Fish, the

American Shad (*Alosa Sapidissima*)." Journal of the Acoustical Society of America **104**(1): 562-568.

Mason, A. C., M. L. Oshinsky and R. R. Hoy (2001). "Hyperacute directional hearing in a microscale auditory system." Nature **410**: 686-690.

McCauley, R. D. and D. H. Cato (2000). "Patterns of Fish Calling in a Nearshore Environment in the Great Barrier Reef." Philosophical Transactions of the Royal Society B **355**(1401): 1289-1293.

Meinhart, C. D., S. T. Wereley and J. G. Santiago (2000). "A PIV Algorithm for Estimating Time-Averaged Velocity Fields." Journal of Fluids Engineering **122**(2): 285-289.

Mercado III, E. and L. N. Frazer (1999). "Environmental Constraints on Sound Transmission by Humpback Whales." Journal of the Acoustical Society of America **106**(5): 3004-3016.

Miyagi, T. and K. Nakahasi (1975). "Secondary Flow Induced by an Unharmonically Oscillating Circular Cylinder." Journal of the Physical Society of Japan **39**(2): 519-526.

Nyborg, W. L. (1998). "Acoustic Streaming." Nonlinear Acoustics. M. F. Hamilton and D. T. Blackstock, Eds. San Diego, Academic Press.

Nyborg, W. L. M. (1965). "Acoustic Streaming." Physical Acoustics: Principles and Methods. W. P. Mason, Ed. New York and London, Academic Press pp. 265-331.

Odar, F. and W. S. Hamilton (1964). "Forces on a Sphere Accelerating in a Viscous Liquid." Journal of Fluid Mechanics **18**(2): 302-314.

Oestreicher, H. L. (1951). "Field and Impedance of an Oscillating Sphere in a Viscoelastic Medium with an Application to Biophysics." Journal of the Acoustical Society of America **23**(6): 707-714.

Peleshanko, S., M. D. Julian, M. Ornatska, M. E. McConney, M. C. LeMieux, N. Chen, C. Tucker, Y. Yang, C. Liu, J. A. C. Humphrey and V. V. Tsukruk (2007). "Hydrogel-Encapsulated Microfabricated Haircells Mimicking Fish Cupula Neuromast." Advanced Materials **19**: 2903-2909.

Petit, L. and P. Gondret (1992). "Redressement D'un Écoulement Alternatif." Journal de Physique II France **2**: 2115-2144.

Piddington, R. W. (1972). "Auditory Discrimination between Compressions and Rarefactions by Goldfish." Journal of Experimental Biology **56**: 403-419.

Pierce, A. D. (1994). Acoustics: An Introduction to Its Physical Principles and Applications. Woodbury, NY, Acoustical Society of America through the American Institute of Physics.

Platt, C. and A. Popper (1981). "Fine Structure and Function of the Ear." Hearing and Sound Communication in Fishes. W. N. Tavolga, A. N. Popper and R. R. Fay, Eds. New York, Springer-Verlag pp. 3-38.

Pope, S. B. (2000). Turbulent Flows. Cambridge, UK, Cambridge University Press.

Popper, A. N. and S. Coombs (1980). "Auditory Mechanisms in Teleost Fishes." American Scientist **68**: 429-440.

Popper, A. N. and R. R. Fay (1993). "Sound Detection and Processing by Fish: Critical Review and Major Research Questions." Brain, Behavior and Evolution **41**: 14-38.

Popper, A. N., R. R. Fay, C. Platt and O. Sand (2003). "Sound Detection Mechanisms and Capabilities of Teleost Fishes." Sensory Processing in Aquatic Environments. S. P. Collin and N. J. Marshall, Eds. New York, Springer-Verlag pp. 3-38.

Popper, A. N. and Z. Lu (2000). "Structure-Function Relationships in Fish Otolith Organs." Fisheries Research **46**: 15-25.

Popper, A. N. and personnel. (2003). "Scanning Electron Micrographs of Fish Ears." Retrieved August 5, 2005, from http://www.life.umd.edu/biology/popperlab/background/ultrastructuresurface.htm.

Popper, A. N., J. Ramcharitar and S. E. Campana (2005). "Why Otoliths? Insights from the Inner ear Physiology and Fisheries Biology." Marine and Freshwater Research **56**(5): 497-504.

Popper, A. N., P. H. Rogers, W. M. Saidel and M. Cox (1988). "Role of the Fish Ear in Sound Processing." Sensory Biology of Aquatic Animals. J. Atema, R. R. Fay, A. N. Popper and W. N. Tavolga, Eds. New York, Springer-Verlag pp. 687-710.

Pozrikidis, C. (1989). "A Study of Linearized Oscillatory Flow Past Particles by the Boundary -Integral Method." Journal of Fluid Mechanics **202**: 17-41.

Raney, W. P., J. C. Corelli and P. J. Westervelt (1954). "Acoustical Streaming in the Vicinity of a Cylinder." Journal of the Acoustical Society of America **26**(6): 1006-1014.

Rayleigh, J. W. S. (1883). "On the Crculation of Air Observed in Kundt's Tubes, and Some Allied Acoustical Problems." Philosophical Transactions of the Royal Society of London A **175**: 1-21.

Rednikov, A. Y. and S. S. Sadhal (2004). "Steady Streaming from an Oblate Spheroid Due to Vibrations Along Its Axis." Journal of Fluid Mechanics **499**: 345-380.

Riley, N. (1966). "On a Sphere Oscillating in a Viscous Fluid." Quarterly Journal of Mechanics and Applied Mathematics **19**(4): 461-472.

Riley, N. (1967). "Oscillatory Viscous Flows. Review and Extension." Journal of the Institute of Mathematics and its Applications **3**: 419-434.

Riley, N. (1998). "Acoustic Streaming." Theoretical and Computational Fluid Dynamics **10**: 349-356.

Riley, N. (2001). "Steady Streaming." Annual Review of Fluid Mechanics **33**: 43-65.

Roederer, J. (1973). Introduction to the Physics and Psychophysics of Music. London, The English Universities Press.

Rogers, P. H. and M. Cox (1988). "Underwater Sound as a Biological Stimulus." Sensory Biology of Aquatic Animals. J. Atema, R. R. Fay, A. N. Popper and W. N. Tavolga, Eds. New York, Springer-Verlag pp. 131-149.

Rogers, P. H., A. N. Popper, M. C. Hastings and W. M. Saidel (1988). "Processing of Acoustic Signals in the Auditory System of Bony Fish." Journal of the Acoustical Society of America **83**(1): 338-349.

Sand, O. and P. S. Enger (1973). "Evidence For an Auditory Function of the Swimbladder in the Cod." Journal of Experimental Biology **59**: 405-414.

Sand, O. and H. E. Karlsen (1986). "Detection of Infrasound by the Atlantic Cod." Journal of Experimental Biology **125**(1): 197-204.

Sand, O. and H. E. Karlsen (2000). "Detection of Infrasound and Linear Acceleration in Fishes." Philosophical Transactions of the Royal Society of London B: Biological Sciences **355**: 1295-1298.

Sand, O. and A. Michelsen (1978). "Vibration Measurements of the Perch Saccular Otolith." Journal of Comparative Physiology A **123**: 85-89.

Schellart, N. A. and R. J. Wubbels (1997). "The Auditory and Mechanosensory Lateral Line System." The Physiology of Fishes. D. H. Evans, Ed. Boca Raton, CRC Press pp. 285-314.

Schlichting, V. H. (1932). "Berechnung Ebener Periodischer Grenzschichtstromungen." Physikalische Zeitschrift **33**: 327-335.

Schuijf, A. (1975). "Directional Hearing of Cod (*Gadus morhua*) under Approximate Free Field Conditions." Journal of Comparative Physiology **98**(4): 307-332.

Schuijf, A. (1981). "Models of Acoustic Localization." Hearing and Sound Communication in Fishes. W. N. Tavolga, A. N. Popper and R. R. Fay, Eds. New York, Springer-Verlag pp. 267-310.

Secomb, T. W. (1978). "Flow in a Channel with Pulsating Walls." Journal of Fluid Mechanics **88**: 273-288.

Shankar, P. N. and M. D. Deshpande (2000). "Fluid Mechanics in the Driven Cavity." Annual Review of Fluid Mechanics **32**: 93-136.

Shatz, L. F. (1998). "The Effect of Shape on the Hydrodynamics of a Hemispheroid Projecting from a Plate in Irrotational Fluid." Physics of Fluids **10**(9): 2177-2187.

Skavlem, S. and S. Tjötta (1955). "Steady Rotational Flow of an Incompressible, Viscous Fluid Enclosed between Two Coaxial Cylinders." Journal of the Acoustical Society of America **27**(1): 26-33.

Solomon, J. H. and M. J. Hartmann (2006). "Robotic whiskers used to sense features." Nature **443**: 525.

Steele, C. R. (1973). "A Possibility for Sub-Tectorial Membrane Fluid Motion." Basic Mechanisms in Hearing. A. R. Møller and P. Boston, Eds. New York, Academic Press, Inc. pp. 69-93.

Stokes, S. G. G. (1850). "On the Effect of the Internal Friction of Fluids on the Motion of Pendulums." Transactions of the Cambridge Philosophical Society **9**: 8-.

Stuart, J. T. (1963). "Unsteady Boundary Layers." Laminar Boundary Layers. L. Rosenhead, Ed. Oxford, Clarendon Press pp. 349-406.

Stuart, J. T. (1966). "Double Boundary Layers in Oscillatory Viscous Flow." Journal of Fluid Mechanics **24**(4): 673-687.

Taneda, S. (1979). "Visualization of Separating Stokes Flows." Journal of the Physical Society of Japan **46**(6): 1935-1942.

Tatsuno, M. (1981). "Secondary Flow Induced by a Circular Cylinder Performing Unharmonic Oscillations." Journal of the Physical Society of Japan **50**(1): 330-337.

ten Kate, K. H. and J. W. Kuiper (1970). "The Viscosity of the Pike's Endolymph." Journal of Experimental Biology **53**: 495-500.

Thomson, D. H. and W. J. Richardson (1995). "Marine Mammal Sounds." Marine Mammals and Noise. W. J. Richardson, J. Charles R. Greene, C. I. Malme and D. H. Thomson, Eds. San Diego, Academic Press pp. 159-204.

Tonndorf, J. (1958). "Harmonic Distortion in Cochlear Models." Journal of the Acoustical Society of America **30**(10): 929-937.

Tonndorf, J. (1960). "Dimensional Analysis of Cochlear Models." Journal of the Acoustical Society of America **32**(4): 493-497.

Tonndorf, J. (1986). "Auditory Nonlinearities: The Role of Cochlear Hydromechanics." Hearing Research **22**: 223-227.

van Bergeijk, W. A. (1967). "The Evolution of Vertebrate Hearing." Contributions to Sensory Physiology. W. D. Neff, Ed. New York and London, Academic Press pp. 1-49.

van den Berg, A. V. and R. J. A. Buwalda (1994). "Source Localization in Underwater Sound Fields." Biological Cybernetics **70**: 255-265.

Venkatalaxmi, A., B. S. Padmavathi and T. Amaranath (2004). "A General Solution of Unsteady Stokes Equations." Fluid Dynamics Research **35**: 229-236.

Vogel, M. J., A. H. Hirsa and J. M. Lopez (2003). "Spatio-Temporal Dynamics of a Periodically Driven Cavity Fow." Journal of Fluid Mechanics **478**: 197-226.

von Békésy, G. (1960). Experiments in Hearing. New York, Acoustical Society of America.

von Békésy, G. (1964). "Concerning the Pleasures of Observing, and the Mechanics of the Inner ear, Nobel Lecture, December 11, 1961." Nobel Lectures, Physiology or Medicine 1942-1962. Amsterdam, Elsevier Publishing Company, pp. 722-746.

Wang, C.-Y. (1965). "The Flow Field Induced by an Oscillating Sphere." Journal of Sound and Vibration **2**(3): 257-269.

Weiss, T. F. and R. Leong (1985). "A Model for Signal Transmission in an Ear Having Hair Cells with Free-Standing Stereocilia. III. Micromechanical Stage." Hearing Research **20**: 157-174.

Westerweel, J. and F. Scarano (2005). "Universal Outlier Detection for PIV Data." Experiments in Fluids **39**(6): 1096-1100.

Wubbels, R. J. and N. A. M. Schellart (1997). "Neuronal Encoding of Sound Direction in the Auditory Midbrain of the Rainbow Trout." Journal of Neurophysiology **77**(6): 3060-3074.

Wybrow, M. F. and N. Riley (1996). "Oscillatory Flow over a Cylinder Resting on a Plane Boundary." European Journal of Applied Mathematics **7**: 545-558.

Wybrow, M. F., B. Yan and N. Riley (1996). "Oscillatory Flow over a Circular Cylinder Close to a Plane Boundary." Fluid Dynamics Research **18**: 269-288.

Yan, B., D. B. Ingham and B. R. Morton (1993). "Streaming Flow Induced by an Oscillating Cascade of Circular Cylinders." Journal of Fluid Mechanics **252**: 147-171.

Yoda, M., P. H. Rogers and K. E. Baxter (2001). "Is The Fish Ear an Auditory Retina? Steady Streaming in the Otolith-Macula Gap." Bioacoustics-The International Journal of Animal Sound and Its Recording **12**(2/3): 131-134.

Zhang, P. X. and W. M. Hartmann (2006). "Lateralization of Sine Tones-Interaural Time *vs* Phase." Journal of the Acoustical Society of America **120**(6): 3471-3474.